![NASA logo]

Active Sensing of CO$_2$ Emissions over Nights, Days, and Seasons (ASCENDS): Final Report of the ASCENDS Ad Hoc Science Definition Team

S. Randolph Kawa, James B. Abshire, David F. Baker, Edward V. Browell, David Crisp, Sean M. R. Crowell, Jason J. Hyon, Joseph C. Jacob, Kenneth W. Jucks, Bing Lin, Robert T. Menzies, Lesley E. Ott, and T. Scott Zaccheo

X$_{CO2}$ July 1 - 16

392   ppm   408
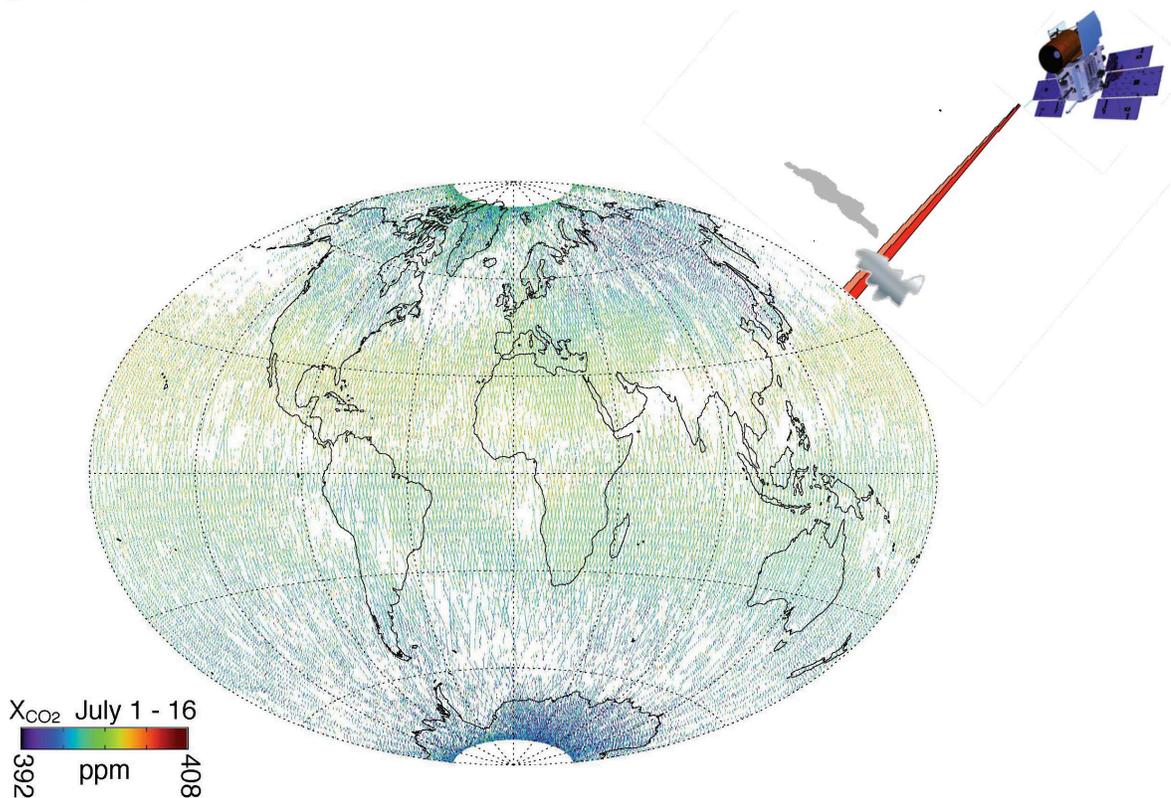
National Aeronautics and
Space Administration

**Goddard Space Flight Center
Greenbelt, Maryland 20771**

November 2018

NASA STI Program ... in Profile

Since its founding, NASA has been dedicated to the advancement of aeronautics and space science. The NASA scientific and technical information (STI) program plays a key part in helping NASA maintain this important role.

The NASA STI program operates under the auspices of the Agency Chief Information Officer. It collects, organizes, provides for archiving, and disseminates NASA's STI. The NASA STI program provides access to the NASA Aeronautics and Space Database and its public interface, the NASA Technical Report Server, thus providing one of the largest collections of aeronautical and space science STI in the world. Results are published in both non-NASA channels and by NASA in the NASA STI Report Series, which includes the following report types:

- TECHNICAL PUBLICATION. Reports of completed research or a major significant phase of research that present the results of NASA Programs and include extensive data or theoretical analysis. Includes compilations of significant scientific and technical data and information deemed to be of continuing reference value. NASA counterpart of peer-reviewed formal professional papers but has less stringent limitations on manuscript length and extent of graphic presentations.

- TECHNICAL MEMORANDUM. Scientific and technical findings that are preliminary or of specialized interest, e.g., quick release reports, working papers, and bibliographies that contain minimal annotation. Does not contain extensive analysis.

- CONTRACTOR REPORT. Scientific and technical findings by NASA-sponsored contractors and grantees.

- CONFERENCE PUBLICATION. Collected papers from scientific and technical conferences, symposia, seminars, or other meetings sponsored or co-sponsored by NASA.

- SPECIAL PUBLICATION. Scientific, technical, or historical information from NASA programs, projects, and missions, often concerned with subjects having substantial public interest.

- TECHNICAL TRANSLATION. English-language translations of foreign scientific and technical material pertinent to NASA's mission.

Specialized services also include organizing and publishing research results, distributing specialized research announcements and feeds, providing help desk and personal search support, and enabling data exchange services. For more information about the NASA STI program, see the following:

- Access the NASA STI program home page at http://www.sti.nasa.gov

- E-mail your question via the Internet to help@sti.nasa.gov

- Phone the NASA STI Information Desk at 757-864-9658

- Write to:
  NASA STI Information Desk
  Mail Stop 148
  NASA's Langley Research Center
  Hampton, VA 23681-2199

Active Sensing of CO$_2$ Emissions over Nights, Days, and Seasons (ASCENDS): Final Report of the ASCENDS Ad Hoc Science Definition Team

S. Randolph Kawa, NASA's Goddard Space Flight Center, Greenbelt, MD

James B. Abshire, NASA's Goddard Space Flight Center, Greenbelt, MD

David F. Baker, CIRA/ Colorado State University, Fort Collins, CO

Edward V. Browell, NASA's Langley Research Center, Hampton, VA

David Crisp, NASA's Jet Propulsion Laboratory / California Institute of Technology, Pasadena, CA Sean

M. R. Crowell, University of Oklahoma, Norman, OK

Jason J. Hyon, NASA's Jet Propulsion Laboratory/ California Institute of Technology, Pasadena, CA

Joseph C. Jacob, NASA's Jet Propulsion Laboratory/ California Institute of Technology, Pasadena, CA

Kenneth W. Jucks, NASA Headquarters, Washington, DC

Bing Lin, NASA's Langley Research Center, Hampton, VA

Robert T. Menzies, NASA's Jet Propulsion Laboratory/ California Institute of Technology, Pasadena, CA

Lesley E. Ott, NASA's Goddard Space Flight Center, Greenbelt, MD

T. Scott Zaccheo, Atmospheric and Environmental Research, Inc., Lexington, MA

AUTHORS, CONTRIBUTORS, AND REVIEWERS

Lead Authors

S. Randolph Kawa	NASA Goddard Space Flight Center
James B. Abshire	NASA Goddard Space Flight Center
David F. Baker	CIRA/ Colorado State University
Edward V. Browell	NASA Langley Research Center
David Crisp	Jet Propulsion Laboratory / California Institute of Technology
Sean M. R. Crowell	University of Oklahoma
Jason J. Hyon	Jet Propulsion Laboratory/ California Institute of Technology
Joseph C. Jacob	Jet Propulsion Laboratory/ California Institute of Technology
Kenneth W. Jucks	NASA Headquarters
Bing Lin	NASA Langley Research Center
Robert T. Menzies	Jet Propulsion Laboratory/ California Institute of Technology
Lesley E. Ott	NASA Goddard Space Flight Center
T. Scott Zaccheo	Atmospheric and Environmental Research, Inc.

Contributors

Dorit M. Hammerling	National Center for Atmospheric Research
Anna M. Michalak	Carnegie Institution for Science, Stanford
Berrien Moore III	University of Oklahoma
Christopher W. O'Dell	Colorado State University
Michael D. Obland	NASA Langley Research Center
Mulugeta Petros	NASA Langley Research Center
Tamer F. Refaat	NASA Langley Research Center
Haris Riris	NASA Goddard Space Flight Center
Otilia I. Rodriguez-Alvarez	NASA Goddard Space Flight Center
Andrew E. Schuh	Colorado State University
Yoichi Shiga	Stanford University
Upendra N. Singh	NASA Langley Research Center
Gary D. Spiers	Jet Propulsion Laboratory/ California Institute of Technology
James S. Wang	NASA Goddard Space Flight Center

Reviewers

Abhishek Chatterjee	Universities Space Research Association/ NASA Goddard Space Flight Center
Charles E. Miller	Jet Propulsion Laboratory/ California Institute of Technology
David S. Schimel	Jet Propulsion Laboratory/ California Institute of Technology

Contributing Editor

Felicia M. Vilnrotter	Raytheon

Revision History:

Version	Date	Description/Comments
1.0	11/16/2018	Active Sensing of CO$_2$: ASCENDS Mission Definition Final Report

TABLE OF CONTENTS

LIST OF FIGURES

LIST OF TABLES

LIST OF BOXES

Executive Summary

Improved remote sensing observations of atmospheric carbon dioxide (CO_2) are critically needed to quantify, monitor, and understand the Earth's carbon cycle and its evolution in a changing climate. The processes governing ocean and terrestrial carbon uptake remain poorly understood, especially in dynamic regions with large carbon stocks and strong vulnerability to climate change, for example, the tropical land biosphere, the northern hemisphere high latitudes, and the Southern Ocean. Because the passive spectrometers used by GOSAT (Greenhouse gases Observing SATellite) and OCO-2 (Orbiting Carbon Observatory-2) require sunlit and cloud-free conditions, current observations over these regions remain infrequent and are subject to biases. These shortcomings limit our ability to understand and predict the processes controlling the carbon cycle on regional to global scales.

In contrast, active CO_2 remote-sensing techniques allow accurate measurements to be taken day and night, over ocean and land surfaces, in the presence of thin or scattered clouds, and at all times of year. Because of these benefits, the National Research Council recommended the National Aeronautics and Space Administration (NASA) Active Sensing of CO_2 Emissions over Nights, Days, and Seasons (ASCENDS) mission in the 2007 report Earth Science and Applications from Space: National Imperatives for the Next Decade and Beyond. The ability of ASCENDS to collect low-bias observations in these key regions is expected to address important gaps in our knowledge of the contemporary carbon cycle.

The ASCENDS ad hoc Science Definition Team (SDT), comprised of carbon cycle modeling and active remote sensing instrument teams throughout the United States (US), worked to develop the mission's requirements and advance its readiness from 2008 through 2018. Numerous scientific investigations were carried out to identify the benefit and feasibility of active CO_2 remote sensing measurements for improving our understanding of CO_2 sources and sinks. This report summarizes their findings and recommendations based on mission modeling studies, analysis of ancillary meteorological data products, development and demonstration of candidate technologies, and design studies of the ASCENDS mission concept.

The ASCENDS modeling studies have demonstrated that:

1. ASCENDS will resolve statistically significant differences in total column CO_2 concentrations, resulting from foreseeable changes in surface flux over the entire globe. These flux changes could include identifying CO_2 emissions from permafrost thaw at high latitudes, shifting patterns in regional fossil fuel emissions, the evolving nature of the Southern Ocean carbon flux, and/or changes to tropical and mid-latitude terrestrial sinks.
2. ASCENDS will substantially advance our understanding of the carbon cycle through improved flux estimates with reduced uncertainty at global to regional scales. Reduced flux uncertainties at regional scales are necessary for improved understanding of the processes controlling long-term carbon sinks.
3. ASCENDS measurements also have the potential to reduce biases due primarily to lower susceptibility to errors from atmospheric scattering and those due to changes in illumination geometry. This can contribute significantly towards improving constraints on surface fluxes beyond passive sensors such as GOSAT and OCO-2.

During the past decade, NASA has invested in the development of several different Integrated Path Differential Absorption (IPDA) lidar approaches and associated technologies that are candidates for ASCENDS. The IPDA approach measures the range to the scattering surface and the column

abundance of CO_2 with increased sensitivity across the mid and lower troposphere. Several aircraft field campaigns using space simulator instruments demonstrated that:

1. Accurate CO_2 column mixing ratios can be retrieved from airborne lidar data.
2. Evaluation against in situ aircraft observations show that CO_2 column absorption measurements can be made with high precision and low bias over a wide range of surface types and between scattered clouds.
3. High-quality observations can be made to cloud tops and through thin clouds and aerosol layers.

In addition, evaluation of the magnitude of errors in current meteorological reanalyses helped to clarify the need for ancillary atmospheric measurements and to define the error budget for ASCENDS measurements. Statistical analysis of meteorological products from three different atmospheric modeling centers shows that uncertainty in current surface pressure estimates from models is typically less than 0.1% except in high latitudes regions. These findings were used to eliminate the need for a coincident oxygen measurement to meet the desired CO_2 mixing ratio accuracy for ASCENDS.

These studies and field activities have greatly improved our understanding of the space-based capabilities required for ASCENDS, and represent significant progress toward meeting the demands of an active remote-sensing mission. Integrating results from the measurement campaigns and modeling studies, the ASCENDS ad hoc SDT developed a set of measurement requirements as well as a study of the ASCENDS mission that demonstrates the mission is feasible. The results of this study show that multiple commercially-available spacecraft buses should be able to accommodate an ASCENDS instrument. In addition, the Falcon 9 or other smaller launch vehicles can accommodate an ASCENDS observatory.

An active CO_2 mission would provide a unique complement to the expanding international constellation of passive CO_2 missions, helping to fill critical gaps in coverage and to reduce biases in key areas through cross calibrations. This report also outlines areas where further research is needed. These include but are not limited to:

1. Modeling studies that examine the role of ASCENDS in a future international constellation of planned passive and active space sensors as well as studies to evaluate the impact of different orbit choices and vertical information on flux inference.
2. Aircraft campaigns targeting observations over high latitudes and the tropics, including those to coincide with CO_2 observations from passive satellite instruments on orbit.
3. Improve techniques for the retrieval of vertical profile information.
4. Developing candidate mission approaches to have a lower cost to NASA in order to meet limitations of the Explorer class of missions recommended by the 2017 Decadal Survey. Potential approaches include pursuit of international partnerships or deployment to the International Space Station (ISS).

It is hoped that the findings and activities of the ASCENDS ad hoc SDT will continue to advance mission readiness in coordination with the carbon cycle science community.

1. Introduction

1.1 Justification and Key Science Questions

The fourth and fifth Assessment Reports of the Intergovernmental Panel on Climate Change (IPCC) conclude that warming of the global climate system is unequivocal, and anthropogenic emissions of greenhouse gases are responsible for most of the increase (IPCC, 2007 and IPCC, 2013). Additionally, the reports state that the interaction between the global carbon cycle and the physical climate system is still a substantial source of uncertainty in climate projections.

The difference between observed increases in atmospheric CO_2 concentrations and anthropogenic CO_2 emissions indicates that terrestrial and oceanic sinks have absorbed approximately 55% of the CO_2 generated by human activities. There are, however, significant year to-year variations. Although these variations are attributed to changes in the net sinks, the processes governing sink strengths and the relative partitioning of CO_2 between terrestrial, oceanic, and atmospheric reservoirs are poorly understood.

Errors in the representation of these processes in existing coupled carbon-climate models lead to large uncertainties in long-term climate projections. Therefore, improving our understanding of carbon feedback processes is critical to improving projections of atmospheric CO_2 levels and Earth's climate.

In order to address the gaps in our current understanding of atmospheric CO_2 and its relationship to climate change, three overarching needs have been defined (NASA, 2008). They are to:

- *Improve our understanding of the current magnitude and distribution of terrestrial and oceanic sources and sinks, distinguishing between natural and anthropogenic sources and sinks,*

- *Improve our understanding of the time scales of natural sources and sinks, from short (e.g. diurnal) to medium (seasonal/annual) to extended (climatological) time scales, including processes resulting from ecosystem/biosphere disturbances, and*

- *Improve our ability to predict/model long-term changes in the climate system due to natural variability of carbon sources and sinks, as well as the transport of carbon through the atmosphere.*

Globally distributed atmospheric CO_2 measurements are critical to address these needs. The fluxes of CO_2 to/from the surface vary widely in space and time. The resulting gradients in concentration caused by the fluxes are relatively small and are mixed and integrated by atmospheric transport. Sampling atmospheric CO_2 in time and space can be used, along with appropriate transport and inversion models, to quantify the surface fluxes. The remote sensing challenge is to provide the atmospheric CO_2 measurements with sufficient global coverage, accuracy, and sampling frequency to support accurate inference of the locations and magnitudes of the sources and sinks.

1.2 CO₂ Measurements Near the Surface

The modern atmospheric CO_2 measurement record began in 1957 with flask measurements taken atop Mauna Loa. These provided samples of the global background concentration of atmospheric CO_2. Over the years, our understanding of the spatial and temporal variations in atmospheric CO_2 concentrations has improved via the establishment of additional ground measurement sites providing both surface and tower measurements, aircraft campaigns and routine airborne observations, and most recently, contributions from space-based remote sensing. Yet there remain

significant gaps in our understanding that result from limited measurements, particularly related to the distribution and variability of terrestrial and oceanic sinks and the processes controlling this variability.

1.3 Space Missions Using Passive Remote Sensing

The important first steps toward measuring greenhouse gases globally from space were demonstrated using spectrometers that viewed the Earth's thermal emission or reflected sunlight, e.g., SCIAMACHY (SCanning Imaging Absorption spectroMeter for Atmospheric CartograpHY) on ENVISAT (Environmental Satellite), AIRS (Atmospheric Infrared Sounder), and IASI (Infrared Atmospheric Sounding Interferometer). Their observations have been critical in demonstrating the use of space-based spectrometers to address questions about atmospheric composition. However, all these early multi-purpose instruments had relatively coarse spectral resolution and large measurement footprints that limited their coverage and the precisions and accuracies of their retrievals.

Subsequently several satellite missions have been developed specifically for measuring atmospheric CO_2 using higher resolution passive spectrometers. In particular, the Japanese Greenhouse gas Observing Satellite (GOSAT) was launched in 2009 and NASA's OCO-2 mission was launched during July 2014. The precision of OCO-2 and GOSAT CO_2 measurements has been assessed by comparing the measurements to those from ground-based spectrometers, i.e., the Total Column Concentration Observing Network (TCCON). While OCO-2 data show higher precision observations from space than previous missions, questions remain regarding measurement biases that can impact CO_2 flux calculations. More details on these missions are in Section 2.

1.4 Benefits of Active (Laser-Based) CO₂ Measurements

Passive measurement techniques have some inherent limitations. Conditions favorable to accurate measurement of the atmospheric gases require sunlit scenes, cloud-free conditions, and accurate estimates of surface elevation.

The Earth's atmosphere is complex and optical scattering by clouds and aerosols is common. For passive sensors, this scattering causes variability in the optical path length and hence contributes to spatially and temporally varying biases. There are also wide variations in surface elevation, due to topography and vegetation, which change the length of the measurement path and the CO_2 column. The accuracy of measurements at large solar zenith angles is also limited due to scattering and by variability in surface reflectance. The resulting sparse coverage of passive spectrometers at high latitudes is a serious limitation, particularly for the Northern Hemisphere, since these regions exhibit substantial emissions during the year.

In contrast, an active (laser) remote sensor carries its illumination source whose characteristics have been carefully optimized for these measurements. It involves a simple fixed observational geometry, with a common vertical illumination and observation path. The range-resolved laser measurements eliminate errors from atmospheric scattering. This approach allows measurements to be taken day and night, over ocean and land surfaces, at all latitudes, and at all times of year. Active CO_2 remote sensing also enables enhanced sensitivity to CO_2 in the lower troposphere, where the atmospheric concentrations respond most strongly to surface fluxes. Over oceans, a lidar enables more frequent observations of the Southern Ocean, especially in the wintertime, where dark oceans are virtually inaccessible to shortwave passive systems.

The ability of active CO_2 sensors to measure during day and night provides information that is unavailable to passive systems that rely on reflected sunlight. Nocturnal measurements with atmospheric weighting toward the surface are desired for investigations of respiration and urban areas. Since lidar can make effective measurements regardless of local observation time, various non-Sun synchronous orbits also can be considered to provide additional information about diurnal cycles on different time scales.

Depending on the approach chosen, there are other potential benefits from lidar measurements. Higher spatial sampling, for example, would allow detection of strong, localized gradients in CO_2 concentration to facilitate investigations in complex terrain. It could also enable measurements through small gaps in scattered clouds and to cloud tops, significantly improving the measurement density and coverage under these conditions. Lidar measurements may also provide additional information on the vertical profile of CO_2, which could support more direct quantification of surface fluxes.

1.5   Objectives for ASCENDS

To address these unmet needs, more accurate remote sensing measurements of atmospheric CO_2 are required with more complete, unbiased global coverage. In the US, the National Research Council's 2007 Decadal Survey (NRC, 2007) recommended the Active Sensing of CO_2 Emissions over Nights, Days, and Seasons (ASCENDS) mission (NASA Goddard, n.d.). The stated objectives of ASCENDS were to:

1) Quantify the global spatial distribution of atmospheric CO_2 on scales of weather models in the 2010-2020 era;
2) Quantify the current global spatial distribution of terrestrial and oceanic sources and sinks of CO_2 on 1-degree grids at weekly resolution; and
3) Provide a scientific basis for future projections of CO_2 sources and sinks through data-driven enhancements of the Earth-system process modeling.

An important consideration for this mission is that the CO_2 fluxes from the surface cause only small changes in the spatial distributions of CO_2 concentrations in the troposphere. Hence the remote sensing challenge is to accurately measure these small changes in CO_2 concentrations globally. The required levels of measurement uncertainty that must be attained over a wide range of atmospheric and surface conditions are typically <0.25% (<1 ppm).

1.6   The ASCENDS Approach

Greenhouse gas measurements made using a range-resolved IPDA lidar approach are independent of solar angle and of prior knowledge of scattering surface elevation. Measurements with high precision and low bias can be made under a wide variety of atmospheric and topographic conditions thus allowing extended spatial coverage. The lidar can sample a selected gas absorption line, measure the surface elevation, and retrieve the gas column abundance. The range resolving capability of the lidar enables accurate measurement of scattering surface elevation and atmospheric path length, as well as excluding biases due to the optical scatter by clouds and aerosols.

The basic approach for the ASCENDS measurements of CO_2 is shown in Figure 1-1. This example depicts a pulsed approach using the minimum of two wavelengths to sample the absorption line. The figure shows two beams (red and blue) directed at nadir, corresponding to the laser pulses tuned on and off the absorption line. They pass through the atmospheric column containing an unknown concentration of CO_2 and illuminate nearly the same area on the scattering surface, either the

Earth's surface or cloud top. The light reflected by the surface passes back through the atmosphere and a small fraction is collected by the receiver telescope. The lidar receiver measures the energies of the on- and off-line pulses (E_{on} and E_{off}) and the range to the surface.

The insert shows a sketch of the shape of the CO_2 line's transmission (top) and optical depth (OD) when measured from space. The maximum CO_2 absorption occurs for laser wavelengths tuned to the line's center. The wavelength of the laser's "on-line" pulse is usually selected to be offset from the peak of the CO_2 absorption line and is indicated by the red vertical line. The wavelength of the laser's "off-line" pulse, that undergoes minimal CO_2 absorption, is indicated by the blue line.
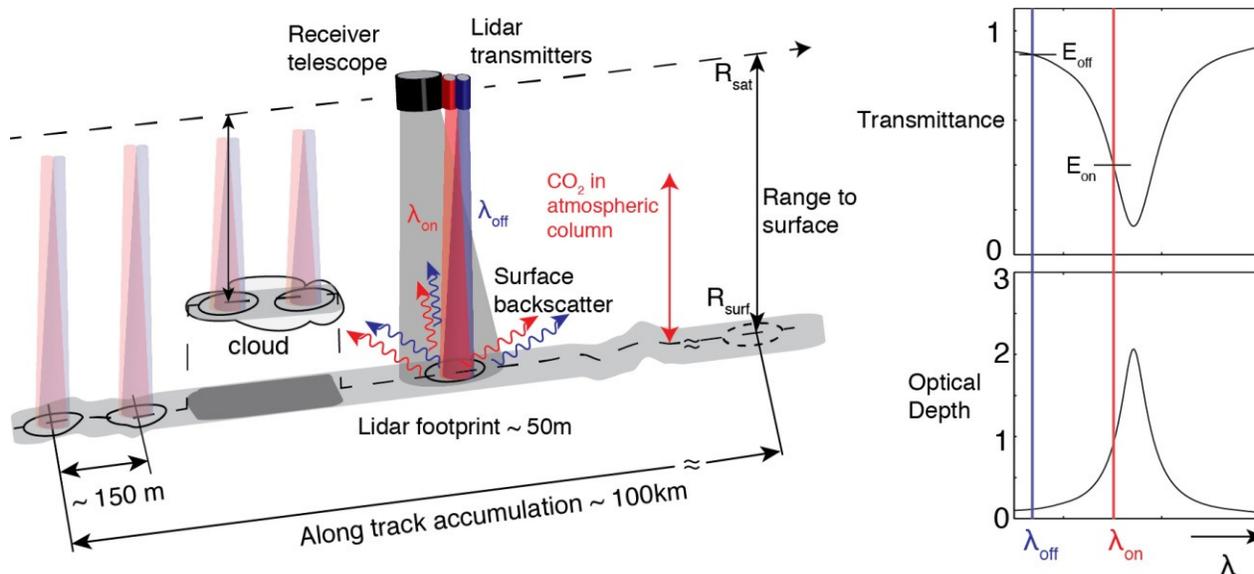
Figure 1-1 Example approach for IPDA measurement from space to scattering surfaces on or near the Earth's surface. While there are several different IPDA measurement approaches, this drawing is for the two-wavelength pulsed approach that was considered for the ESA (European Space Agency) A-SCOPE (Advanced Space Carbon and Climate Observation of Planet Earth) Mission (ESA, 2008). Several IPDA approaches use more than two wavelengths to sample the absorption line shape to provide additional information.

The CO_2 column abundance is calculated from the lidar measurements of range to the scattering surface and ratio of the energies in the on- and off-line echo pulse signals. The column-averaged CO_2 dry air mole fraction, XCO_2, is calculated using additional information about the density of dry air in the same measurement column. A simultaneous O_2 lidar measurement had been considered as an additional capability of the instrument, but it appears a more practical approach is to use a numerical weather model analysis sampled at the location and time of the CO_2 lidar measurement (ESA, 2008).

1.7 The Benefits of the ASCENDS Approach

The IPDA lidar approach offers a number of unique and important capabilities for the ASCENDS mission, allowing accurate column measurements of CO_2 with extended coverage. These are summarized in Table 1-1. The ASCENDS approach will allow accurate measurements of greenhouse gas concentrations over a much wider variety of conditions than is possible with passive sensors. Such measurements are key to addressing important questions about the locations, strengths and evolution of the regional CO_2 fluxes needed for coupled carbon-climate models.

Table 1-1 Unique Benefits of the ASCENDS Approach

1. The lidar measurements work well in darkness or light and are independent of sun angle.
2. It measures in a single vertical column, using a common illumination and observation path.
3. The same nadir-zenith viewing geometry is also the "glint mode" for the ocean and water surfaces. This allows ocean and land measurements to be made continuously using the same spacecraft orientation.
4. The laser line-width is much narrower than the gas absorption line, and so the absorption lines measured can be fully resolved. Using on-line measurements on the side of the gas line allows weighting of the column measurements preferentially in the lower troposphere, which contains a stronger signature from the surface fluxes. On-line measurements near the peak of the line also allow additional measurements weighted toward the upper atmosphere.
5. The laser can target gas absorption lines to minimize temperature sensitivity and contamination from other gases. The spectroscopic knowledge needed for accurate retrievals involves only the region around the single gas line sampled by the lidar, and is independent of the solar spectrum.
6. The small (typically 100 m) lidar spot size also enables utilizing small gaps in clouds to obtain gas column measurements to the surface in partially cloudy scenes and through broken cloud fields.
7. The lidar measures range to the scattering surface simultaneously with column gas absorption. This provides accurate determination of the scattering surface elevation and column length. This also allows simple range gating to eliminate signals scattered by thin clouds and aerosols. The range measurements are particularly important when measuring over regions with varying topography and tree cover that cause the range to vary significantly.
8. The ranging information also enables accurate column measurements to the tops of some clouds, providing some vertical resolution in the column concentrations.

1.8   Overview of NASA's Development of the ASCENDS Mission

Over the past decade NASA has supported the development of several lidar concepts and their associated technologies for its planned ASCENDS mission (NRC, 2007). The approaches all use the IPDA technique. An ASCENDS ad hoc SDT leads the mission definition activities. Team members are from NASA Goddard, NASA Langley Research Center (LaRC) and NASA Jet Propulsion Laboratory (JPL) as well as the University of Oklahoma, Colorado State University, and others. Their work has focused on four areas: developing the mission's science objectives and requirements, conducting science mission modeling studies, deploying airborne space simulator instruments, and carrying out initial engineering studies of candidate lidars and spacecraft. NASA's Earth Science Technology Office has supported the development of the key lidar technologies used by the investigators.

Observing System Simulation Experiments (OSSEs) have been conducted to assess the characteristics of the CO_2 fluxes that can be inferred from space-based lidar measurements with various levels of measurement precision and accuracy. The mission simulations have used a realistic, observation-based lidar measurement model to identify the impact of some mission science tradeoffs and to help formulate a set of ASCENDS measurement requirements.

A large fraction of the ASCENDS effort was directed at developing and demonstrating candidate lidar approaches from aircraft. Candidate lidar techniques that include two direct detection lidar approaches have been demonstrated that measure both range and selected CO_2 lines near 1571 and

1572 nm. One uses sine-wave laser intensity modulation that is swept in modulation frequency. The other uses pulsed laser modulation that samples the absorption line at multiple wavelengths and uses a time resolved receiver to measure the laser backscatter profile and range to the surface. Two approaches have demonstrated measurements of the CO_2 line near 2051 nm. A continuous wave (CW) heterodyne approach measures this line at two wavelengths, and a pulsed direct detection approach measures both range and CO_2 absorption using the same line.

Preliminary instrument and space mission engineering studies also have been conducted on lidar candidates that are suitable for the mission. The payload parameters are consistent with a medium-sized spacecraft bus to be flown in a polar ~400 km altitude orbit.

The 2017 Earth Science and Applications from Space Decadal Survey Recommendations (NASEM, 2018) recommended that future NASA greenhouse gas missions compete with other types of missions through a new cost-capped Explorer Mission category. While such limitations pose a particular challenge for active remote sensing approaches, several paths to space for lidar CO_2 measurements may still exist. Sellers et al. (2018) emphasize the synergy between active and passive remote sensing approaches. The increasing number of planned passive missions may provide new opportunities for international partnerships and cost sharing. Alternatively, deployment of a CO_2 lidar to the International Space Station (ISS) could satisfy many, though not all, of the science objectives of ASCENDS at a lower cost.

1.9 Remainder of Report

The remaining sections of this report expand on the topics briefly introduced here. Section 2 summarizes the science of CO_2 and history of atmospheric CO_2 measurements. Section 3 summarizes studies on the impact of the ASCENDS mission on carbon cycle science and modeling. Section 4 assesses the influence from uncertainties in the atmospheric state on the space-based measurements of XCO_2. Section 5 provides a summary of the mission measurement requirements, an overview of the various candidate lidar techniques, and several promising measurement demonstrations during airborne campaigns. Section 6 summarizes the result from an initial space mission engineering study. Finally, Section 7 summarizes the report and discusses next steps.

2. Science of Atmospheric CO$_2$ and Measurement History

2.1 Introduction

At the beginning of the industrial era in the late 18th century, the atmospheric carbon dioxide (CO$_2$) concentration (or "dry air mole fraction") was about 280 parts per million (e.g. Etheridge et al., 1996). Since that time, fossil fuel combustion, deforestation, and other human activities have emitted more carbon dioxide (CO$_2$) into the atmosphere each decade, driving the weekly global average atmospheric CO$_2$ mole fraction past the 400-ppm mark in May 2013. Recent estimates of fossil fuel emissions derived from fossil fuel inventories (Boden et al., 2017) show that this source alone was adding more than 36 billion tons (Gigatons or Gt) of CO$_2$ to the atmosphere each year (Peters et al., 2012; Le Quéré et al., 2018).

The CO$_2$ emissions from fossil fuel combustion are superimposed on an active, global carbon cycle that incorporates the exchange of carbon among reservoirs in the ocean, land biosphere, and atmosphere (Figure 2-1). Each year, the land biosphere absorbs and then re-emits over 450 Gt of CO$_2$ into the atmosphere through photosynthesis and respiration, respectively (Beer et al., 2010). The ocean is also a massive reservoir of carbon, adding and reabsorbing about 300 Gt of CO$_2$ from the atmosphere each year across the air-sea interface (Ciais et al, 2013). Because these natural fluxes of CO$_2$ are roughly balanced over the annual cycle, globally, ice core records show that atmospheric CO$_2$ mole fractions have varied only between ~180 and 300 ppm for at least the past several hundred thousand years (cf. Archer et al., 2009). The CO$_2$ emissions associated with human activities are still only about 1/20th as large as these natural fluxes, but they are not balanced, and are now pushing the atmospheric CO$_2$ mole fractions to levels not seen throughout the 800,000-year ice core record (Lüthi et al., 2008) and perhaps for as long ago as 3-4 million years (cf. Badger et al., 2013).

A precise, continuous record of direct atmospheric CO$_2$ measurements was started in 1958, when Charles Keeling of Scripps Institute of Oceanography installed a CO$_2$ monitoring station on the flanks of the Mauna Loa volcano in Hawaii (Keeling, 1960). The initial measurements showed CO$_2$ mole fractions near 315 ppm, about 35 ppm above the pre-industrial values of ~280 ppm. Within a couple of years, his measurements clearly documented the global atmospheric seasonal cycle of photosynthesis and respiration by land plants. They showed a ~7 ppm CO$_2$ drawdown during the northern hemisphere spring and summer, when forests and grasslands are growing rapidly, and a comparable CO$_2$ buildup during NH fall and winter, when these plants drop their leaves and go dormant or die. As this measurement record continued through the 1960's and 1970's, a clear trend emerged underneath this seasonality, revealing an increase in the background CO$_2$ mole fraction of over 1 ppm per year.

The National Oceanic and Atmospheric Administration (NOAA) joined the atmospheric CO$_2$ monitoring effort in 1974. The NOAA Earth System Research Laboratory Global Monitoring Division (ESRL GMD) now operates the Carbon Cycle Greenhouse Gas (CCGG) Cooperative Air Sampling Network, which currently includes close to 100 active surface stations and 16 airborne vertical profiling sites. This network has been incorporated into the World Meteorological Organization (WMO) Global Atmospheric Watch (GAW) Program, which now includes ~145 surface stations that report CO$_2$ mole fraction measurements on time scales varying from minutes to one week. These data are collected and distributed by the World Data Centre for Greenhouse Gases (WDCGG) at the Japan Meteorological Agency. Stringent quality control procedures and frequent, rigorous calibration efforts ensure that measurements from these stations are not only

extremely precise, but also accurate, through comparisons to standards with accuracies of ~0.2 ppm (cf. Conway et al., 2009; Conway et al., 1994; Zhao and Tans, 2006; Dlugokencky and Tans, 2018).

Recent measurements from this surface-based greenhouse gas network show that the annual growth rate of CO_2 has increased by about a factor of two since the 1960's, and now exceeds 2 ppm (0.5%) each year. Comparisons of these measurements with CO_2 emission inventories reveal an intriguing puzzle. If all of the CO_2 emitted by human activities remains in the atmosphere, the atmospheric CO_2 abundance should be increasing at twice the observed rate. This apparent discrepancy was initially somewhat surprising because CO_2 is a chemically stable atmospheric constituent, with an estimated atmospheric half-life of almost 900 years. The accuracies of both the CO_2 emissions estimated from fossil fuel inventory and the atmospheric measurements are more than adequate to address a difference this large. Apparently, since the beginning of the industrial age, natural "sinks" in the ocean and land biosphere have kept pace with the rapidly growing emission rates, and have been absorbing slightly over half of the CO_2 emitted by human activities (cf. Le Quéré et al., 2017).
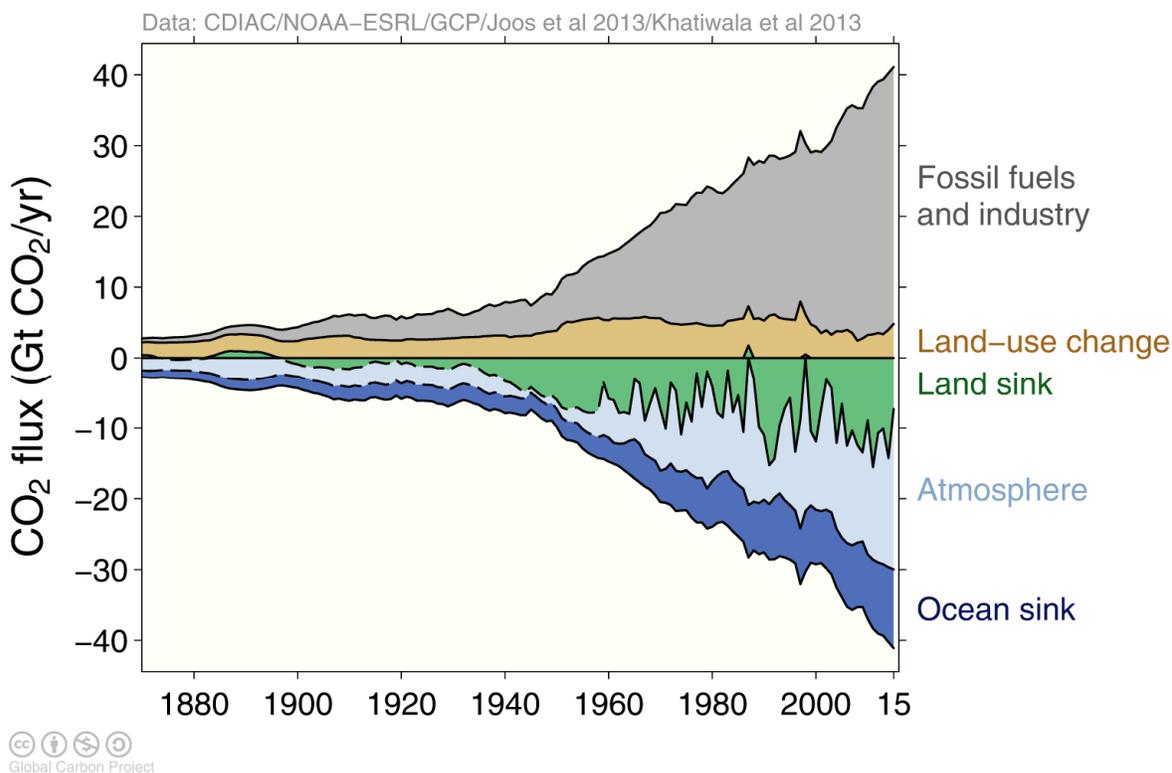
Figure 2-1 About half of the CO_2 emitted by fossil fuel combustion, industry, and land use change stays in the atmosphere. The remainder is absorbed by carbon sinks on land and in the ocean (Credit: Le Quéré et al., 2018).

As atmospheric CO_2 is absorbed by the ocean, it produces carbonic acid, and recent measurements of increases in the ocean acidity indicate that the ocean has been absorbing about half of the "missing" CO_2. The rest (~9.6 Gt CO_2 y^{-1}) is apparently being absorbed by sinks in the terrestrial biosphere, whose identity, location, and driving mechanisms are still poorly understood. While the terrestrial biosphere and oceans absorb about half of the CO_2 emitted by human activities, when averaged over decadal time scales, their efficiency appears to vary dramatically from year to year. In some years, almost all of CO_2 emitted by human activities is absorbed, while in others almost none is absorbed (Dlugokencky and Tans, 2018). The climate and other processes responsible for

modulating the efficiency of these sinks from year to year are highly uncertain (i.e. Friedlingstein et al., 2006; Poulter et al., 2011). There are also large uncertainties in the response of these natural sinks to climate change. Will the land biosphere and ocean continue to absorb roughly half of all the CO_2 emitted by human activities, or will they eventually saturate (or perhaps even become sources) as the climate changes in response to greenhouse-gas-induced warming? An improved understanding of these natural sinks and the processes that control them is therefore critical for predictions of future atmospheric CO_2 increases and feedbacks to the climate.

An improved understanding of CO_2 emissions from human activities is needed to predict future CO_2 growth rates. Until recently, these emissions were dominated by fossil fuel combustion in the developed world. The inventory-based CO_2 emission estimates have grown progressively more accurate for this particular source, with uncertainties as small as ~5% in Europe and North America (cf. EPA, 2010; Boden et al. 2013). However, since the turn of the 21st century, fossil fuel CO_2 emissions from China, India, the Russian Federation, and other developing nations have grown rapidly, and now account for more than 57% of all emissions from fossil fuel combustion (cf. Le Quéré et al., 2013). The uncertainties in these emissions are much higher than those for Europe and North America, and their future rate of increase is difficult to predict given recent changes. CO_2 emissions from other sources in the developing world, including biomass burning and other land use practices, are also less well known. When these uncertainties in CO_2 emission sources are combined with those associated with possible changes in natural CO_2 sinks, predictions of the atmospheric CO_2 concentration at the end of this century are uncertain by amounts exceeding the current atmospheric CO_2 abundance (Friedlingstein et al., 2006; Poulter et al., 2011).
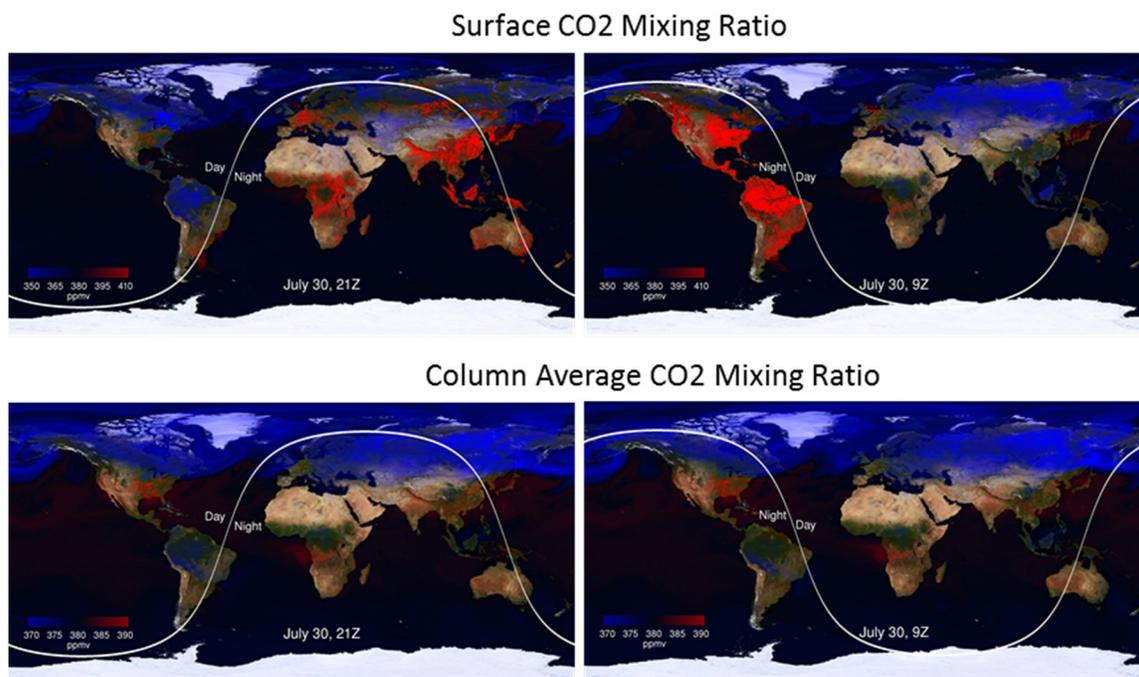
Figure 2-2 Simulated surface (top) and column average (bottom) CO_2 fields for July from the Goddard Earth Observing System Model, Version 5 (GEOS-5; Ott et al., 2015) illustrate the effects of diurnal variations in surface sources. The white line indicates the position of the terminator.

The quantity and accuracy of the measurements of CO_2 and other greenhouse gases from the surface-based greenhouse gas monitoring network have improved progressively since 1958, and now produce a highly accurate integral constraint on the global abundance of CO_2 and its rate of

change. These precise atmospheric measurements have been augmented by CO_2 flux networks, which quantify the exchange of CO_2 between the surface and atmosphere associated with natural processes. Ground-based remote sensing measurements of the column-average dry air mole fractions of CO_2, CH_4 (methane), and other gases by the 21-station Total Carbon Column Observing Network (TCCON) are providing additional insight into the emission, absorption, and transport of the species (cf. Keppel-Aleks et al., 2012; Geibel et al., 2012; Wennberg et al., 2012; Messerschmidt et al., 2013; Wunch et al., 2013).

The existing ground-based greenhouse gas network was not designed to quantify emissions from large point sources such as cities or power plants. In fact, most of its stations were deployed away from large point sources or strong sinks to observe large-scale global trends . The simulation of the atmospheric CO_2 distribution shown in Figure 2-2 illustrates another reason why it has been difficult to identify and study sources and sinks with the existing ground-based network. As CO_2 is emitted into the atmosphere or absorbed by surface processes, the resulting CO_2-rich or CO_2-poor air is transported by the prevailing winds, mixing the CO_2 with the ambient air mass. To track these air masses, the measurement system must be able to resolve the wind field as well as the spatial scales of the sources and sinks. This is challenging because the atmosphere already contains a substantial amount of CO_2 (~400 ppm), such that even the most intense sources and sinks rarely produce CO_2 perturbations larger than 10% near the surface, where their amplitudes are largest. The amplitude of these CO_2 anomalies decays rapidly with altitude, yielding column-integrated variations in the background CO_2 distribution that rarely exceed 2%, and are typically no larger than a few tenths of a percent on local to regional scales.

2.2 History of Atmospheric CO₂ Measurements from Space

The ground-based greenhouse gas monitoring network is reasonably dense in some areas (e.g. North America, Europe), but far sparser elsewhere, especially over tropical and polar land masses and the ocean basins. The site selection strategy and measurement protocols also favored locations far from known strong sources or sinks to monitor background levels and trends, rather than intense emissions from localized sources. A dramatic expansion of this network would be needed to identify and quantify sources and sinks of CO_2 on urban to regional scales over the globe. One way to improve the spatial and temporal resolution and coverage is to acquire global measurements of the column averaged dry air mole fraction, XCO_2, at high spatial resolution from instruments in orbit around the Earth (Rayner and O'Brien 2001; O'Brien and Rayner, 2002; Rayner et al., 2002; Houweling et al., 2004; Chevallier et al., 2007; Hungershoefer et al., 2010). The principle challenge to this approach has been the need for space-based CO_2 measurements with unprecedented precision and accuracy. High precision and high sensitivity to the near-surface CO_2 distributions are needed to quantify the small CO_2 anomalies associated with surface sources and sinks. High accuracy is essential because CO_2 fluxes are derived from spatial and temporal gradients in the observed XCO_2 field, and small biases can be introduce unacceptably-large errors in the retrieved fluxes.

Estimates of XCO_2 can be retrieved from space-based observations of reflected sunlight in near-infrared CO_2 and O_2 bands. The European Space Agency's (ESA) ENVISAT (Environmental Satellite) SCIAMACHY (SCanning Imaging Absorption spectroMeter for Atmospheric CartograpHY), the Japanese GOSAT (Greenhouse gases Observing SATellite) TANSO-FTS (Thermal And Near infrared Sensor for carbon Observation-Fourier Transform Spectrometer), and the NASA OCO-2 (Orbiting Carbon Observatory-2) were the first three satellite instruments designed to use this approach. These early pioneers were recently joined by the Chinese TanSat

ACGS (Atmospheric CO_2 Grating Spectrometer), FY-3D (FengYun-3D) GAS (Greenhouse gases Absorption Spectrometer) and GMI (Gaofen-5 Greenhouse-gases Monitoring Instrument) sensors.

ENVISAT was launched into 800-km altitude, sun-synchronous polar orbit in 2002 and returned global maps of XCO_2 and XCH_4 through 2012. SCIAMACHY was designed to measure several trace gases, but was the first space-based sensor designed to collect moderate-resolution ($\lambda/\Delta\lambda \approx$ 1000) spectra within the short-wavelength infrared (SWIR) CO_2 absorption bands near 1580 and 1610 nm and the CH_4 band near 1670 nm. It was also the first space-based instrument to collect co-located moderate-resolution ($\lambda/\Delta\lambda \approx$ 1600) spectra of the near-infrared (NIR) molecular oxygen (O_2) A-band at 765 nm to retrieve estimates of the dry air column. Because of the large surface footprints, large single-sounding random errors, and lack of coverage over oceans, there is limited use of these data to infer significant information on CO_2 sources and sinks (Buchwitz et al., 2017).

GOSAT was launched in January, 2009, and flies in a 666 km altitude, sun synchronous orbit with a 12:47 PM equator crossing time and a 3-day ground track repeat cycle. Its TANSO (Thermal And Near infrared Sensor for carbon Observation) FTS (Fourier Transform Spectrometer) returns high resolution (0.27 cm^{-1}) spectra of reflected sunlight in the CO_2 bands near 1.57, 1.61, and 2.06 microns, and the CH_4 band near 1.67 microns, as well as high resolution (0.37 cm^{-1}) spectra of the O_2 A-band near 0.765 microns. Single sounding random errors are typically less than 0.5% (2 ppm) and biases are typically <0.25% (1 ppm) on regional scales (Wunch et al., 2011; Yoshida et al., 2013; Inoue et al., 2013; Crisp et al., 2012). GOSAT observations also led to the discovery that solar induced chlorophyll fluorescence (SIF) could be detected from space in the O_2 A-Band, and that it had to be corrected to avoid introducing biases in the dry air column (Frankenberg et al., 2011a). This new product provides additional information about gross primary productivity and thus the uptake of CO_2 by the land biosphere (Frankenberg et al., 2011b; Joiner et al., 2011; 2012; Guanter et al., 2012) and has helped to spawn a new field of investigation.

The principal limitations of the GOSAT data set have been its coverage and resolution. The TANSO-FTS acquires about 10,000 soundings over the sunlit hemisphere each day. Over land, individual ~10.5 km diameter sounding footprints are separated by ~253 km. With this relatively large sounding footprint (85 km^2), more than 95% of the soundings are too contaminated by clouds or optically-thick aerosols to yield accurate estimates of XCO_2 with the current retrieval algorithms. Persistent cloudiness over the tropics, south Asia (monsoons), and at high latitudes in the winter hemisphere further reduces the coverage there. Over the ocean, the TANSO-FTS coverage is restricted to ±40° of the sub-solar latitude, where its pointing mechanism can target the bright "glint spot" in which sunlight is specularly reflected from the surface. In spite of these limitations in coverage and resolution, XCO_2 estimates from GOSAT TANSO-FTS are being used in flux inversion models and are beginning to improve our understanding of CO_2 sources and sinks in data poor regions, such as Africa and central Asia (Basu et al. 2013; Belikov et al., 2014; Guerlet et al. 2013). At this time, spatial and temporal coverage gaps in the GOSAT measurements, as well as residual biases in the bias-corrected data, still limit its ability to accurately resolve fluxes down to the sub-continental or sub-ocean basin scale (Wang et al., 2018).

The NASA Orbiting Carbon Observatory-2 (OCO-2) was launched from Vandenberg Air Force Base (AFB) in California (CA) on 2 July 2014. It flies at the head of the 705-km Afternoon Constellation ("A-Train"). The OCO-2 spacecraft carries a single instrument that incorporates three co-bore-sighted, high-resolution ($\lambda/\Delta\lambda$ >17,000, where λ is wavelength), imaging, grating spectrometers designed to measure reflected sunlight in the 0.765-micron O_2 A-band, and within the CO_2 bands near 1.61 and 2.06 microns. Each spectrometer collects 24 soundings per second

along a narrow (<10.6 km) ground track, yielding up to one million soundings over the sunlit hemisphere each day. To provide higher sensitivity to point sources and more useful data in partially cloudy regions, the surface footprint of each OCO-2 sounding has an area of less than 3 km^2.

For routine science operations, the spacecraft points the instrument's boresight at the local nadir or near the "glint spot", where sunlight is specularly reflected from the Earth's surface. The nadir observations yield slightly more cloud-free images over land, while the glint observations provide higher sensitivity over the ocean. The spacecraft can also point the instrument boresight at a stationary surface target near the ground track to collect thousands of measurements as the spacecraft flies overhead. This "target" mode is used primarily to collect data over well-instrumented surface calibration sites, such as Railroad Valley, Nevada, USA, and validation sites, including TCCON stations. With these capabilities, OCO-2 provides better precision, accuracy, resolution, and coverage than previous missions.

OCO-2 has been in orbit now for 4 years and the data have exceeded expectations. With its small footprint, about 8.5% of the soundings (85,000/day) are sufficiently cloud-free to yield full-column estimates of XCO_2 with single-sounding precision typically around 0.5 ppm (or 0.125%). This precision is adequate to quantify CO_2 anomalies associated with anthropogenic sources on regional scales (Hakkarainen et al., 2016) to megacity scales (Schwandner et al., 2017) and even for individual large powerplants (Nassar et al., 2017). After implementing a simple bias correction, comparisons to TCCON indicate a global mean bias <0.4 ppm (Wunch et al., 2017).

OCO-2 data collected between March 2015 and June of 2016 provided a unique opportunity to study the carbon-climate feedbacks associated with the intense 2015-2016 El Niño. Chatterjee et al. (2017) used GOSAT and OCO-2 data to show that the XCO_2 over the tropical Pacific initially decreased during the spring and early summer of 2015 as the upwelling of deep CO_2-rich surface water was suppressed near the equator. However, by July of 2015, while the ocean emissions of CO_2 remained low, the XCO_2 increased sharply as the land biosphere responded to the drought and heat stress associated with this El Niño. Liu et al. (2017) combine GOSAT observations of XCO_2 and SIF from 2011 with OCO-2 observations of these quantities to assess the impact of the El Niño on the terrestrial carbon cycle. They found that CO_2 fluxes from the land biosphere into the atmosphere increased over the Amazon, tropical Africa, and Southeast Asia/Oceania, but different mechanisms dominated in each area. Drought and high temperatures increased fire incidence over Indonesia. Tropical Africa experienced unusually high temperatures, but near normal rainfall, leading to increased plant respiration. In the Amazon, drought and heat stress reduce primary production. These results are reinforced by more global studies of the carbon cycle response to El Niño (Patra et al., 2017) and by studies of CO_2 emissions from fires in Indonesia (Heymann et al., 2017).

Several new missions have either entered development, formulation, or pre-formulation stages within the last few years. As noted above, the Chinese TanSat was launched in December 2016 and started delivering Level 1B products (calibrated radiances) in October 2017. They have shown examples of their XCO_2 and SIF products (Yang et al., 2018) but had not yet started delivering these products at the time of this document. The Chinese FengYun-3D was launched in late November 2017, and Gaofen-5 was launched in May 2018, with both completing their in-orbit check-out phases when this document was written.

Impending missions include the Japanese GOSAT-2 mission, which is scheduled to launch in late 2018 carrying TANSO-FTS-2, a substantially-updated version of the instrument carried by

GOSAT. This instrument includes the same spectral channels as the GOSAT TANSO-FTS, as well as a new channel near 2.3 microns to measure carbon monoxide (CO). In addition, it is designed to yield much smaller single-sounding random errors (0.125% vs 0.5%), and includes an intelligent pointing system to identify cloud-free scenes. The Orbiting Carbon Observatory-3 (OCO-3) mission will deploy the flight spare OCO-2 instrument on the International Space Station (ISS) in February 2019. The main differences between OCO-3 and OCO-2 are in their orbital coverages and pointing capabilities. Because of the low-inclination orbit of the ISS, OCO-3 will only cover the latitude ranges of +- 52 degrees latitude, but this precessing orbit will provide opportunities to acquire XCO_2 and SIF observations at a wide range of local times between dawn and dusk. OCO-3 also includes an agile, 2-axis pointing mechanism to enable nadir, glint, and target observations from the ISS, as well as a "snapshot" mode that allows mapping of 100 km x 100 km areas, such as large metropolitan areas. The Geostationary Carbon Observatory (GeoCarb) mission was selected as part of the NASA Earth Venture Mission program. GeoCarb will be the first greenhouse gas mission in geostationary orbit. It carries an imaging grating spectrometer with 0.765, 1.61, and 2.06 micron channels like those on OCO-2, as well as a 2.3-micron spectral channel to observe both CH_4 and CO. It will be stationed near 100° west longitude to map out CO_2, CH_4 and CO from the terrestrial biosphere above North and South America. GeoCarb is due to launch in the 2022-2024 time frame. The Centre National d'Etudes Spatiales (CNES) MicroCarb mission will deploy a micro satellite that carries a compact, 4-channel, imaging Echelle grating spectrometer that includes the 3 channels measured by OCO-2 and OCO-3 as well as the O_2 channel at 1.27 microns.

Several other mission concepts are in early planning stages. The most ambitious of these are the Chinese TanSat-2 and European Commission Sentinel CO_2 constellations. TanSat-2 is a Low Earth Orbit (LEO) constellation of 6 satellites that carry wide-swath (100-km) imaging grating spectrometers that measure CO_2, CH_4, and CO at a spatial resolution of 2 km by 2 km. The current plan is to deploy three of these satellites in a late morning sun-synchronous orbit and three in an early afternoon sun-synchronous orbit to provide some coverage of the diurnal cycle. This constellation could be launched as early 2022. The Sentinel CO_2 constellation will include 3 or 4 satellites with wide-swath (200-350 km) imaging grating spectrometers designed to measure CO_2, CH_4, and nitrogen dioxide (NO_2) at a spatial resolution of 2 km by 2 km. The current plan is to deploy the entire constellation in a late morning sun-synchronous orbit in the 2025-2026 timeframe.

The primary challenge in retrieving atmospheric CO_2 from space is the need for very high accuracy. Biases that are spatially and temporally varying are of greatest concern because they can contribute flux errors in any flux inversion system. A wide range of factors contribute to biases in the retrieved concentrations of CO_2 including instrument calibration errors, uncertainties in gas absorption cross sections, retrieval algorithm limitations, errors in the surface reflectance, and uncertainties in aerosol scattering properties. For passive spectroscopic measurements like those described above, these biases can change with solar illumination angle and observation angle. Correcting these biases requires validation sites over the range of conditions seen in the observations.

In principal, active remote sensing methods can reduce potential biases in XCO_2 retrievals because all observations are taken with the same near-nadir viewing and near-nadir observation geometry. Also, the return signal from a laser source can be processed so that only the return from the surface is considered, reducing potential bias from scattering in the atmosphere. Finally, measurements can be made at night and at high latitudes in winter and through small gaps in clouds, thereby minimizing spatiotemporal sampling bias. These advantages are discussed below.

3. Impact to Carbon Science and Modeling

3.1   Introduction

The primary science goal of the ASCENDS Mission, as outlined above, is to establish quantitative constraints on terrestrial and oceanic CO_2 surface fluxes at both global and regional scales from measurements of CO_2 column concentrations. In order to achieve this goal, it is critical to thoroughly understand the impact of measurement coverage, accuracy, and precision on the flux estimates. These are important because even the largest sources and sinks produce local perturbations in the background concentration of CO_2 no larger than a few percent. Biases in the measurements are particularly problematic since their impact cannot be reduced via averaging.

This section summarizes the modeling efforts undertaken by the ASCENDS ad hoc SDT to assess the ability of expected ASCENDS measurements to constrain flux estimates. Under reasonable assumptions for ASCENDS technical performance, the modeling efforts consistently demonstrate the following major points (as quantified below):

- ASCENDS will resolve statistically-significant differences in total column CO_2 concentrations, resulting from foreseeable changes in surface flux, over the entire globe including at high latitudes throughout the year.

- ASCENDS will substantially advance our understanding of the global carbon budget through improved flux estimates with reduced uncertainty at global to regional scales.

- The smaller biases and greater coverage and representation of ASCENDS measurements will contribute significantly to improved constraints on surface fluxes beyond what passive sensors such as GOSAT and OCO-2 provide.

We elaborate on these results through the use of three common, overlapping modeling approaches or Observing System Simulation Experiment (OSSE) frameworks. These approaches are: 1) Signal detection simulations that test the global measurement significance for perturbation flux scenarios of interest; 2) Inverse modeling OSSEs that quantify the reduction in flux uncertainty provided by the ASCENDS data at global and regional scales, and 3) OSSEs that compare the impact of ASCENDS data to that of current passive measurements from GOSAT and OCO-2 at the global scale. Most of the modeling is performed using a range of possible technology implementations and performance specifications for ASCENDS to bracket projected measurement error levels and ultimately to help guide requirements for the mission formulation.

3.2   Detection of CO_2 Flux Perturbations by ASCENDS

Several example CO_2 flux perturbations are imposed in model transport runs and compared quantitatively to the XCO_2 field as it would be measured by ASCENDS. ASCENDS measurement characteristics (see Box 3-1) are derived from instrument models consistent with airborne demonstrations detailed in Section 5. Four different flux examples are presented here. In addition, a wider variety of flux scenarios is being analyzed as part of the NASA Carbon Cycle OSSE Initiative (Ott et al., 2017), which includes multiple space-based greenhouse gas (GHG) sensors including ASCENDS.

The ability of ASCENDS to detect changes in total column CO_2 resulting from variations in underlying fluxes is tested in the two-step methodology of Hammerling et al. (2015). First, a realistic baseline set of CO_2 sources and sinks is perturbed to generate a simulated atmosphere, which represents the science hypothesis in question. Second, the control and perturbed CO_2 fields

are sampled according to the projected ASCENDS sampling and error characteristics, and the 'observed' differences are evaluated statistically. This procedure is carried out for three hypothetical flux scenarios (Hammerling et al., 2015): emissions from thawing permafrost (Section 3.2.1), a shift in fossil fuel emissions from Europe to China (Section 3.2.2), and simulated interannual variability in the Southern Ocean (Section 3.2.3). These scenarios are subsequently introduced into an inversion model framework to calculate the fluxes and uncertainties inferred from the pseudo data (Crowell et al., 2018).

Box 3-1 Simulation of Random Errors

Prospective ASCENDS sampling and measurement error characteristics are derived in a realistic scheme from observations and model output using the Cloud-Aerosol Lidar and Infrared Pathfinder Satellite Observations (CALIPSO) orbital track for the ASCENDS orbit (Kawa et al., 2010, Kiemle et al., 2014). CALIPSO optical depth (OD) data are reported every 5 km along track and this forms our basic ASCENDS sample set. We have also tested sample error calculated using OD derived for a subset of single-shot 20-Hz CALIPSO data and found that the global statistics are very similar to those using the 5-km data.

Since ASCENDS laser measurements of atmospheric CO_2 will be made using the IPDA technique, the dominant random error source is likely to be the shot noise in the signal, i.e., the statistical variability in the number of detected signal photons. Hence the measured signal to noise ratio (SNR) of the optical depth of the gas absorption depends on the square root of the received signal energy. In general, the SNR of an individual measurement of 2-way optical depth (SNR_i), can be related to that measured under reference conditions (SNR_0) by:

$$SNR_i = SNR_0 \left[\frac{\beta_i}{\beta_0} \frac{T_i^2}{T_0^2} \right]^{1/2} \tag{3-1}$$

Here β_i is the average backscatter factor (sr-1) of the measured surface, β_0 is the backscatter for the reference surface, T_i is the one-way atmospheric transmission to the surface due to aerosols and clouds for measurement i, and T_0 is the transmission for the reference measurement. For the reference conditions, we have chosen clear air with the high reflectivity of a desert like Railroad Valley, NV (Nevada) in summer and a 10-s sample integration time. The measurement at this reference location is assumed to be aerosol and cloud free, thus $T_0 = 1$. Using Equation (3-1), we estimate the random relative error   (= $1/SNR_i$) globally from an estimate of the error under the reference conditions.

The optical transmission for each ASCENDS pseudo data sample is taken directly from the CALIPSO OD data: where τ_i is the one-way integrated aerosol and cloud OD to the surface reported by CALIPSO. The aerosol OD is taken from the 1064-nm channel and the cloud OD from the 532-nm channel, and these values are assumed to apply equally at each of the possible ASCENDS measurement wavelengths (i.e., 1.57 and 2.05 μm). Samples are excluded where CALIPSO cannot see to the surface due to thick clouds. Global backscatter estimates over land have been assembled for wavelength bands at 1.57 and 2.05 μm for CO_2, and 0.76 and 1.26 μm for O_2 measurement using MODIS (Moderate Resolution Imaging Spectroradiometer) bands 6, 7, 2, and 5, respectively, which are then interpolated to the CALIPSO-based sampling points. The details vary slightly from band to band. Backscatter over water is calculated according to Hu et al. (2008) using surface wind speeds from GEOS-5.

For the modeling studies, a range of nominal reference random error levels ($1/SNR_0$) is considered (0.25, 0.5, 1.0, 2.0 ppm over a 10-s averaging time) to represent a range of possible instrument precision levels. Note that the 10-s averaging is just a convenient reference for using the XCO_2 data. Space data will be returned at 50-Hz sampling (~140 m) along track (Section 5.2) and can be flexibly averaged in post processing to optimize SNR versus spatial resolution for varying conditions or conditionally sampled in the presence of clouds. Scaled global median errors are about 3 times the ideal/desert-like nominal reference value for the 1.57 μm case when screened for samples with cloud/aerosol optical depth less than 1.0. All of the models use the same sample distribution and measurement error scaling described here, however, different modeling teams employ somewhat different techniques to aggregate the pseudo data and determine the model-data mismatch errors that are ultimately used in the flux estimation experiments (Appendix C).
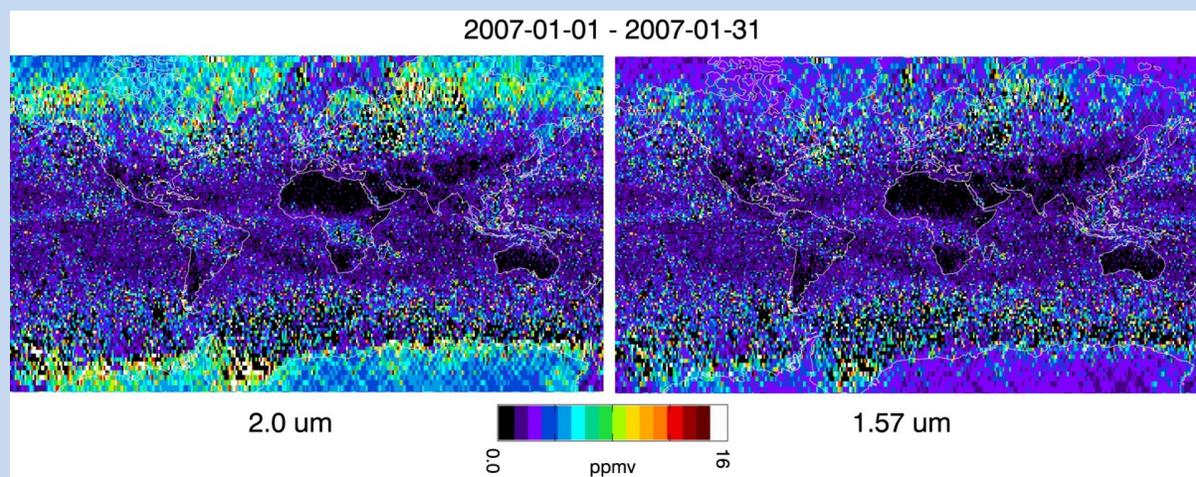
Figure 3-1 Global monthly root mean square (RMS) ASCENDS random measurement errors for January 2007 computed using Equation (3-1), relative to 1-ppm/10-s nominal error, aggregated to 1x1 ° grid for the two candidate CO_2 measurement wavelengths. Samples with total column OD >1 are excluded.

3.2.1   Arctic Permafrost Thawing Emissions

Permafrost soils occupy about 24% of the exposed land area in the high latitude Northern Hemisphere (Zhang et al., 1999) and contain approximately 1700 Gt of carbon in the form of frozen organic matter (Tarnocai et al., 2009). As temperatures increase and the permafrost thaws, the organic material begins to decay, releasing CO_2 and methane into the atmosphere. This results in enhanced atmospheric concentrations of these greenhouse gases and further warming. The rate of this feedback is highly uncertain, however, prompting calls for enhanced pan-Arctic greenhouse gas monitoring including satellite observations (NRC, 2013; Parazoo et al., 2016). Measurements at high latitudes with required sensitivity near the surface are particularly difficult, and at times impossible, for passive sensors making this a unique area of contribution for the ASCENDS lidar approach. Airborne data over complex surfaces in the Arctic (Section 5.5) and elsewhere demonstrate that quality ASCENDS measurements will be available for cloud-free scenes throughout the year including over snow and ice surfaces (Abshire et al., 2018a; Spiers et al., 2016).
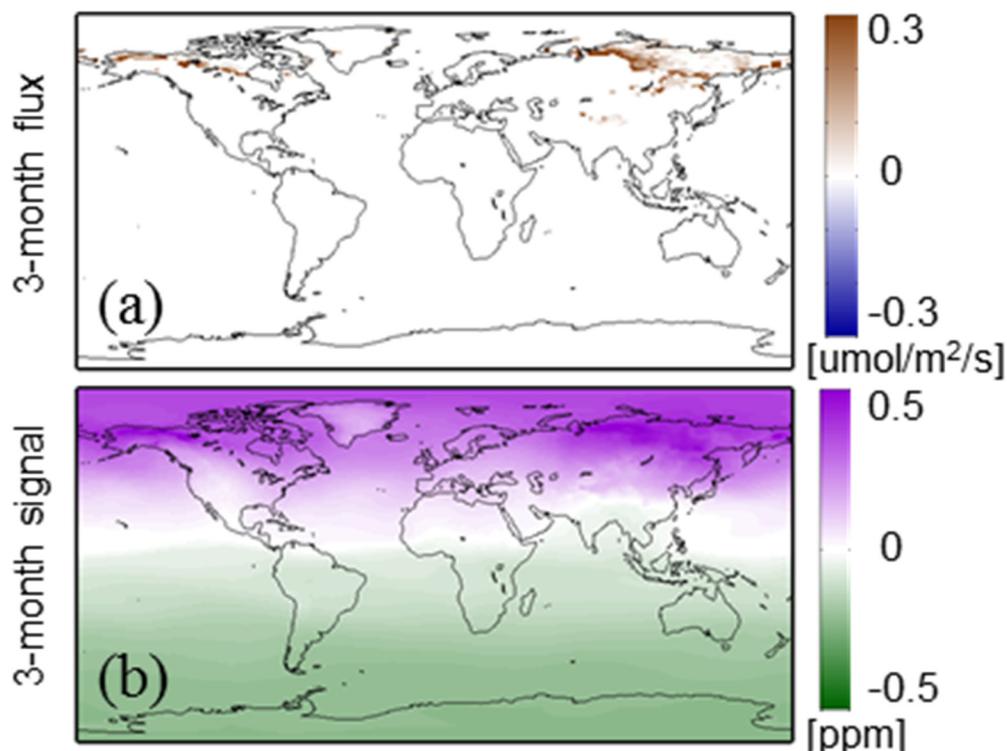
Figure 3-2 Perturbation flux and column average CO$_2$ mixing ratio for carbon release experiment (a) 3-month average (May – July) CO$_2$ flux for 2022 and (b) resulting 3-month average CO$_2$ perturbation. Negative mixing ratio values in the Southern hemisphere are a result of the global mean adjustment to create an overall flux neutral scenario (Hammerling et al., 2015).

The permafrost carbon emission scenario tested here derives from the simulations of Schaefer et al. (2011). Emission distributions are formed from the ensemble mean of CO$_2$ flux projections calculated in the Simple Biosphere/Carnegie-Ames-Stanford Approach (SiB-CASA) land biosphere model, driven by output from several General Circulation Models for the A1B scenario from the Intergovernmental Panel on Climate Change (IPCC) Fourth Assessment report (Lemke et al., 2007). The 2020 and 2021 fluxes were used to spin up the Parameterized Chemistry and Transport Model (PCTM; Kawa et al., 2004) and create corresponding atmospheric CO$_2$ concentrations. The atmosphere resulting from the 2022 fluxes was taken as the perturbation field. The 2022 permafrost fluxes and CO$_2$ perturbation are shown in Figure 3-2.
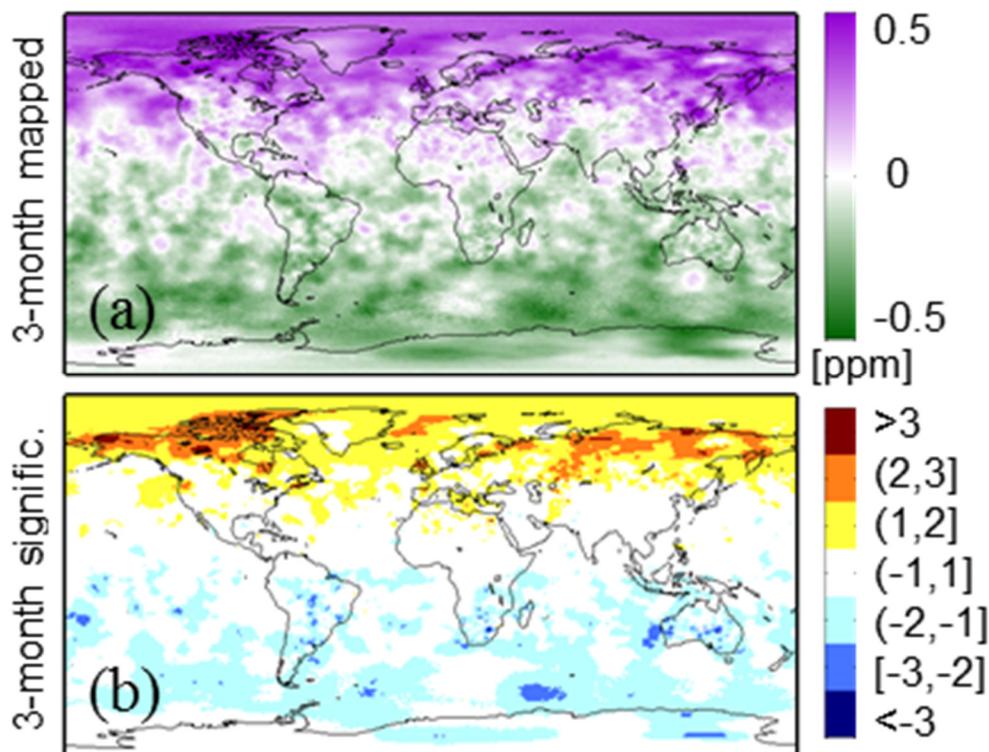
Figure 3-3 Results from the permafrost carbon release experiment (a) 3-month (May-July) ASCENDS-mapped CO_2 signal (perturbation minus baseline) and (b) significance level of the 3-month mapped signal. Significance is the mapped signal divided by the uncertainty of the mapped signal in units of standard deviations. The values are discretized for improved visualization. Yellow, orange and dark red (light, medium and dark blue) represent areas where the mapped CO_2 perturbation is larger (smaller) than the mapped baseline CO_2 concentration by more than one, two or three standard deviations, respectively, of the uncertainty of the mapped signal. This example uses the ASCENDS 1-ppm random measurement noise, 1.57 µm case (See Box 3-1 and Hammerling et al., 2015).

Signal Detection Significance

The detectability of a significant signal is relatively straightforward in the case of the anticipated permafrost carbon emissions (Figure 3-3). The challenge is in capturing longitudinal and latitudinal gradients in atmospheric CO_2, which can better attribute the increase to the permafrost thawing process. Because of the seasonality of the permafrost fluxes, the gradients in the atmospheric CO_2 distribution are most evident in the months following the start of the spring thaw. By August, atmospheric mixing, which occurs rapidly in the Arctic, spreads the spatial signature of the tundra thawing into a near-uniform zonal increase. While the concentration signal is highest around September, or even later in the year, when most of the seasonal melting has occurred, the diagnostic concentration signals are mostly indicative of the spatial pattern of the tundra thawing fluxes that occur in the late spring/early summer before the effects of atmospheric mixing take over. This phenomenon is caused by the specific combination of the temporal pattern of the permafrost carbon release and rapid atmospheric mixing in the High Northern Latitudes. Overall, the permafrost thawing signal is readily detectable (i.e., SNR >2-3) for either level of ASCENDS measurement noise cases considered (0.5, 1.0 ppm, see Box 3-1), and spatial gradients are best detected using two to three-month aggregation periods in the late spring/early summer.

Flux Estimation

Flux estimation experiments were conducted by Crowell et al. (2018) using the Transport Model, version 5 (TM5; Krol et al., 2005) together with a 4-Dimensional Variational (4DVAR) inversion system (see Table 3-1, Box 3-2, and Basu et al., 2013). The 'true' fluxes are used to drive TM5, whose output is sampled with the ASCENDS weighting functions for the two instrument wavelengths considered. The observation errors are as detailed in Appendix C, and the total grid-scale XCO_2 uncertainty also incudes transport and representativeness errors (see Crowell et al., 2018). Prior fluxes lack the permafrost source and additionally vary the ecosystem and ocean fluxes from the 'true' baseline. The prior error covariance is taken to be the gridded difference between the two biosphere and ocean flux estimates plus 100% of the permafrost emissions themselves. The spatial pattern is important to the 4DVAR assimilation system, because the optimization makes the largest corrections where the prior uncertainty is largest. In general, including this uncertainty in the spatial pattern improved posterior errors.
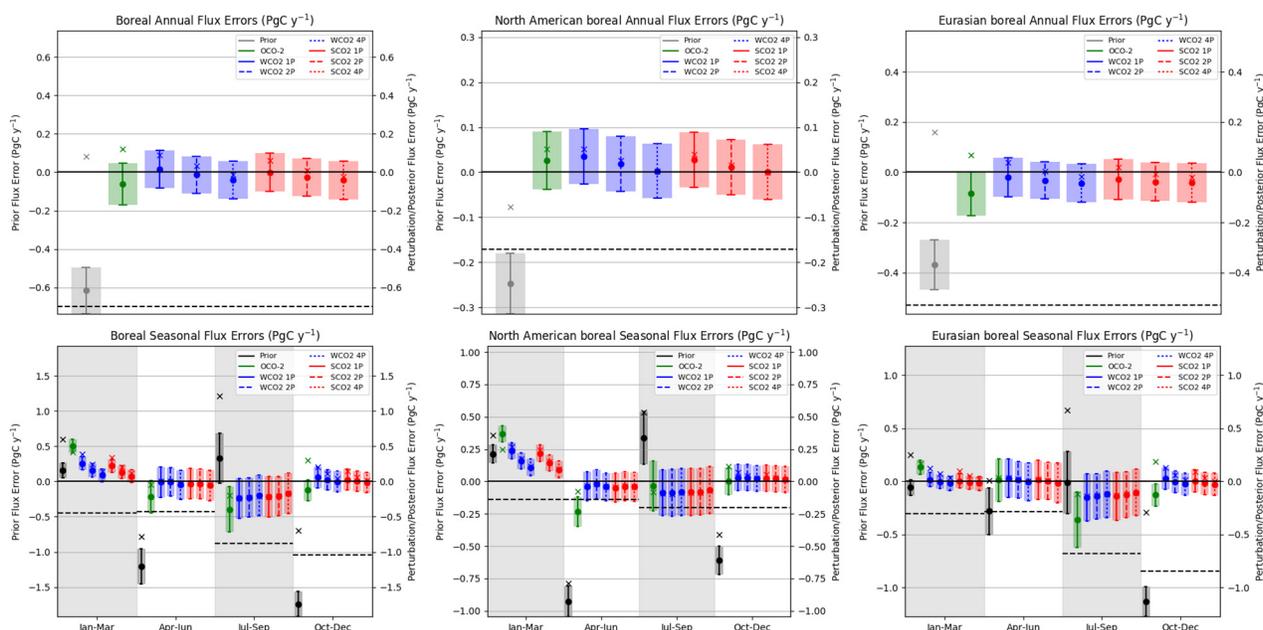
Figure 3-4 Regional inversion results from the permafrost carbon release experiment. (top row) Annual and (bottom row) seasonal errors for the permafrost perturbation experiment. (left column) The flux errors for the boreal land region, (center column) North American boreal, and (right column) Eurasian boreal region. The bars represent the a 1-σ uncertainty about the mean flux. The X markers represent the prior and posterior flux errors from the baseline experiment. The colors represent the prior (grey), OCO-2 (green), ASCENDS WCO2 (blue) and ASCENDS SCO2 (red). For the ASCENDS experiments, the reference precisions improve from 1 (left) to 0.5 (middle) to 0.25 (right) ppm. The dashed horizontal line represents the magnitude of the permafrost flux perturbation (Crowell et al., 2018).

The results are depicted in Figure 3-4. The optimized fluxes are found at the monthly time scale, at a global resolution of 6° longitude by 4° latitude, and the resulting fluxes are aggregated to regions that contain the permafrost flux signal of interest. Annual and seasonal results are shown. For the boreal regions, ASCENDS significantly improves detection of concentration, and hence flux, anomalies in the fall-winter-spring seasons relative to the prior error as well as to that inferred for OCO-2 data. The cases with greater measurement precision generally result in greater uncertainty reductions as expected, while the posterior uncertainties for the 1.57 (WCO2) and 2.05

(SCO2) μm weighting functions are similar. ASCENDS can successfully detect the boreal permafrost signal seasonally, which is an important aspect of attribution, while OCO-2 cannot (Crowell et al., 2018). These results reinforce the signal detection experiment conclusions, which show detectability after a few months of observations. A lesser measurement time requirement in the inversion is expected, since the transport model and its adjoint provide source information in the identification problem, reducing the need for the temporal averaging in the signal detection. These results assume the presence of transport and representativeness errors.

Table 3-1 ASCENDS Inverse Models Summary

			Modeling Approaches		
	4DVAR-TM5	**4DVAR-PCTM**	**EnKF-GEOS-Chem**	**Bayesian**	**GIM**
Team	OU/Melbourne	CSU-CIRA	CSU-CIRA	GSFC/AER	Stanford-Carnegie
Inversion Method	Four-dimensional variational data assimilation	Four-dimensional variational data assimilation	Ensemble Kalman filter	Batch Bayesian synthesis inversion	Batch geostatistical synthesis inversion
Transport Model	TM5 (Eulerian), ECMWF winds	PCTM (Eulerian), MERRA winds	GEOS-Chem (Eulerian), MERRA winds	STILT (Lagrangian), WRF winds	STILT (Lagrangian), WRF winds
Domain and Flux Resolution	Global, 6°x4°, monthly	Global, 6°x4.5°, weekly	Global, 2°x2.5°, two weeks	North America, 1°x1°, weekly	North America, 1°x1°, 3-hourly
Sections	3.2.1-3.2.3	3.3.3, 3.4.1-3.4.2	3.2.4	3.3.2	3.3.1
Reference	Crowell et al (2018); Basu et al. (2013); Krol et al. (2005)	Baker et al. (2006); Kawa et al. (2004)	Tippet et al. (2003); Bey et al. (2001)	Wang et al. (2014)	Shiga et al. (2014)

OU – Universtiy of Oklahoma
CSU – University of Colorado
CIRA - Cooperative Institute for Research in the Atmosphere
GSFC - Goddard Space Flight Center
AER - Atmospheric and Environmental Research

ECMWF – European Centre for Medium-Range Weather Forecasts
MERRA - Modern Era Retrospective-analysis for Research and Applications
STILT – Stochastic Time-Inverted Lagrangian Transport
WRF – Weather Research and Forecasting

> **ASCENDS data will readily enable detection of realizable permafrost thawing CO₂ emissions at high latitudes on a seasonal time scale.**

3.2.2 Fossil Fuel Emission Shift

As fossil fuel burning increases rapidly in the developing world and potentially decreases as a result of policy implementation in industrialized countries, more accurate and better-resolved emissions information is needed (Duren and Miller, 2012). Fossil fuel emissions from China have increased rapidly over the last decades (Olivier et al., 2012; Peters et al., 2011), while those from Europe decreased by 3% in 2011 relative to 2010 with an overall decline over the last two decades (Olivier et al., 2012). Satellite data, such as those available from the ASCENDS mission, increasingly play a role in both validating bottom-up estimates (e.g., Bovensmann et al., 2010) and directly inferring

fossil fuel emissions. In this section, we describe results from experiments to test the capability of the ASCENDS data to constrain fossil fuel distributions.
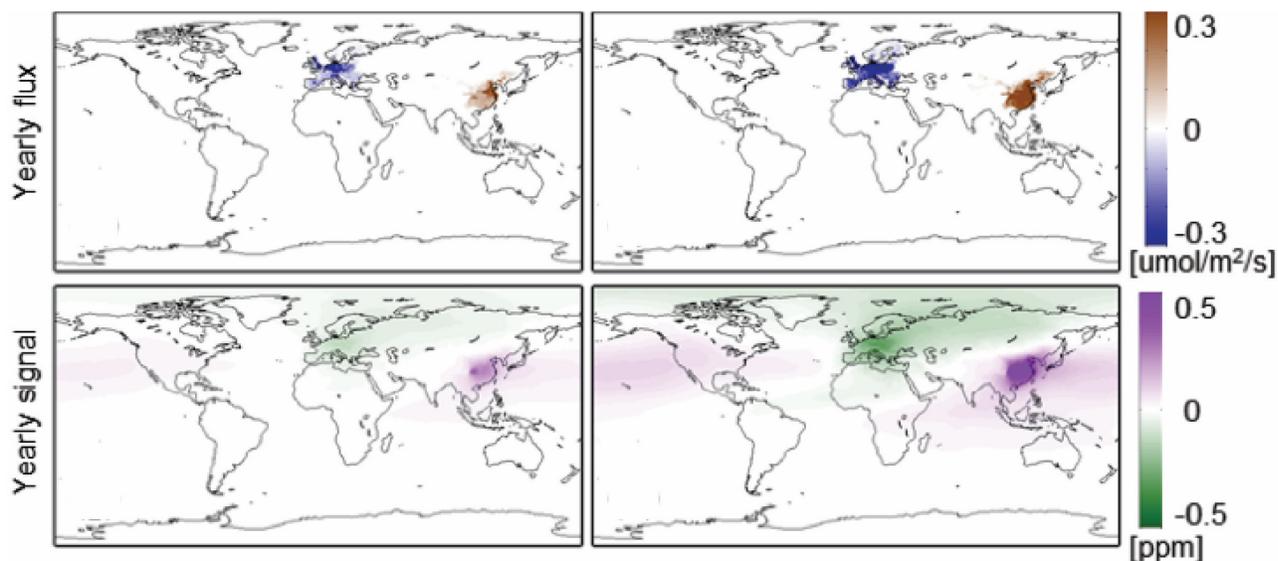
Figure 3-5 Perturbation flux and column CO$_2$ mixing ratio for the fossil fuel experiments. First row: Yearly average CO$_2$ flux shift. Second row: Yearly average column CO$_2$ concentration perturbation. Left (right) panels show the lower (higher) emission change case.

Two "flux neutral" emission scenarios valid around the year 2022 were derived to test ASCENDS ability to detect potential fossil fuel emissions changes (Hammerling et al., 2015). The emissions scenarios and corresponding CO$_2$ column average mixing ratio perturbation are depicted in Figure 3-5. The lower emission change scenario represents a 20% decrease (compared to 2007 Carbon Dioxide Information Analysis Center (CDIAC) levels (Andres et al., 2011)) of European emissions, with a corresponding 12% increase in China. The higher signal case includes a 50% decrease of emissions in Europe with a corresponding 30% increase in China, and is used for illustration purposes; a decrease of this size is not expected in Europe within a decade.
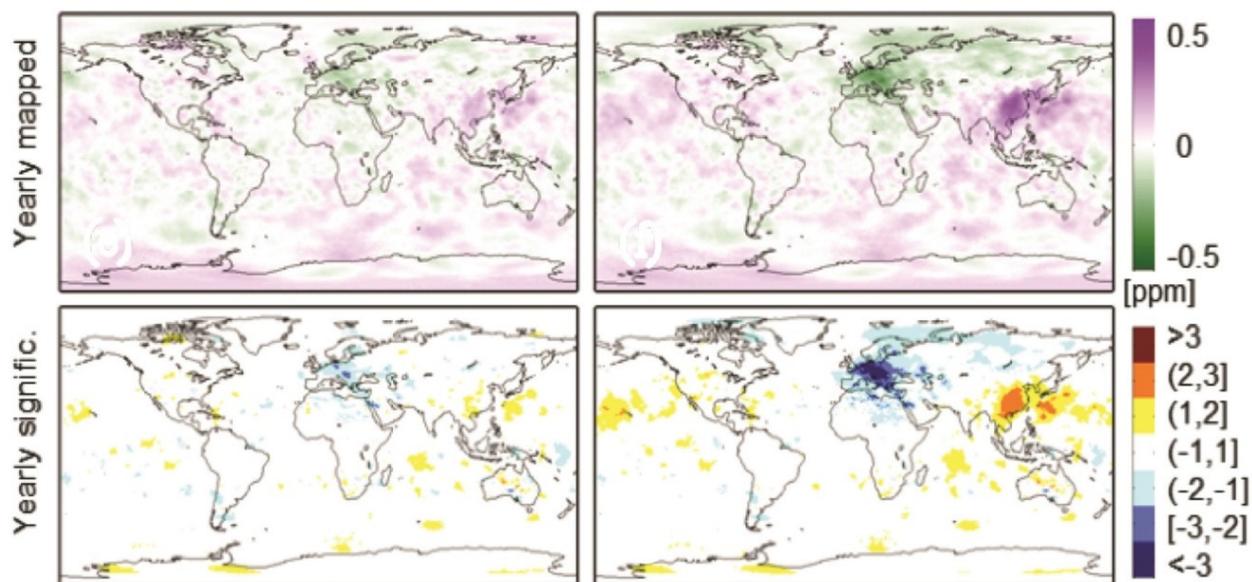
Figure 3-6 Significance results for the fossil fuel experiments for ASCENDS using nominal measurement noise of 1 ppm/10 s for the 1.57 µm case (Box 3-1). First row: yearly mapped CO_2 signal. Second row: significance of the yearly mapped CO_2 signal. The mapped signal is calculated and plotted as described in **Figure 3-3**. Left (right) panels show the lower (higher) emission change case.

Signal Detection Significance

The imposed fossil fuel emissions perturbations lead to a pronounced CO_2 spatial signature that is localized over Europe and China (Figure 3-6). This is in contrast to other experiments at mid-to-high latitude, where the spatial signatures are largely diffused and the signals in atmospheric CO_2 are seen primarily as zonal increases. The magnitude of the lower fossil fuel perturbation signal, however, is very small, and likely to be difficult to detect.

Given the relative lack of seasonality in the imposed fossil fuel perturbation scenarios, averaging over longer periods of time leads to better detectability, i.e., the annual signals are greater than those aggregated for 3 months. Although the diffusive nature of the atmospheric transport clearly plays a role, the atmospheric signal still localizes the source region of the perturbation flux throughout all the seasons. The effect of varying measurement noise levels on the detectability is as expected: increasing measurement noise leads to decreased significance in the results and requires in turn longer averaging periods. For the higher signal case, however, all considered instrument noise levels (Box 3-1) capture the signal in the annual results. Overall, these findings imply that ASCENDS can detect changes in fossil fuel emissions, but depending on the strength of the signal, detection may require multiple years of observations.

Flux Estimation
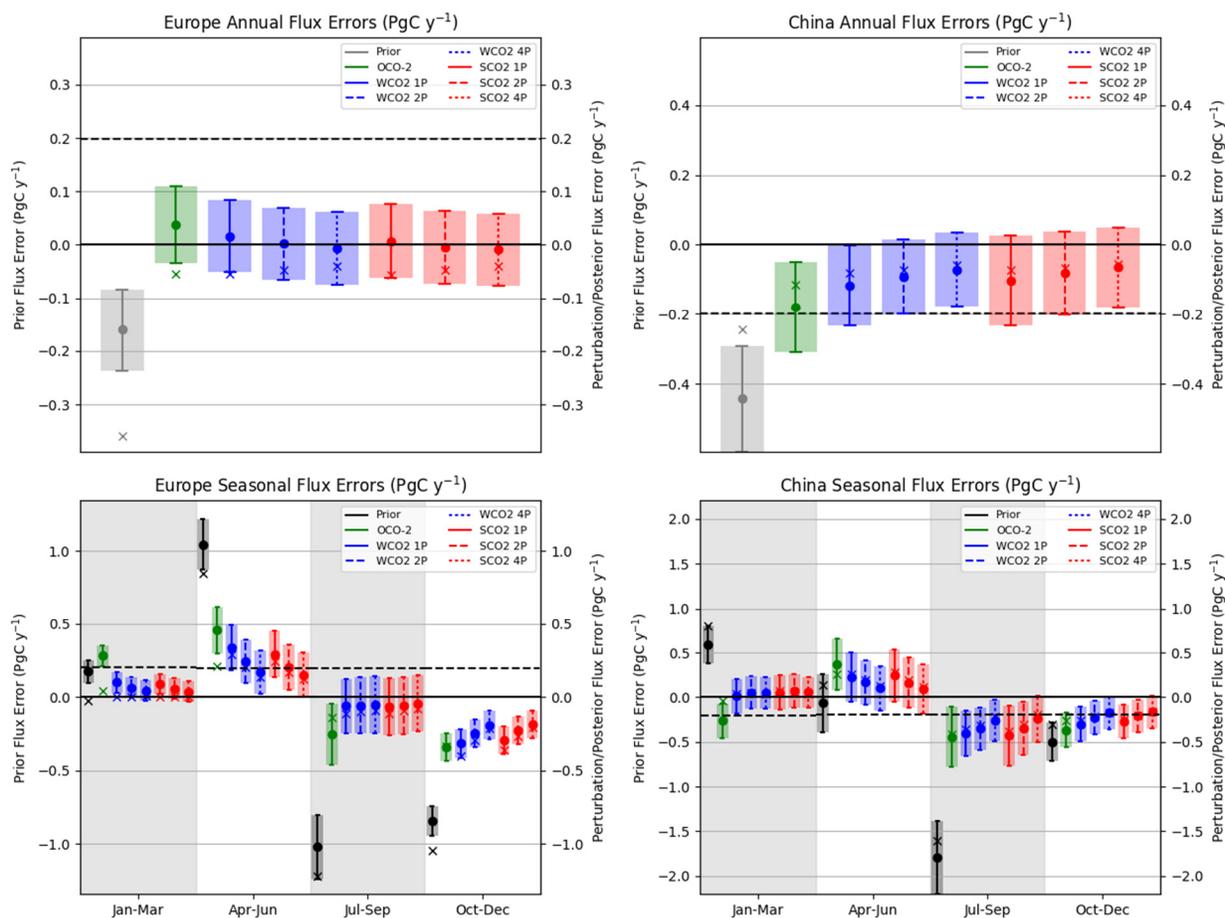
Figure 3-7 Regional flux errors for the 20% European fossil fuel emission shift scenario as in **Figure 3-4**. (top row) Annual and (bottom row) seasonal errors in the fossil fuel shift scenario prior emissions, as well as the posterior emissions after assimilating each of the pseudo-data sets as indicated by the legend. The bars represent the a 1-σ uncertainty about the mean flux. The X markers represent the baseline prior and posterior flux errors. The colors represent the prior (gray), OCO-2 (green), ASCENDS WCO₂ (blue) and ASCENDS SCO₂ (red). For the ASCENDS experiments, the precisions improve from 1 (1P left) to 0.5 (2P middle) to 0.25 ppm (4P right). The dashed horizontal line represents the magnitude of the flux perturbation (Crowell et al., 2018).

For the TM5-4DVAR inverse experiment, the true fluxes are the baseline emissions together with the low fossil fuel shift scenario pictured in the left panels of Figure 3-5. The perturbation adds about 0.2 PgC for Europe and subtracts the same from China. The prior uncertainty was taken to be the background uncertainty described above together with 25% of the CDIAC emissions for 2015. This relatively small value for the fossil fuel emissions is enough to provide the 4DVAR system with some spatial information on the location of the sources. Results for the flux estimation are shown in Figure 3-7. These figures suggest that ASCENDS is able to reduce errors in the prior emissions for each region in each case, and to significantly improve upon those from OCO-2 as a consequence of the greater coverage. The flux perturbation is detectable over Europe both annually and seasonally, while detection over China is more difficult as a result of larger background and measurement errors there, where only the highest precision ASCENDS design can achieve

detection (Crowell et al., 2018). This greatly strengthens the results of the signal detection experiment. Again, this is due to the inclusion of the transport model adjoint, which is able to correctly trace concentration differences back to source regions as large as Europe and China.

> **ASCENDS will be able to identify a foreseeable shift in annual and seasonal fossil fuel emissions at the scale of Europe and China, presuming a sufficiently accurate instrument.**

3.2.3   Flux Changes in the Southern Ocean

The Southern Ocean is a very sparsely sampled region that represents a key uncertainty in the carbon cycle. This region has high sensitivity to climate change (Le Quéré et al., 2009), and understanding its regional carbon-climate feedback has implications for quantifying the region's future as a carbon sink. Studies have shown that the Southern Ocean contribute half of the ocean uptake of anthropogenic CO_2 (e.g., Le Quéré et al., 2009; Meredith et al., 2012), although uncertainties on the magnitude of this uptake and its trend over time are high. Given that the Southern Ocean is also very difficult to monitor in situ, the ability of the ASCENDS mission to observe in this region will provide invaluable insights into changes in the ocean carbon sink. The airborne instrument simulators have successfully demonstrated good XCO_2 measurements over rough ocean and through broken cloud fields (Section 5.5; Mao et al., 2018; Dobler et al., 2013) as required for this regime.
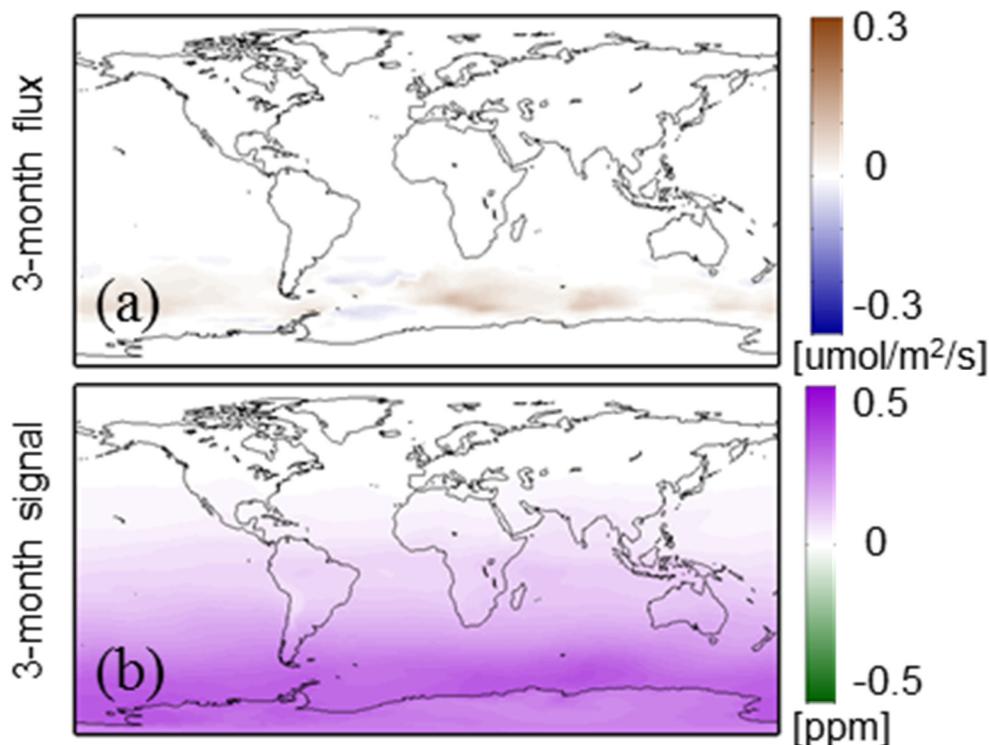
Figure 3-8 Southern Ocean experiment flux difference and column average CO_2 mixing ratio perturbation using the 1-ppm, 1.57 µm nominal ASCENDS error case. (a) 3-month (April – June) average CO_2 flux and (b) 3-month average CO_2 concentration.

Variations in climatic modes, such as the El Nino-Southern Oscillation (ENSO), are key drivers of interannual variability in ocean carbon exchange. For this reason, scenarios for opposing ENSO modes were chosen to test detectability of Southern Hemisphere (SH) ocean flux changes that ASCENDS expects to encounter. The Southern Ocean fluxes used for this scenario are based on a hindcast simulation of the Community Climate System Model (CCSM) Ocean Biogeochemical Elemental Cycle model as described by Doney et al. (2009). Fluxes were obtained at one degree spatial and monthly temporal resolution. The years 1977 and 1979 were chosen as prototypical example flux patterns, as they represent large differences in ocean fluxes due to variations in climatic modes. The simulated air-sea CO_2 flux in 1979 was about half of that for 1977 averaged across the Southern Ocean. The flux difference between 1977 and 1979 in the Southern Ocean is used for the perturbation scenario. Figure 3-8 shows the average fluxes and column mixing ratio change for April through June (from Hammerling et al. (2015)).

Signal Detection Significance

The detection of changes in the Southern Ocean source/sink characteristics is the most challenging of the three signal detection scenarios considered, for several reasons. The overall magnitude of the CO_2 difference signal in the Southern Ocean is weak, with an absolute value never exceeding 0.4 ppm in the column. In addition, this scenario contains sub-seasonal and sub-regional-scale flux variability, superimposed on the seasonal pattern in the fluxes, which makes the perturbation more difficult to distinguish. Atmospheric mixing also plays a role in obscuring the longitudinal fingerprint of the Southern Ocean as the origin of the signal, similar to what was observed in the permafrost carbon release scenario described above.
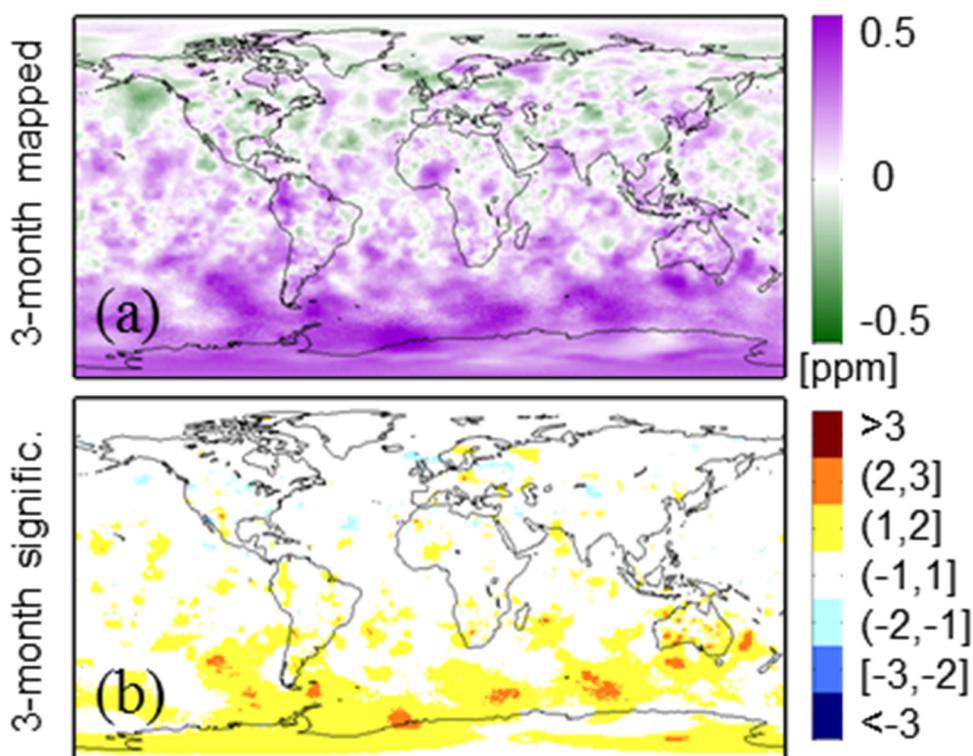
Figure 3-9 Significance results for Southern Ocean experiment for medium measurement noise (1 ppm, 1.57 µm case, Box 3-1). (a) 3-month mapped CO_2 signal, (b) Significance of the 3-month mapped CO_2 signal as described in **Figure 3-4**.

Figure 3-9 shows areas of the SH ocean are distinguishable at the 2 to 3 sigma level for 3-month aggregated ASCENDS sampling with 1-ppm/10-s nominal random error levels, but the signal is not strong. For annually aggregated measurements (not shown), the yearly results clearly indicate a zonal increase in the High Southern Latitudes, however, the pattern indicative of the Southern Ocean flux difference within the zonal band is less clear.

Flux Estimation

A surface flux estimation experiment was performed for the Southern Ocean background flux, similar to those described in Sections 3.2.1 and 3.2.2. The prior covariance for the Southern Ocean is the flux difference between the National Center for Atmospheric Research (NCAR) CCSM Ocean Biogeochemistry Model (e.g., Doney et al., 2009) and Takahashi et al. (2009) for the reference year 2000.

The prior and posterior errors aggregated for the Southern Ocean are shown in Figure 3-10. Despite the weak signal strength, ASCENDS would be able to provide a >60% reduction (depending on instrument configuration) in uncertainty in variability of the emissions of the Southern Ocean. Although none of the tested instrument model posterior distributions includes the truth, implying they are not sufficient to determine the annual (or seasonal) flux given this estimate of the background error, ASCENDS is able to provide some information about the spatial gradient from east to west in the Southern Ocean by aggregating along lines of longitude in the Southern Ocean (not shown). This type of spatial information would be unavailable using the current surface network, which could only provide a few pieces of information that would represent local flux variations only.
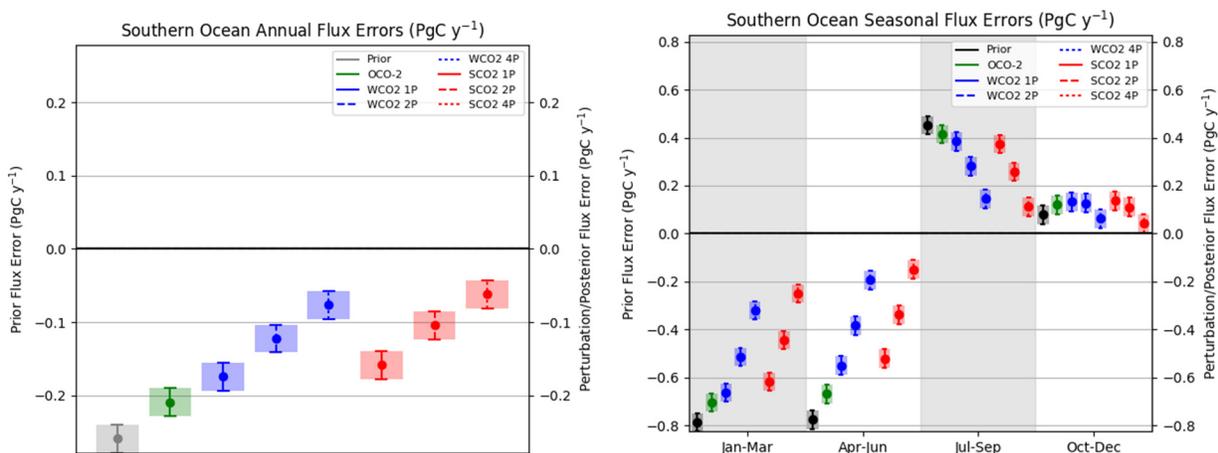
Figure 3-10 Inversion results from the Southern Ocean flux variability experiment. (left) Annual and (right) seasonal prior errors and posterior errors for the Southern Ocean region in the baseline experiment. The bars represent the a 1-σ uncertainty about the mean flux. The colors represent the prior (gray), and posterior errors after assimilating observations from OCO-2 (green), ASCENDS WCO₂ (blue) and ASCENDS SCO₂ (red). For the ASCENDS experiments, the precisions improve from 1 (1P left) to 0.5 (2P middle) to 0.25 ppm (4P right) as in Crowell et al. (2018).

ASCENDS observations, coupled with an accurate transport model, have potential to substantially reduce uncertainty in Southern Ocean fluxes and provide some constraint on their spatial and temporal variability.

3.2.4   Enhanced Sink Due to Carbon Fertilization

The previous experiments examine realistic perturbations to one aspect of the carbon cycle. In reality, CO_2 datasets and models will be used to examine multiple possible perturbations to land and ocean fluxes occurring simultaneously. Here, we create a more complex signal detection experiment by combining several realistic perturbations to test the ability of the ASCENDS data to constrain Net Ecosystem carbon Exchange (NEE) over different times and locations. These perturbations include:

- Respiration reduced by 5% over Northeastern United States (US) forests to simulate forest regrowth after land use change. There is strong evidence (Houghton et al., 1999; SOCCR, 2007; Pan et al., 2011) to support an enhanced carbon sink as forests re-grow after centuries of clearing for agriculture.

- Forest Gross Primary Production (GPP) increased by up to 10% over regions of Western Europe and the Central US as a function of nitrogen deposition, with peak effect over areas of known industrial nitrogen emissions.

- GPP amplified by 5% over tropical broadleaf forest regions between 30°S and 30°N to account for a CO_2 fertilization effect in tropical forests. Both basic plant physiology, as well as experimentation (Oren et al., 2001) support the idea that increased atmospheric carbon dioxide levels should lead to increased plant uptake.

- A reduction of overall atmospheric-ocean exchange (as might result from decreasing winds) imposed by providing a zonal variation to the flux, from a 5% reduction in flux over the Northern Oceans to a 15% reduction over the Tropical Oceans, to a 25% reduction over the Southern Ocean (e.g., Le Quéré et al., 2009).
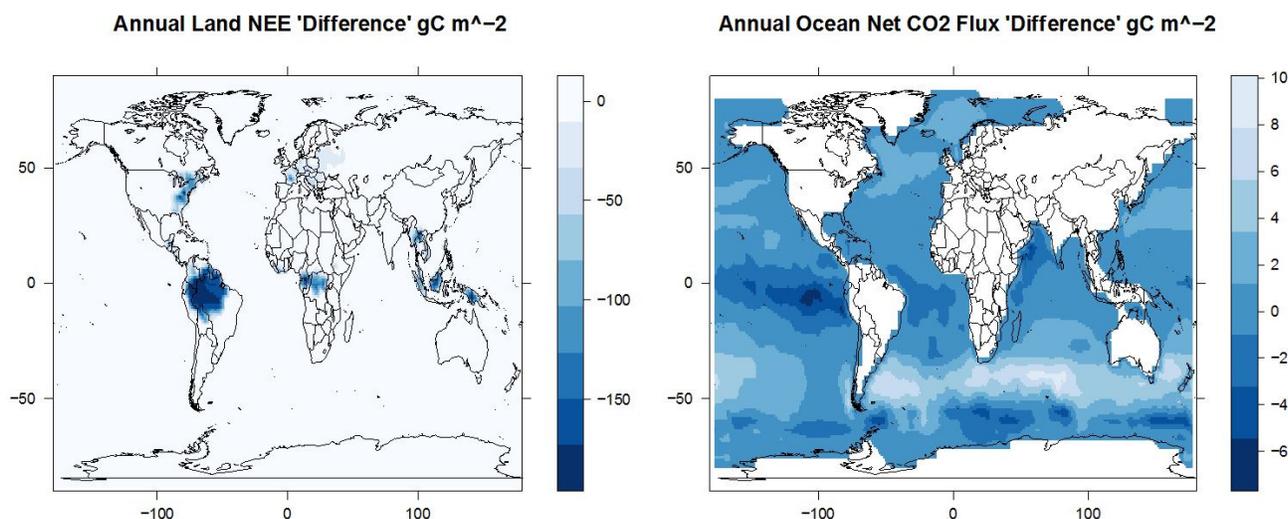
Figure 3-11 The simulated net CO$_2$ flux anomalies that arise from the GPP and ocean flux perturbations used in the multiple signal detection exercise and inversions. Note the dominance of Amazon GPP sink enhancement.

The flux perturbations shown in Figure 3-11 were used to drive GEOS-Chem for 2006 and 2007 to produce 3-D CO$_2$ anomaly fields for 2007. The fields were then sampled using the ASCENDS weighting functions resulting in XCO$_2$. The mean zonal gradient for each month was then subtracted from the monthly perturbation XCO$_2$ fields in order to isolate the local effects of sinks on XCO$_2$. Finally, this average perturbation field was divided by the expected ASCENDS errors. The absolute perturbation signal-to-noise of the ASCENDS pseudo measurements (Figure 3-12) is often greater than 0.5 for *individual* retrievals at 1-ppm nominal error (Box 3-1), with slightly stronger signals during the Amazonian wet season. These results suggest that the strong Amazon drawdown would be evident from ASCENDS by carefully aggregating individual satellite retrievals. While the weakened surface exchange of CO$_2$ in the oceans seems unlikely to be detectable from individual ASCENDS retrievals, the combined effect of reduced respiration and N fertilization effects on regrowing Northeastern US forests, most evident in the late spring and summer, is evident, although at much lower signal to noise than the Amazon.

Flux Estimation
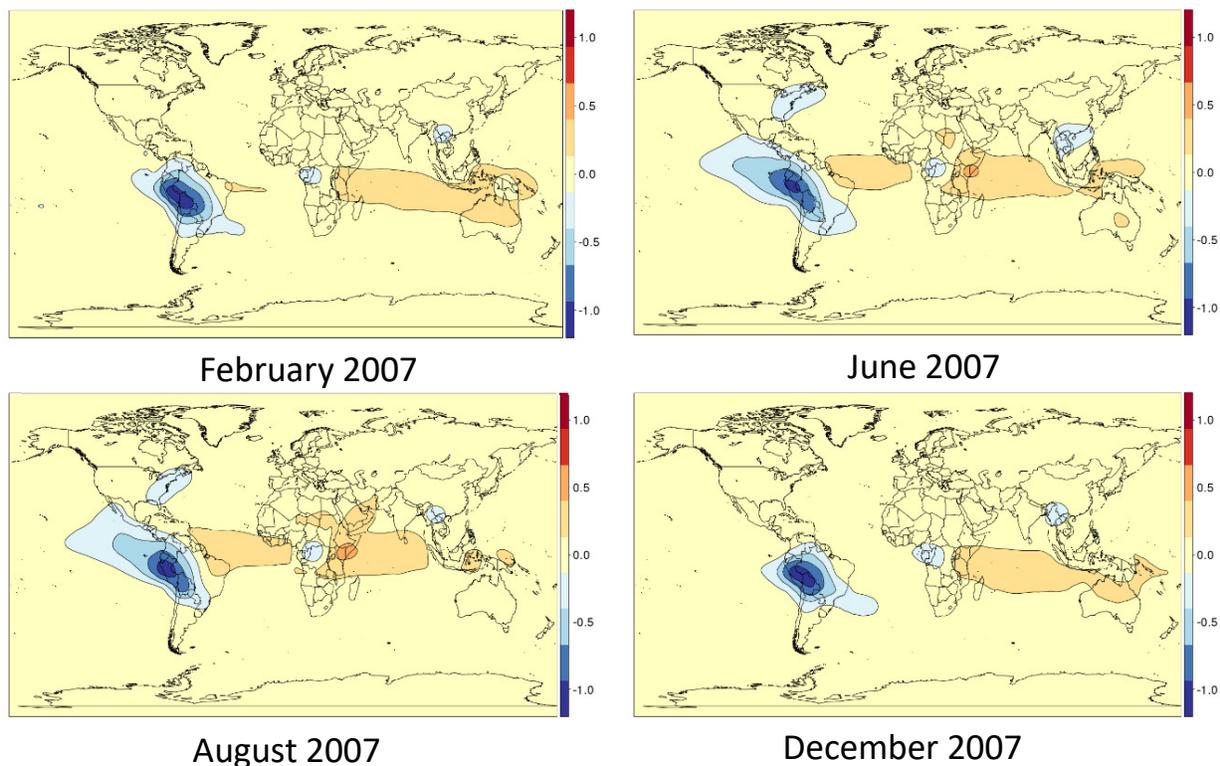
Figure 3-12 Simulated perturbation signal-to-noise for XCO₂ with 2.05 µm weighting function (See **Box 3-1** and **Figure 5-2**) for the multiple flux perturbations of **Figure 3-11**.

The results above suggest the ability of individual retrievals to detect realistic flux perturbations. An EnKF-based inversion (Table 3-1, Box 3-2, Appendix C) was run on the perturbed CO₂ field to determine to what degree the true perturbed fluxes could be estimated using ASCENDS observations. Figure 3-13 shows the true and the posterior estimated fluxes: their similarity indicates that large perturbations in land fluxes, such as the Amazon, will be attributable via inversions of atmospheric CO₂ measurements from ASCENDS. Figure 3-14 shows that the difference between the ensemble mean CO₂ flux estimate for the Tropical South American region (Transcom; Gurney et al., 2002) and the "truth" is approximately 100 Teragrams of Carbon per year (TgC y^{-1}) with a standard deviation (uncertainty) of the posterior estimate at approximately the same magnitude. The recovered sink is approximately 18 times that, indicating a strong recovery by the inversion system.

(a)

(b)
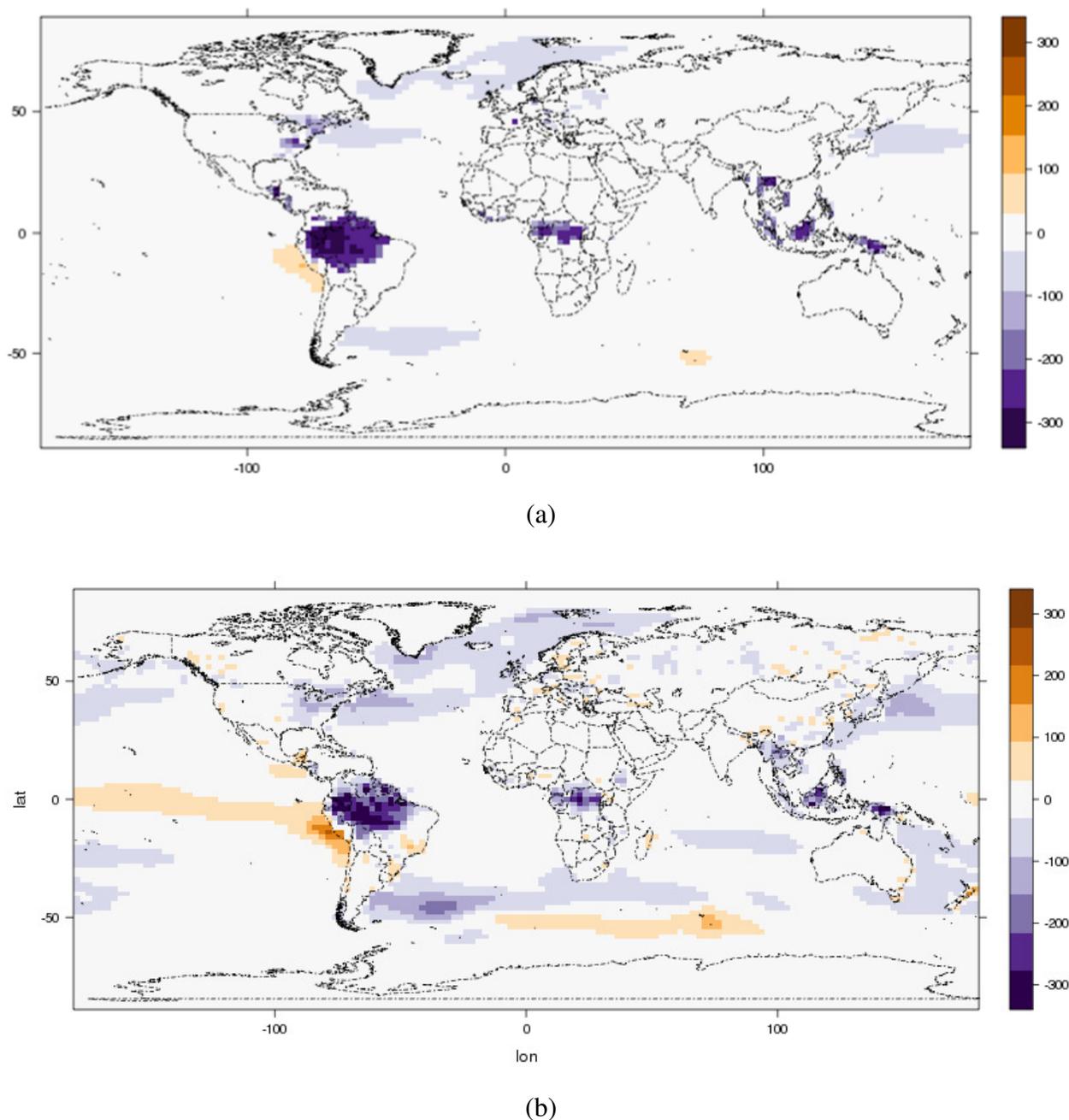
Figure 3-13 Comparison of 'truth' and model annual Net Ecosystem Exchange (NEE, gC m^{-2} yr^{-1}) (a) the 'truth' representing the sum of the two sets of perturbations shown in **Figure 3-11** and (b) model estimated posterior mean NEE from the atmospheric inversion. Posterior uncertainty can be seen below in **Figure 3-14**.

Weaker land signals such as those generated by regrowth of forests in the northeastern US and nitrogen fertilization of Europe are also generally improved by the inversion system, although the pattern is more diffuse than that specified in the "true" fluxes. The difference between the ensemble mean CO₂ flux estimate for the Temperate North American region and the "truth" is approximately 38 TgC y^{-1} with the standard deviation of the estimate at approximately 40 TgC y^{-1}, significantly smaller than the recovered sink (~200 TgC y^{-1}). Spatial differences of up to 100 gC m^{-2} within the

region are seen (Figure 3-13) although the integrated average difference is much smaller. Ocean perturbations are not seen well by the inversion system, which could be due to a misspecification of the prior covariance for the ocean fluxes in the simulations, weaker magnitudes of the ocean flux perturbations, or likely some combination of the two.

> **ASCENDS will provide data sufficient to constrain large tropical land sinks as well as some weaker Northern mid-latitude regional land sinks.**
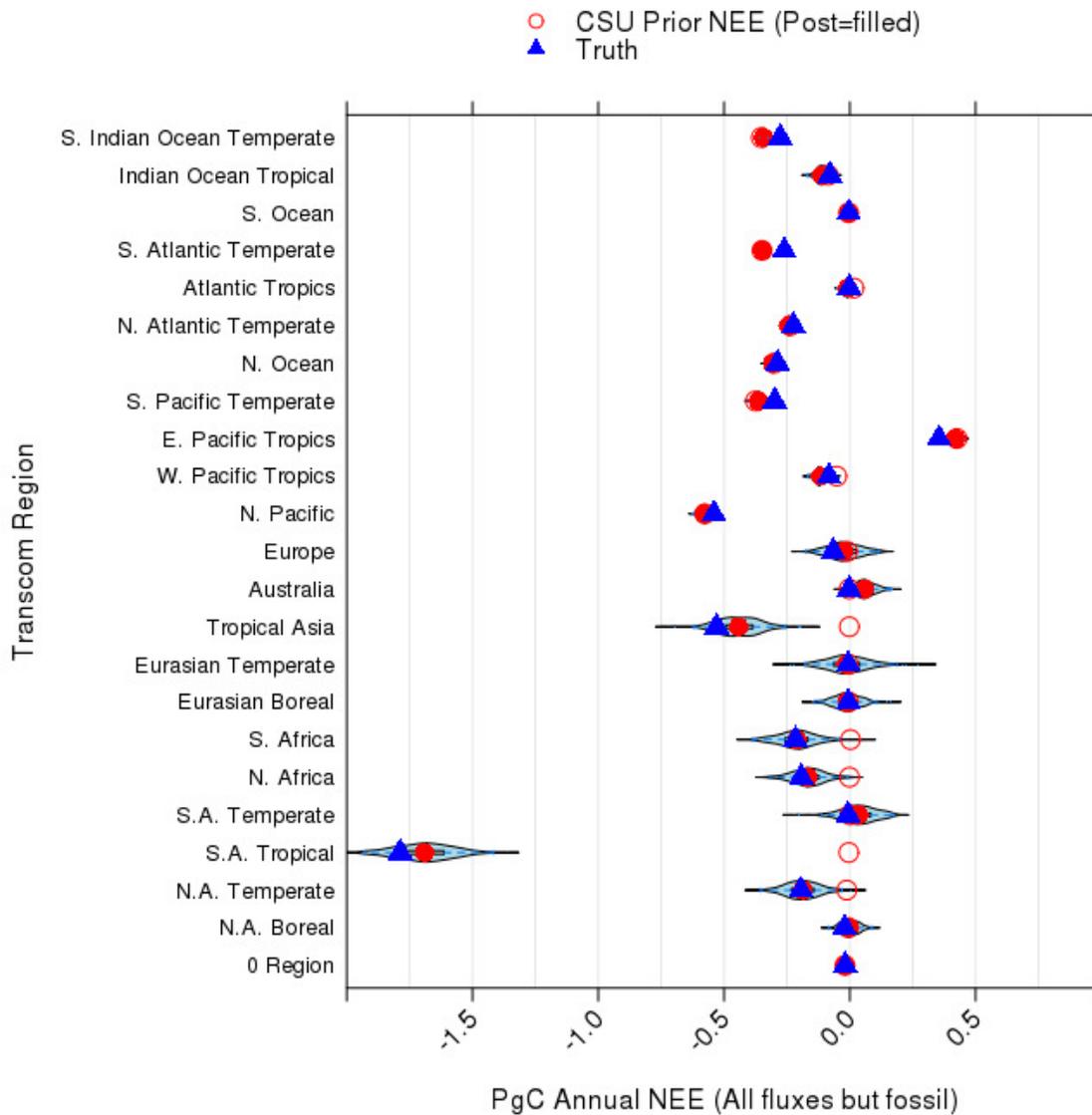
Figure 3-14 Regional integrated annual NEE for atmospheric inversion test. The blue shaded area can be interpreted as the probability density function estimate for the ENKF ensemble (Hintze et al., 1998).

3.3 Improved Flux Estimates at Global and Regional Scales

The experiments in Section 3.2 evaluated the ability of ASCENDS measurements to address specific science hypotheses that were posed as potential perturbations to carbon fluxes. Here, we broaden this approach to test the general impact of prospective ASCENDS data on flux inversions at both regional and global scales. A major goal of this exercise is to test the impact of a range of possible mission and instrument implementation options (Section 5) on the ability of ASCENDS to reduce uncertainty in our knowledge of the carbon budget. Some of these parameter explorations were already exhibited in the inversions in Section 3.2. A variety of modeling approaches is used in order to bolster the robustness of the findings from any individual model, whose flux retrieval performance may well depend on model-specific methods and assumptions (Table 3-1). The general Bayesian inverse modeling approach, and its variants, employed for these experiments are briefly outlined in Box 3-2, and in more detail in Appendix C. The instrument models that are tested include sampling with vertical weighting functions applicable to measurement wavelengths of 1.57 and 2.05 µm (Figure 5-2), several levels of nominal random error (0.25 to 2.0 ppm) scaled globally (Box 3-1), and several possible forms of bias error (in the global inverse model only).

Box 3-2 Flux Estimation Techniques

The basic premise of the inverse modeling approaches is that, given a set of atmospheric concentration observations and using a model of atmospheric transport and chemistry, it is possible to infer information on the distribution of sources and sinks at the surface of the Earth (Enting, 2002). The approach most commonly adopted in atmospheric inverse modeling of CO_2 sources and sinks is based on Bayesian inverse modeling, in which one seeks the optimal flux estimate $\hat{\mathbf{s}}$ that minimizes:

$$J(\mathbf{s}) = (\mathbf{s} - \mathbf{s_o})^{\mathrm{T}}\mathbf{B}^{-1}(\mathbf{s} - \mathbf{s_o}) + (\boldsymbol{h}(\mathbf{s}) - \mathbf{y})^{\mathrm{T}}\mathbf{R}^{-1}(\boldsymbol{h}(\mathbf{s}) - \mathbf{y}) \qquad (3\text{-}2)$$

where y is a vector of atmospheric CO_2 observations, $\mathbf{h}$ is a vector of modeled observations given by sampling the atmospheric transport model, $\mathbf{s}$ is a vector of the discretized unknown surface flux distribution, $\mathbf{R}$ is the model-data mismatch covariance, $\mathbf{s_o}$ is the prior estimate of the flux distribution $\mathbf{s}$, and $\mathbf{B}$ is the covariance of errors in the prior estimate $\mathbf{s_o}$. The final solution in the form of a posteriori means and covariances is given by:

$$\hat{\mathbf{s}} = \mathbf{s}_0 + \mathbf{B}\mathbf{H}^T\left(\mathbf{H}\mathbf{B}\mathbf{H}^T + \mathbf{R}\right)^{-1}\left(\mathbf{y} - \mathbf{H}\mathbf{s}_0\right) \qquad (3\text{-}3)$$

$$\mathbf{V}_{\hat{s}} = \mathbf{B} - \mathbf{B}\mathbf{H}^T\left(\mathbf{H}\mathbf{B}\mathbf{H}^T + \mathbf{R}\right)^{-1}\mathbf{H}\mathbf{B} \qquad (3\text{-}4)$$

where $\hat{\mathbf{s}}$ is the posterior best estimate of the surface flux distribution and $\mathbf{V_s}$ is the a posteriori covariance of that best estimate, where the diagonal elements represent the predicted error variance of individual elements in $\mathbf{s}$. $\mathbf{H}$ (a.k.a. the sensitivity matrix) is calculated by sampling the atmospheric transport model and represents the sensitivity of the observations $\mathbf{y}$ to the fluxes $\mathbf{s}$. Participating modeling groups (Table 3-1) have employed different techniques to find the solution to the atmospheric inverse problem posed in the equations above. Further detailed information can be found in Appendix C.

3.3.1 North American Regional Flux Estimates
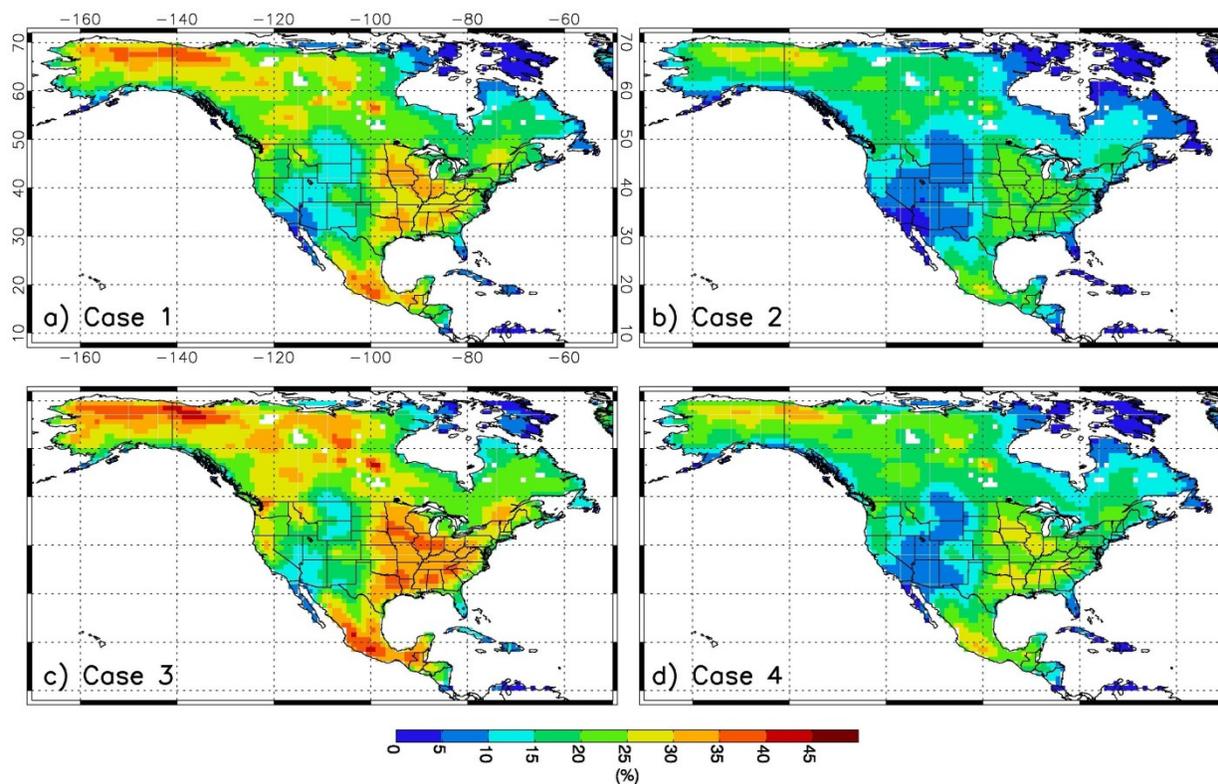
Figure 3-15 Weekly flux uncertainty reduction (RMS over Jan, Apr, Jul, and Oct) over North America for a) Case 1 (1.57 µm and 0.5 ppm/10 s nominal error), b) Case 2 (1.57 µm and 1.0 ppm), c) Case 3 (2.05 µm and 0.5 ppm), and d) Case 4 (2.05 µm and 1.0 ppm).

Bayesian synthesis (batch) inversions are used to quantify the precision with which ASCENDS measurements can constrain land carbon sinks and sources at relatively high spatial resolution over a region such as North America (Wang et al., 2014). We consider four possible instrument configurations, including two weighting functions (for the 1.57 µm and 2.05 µm wavelengths) and two nominal random error levels (0.5 ppm and 1.0 ppm, see Box 3-1). ASCENDS observations in this modeling framework reduce flux uncertainties substantially at fine scales. At 1° x 1° resolution, weekly uncertainty reductions up to 30-45% (averaged over the year) are achieved depending on the instrument configuration (Figure 3-15). Relatively large uncertainty reductions occur year-round in southern Mexico and the US Pacific Northwest and seasonally over the southeastern and mid-western US and parts of Canada and Alaska. The magnitude of uncertainty reduction is dependent on the observational coverage, the specified model-data mismatch and the prior flux errors. Uncertainty reductions at the annual, biome scale range from ~40% (desert) to ~75% (eastern temperate forest and temperate grassland/shrubland) over the four experimental cases, and from ~65% to ~85% for the continent as a whole (Figure 3-16). The uncertainty reductions for the 1.57 µm candidate wavelength are on average 8% smaller than those for 2.05 µm, and for 0.5 ppm reference error are on average ~15% larger than those for 1.0 ppm error.
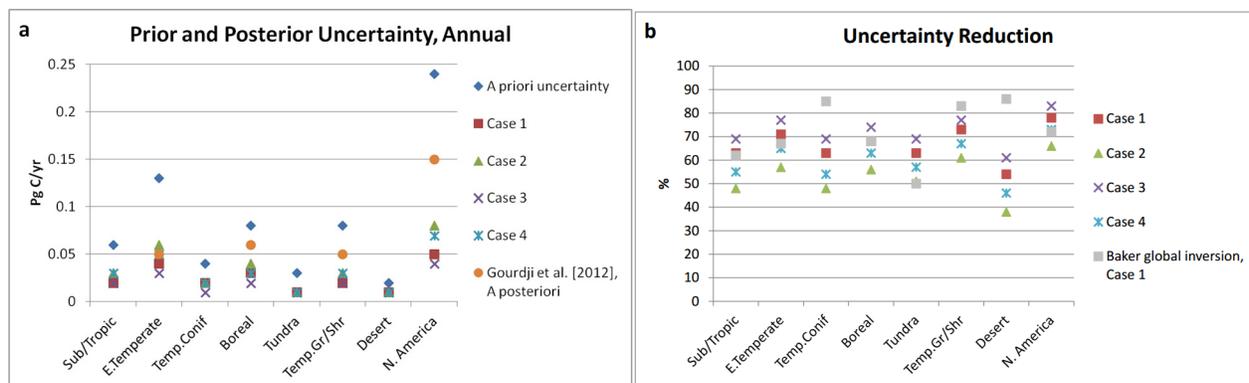
Figure 3-16 Results aggregated to biomes and continent, and compared with other studies a) A priori and a posteriori uncertainties for the year, including results from Gourdji et al. (2012). b) Fractional uncertainty reductions, including results from the CSU-PCTM OSSE described in Section 3.3.3. Gourdji et al. reported results for only the three biomes that were well constrained by their in situ observation network, along with results aggregated over the full continent; we show the approximate average of their "Simple" and "NARR" inversions. The Gourdji et al. method does not rely on prior flux estimates.

The uncertainty reductions in this regional OSSE are similar in magnitude on average to those of the global ASCENDS inversion detailed in Section 3.3.3.1 when aggregated to the latter's coarser 4.5° x 6° model grid and to the biome and continent scales (Figure 3-16).

Based on the flux precision level suggested by Hungershoefer et al. (2010), ASCENDS observations would meet the threshold requirement (flux uncertainty of less than 0.1 Pg C yr^{-1} at the annual, biome scale) for all biomes within the range of measurement designs considered here (Figure 3-16). The observations constrain a posteriori flux uncertainties to a level of 0.01-0.06 Pg C yr^{-1}, and could thus help identify the location and magnitude of long-term carbon sinks. With regard to the more stringent target requirement (less than 0.02 Pg C yr^{-1}), a subset of the instrument designs would meet the target for a majority of biomes.

These results represent a best-case scenario, as measurement biases and other sources of systematic errors not considered here (e.g., transport model, boundary condition) degrade inverse flux estimates. However, abundant concentration measurements by ASCENDS can be expected to mitigate the impact of boundary condition uncertainties on regional flux estimates (Wang et al., 2014).

> **ASCENDS observations are expected to reduce flux uncertainties substantially at biome and finer (e.g. approximately 100 km by 100 km) scales, addressing requirements for an improved understanding of long-term carbon sinks.**

3.3.2 Regional Fossil Fuel Emissions

In this experiment, we explore the ability of ASCENDS CO₂ measurements to distinguish between fossil fuel and natural biospheric fluxes. This analysis is performed with a regional Geostatistical Inverse Modeling (GIM) framework over North America (NA) that examines fluxes at a 1° by 1° spatial and 3-hourly temporal resolution (Table 3-1). We examine the potential of ASCENDS measurements to detect and attribute variations in the spatio-temporal patterns of Fossil Fuel CO₂

(FFCO$_2$) emissions from sub-continental regions in NA during January. January is selected because it represents a time when the confounding effects of biospheric CO$_2$ flux are at a minimum. Simulated CO$_2$ observations are created using biospheric fluxes from CASA- GFEDv2 (Global Fire Emissions Database, Version 2; Randerson et al., 1997), FFCO$_2$ emission from the Vulcan Project (Gurney et al., 2009) over the continental US and Open-source Data Inventory for Anthropogenic CO$_2$ (ODIAC; Oda and Maksyutov, 2011) over Alaska, Canada and Mexico, and various levels of random error. Detection is evaluated by the ability to attribute variations in three-hourly ASCENDS CO$_2$ observations to patterns consistent with the simulated FFCO$_2$ emissions. A more detailed description of the FFCO$_2$ emissions pattern detection methodology can be found in Shiga et al. (2014).

Four cases representing different instrument configurations are explored using the two weighting functions (1.57 µm and 2.05 µm) and two random error levels (0.5 ppm and 1.0 ppm) as in the previous section. For the 1 ppm nominal error cases, both 1.57 µm and 2.05 µm instrument configurations could detect the FFCO$_2$ emissions from only one region, i.e., the Northeast US region (Figure 3-17a). For the 1.57 µm instrument case, reducing errors to the 0.5 ppm nominal error level did not improve detectability. However, for the 2.05 µm instrument case, when reducing errors to the 0.5 ppm nominal error level, detection of the FFCO$_2$ emissions patterns from the Midwest and Southeast US regions becomes possible (Figure 3-17b). This result shows that the impact of reducing errors for the 2.05 µm instrument are greater with regards to detecting FFCO$_2$ emissions than for the 1.57 µm instrument configuration. For all configurations, the ASCENDS CO$_2$ observations, in the absence of in-situ observations, will be able to detect the FFCO$_2$ emissions patterns of the largest emitting sub-continental regions over NA.
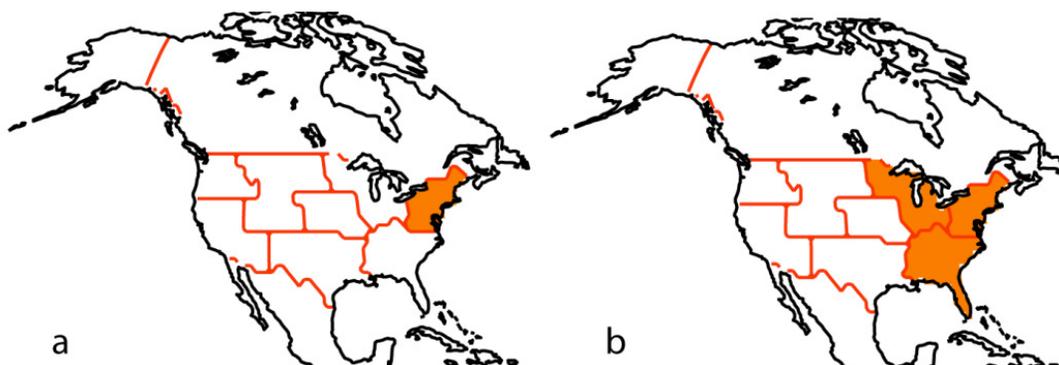
Figure 3-17 The regions where fossil fuel CO$_2$ emissions are detected for January (in orange) using ASCENDS 2.05µm weighting function with (a) 1 ppm nominal error and (b) 0.5 ppm nominal error. Detection results for the 1.57 µm weighting function for both error levels mirror panel (a).

> **ASCENDS will be able to discern the FFCO$_2$ emissions patterns from the largest emitting sub-continental regions over North America, particularly with the 2.05 µm weighting function.**

3.3.3   Global Flux Estimation with ASCENDS

In this section we quantify the reduction in the uncertainty in the flux estimates globally that is possible by using CO_2 measurements from ASCENDS in the 4DVAR-PCTM inverse model (Table 3-1). The flux errors are constructed by selecting two reasonable models of global land biospheric fluxes and air-sea fluxes, each set having the seasonal variability of a representative year (Table 3-1, Box 3-2, Baker et al., 2010). Net fluxes from the Lund–Potsdam–Jena (LPJ) land biosphere model (Sitch, et al., 2003) plus ocean fluxes from a run of the National Center for Atmospheric Research (NCAR) ocean model that captures the impact of rising anthropogenic CO_2 concentrations (Doney et al., 2006; Najjar et al., 2007) are assigned the role of the "true" fluxes. Net CASA land biospheric flux from Randerson et al. (1997) plus air-sea fluxes from Takahashi et al. (1999) are used as the prior flux estimate. The difference between the two can be thought of as a global net CO_2 flux error "signal" to be estimated in the assimilation, analogous to the sum of process-based signals like those used in Section 3.2. The difference is that this "signal" is perhaps more representative of the actual flux error we expect to encounter in the real world. Insofar as the inversion problem is made more difficult by having to distinguish between large fluxes in close proximity to each other, this simulation should provide a more general test of the ability of ASCENDS data to constrain fluxes. Other than not having errors due to uncertainties in the fossil fuel flux distribution (which are relatively small except over the strongest fossil emission areas), this case should provide flux estimation errors similar to what would be obtained using real ASCENDS data.

3.3.3.1   Impact of Random Observational Errors

To test the global flux impact of different instrument design possibilities, weekly fluxes for a full year were estimated at 4.5º x 6º resolution (lat/long) for six ASCENDS cases: the 2.05 and 1.57 μm weighting functions with nominal random measurement errors at three levels: 0.25, 0.5 and 1.0 ppm/10 s (Box 3-1). In this model setup, measurement uncertainties across the globe were estimated by multiplying the spatial patterns like those in Figure 3-1 (in Box 3-1) by a given error value (e.g., 0.5 ppm) on a monthly-varying basis (see Appendix C).
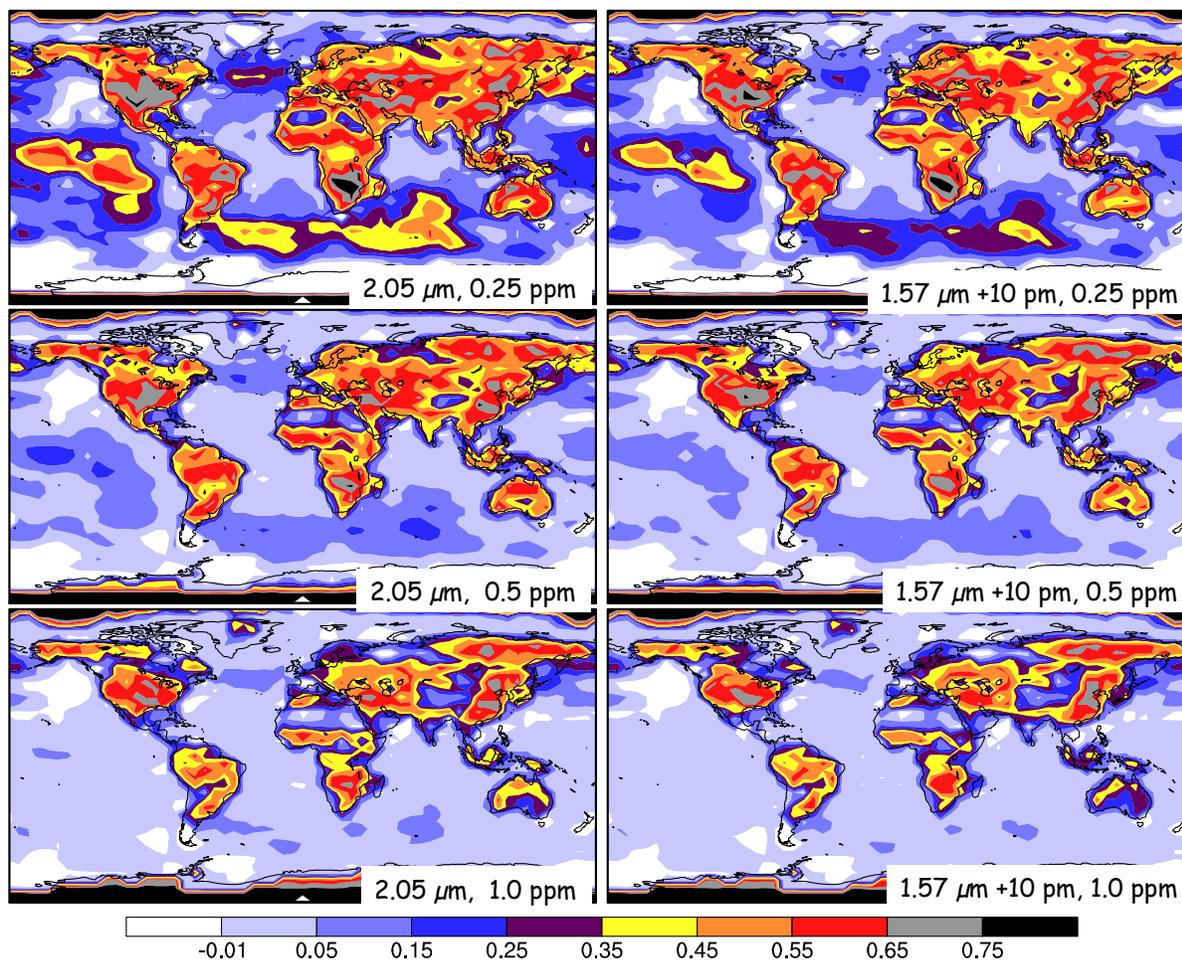
Figure 3-18 Fractional error reduction in weekly flux at 4.5°x6° resolution (lat/long) for six cases: using the 2.05 μm and 1.57 μm vertical weighting and measurement uncertainties at 0.25, 0.5, and 1.0 ppm.

Figure 3-18 shows the fractional error reduction with respect to the prior for the six cases. Substantial improvements in the flux estimates are obtained in all cases (Table 3-2). At the 0.5 ppm nominal measurement error, flux uncertainty reductions of 50% or better are obtained over most of the vegetated land areas. As expected, reducing the measurement error from 1.0 to 0.5 to 0.25 ppm reduces flux error over both land and ocean areas. At 0.25 ppm error, major improvements are seen over ocean basins as well. The improvements obtained for the 2.05 μm case, whose vertical sensitivity (Figure 5-2) peaks nearer the surface, are generally slightly larger than for the 1.57 μm case. This is true despite the fact that the measurement uncertainties for the 2.05 μm case are somewhat larger over most land regions (Figure 3-1 in Box 3-1): the stronger near-surface vertical sensitivity outweighs the impact of the larger random errors.

The a posteriori flux uncertainties obtained here should be applicable to localized net fluxes from any part of the globe, since they primarily reflect the constraint provided by the measurements rather than the prior flux uncertainties. To compare these results to those of the signal detection experiments in Section 3.2, we sample the grid-scale errors for the regions of interest. Fluxes north

of 65ºN are retrieved here with a precision of 0.38 gC m^{-2} d^{-1} (1σ) during June-August, and to 0.26 gC m^{-2} d^{-1} across the full year, using ASCENDS data at the 0.5 ppm nominal measurement uncertainty. This corresponds to a weekly flux uncertainty of ~200 TgC y^{-1}. Uncertainty totals for the North American and Siberian areas are ~80 and ~180 TgC y^{-1}, respectively. These numbers give the precision of the estimate of net CO_2 flux coming from the permafrost region – that is, the combined impact of photosynthesis, respiration, fire, and any other permafrost-related emissions (e.g. methane oxidized to CO_2) – but cannot say how much is due strictly to permafrost-related emissions. The magnitude of the permafrost emission perturbation is 613 to 752 TgC y^{-1} for 2020 to 2022 (Hammerling et al., 2015), which should be readily attributable, consistent with the findings from Section 3.2 above.

Table 3-2 Flux Inversion Fractional Error Reduction*

Mission Sampling	ASCENDS 1.57 um			ASCENDS 2.05 um			In situ + TCCON	GOSAT ACOS**	OCO-2
Mmt Error (ppm)	0.25	0.5	1.0	0.25	0.5	1.0			
Land	0.55	0.49	0.41	0.58	0.51	0.44	0.22	0.30	0.59
Ocean	0.28	0.21	0.14	0.32	0.24	0.17	0.09	0.10	0.31

* Reduction is equal to (prior-posterior)/prior error where the prior error is the grid-scale RMS flux difference between two carbon models and the posterior error is the flux difference after assimilating each data stream separately. Values are the RMS of 52 weekly flux differences. Global prior errors are 2.84 and 0.33 (10^{-8} kgCO$_2$ m^{-2} s^{-1}) for land and ocean, respectively.

**Atmospheric CO_2 Observations from Space

In the Southern Ocean (taken as south of 47ºS), weekly net CO_2 fluxes at the scale of the 4.5ºx6º grid boxes were retrieved with a precision of ~0.05 gC m^{-2} d^{-1} using ASCENDS data at the 0.5 ppm measurement uncertainty. This is accurate enough to track strong local spatial and temporal variability. In terms of the precision of the flux integrated across the full extent of the Southern Ocean, the measurements can constrain fluxes with an uncertainty of ~300 TgC y^{-1}, a precision that is not very sensitive to the time-scale of the solution (weekly to seasonal). The magnitude of the flux perturbation for this case in Section 3.2 is +/- 180 TgC y^{-1} (Hammerling et al., 2015), which is near the detection limit if taken to be at signal to noise of 1, again consistent with the previous assessments.

> **Substantial flux uncertainty reductions are obtained for all tested cases of ASCENDS measurement error and vertical weighting function. Simulations with the 2.05 μm weighting function are slightly better than for 1.57 μm at the same nominal error levels.**

Along with the ASCENDS OSSE results, Table 3-2 also includes aggregate flux uncertainty reductions from the 4DVAR-PCTM model for a case using CO_2 from the current NOAA in situ network (flasks, observatories, tall towers, and routine light aircraft profiles) plus the TCCON network, as well as that using the GOSAT satellite in 3-point cross-scan mode. The global flux estimation OSSEs are well-suited to address these comparisons because they can be constructed to

estimate the flux uncertainty reduction provided by any hypothetical set of measurements. For weekly fluxes at the scale of ~$(500km)^2$, the existing ground network provides only a weak constraint, except over certain well-instrumented areas like Temperate North America. The GOSAT satellite improves upon this, but due to its relatively large field of view (FOV), ~100 km^2, and consequent sensitivity to clouds, the additional constraint is not great. We have assumed measurement uncertainties of 1.7, 1.5, and 1.0 ppm (1σ) for GOSAT high-gain land, medium-gain land, and ocean glint data, respectively, which is in good agreement with currently-estimated capabilities for ACOS b7.3, Level 2 (Kulawik et al., 2016). GOSAT data add the most value in areas that are poorly constrained by the ground-based measurements. Aggregating results into TRANSCOM (Atmospheric Tracer Transport Model Intercomparison Project) regions (not shown) produces rank-order results consistent with those given in Table 3-2 for global land and ocean. ASCENDS data for any of the tested instrument configurations provide a major improvement in flux uncertainty reduction compared to the current GOSAT observations.

Flux estimates have also been made with the 4DVAR-PCTM using random errors from OCO-2 in the 0.5-1.0 ppm range, obtained by multiplying the uncertainties of Bösch et al. (2011) by a factor of two to account for errors not captured by their analysis. This error range agrees well with an assessment of actual v8 OCO-2 random measurement errors using the method of Kulawik et al. (2016), which obtained 1.0 ppm (1s) for land data and 0.6 ppm for ocean glint data (Kulawik et al., 2018). According to these simulations, OCO-2 provides a much stronger constraint than either GOSAT or the ground-based measurements (Table 3-2). This is a result not only of OCO-2's lower measurement errors but also of its much greater measurement frequency: 24x60 possible measurements per minute, compared to ~15 for GOSAT.

Considering only random errors, ASCENDS measurements with a nominal precision equivalent to 0.5 ppm/10 s provide a somewhat weaker constraint on the fluxes globally at weekly time scales than expected from OCO-2 (Table 3-2). By these global metrics, the denser OCO-2 sampling more than compensates for the extra coverage provided by ASCENDS on the night side of the orbit and at high latitudes. ASCENDS would have to push nominal random errors as low as 0.25 ppm to equal or improve upon OCO-2 in these global random error OSSE results. Random errors of 0.25 ppm were previously considered to be outside of ASCENDS design capabilities; however, recent advances in laser and detector technology, along with retrieval methodology, now indicate that this level of random error is achievable.

Furthermore, Basu et al. (2018) find that spatiotemporal differences in sampling, such as between OCO-2 land and ocean soundings, coupled with imperfect transport, can produce differences in flux estimates that are larger than flux uncertainties due to transport model differences, which comprise a major source of flux uncertainty. This source of error would be much less with the near-uniform coverage of ASCENDS even at similar signal to noise. ***Also, there are other aspects of the ASCENDS measurements that may provide important additional information for flux retrievals, including use of partial column CO₂ data retrieved from above cloud tops (e.g., Mao et al., 2018) and deployment in dawn/dusk or precessing orbits to allow diurnal differentiation of photosynthesis and respiration fluxes from vegetation.*** The latter addresses a key issue for understanding the response of terrestrial vegetation net uptake to changing climate and environmental forcings; however, the measurement requirements for this problem need to be better determined in future studies.

> **ASCENDS data will provide a major improvement in flux uncertainty compared to current observations including in situ, TCCON, and GOSAT. Global flux error reductions from ASCENDS will be similar to those projected for OCO-2 if only random errors are considered; however, improvements in key regions are expected.**

3.4   Impact of Systematic Measurement Errors

Systematic errors can greatly degrade the flux constraints calculated above and, based on GOSAT experience, are suspected to have a larger impact on the flux estimates from satellite data than random errors at this point in time (Chevallier et al., 2014). Systematic errors in remote sensing CO_2 measurements can lead to serious flux errors, even at relatively small magnitudes, because the errors can be correlated with geophysical variations related to flux (e.g., land/ocean, solar zenith, surface reflectance, clouds, etc.). Passive sensors such as OCO-2 and GOSAT are expected to be more susceptible to bias errors than ASCENDS due to their changing observational geometry, difficulty in determining the atmospheric path length, and influence of atmospheric scattering. For these satellite CO_2 measurements, systematic measurement errors can be of a similar magnitude to random measurement errors (O'Dell et al., 2012, Kulawik et al., 2016). Both GOSAT and OCO-2 measurements currently suffer from significant and poorly-characterized systematic errors of from 0.7 to 0.9 ppm (RMS) overall, even after the standard bias correction is applied (Kulawik et al., 2016, 2018; O'Dell et al., 2018). ASCENDS is expected to provide measurements with significantly lower biases than the passive missions as a result of the laser measurement approach (Section 1.4).

The goal here is to use the CO_2 flux and transport models to help assess what levels of bias tolerance are required for the ASCENDS XCO_2 measurements to reliably inform flux inferences for key regions and processes in carbon cycle science. One approach to doing this is to examine the spatial distribution of CO_2 signal perturbations associated with specific flux perturbations of interest. Presumably, the XCO_2 measurement biases would need to be significantly smaller than or uncorrelated with the XCO_2 signals in order to detect a difference in flux. Several examples are discussed below. In addition, a set of potential instrument bias scenarios are derived, and the associated CO_2 perturbation fields are input to the 4DVAR-PCTM inverse model to calculate the resulting flux errors with respect to the unbiased inversion.

3.4.1   XCO₂ Gradient Analysis

Example XCO_2 signals from the flux sensitivity experiments in Section 3.2 above can be seen in Figure 3-2, Figure 3-5, and Figure 3-8 for the permafrost melting, fossil fuel shift, and Southern Ocean variability flux perturbation tests. The permafrost melting case shows an XCO_2 gradient of about 1 ppm from high northern to southern latitudes, while the key gradient for attribution is about 0.4 ppm around longitudes at high latitude in May-July (Hammerling et al., 2015). The nominal fossil fuel shift case produces gradients locally over Europe and China of about -/+ 0.3 ppm, respectively, diminishing downwind of the continents. These simulations suggest ASCENDS biases would have to be calibrated out to less than or on the order of 0.3 ppm regionally to detect such fluxes with signal to noise better than one. Gradients in the Southern Ocean test are smaller still, about 0.3 ppm annually from Antarctica to the tropics.

Similar to the enhanced sink test discussed in Section 3.2.4, a set of examples is shown in Figure 3-19 for the change in XCO_2 that would result from adding a 0.5 Pg C sink to different ecosystem regions. In this GEOS-5 simulation, regions are defined according to the TRANSCOM definitions and a sink is produced by enhancing regional GPP by a small percentage throughout the year. We choose 0.5 Pg C to represent a reasonable uncertainty in the global carbon budget (Le Quéré et al., 2017). In all regions, the sink manifests as a fairly small decrease in XCO_2. The introduction of a sink in boreal regions tends to show the greatest XCO_2 changes during summer months because the flux change is spread over a relatively smaller area and concentrated in the short growing season. In tropical regions, the monthly XCO_2 perturbation is smaller than in midlatitude and boreal regions because the seasonality of fluxes is weak and, consequently, the XCO_2 perturbation is distributed more uniformly through the year. Regardless of region, even a relatively large 0.5 Pg C carbon sink results in XCO_2 changes that are typically smaller than 1 ppm. Because boreal and mid-latitude flux changes tend to be transported zonally by the atmosphere, even small biases in the latitudinal gradient of an observing system could result in an error in fluxes estimated by inverse models.
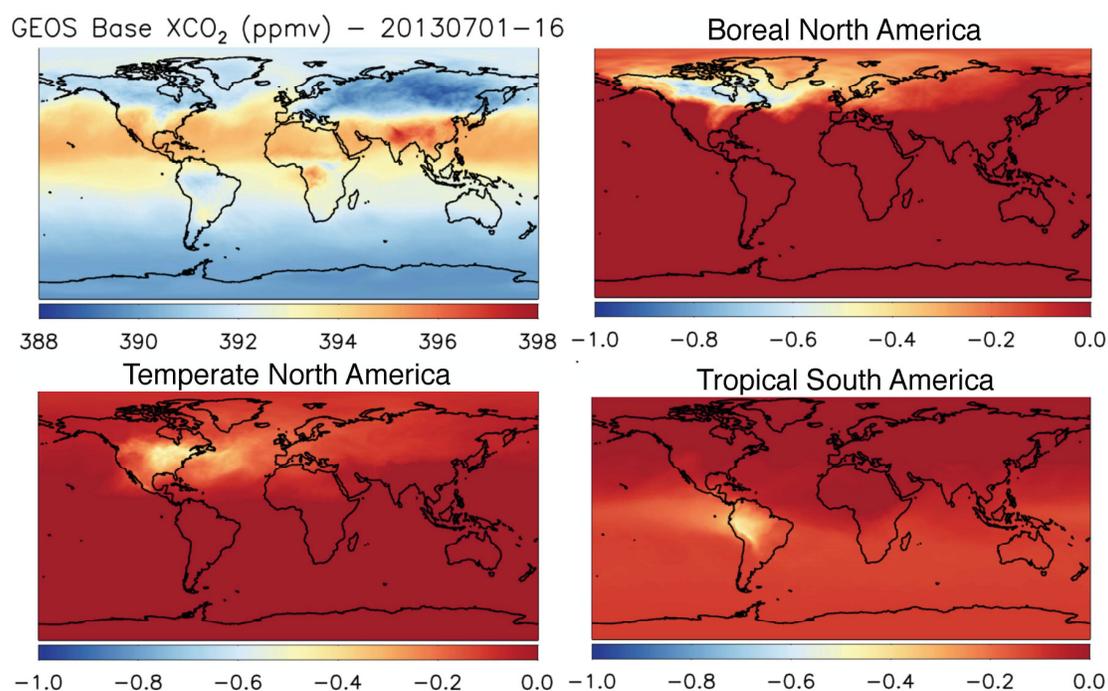
Figure 3-19 GEOS-5 simulation of XCO_2 (top left) and the impact of a 0.5 Pg C sink applied to boreal North America (top right), temperate North America (bottom left), and tropical South America (bottom right) for a 16-day average (typical orbit repeat interval) in July.

> **Model simulations of CO₂ fluxes and transport suggest that measurement biases in XCO₂ need to be held to less than about 0.3 ppm on regional to contintental scales in order to resolve carbon flux changes of interest.**

3.4.2   Potential Measurement Biases and Their Impact on Flux Inversion

Flux OSSEs based on plausible systematic measurement error patterns are used here to demonstrate the impact of systematic errors on flux inference. The impact of systematic errors on flux estimation is assessed in the same OSSE setup as used above, where systematic errors are added to the simulated measurements in parallel with the random errors. Although systematic errors are by their nature hard to foresee (if we knew them, we could calibrate them out), we have derived a set of potential bias cases for ASCENDS that can be scaled and used in flux OSSEs to help guide bias requirements for the instrument development based on their impact in flux estimation.

Table 3-3 ASCENDS Bias Cases

Case #	Bias Error Dependence	Rationale	Initial Error Scaling	Comments
1	Error varies with <u>Sun angle</u> on spacecraft	Instrument temperature changes can cause errors. Sun illumination is a heat source and heating usually depends on angle of the sun relative to the instrument.	Error (x) = 1 ppm * COS (solar zenith angle) for SZA <95.	Instruments usually cool in shadow.
2	Error depends on received <u>signal strength</u>	Plausible to expect small degree of non-linear instrument response, or small offset	Error (x) = -1 ppm * ((1-r) / (1+50*r) + r^2) where r = 0.33 * signal strength (x) / nominal desert signal	Error scaling formula is for a small offset in readings.
3	Error varies with cloud backscatter (i.e., <u>cloud optical depth</u>)	Possible "leakage" of cloud scattered light into signal. Usually, cloud scatter has a shorter path length resulting in negative bias.	Error (x) = -1 ppm * (cloud OD(x)) for OD cutoff <1	Mixed cloud and ground scattering (i.e., cloud OD is not too high)

The ASCENDS measurement teams formulated three possible bias cases based on sources of systematic error that could conceivably be present in actual lidar CO₂ measurements on-orbit (Table 3-3). The maximum magnitudes of the biases were arbitrarily set at 1 ppm. The biases in Table 3-3 were then added to the simulated true CO₂ concentrations in separate OSSEs, in addition to the 0.5 ppm (1 sigma) nominal random errors added above. An example of the global change in XCO₂ produced by these biases is shown in Figure 3-20, along with the random error. The magnitude of the shift in the flux estimates caused by the measurement biases is then compared to the magnitude of the random flux errors computed previously.

Random Error

Signal Bias

SZA Bias

Optical Depth Bias
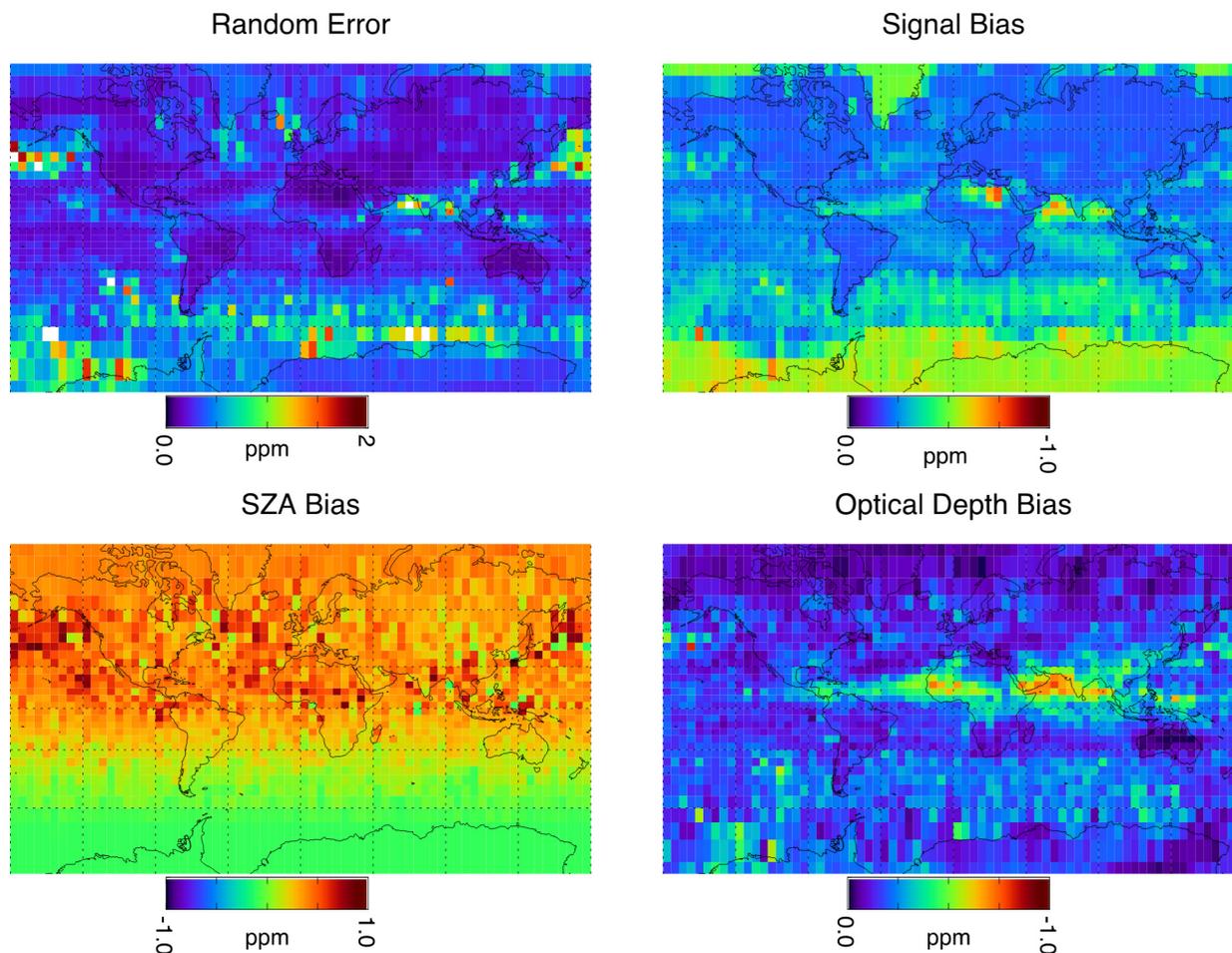
Figure 3-20 Global distribution of XCO₂ change in NH summer resulting from measurement bias scenarios described in **Table 3-3** together with RMS random error calculated as in Box 3-1. Errors are gridded averages at 5° latitude x 5° longitude based on ASCENDS sampling for July 1-16 and screened for maximum optical depth = 1.

The impact of these biases on the fluxes at seasonal time scales is significant (Figure 3-21). They cause a bias in the flux estimates that is generally 25-50% of the magnitude of the a posteriori random errors over land, with a smaller impact over the oceans. Bias case #2 (the signal strength-dependent bias) caused the largest impact at these longer time scales. A fourth case (not shown), which tested snow under northern trees biasing the apparent surface height, had a much smaller impact on the fluxes.
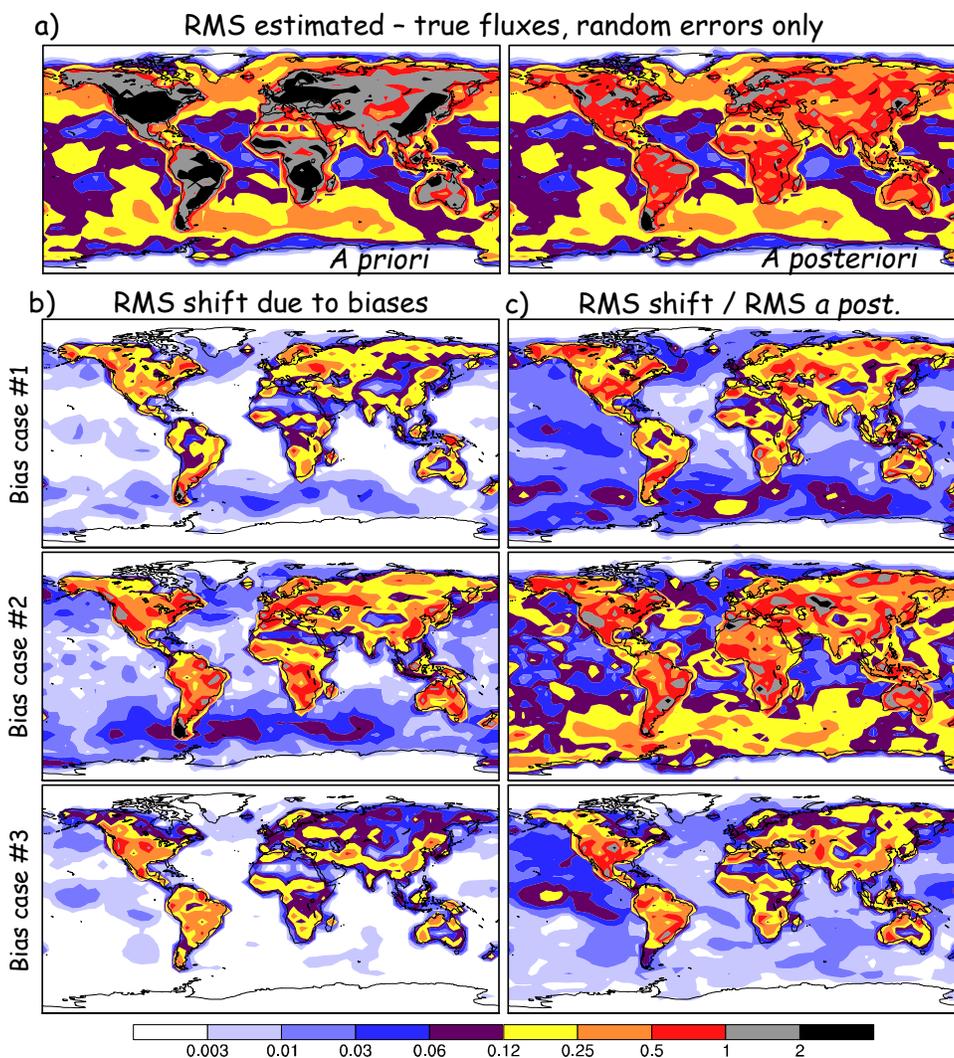
Figure 3-21 Seasonal RMS flux shift for bias cases compared to a priori and a posteriori random errors. a) the a priori and a posteriori RMS seasonal flux errors [10^{-8} kgCO$_2$ m^{-2} s^{-1}] caused by random errors only, b) The RMS of the shift or bias in the seasonal fluxes caused by the three ASCENDS bias cases at the ± 1 ppm level, c) The ratio of the RMS flux bias to the RMS a posteriori random errors is also given according to the same color scale (unitless). All results are for the 1.57 μm, 0.50 ppm random error case.

These experiments illustrate the importance of considering the impact of systematic errors when assessing the scientific return and science measurement requirements for a space mission like ASCENDS. Experience with airborne instrument simulators and current design guidelines indicate that ASCENDS will be able to achieve measurement bias levels much less than those tested here (Section 5). Systematic errors are significant for CO$_2$ measurements of current satellites (Kulawik et al., 2016; 2018; Wunch et al., 2017; Worden et al., 2017; Miller et al., 2018) and will likely play a significant role for future satellites such as OCO-3 and others. The potential reduction in bias for ASCENDS in comparison with other measurements is a major impetus for its deployment.

3.4.3   ASCENDS in the Context of Other CO₂ Observing Systems

In this section we attempt to compare the potential benefit for flux inference of ASCENDS with reduced bias errors relative to those estimated for current sensors based on GOSAT and OCO-2 data. Bias patterns for such passive measurements are estimated from biases currently being calculated for GOSAT and OCO-2 based on validation data. For ASCENDS, we added scaled multiples of the hypothetical bias distributions given by Table 3-3. The respective bias fields are added to the random errors and run through the 4DVAR-PCTM inversion model.

Figure 3-22 shows the annual mean of a seasonally-varying bias field used to simulate systematic measurement error for OCO-2. Although the true OCO-2 systematic errors are not known with such spatial detail, the fields in Figure 3-22 do resemble the difference between version 8 and version 7 of OCO-2 data in magnitude and spatial correlation (O'Dell et al., 2018). Presuming continued improvement in the data, the difference between versions stands as a measure of bias determined in the data at a point in time about 3 years after launch. Recent work suggests that overall systematic error levels for OCO-2 are similar to those for GOSAT after bias correction: ~0.8 ppm RMS across all the TCCON sites examined (Kulawik et al., 2016, 2018), while O'Dell et al. (2018) find residual errors of about 1.0 ppm versus TCCON overpasses. The biases shown in Figure 3-22, that were added onto our OCO-2 simulations, are at least a factor of two lower than this in an RMS sense across the full globe and year. Thus, these simulations may well under-estimate the impact on our OCO-2 flux results in Figure 3-23.
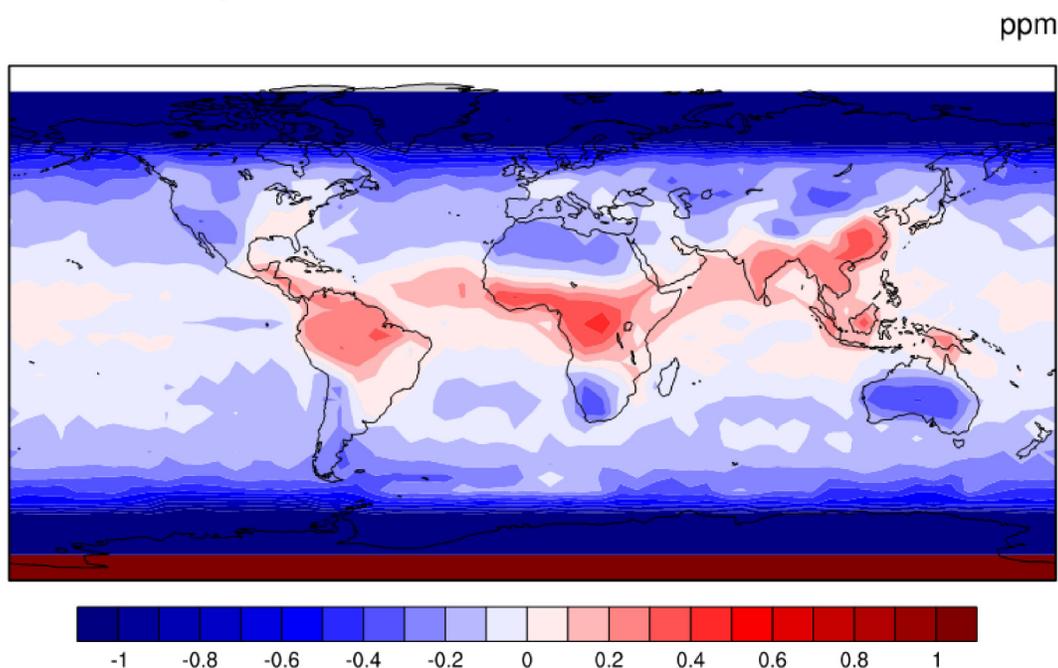
Figure 3-22 The annual mean of the measurement bias [ppm] derived from a seasonal comparison of raw ACOS B2.10 GOSAT XCO₂ values to modeled values, used to approximate OCO-2 bias distribution.
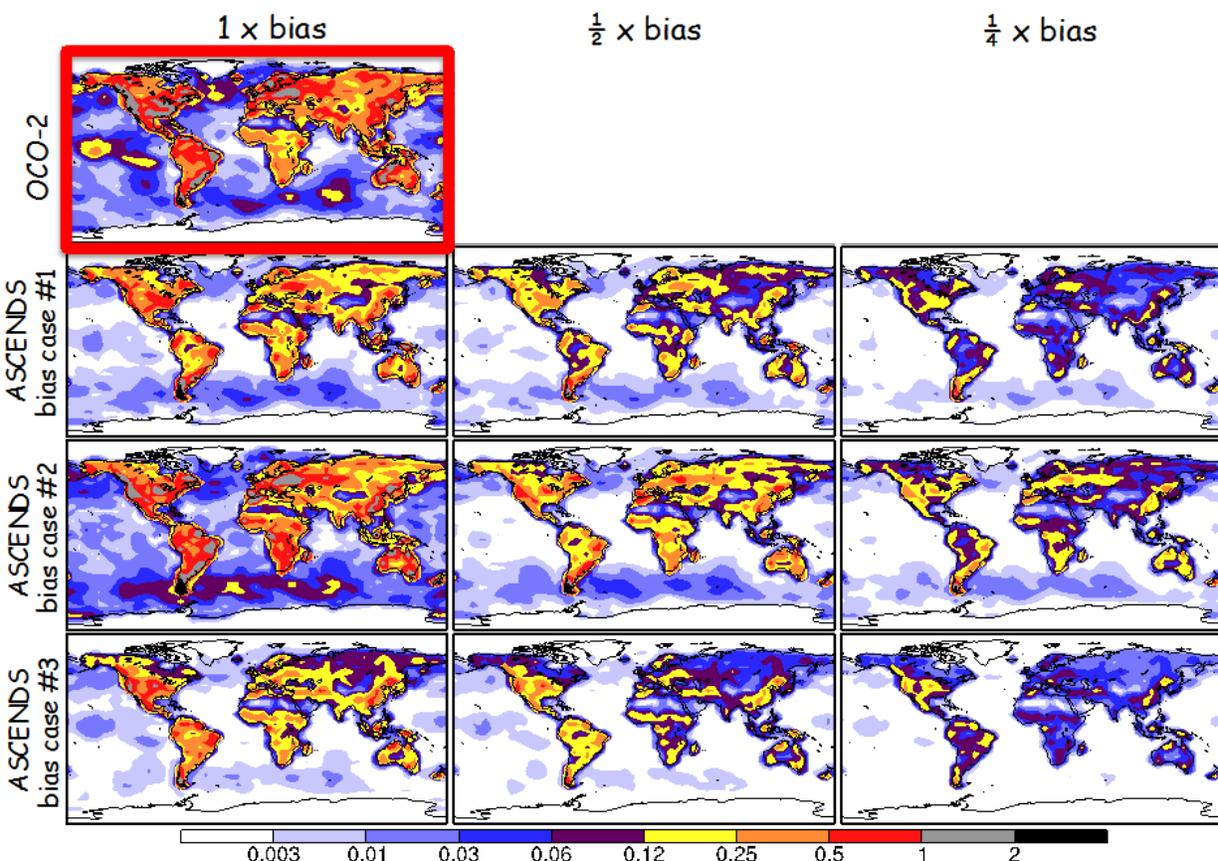
Figure 3-23 The shift in the weekly flux estimates caused by the addition of measurement biases of three different magnitudes (1x, 0.5x, & 0.25x) for OCO-2 and for the three different forms of ASCENDS bias given in **Table 3-3**. The RMS of 52 weekly flux shifts [10^{-8} kgCO₂ m^{-2} s^{-1}] is shown for each case. The case in the red box is thought to represent a realistic impact of OCO-2 biases although the magnitude may be somewhat low: ASCENDS can improve upon this by limiting biases to the ±0.5 ppm level. Note the highly nonlinear color scale.

The impact of the measurement biases can be seen by comparing the magnitude of the shift in fluxes globally in Figure 3-23. When the degraded OCO-2 estimates are compared to the ASCENDS results, it is seen that the flux errors for OCO-2 are about comparable to those for ASCENDS biases at the 1 ppm level. This is true both over land as well as most ocean regions, where OCO-2 has lower random errors in sun glint mode. When the biases are added into the glint-mode OCO-2 OSSE, most of the improvement in the fluxes over the oceans seen in the random error OSSEs (Table 3-2) disappears: the relatively low-magnitude ocean fluxes are the first to be thrown off by the systematic errors. The improvements over land are also degraded to a lesser relative extent. For many regions, ASCENDS does not even need to reduce its systematic errors below OCO-2's to achieve better results, e.g., Boreal NA. The benefit of not experiencing SZA-dependent biases at high latitudes is significant.

Relatively speaking, ASCENDS would need to keep its systematic errors to about half of those shown in Table 3-3 (i.e. to the ±0.5 ppm level or better) to achieve a flux estimate with significantly lower errors than that projected for OCO-2 (highlighted in Figure 3-23 with the red box). This is

even more the case if we believe that the biases added to our OCO-2 run were actually 2x too low. Such accuracy is thought to be a realistic design goal for ASCENDS (Section 5). Since biases in the CO_2 retrievals of passive missions such as GOSAT and OCO-2 are currently widely held to be the limiting factor in the usability of their data, not the random errors, reducing these biases is of primary interest for future CO_2 missions such as ASCENDS.

Given the existing and internationally-planned space-based CO_2 missions (Section 2.2), and the possible deployment time frame for ASCENDS, a compelling set of OSSEs is needed to test the impact on flux retrieval of ASCENDS measurements among a constellation of passive CO_2 sensors. In other words, how can the unique attributes of ASCENDS, i.e., all-season, high-latitude, day-night, low bias measurements perhaps with multiple vertical levels, best be exploited to optimize the overall science return of the global observing system (Sellers et al., 2018)? This framework is being pursued further in the aforementioned NASA Carbon Cycle OSSE Initiative, where requirements for ASCENDS will be reexamined in this light. For example, can the ASCENDS measurements, which are essentially insensitive to light cloud and aerosol loading, be used like a flying TCCON to better reduce bias in the passive measurements, or can the vertical information in ASCENDS retrievals, e.g., over cloud, serve to better constrain model transport uncertainty? These studies remain to be completed at this time.

> **The smaller systematic errors expected for ASCENDS XCO₂ measurements compared to prior CO₂ missions implies that ASCENDS will contribute to substantially reduced errors in inferred fluxes within the future constellation of space-based CO₂ missions.**

3.5   Summary

A series of modeling tests is used to explore the impact of prospective ASCENDS observations in inferring surface sources and sinks of CO_2. A fairly realistic representation of expected random and systematic measurement errors for ASCENDS has been constructed to test the impact of instrument implementation alternatives on the models' ability to infer fluxes and, thus, to begin to establish measurement performance requirements for the mission. A variety of modeling approaches have been employed to bolster the findings from any individual model, given that flux retrieval performance typically depends on model-specific assumptions.

The results show: 1) ASCENDS will resolve statistically significant differences in total column CO_2 concentrations, resulting from foreseeable changes in surface flux, over the entire globe, including high latitude land and oceans throughout the year; 2) ASCENDS will advance our understanding of the carbon cycle through improved flux estimates with reduced uncertainty at global to regional scales; and 3) ASCENDS data, with lower systematic errors and improved spatial and temporal coverage, can constrain surface fluxes significantly better than current passive sensors such as GOSAT and OCO-2. In summary, the modeling tests consistently demonstrate that, under reasonable assumptions for instrument technical performance, ASCENDS will provide accurate, precise, and representative data to address key carbon cycle science problems and hypotheses. *ASCENDS can provide new science, better science, and continuity of global CO₂ observations from space.*

The mission formulation for ASCENDS is not yet complete, and several modeling exercises are desirable to further explore its potential. For example, simulations using alternate orbits, e.g., dawn/dusk or precessing, can be tested with the latest performance estimates to see if additional information on vegetation respiration and photosynthesis fluxes can be extracted. Tests of the impact on flux estimates of using ASCENDS data retrieved above clouds or of vertical multi-layer CO$_2$ retrievals may also be useful. Finally, as the performance of existing passive CO$_2$ instruments is now becoming clearer, and a varied international fleet of passive space measurements is planned for the future (Section 2), we need to explore the potential role of ASCENDS in a future constellation combining active and passive measurements to obtain robust estimates of the carbon budget at a wide range of spatiotemporal scales.

4. Impact of Uncertainties in Atmospheric State on ASCENDS Measurements

4.1 Introduction

Two aspects of this critical error term impact both mission requirements and general instrument design: 1) Uncertainties in ancillary knowledge of the atmospheric state and 2) The impact of these uncertainties on the derived XCO_2 measurement error. This section provides insight into associated impacts on the XCO_2 measurement accuracy and precision. Special attention is paid to the assessment of uncertainty in surface pressure estimates from meteorological reanalyses to address the need for a simultaneous O_2 lidar measurement, and if needed, what the O_2 lidar requirements would be. ASCENDS provides average column XCO_2 amounts derived from active differential absorption measurements of CO_2 optical depths, in conjunction with collocated estimates of the atmospheric state provided by meteorological analyses. Understanding the propagation of the errors from the uncertainties in the atmospheric state into the derived XCO_2 measurement errors is necessary for a rigorous error budget, which also must include instrument-related CO_2 optical depth uncertainties, to ensure a high quality XCO_2 measurement (e.g., Zaccheo et al., 2014; Crowell et al., 2015).

Overall XCO_2 measurement errors are driven by both the instrument design and the ancillary meteorological data employed in the retrieval process, and the interplay between the two. The observed CO_2 differential optical depth, $\Delta\tau$, associated with a given CO_2 spectral feature, is given by

$$\Delta\tau = \int_0^{P_{sfc}} \Delta\sigma(\lambda_{on}, \lambda_{off}, T, p) \cdot \eta(T, WV, p)\, dp \qquad (4\text{-}1)$$

where $\Delta\sigma$ is the CO_2 differential absorption cross section, η is the dry air CO_2 number density, p_{sfc} is the surface pressure, and $\lambda_{on}/\lambda_{off}$ represent the on/off-line wavelengths. XCO_2 is given by

$$XCO_2 = \frac{\Delta\tau}{\int_0^{P_{sfc}} \Delta\sigma(\lambda_{on}, \lambda_{off}, T, p)\, dp} \qquad (4\text{-}2)$$

Both $\Delta\sigma$ and η vary as a function of pressure (P) and temperature (T). In addition, absorption due to other trace gas features (including water vapor), which are not considered in this simplified formulation, may also impact the observed $\Delta\tau$. As illustrated by these equations, the accuracy of retrieved XCO_2 values depends not only on the error characteristics of the observed $\Delta\tau$, but also the ability to accurately characterize the P, T, and water vapor (WV) concentration along the observed path. In the case of global space-based monitoring systems, retrievals typically rely on values derived from meteorological analyses that combine atmospheric general circulation models (GCMs) with assimilation of both conventional and satellite observations to estimate the atmospheric state globally.

The work below provides an assessment of the uncertainties in atmospheric state variables (vertical temperature and moisture, plus surface pressure), and their impact on a generic instrument implementation for a selected set of spectral lines/features. The impact of these state variable uncertainties, which are dependent on instrument-specific wavelength, must be combined with other instrument oriented CO_2 optical depth uncertainties to arrive at an estimate for the derived

XCO₂ values.   It is only through a comprehensive end-to-end error budget that a candidate instrument can be assessed to meet the XCO₂ measurement requirements for the ASCENDS mission. In addition, these analyses can be used to guide the mission requirements for potential ancillary space-based measurements, e.g. the necessity for a simultaneous O₂ based surface pressure measurement, and provide a common pre-launch ancillary data that may aid in the source selection process. Section 4.2 provides a summary of the uncertainty analysis for the atmospheric state, and Section 4.3 summarizes a baseline analysis of potential impact due to these uncertainties on retrieved XCO₂ column amounts.

4.2   Uncertainties in Observed Atmospheric State

These investigations focused on gathering current state-of-the-art model analysis and forecast fields as a proxy for future ancillary mission data to develop a comprehensive set of statistically-based estimates that bound the expected uncertainties in surface pressure and vertical temperature and moisture profiles. A variety of methods are employed to develop these bounds, including:

1.   Comparison of in situ observations and meteorological short-term forecast data to assess model errors.

2.   Comparison of reanalysis products with independent (not assimilated) datasets, where available.

3.   Inter-comparison of multiple reanalysis products to inform error estimates in poorly observed regions.

Comparing analysis fields to prior short-term forecasts for the same period constrains the error introduced into an operational retrieval relying on forecast fields and the temporal interpolation error that may occur when meteorological information from a different time is assumed during the retrieval process. Differences that arise in comparisons of fields from different modeling systems are due in part to errors in the Numerical Weather Prediction (NWP) model physics, spatial scales, and other implementation differences; such analysis is also valuable in estimating model error in data poor regions. Comparisons of NWP fields to observations is challenging because the majority of high quality, operationally available in situ data are assimilated to produce meteorological analyses. Truly independent observations are limited in number and distribution, and indeed often are near operational sites. Standard in situ observations also have limited precision due to instrument limitations or through data collection procedures (Sun et al., 2010) (NOAA, Office of the Federal Coordinator for Meteorology (OFCM), Washington, D.C., 2017; NOAA, Washington, D.C., 2003; Developmental Testbed Center (DTC), n.d.) (Salstein et al., 2008). Despite these limitations, the collective statistics provide an objective assessment of expected uncertainties in atmospheric state knowledge, and a consistent set of benchmarks that can be used to assess potential mission design solutions.

4.2.1   Uncertainties in Surface Pressure

ASCENDS requires both a precise knowledge of the surface pressure on a fine scale grid and a comprehensive understanding of the associated errors. While state-of-the-art mesoscale NWP models currently have horizontal grid spacings of at least several kilometers, with global-scale models an order of magnitude larger, surface pressure must be characterized on a spatial scale comparable to the measurement of interest. Space-based estimates of surface pressure would normally require a separate sensor, thereby increasing the overall size, weight, power and complexity of the satellite payload. The use of meteorological analyses presents an alternative

approach for estimating surface pressure, but implementation depends on the quality of the analyses and the ability to adjust relatively coarse resolution grid-based information to precise measurement locations. ***A comprehensive understanding of the errors associated with each of these approaches is a critical part of the design characterization of a remote-sensing system whose measurement accuracy depends on knowledge of surface pressure.*** Errors in surface pressure derived from meteorological analyses are addressed here.

4.2.1.1   Comparison of Surface Pressure Model Values and Observations

In this study we compared global in situ measurements with estimates of surface pressure derived from the Global Forecast System (GFS) and the North American Mesoscale Model (NAM) NWP analyses and short-term forecast data. Surface observations were obtained from National Climatic Data Center (NCDC's) Integrated Surface Database (ISD) (NCDC, n.d.). In order to compare measured surface pressure to model fields, a correction must be applied to the surface pressure of the model to account for the altitude difference between the model surface height and the actual terrain height of the station. In this work, the standard lapse rate equation

$$P_{adj} = P_s \cdot exp\left(\frac{-g \cdot dz}{R\left(T_m + L_r \cdot \frac{dZ}{2}\right)}\right)$$
(4-3)

where P_s is the model surface pressure, dZ is the difference between the model terrain height of the two resolutions, R is the dry gas constant*,* T_m is the model two-meter air temperature, and L_r is the lapse rate of 0.0065 K/m, was employed to account for these height differences. This adjustment was also applied, where required, to convert surface observations of sea-level pressure to station pressure. ISD surface pressure observations were converted from sea-level pressure to station pressure and co-located with model estimates that had been corrected for model height error. The results shown in this work are based on data retained every fifth day from the thirteen-month period between January 2012 and August 2013 (inclusive). Observations in the matched pair database are comprised of observations valid at 0000 and 1200 Coordinated Universal Time (UTC). Model data are either analyses valid at 0000 and 1200 UTC or 6-h forecasts from the prior 1800 and 0600 UTC model cycles. The choice of a 6-hour forecast was selected to match the time interval between typical synoptic model runs. In a real-time environment, surface pressure estimates would be computed from both spatially and temporally interpolated NWP data to match the satellite measurement. This approach requires not only the most recent NWP analysis, but also a forecast or set of forecasts that span the observation times. In non-real-time environments, where data are not required to be processed as they are received, one could consider temporally interpolating between analyses or data from alternative applications that provide non-forecast fields on a more frequent basis.

Figure 4-1 illustrates the overall small bias and Root Mean Square Error (RMSE) values at most observing sites. Errors are typically larger in regions with complex topography or at high elevations as evident over the Alps. Model values in these regions are heavily influenced by the veracity of the underlying model initial conditions whose effects are most strongly felt at such short forecast lengths. It is also in these regions that the failures in the corrections using the standard atmospheric lapse rate are most apparent. Figure 4-2 illustrates that even at a 90% confidence level, the majority of stations sampled have 1σ values below 2 mbar. The cumulative distribution functions (CDFs) in this figure illustrate the distribution of RMSE values for selected sets of surface station observations. The minimum annual RMSE for all station approaches 0.25 mbar and the maximum

exceeds 3 mbar for a handful of outlier stations as illustrated in Figure 4-1. Errors for the 6-h forecasts are slightly larger (not shown). Table 4-1 shows biases binned by latitude band for the GFS global analysis typically are small and negative, while RMSE values for (approximately) 1, 2 and 3 standard deviations for a normally-distributed sample are to first order 1, 2 and 3 mbar.
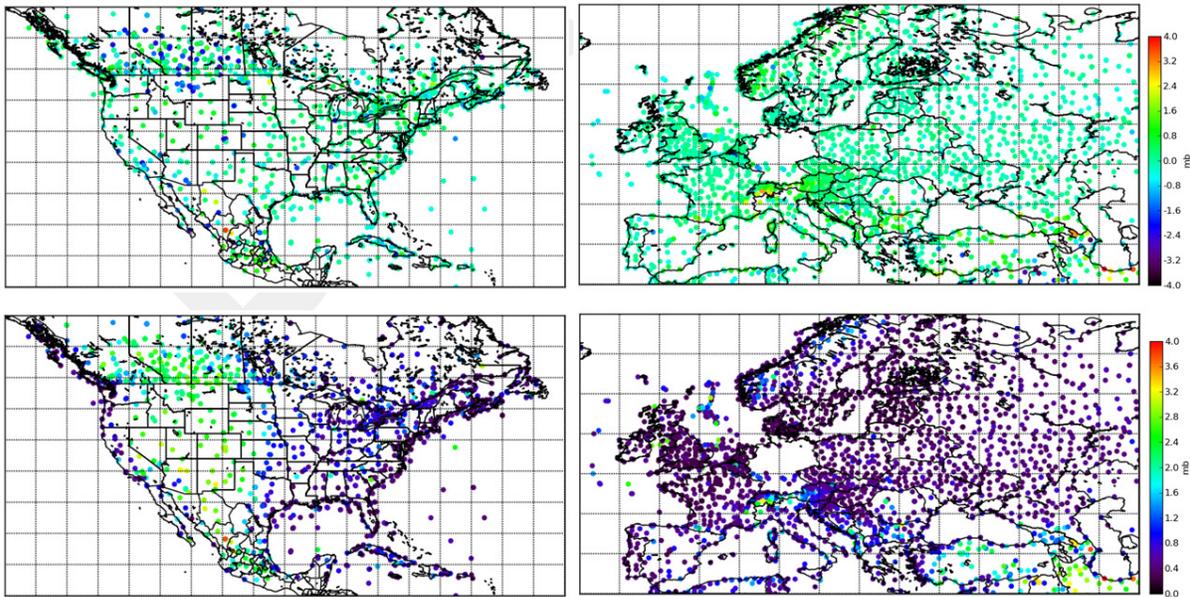
Figure 4-1 Estimated surface pressure biases and RMS errors for the US and Europe. Estimated surface pressure biases (top row) and root-mean-square errors (bottom row) for the US (left column) and Europe (right column). Units are in mbar. Model data are the NAM regional model and GFS global model for the US and Europe, respectively.
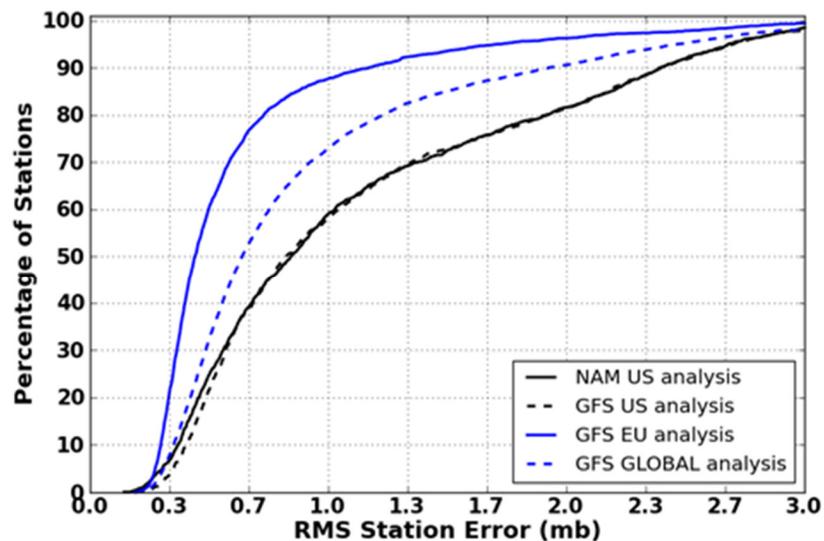
Figure 4-2 RMS differences in surface pressure observations vs fraction of stations with annual RMSE less than defined error. Cumulative distribution functions for the number of stations whose RMSE surface pressure errors, the RMS difference between NAM/GFS analysis values and surface observations for the United States (US), Europe (EU), and global regions. The percent of observation denotes the fraction of stations who yearly average RMSE is less than or equal to the defined error in mbar.

Table 4-1 Regional Differences Mean Bias and RMSE, and Inter-model Range RMSE Thresholds (in mbar) for GFS Analysis

Region	Mean Bias	Mean RMSE	65%	90%	95%	99%
NH High Latitudes >60°N	-0.14	0.74	0.67	1.19	1.67	2.57
NH Mid Latitudes 15°-60°N	-0.01	0.88	0.70	2.02	2.47	3.24
Tropics 15°N-15°S	-0.13	1.02	0.91	1.86	2.52	3.78
SH Mid Latitudes 15°-60°S	0.02	0.86	0.80	1.35	1.84	2.83
SH High Latitudes >60°S	-0.41	1.25	1.27	1.93	2.12	2.65
All Latitudes	-0.06	0.90	0.75	1.86	2.40	3.31

4.2.1.2   Inter-model Comparison of Surface Pressure Differences

While comparisons with available observations provide the best assessment of errors in meteorological analyses, large areas of the globe remain unobserved including high latitude regions of both hemispheres, southern hemisphere oceans, South America, Africa, and Siberia. In these regions, comparisons of different meteorological analyses provide the only possible estimate of uncertainty. To characterize uncertainty in these regions, we compared surface pressure fields from the Modern Era Retrospective-analysis for Research and Applications (MERRA-2) (Rienecker et al., 2011), the European Centre for Medium-Range Weather Forecasts' (ECMWF) ERA-Interim reanalysis (Dee et al., 2011), and NOAA's Climate Forecast System Reanalysis (CFSR) (Saha et al., 2010). The range of reanalysis surface pressure estimates was computed every 6 hours during January, April, July, and October 2009. All reanalysis fields were re-gridded to MERRA's nominal half-degree resolution. The lapse rate altitude correction discussed above is applied to reduce effects of underlying topography differences. While this correction reduces intermodal differences due to topography, it does not entirely remove them. Annual mean surface pressure differences are subtracted as a type of bias correction because we assume that persistent errors in surface pressure from analyses will be successfully diagnosed and adjusted for as part of the ASCENDS retrieval process. Monthly means and standard deviations of the instantaneous differences were computed. Standard deviations of the surface pressures are shown in Figure 4-3.

In most regions, intermodal differences are less than 1 hPa, consistent with the analysis based on surface pressure observations. Largest differences among analyses exist in data poor regions where Atmospheric General Circulation Model (AGCM) model physics dominate pressure estimates rather than data constraints, which are fairly consistent among models. In particular, ***large errors***

are evident in the Southern Ocean translating to 0.5-0.8 ppm in XCO₂. Not only is this area virtually unobserved by conventional observations (radiosonde, aircraft, and automated land and ocean stations), but assimilation of satellite observations of other meteorological state variables, which provide some constraint on surface pressure, is obstructed by persistent cloudiness.
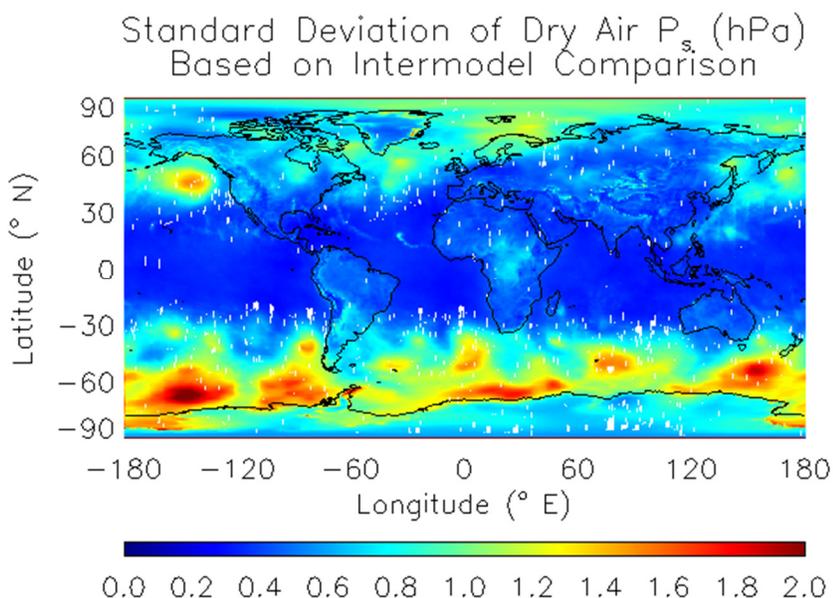
Figure 4-3 Model comparison between reanalysis surface pressure estimates for dry air. Comparison providesinsight into model error in data poor regions. Instantaneous ranges were computed between three reanalysis datasets for 2009 to determine the standard deviation.

4.2.1.3   Spatial Interpolation Errors in Surface Pressure

In addition to errors in the surface pressure provided by meteorological re-analyses, further error can be introduced when surface pressure is adjusted to the measurement location as part of an XCO₂ calculation. To estimate the magnitude of such errors, we use a combination of MERRA surface pressure estimates and the United States Geological Survey (USGS) GTOPO30 (30-arc second resolution Digital Elevation Model) map that provides estimates of surface elevation at 1km resolution. We use the lapse rate based correction discussed above to adjust from MERRA's ~50 km grid-based surface pressure estimates to calculate the 'true' surface pressure at all GTOPO30 elevations. To estimate potential errors, we perform the same calculation assuming a 1 K (Kelvin) temperature error and then calculate the difference in surface pressure from the 'truth'. Figure 4-4 shows the standard deviation of surface pressure errors within each 50 km grid cell. Over most of the world, the topographic correction assuming a realistic error in temperature introduces a small error less than 0.1 mbar. Over regions with large topography gradients, errors are still ~0.2 mbar. Even in areas with significant topographic variation, adjustment errors are much smaller by an order of magnitude than the errors shown in Sections 4.2.1.1 and 4.2.1.2. This analysis assumes that ASCENDS will have perfect information about the elevation associated with a particular measurement based on the altimeter. Errors in altimetry, pointing location, or low level temperature

errors greater than 1 K could all lead to errors larger than those shown in Figure 4-4, but are still likely to be smaller inherent uncertainty in surface pressure reanalysis.
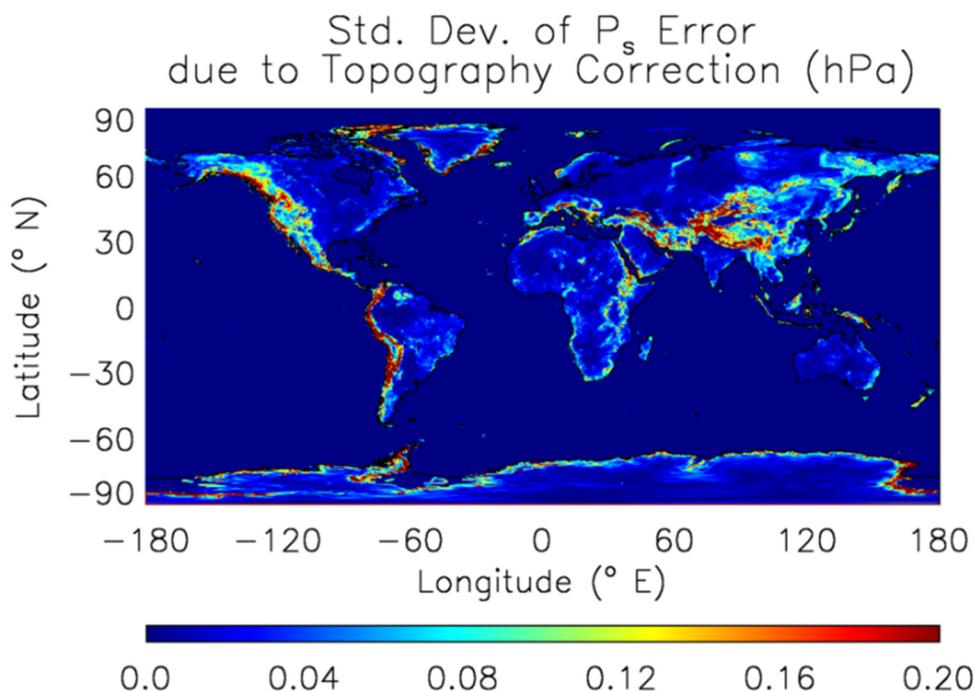
Figure 4-4 Effects of grid scale on surface pressure errors. Errors induced when relatively coarse resolution reanalysis surface pressure fields are adjusted to represent subgrid-scale topographic variations.

The data described in this section and Section 4.2.1 provide confidence that the values derived in Section 4.1 and presented in Table 4-1 are within reason. The long-term goal is to employ these spatially resolved global distributions of surface pressure errors due to both model limitation and/or terrain height differences as a mechanism for constructing globally representative spatially varying maps of expected errors in retrieved XCO₂ that can enhance the inverse model results described in Section 3.

4.2.2   Uncertainties in Temperature and Water Vapor Profiles

The error characteristics of above ground-level model profiles of temperature and moisture were examined by comparing against radiosondes (Figure 4-5). The largest temperature errors appear in the lowest 50 mbar of the troposphere and again at high altitudes near the tropopause and in the stratosphere. Moisture errors are largest near the surface in the boundary layer where water vapor content is most abundant.
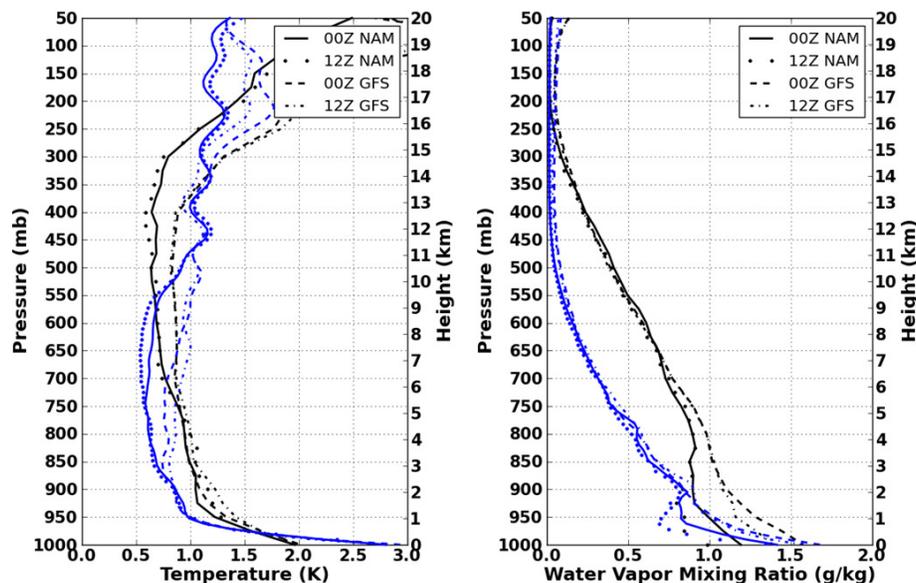
Figure 4-5 Ensemble RMS differences for radiosonde soundings in upper air observations for 5000 randomly selected soundings and corresponding 0000 and 1200 UTC NAM and GFS NWP analyses for temperature (left) and water vapor mixing ratio (right). The black traces are plotted as a function of pressure and blue traces are plotted as a function of height above surface.

4.3   Impact of Uncertainty in Knowledge of Atmospheric State on Retrieved XCO₂

The atmospheric state vector analysis described above was combined with a notional vertical CO_2 profile with a constant concentration of 385 ppm, and input into the Line-By-Line Radiative Transfer Model (LBLRTM) (Clough et al., 2005) to construct sets of simulated optical depths (ODs) over a predefined range of wave numbers. LBLRTM optical depths are computed from Voigt line shape functions at atmospheric levels and with a continuum model that includes self- and foreign-broadened water vapor as well as continua for carbon dioxide, oxygen, nitrogen, ozone and extinction due to Rayleigh scattering. The version used in the study included 2012 updates to the CO_2 line parameters and coupling coefficients based on the work of Devi et al. (2007a,b), the O_2 line parameters based on High Resolution Transmission (HITRAN; Rothman et al., 2009) and additional quadrupole parameters between 7571 - 8171 cm^{-1}.

For each of 5000 profile pairs discussed in Section 4.2.2 a set of simulated truth, signal and model ODs were computed. The Radiosonde Observation (RAOB) data were used to simulate the "true" optical depths observed by the sensor and the model profiles were used construct the "model" optical depths that would be used in the retrieval approach given an estimate of the atmospheric state. In addition, a set of "signal" τs was constructed based on the "truth" profiles and either an augmented CO_2 profile or a change in surface pressure. In the CO_2 case, the nominal CO_2 profile was augmented by adding a pre-defined concentration to each layer between the surface and simulated observation height. In the O_2 case, the surface pressure was adjusted by modifying the surface height to match the desired surface pressure. In this case, the signal pressure values were assumed to be less than the observed or model values to prevent the use of sub-surface profile values. In the O_2 cases, the observed path length, i.e. the height between the observer and the surface, were held fixed to eliminate changes in optical depths due to path length.

These simulated optical depth values (truth, model, and signal) were then employed to generate spectrally dependent noise and average signal values given a defined set of differential wavelength pairs. This work assumes that retrieved CO_2 column or surface pressure values are derived from the difference in optical depths between the absorption at an "off-line" wavelength whose absorption is dominated by the continuum or constituents other than the feature of interest, and the absorption at an "on-line" wavelength whose absorption is primarily driven by the feature of interest. While this approach does not address all retrieval methods or observational techniques that employ multiple measurements along a given absorption feature, it does provide metric values that can in general be used to constrain the fit between the observed data and Radiative Transfer (RT) modeled values. This Monte Carlo based approach provides a mechanism for computing an ensemble-based estimate of the biases and variances associated with retrieved XCO_2 values for a variety of simple line combinations. The inclusion of a high-fidelity RT model enables these results to capture the errors due to both correlated and uncorrelated uncertainties in temperature, water vapor and pressure on the dry-air mixing ratio of CO_2, an input the RT model.

The noise at each spectral location in the given simulated waveband was computed as the RMS error associated with the differences between the simulated true (τ_{signal}) and noise (τ_{noise}) values. In general, these differences in optical depths, for a given off-line wavelength (λ_{off}), are described as

$$\Delta\tau(\lambda) = \left(\tau_b(\lambda_{off}) - \tau_b(\lambda)\right) - \left(\tau_x(\lambda_{off}) - \tau_x(\lambda)\right) \tag{4-4}$$

where $\tau_b(\lambda)$ is the observed or true optical depths derived from RAOB data, and $\tau_x(\lambda)$ are the optical depths associated with atmospheric state of interest. In the noise case, $\Delta\tau_{noise}(\lambda)$, is computed based on $\tau_x(\lambda)s$ derived from NWP model data, and estimated noise values as a function of wavelength are given as the RMS error

$$noise(\lambda) = \sqrt{\frac{1}{N}\sum_N (\Delta\tau_{noise}(\lambda))^2} \tag{4-5}$$

where N is the number of profiles in the match pair dataset. In the signal case, the $\tau_x(\lambda)s$ values were those derived from atmospheric state variables derived from the RAOB data plus an augmented CO_2 column or surface pressure value. The resulting signal term is then given as the absolute average over the ensemble set

$$signal(\lambda) = \frac{1}{N}\left|\sum_N \Delta\tau_{signal}(\lambda)\right| \tag{4-6}$$

In this study, the differential signal and noise spectra are computed for four CO_2 and two O_2 bands of interest. Each band is 300 pm wide and has center wavelengths at approximately 1.5711, 1.5723, 1.5805, and 2.0510 µm (6364.92203, 6359.96733, 6327.06095, and 4875.59 cm^{-1}) for the CO_2 bands. The O_2 bands are centered at approximately 0.76468 and 1.2625 µm (13077.29386 and 7920.5976 cm^{-1}). In addition, a single observational scenario is constructed to evaluate the performance of observations from a space-based mission based on a nadir viewing geometry. The space-based scenario is based on a 20 km fixed path length. While it is well understood that the space-based scenario covers only a fraction of path associated with any proposed viewing geometry, the length selected bounds the limits of the observed and NWP data, and represents the fraction of the atmosphere that has the most severe impact on these measurement techniques.
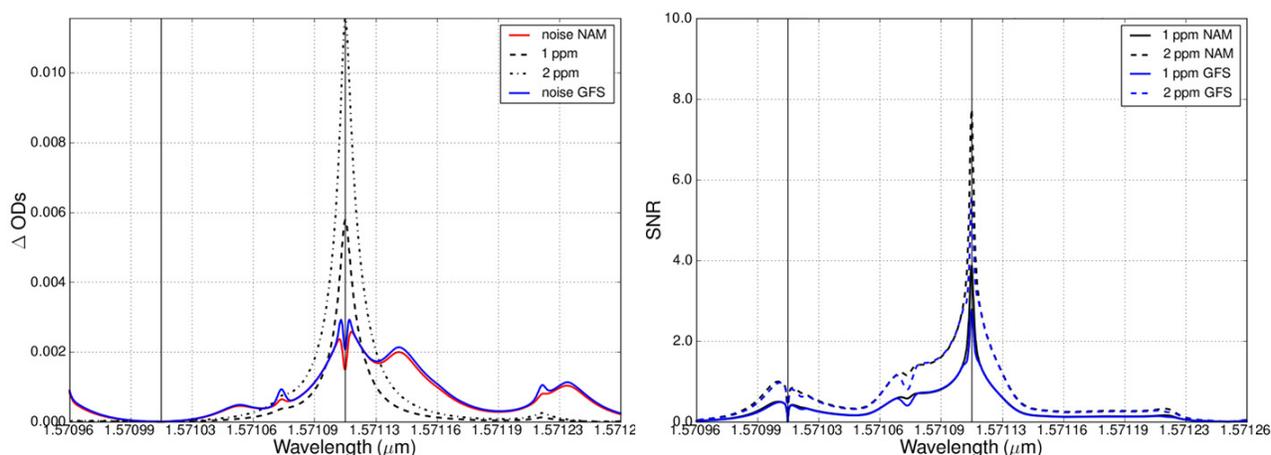
Figure 4-6 Representative signal/noise for 20 km nadir sensor to ground path length. Plots show values (left) and ratios (right).

An example set of computed signal and noise values and the associated signal to noise ratios (SNRs) as a function of wavelength for select off-line locations are provided in Figure 4-6 for a representative CO_2 case. These signal and noise terms form the basis for a number of analyses designed to assess and quantify the impact of uncertainties in atmospheric state knowledge on estimated CO_2 column amounts. The left plot illustrates signal and noise values for a representative CO_2 line for absorption feature centered at 1.5711 µm. The solid lines represent the simulated noise values as a function of wavelength derived from both the Contiguous United States (CONUS) NAM data (red) and the global GFS data (blue). In this CO_2 case, an additional 2.40 mbar uncertainty in surface pressure was also introduced. The dashed and dotted lines in the left hand plot represent the average signal given by a 1 and 2 ppm change in column amount. The on-line (1.5711 µm) and selected off-line (-100 pm) positions are illustrated in the graphs as solid vertical lines. The right plot shows representative SNRs constructed for a 1 and 2 ppm signal derived from CONUS NAM data (black) and global GFS data (blue). An example two-dimensional representation of associated noise equivalent signal for the CO_2 line at 1.5711 µm and 20 km nadir viewing geometry is shown in Figure 4-7. The noise equivalent signals are constructed by interpolating noise ΔOD to signal values for all on/off-line combinations ±150 pm from line center.
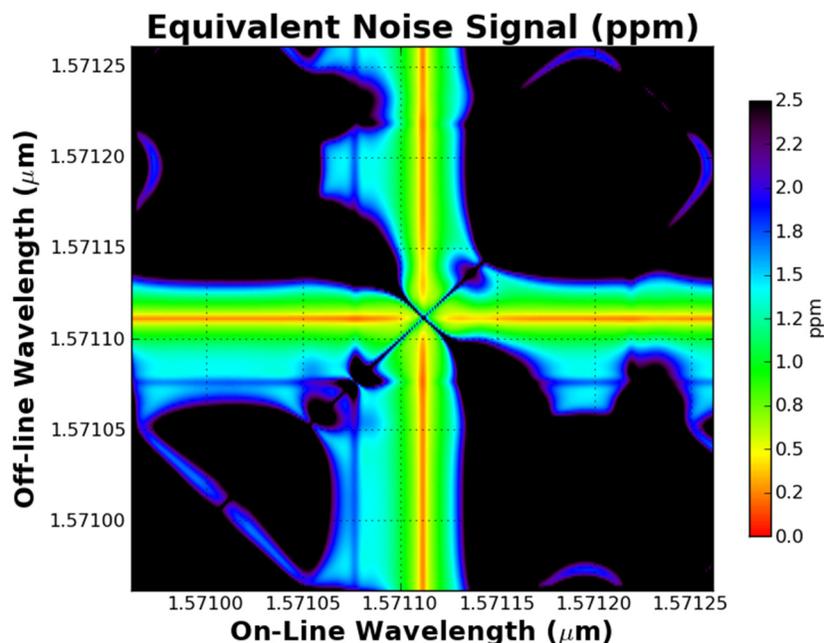
Figure 4-7 Two-dimensional representation of noise equivalent signal for CO_2 line at 1.5711 µm and 20 km nadir viewing geometry.

Figure 4-8 illustrates the minimum equivalent noise for on-line positions ±20 pm from line center for the same sample CO_2 line and geometry. Shown is the minimum equivalent noise associated with uncertainties in vertical temperature and water vapor (T/WV) only, and T/WV uncertainties combined with 0.75, 2.40, and 4.31 mbar uncertainties in surface pressure derived from both CONUS NAM data (black) and global GFS (blue). These surface pressure uncertainty values were chosen based on table 4-1 and the analyses described in Section 4.2.1.1, and provide three global surface pressure uncertainty regimes at the 65%, 95% and 99% confidence levels. Finally, Figure 4-9 shows minimum equivalent noise signals for CO_2 lines centered at 1.5711, 1.5723, 1.5805 and 2.0510 µm given uncertainties in vertical T/WV, a 2.40 mbar uncertainty in surface pressure, and a 20 km nadir viewing geometry derived from CONUS NAM NWP data (black) and the global GFS data (blue). The 2.0510 µm center line is chosen in the wing of the 2 µm absorption feature due to the high absorption of CO_2 in this band, which results in low SNR and smooth equivalent noise signal across the ±20 pm region plotted.

A set of simulated global XCO_2 measurements, based on published laser sounder instrument model and retrieval approach, was constructed as part of these efforts to illustrate the impact of uncertainties in the atmospheric state on global XCO_2 retrievals. Pseudo-data optical depths and measurement random errors were calculated globally based on an approach similar to Kawa et al. (2010), using the instrument model with 16 sample wavelengths, described in Abshire et al. (2018a), operating at 1.572 um (See Section 5.3.1). The simulated XCO_2 observations were obtained using the retrieval approach described in Ramanathan et al. (2018). In the baseline case, MERRA-2 (Gelaro et al., 2017) meteorology was used to generate the input 'measured' optical depths and as the retrieval prior, i.e., assuming perfect knowledge of the NWP fields. These data were then compared to those obtained from a perturbation retrieval performed by substituting temperature, humidity, and pressure profiles sampled from a different analysis (MERRA, ERA-

Interim) as the retrieval prior. Figure 4-10 shows the impact of the alternate NWP data on the difference between retrieved XCO_2 and the input 'true' XCO_2. The results show that introduction of wrong NWP data into the retrieval increases the global RMSE from 0.37 ppm (unbiased) for the perfect NWP data case to about 0.52 ppm. It also adds a small global bias and significant spatial correlation at approximately continental scales (Figure 4-10). The magnitude and distribution of these errors will vary with specific instrument, retrieval, and NWP model variations, but this test serves as a fairly realistic example of the XCO_2 error contribution and reiterates the need for the highest accuracy meteorological data to meet the critical XCO_2 measurement requirements.

Finally, it should also be noted that a long-term comprehensive model of the end-to-end system performance would include the interplay of the uncertainties outlined above with those associated with the ability to precisely describe the underlaying spectroscopy, and the ability to model the instrument observations using Voigt- and/or non-Voigt-based profiles. Ongoing work, in both the active as well as passive remote sensing of GHGs, continues to demonstrate the need to identify and correct for differences between observations and modeled results on a routine basis. These efforts have shown differences in retrieved XCO_2 based RT modeling approach that employ line parameter databases such as ABSCO v5.0 (Payne, 2017) or High Resolution Transmission (HITRAN) 2008, 2012 and 2016 (Rothman et al., 2009; Rothman et al., 2013; Gordon et al., 2017, respectively).

The profile database, simulated optical depths and resulting uncertainties outlined above are more formally presented in (Zaccheo, et al. 2014), and utilized in (Crowell, et al. 2015) to assess the impacts of atmospheric state uncertainty on simultaneous O_2 lidar measurement requirements for the ASCENDS mission.   A consensus assessment by the ASCENDS ad hoc SDT is that the ASCENDS mission can accept the atmospheric state uncertainties from the meteorological analysis without the need for the extreme technical and cost challenge of including both a CO_2 and O_2 measurement capability in the ASCENDS mission.   Information on two candidate O_2 lidar approaches that were initially considered are discussed in Appendix F.

The assertion that uncertainties from the meteorological analysis have only modest impact on overall system performance is also supported by a set of OSSEs, described in section 3.3.3, that combines the atmospheric state results describe above with a flux modeling framework to predict uncertainties in global estimated fluxes given know sources of error. Figure 4-11 illustrates the predicted a posteriori estimation errors (1σ) in average monthly CO_2 flux due to both uncertainties in atmospheric state and notional instrument noise. This works shows that the impact of uncertainties in surface pressure (panel A) are relatively small compared to the random measurement errors from a notional ASCENDS instrument operating at 2.05 μm (panel B) even in areas of complex terrain.
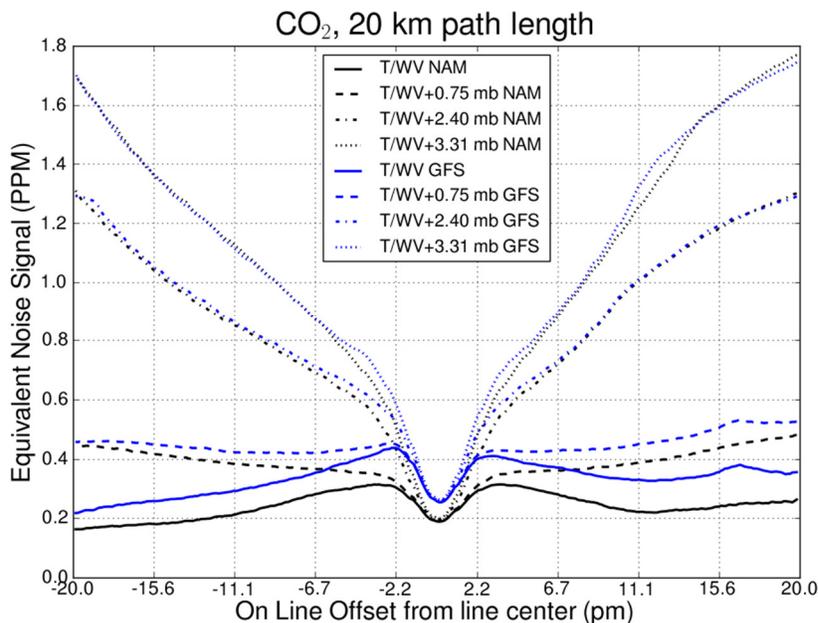
Figure 4-8 Equivalent noise signal errors for sample CO_2 line at 1.5711 µm. Minimum equivalent noise for on-line positions ±20 pm from line center for CO_2 line at 1.5711 µm and 20 km nadir viewing geometry.

> **To ensure the ASCENDS XCO₂ measurements meet the desired precision and accuracy, the total mission error budget must include uncertainties due to instrument design, the knowledge of the atmospheric state parameters and spectroscopic characteristics.**
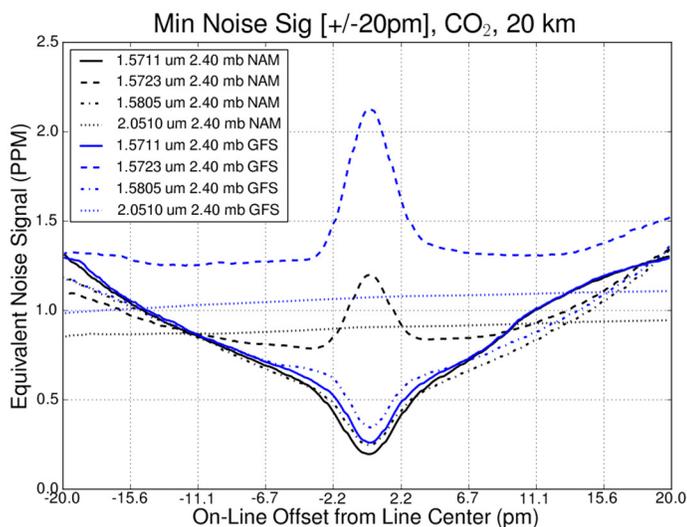
Figure 4-9 Sample set of minimum equivalent noise errors for CO_2 lines between 1.57 and 2.05 CO_2 lines centered at 1.5711, 1.5723, 1.5805 and 2.0510 µm and a 20 km nadir viewing geometry.
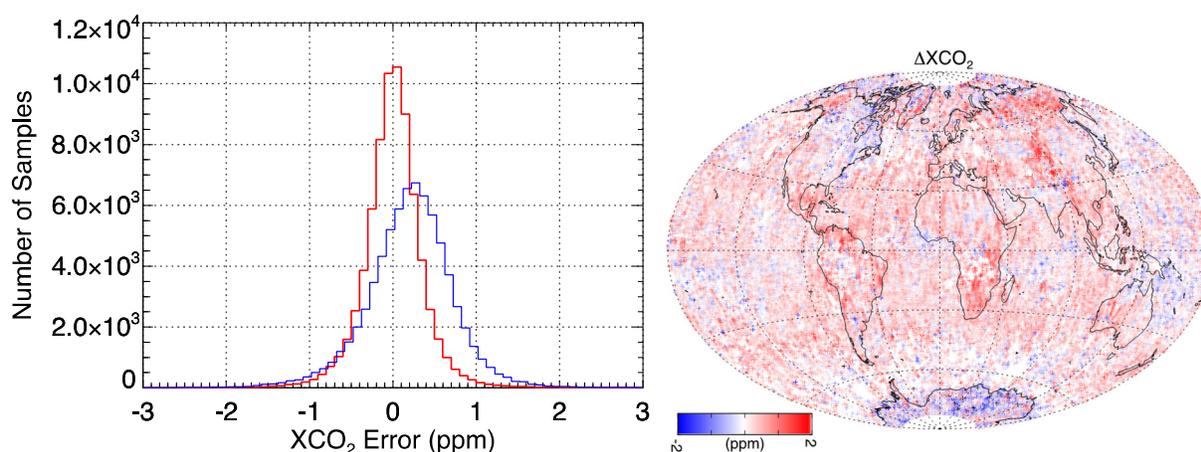
Figure 4-10 Results from simulated global XCO_2 data demonstrating the impact of imperfect knowledge of the atmospheric state in the retrieval. Left panel shows difference (error) between retrieved XCO_2 and the 'truth' input to the optical depth calculation for a 16-day orbit repeat cycle from 2015-01-15 to 30. The red curve is baseline error assuming accurate knowledge of state (MERRA-2) and blue is for retrieval using erroneous (ERA-Interim) NWP data. Right panel is spatial distribution of XCO_2 error for perturbed NWP data simulation. Pseudo data samples with total cloud plus aerosol optical depth greater than 1.0 have been screened out (see Kawa et al., 2010). Similar error results were observed for July-based simulations and the use of MERRA data as the perturbed retrieval prior.
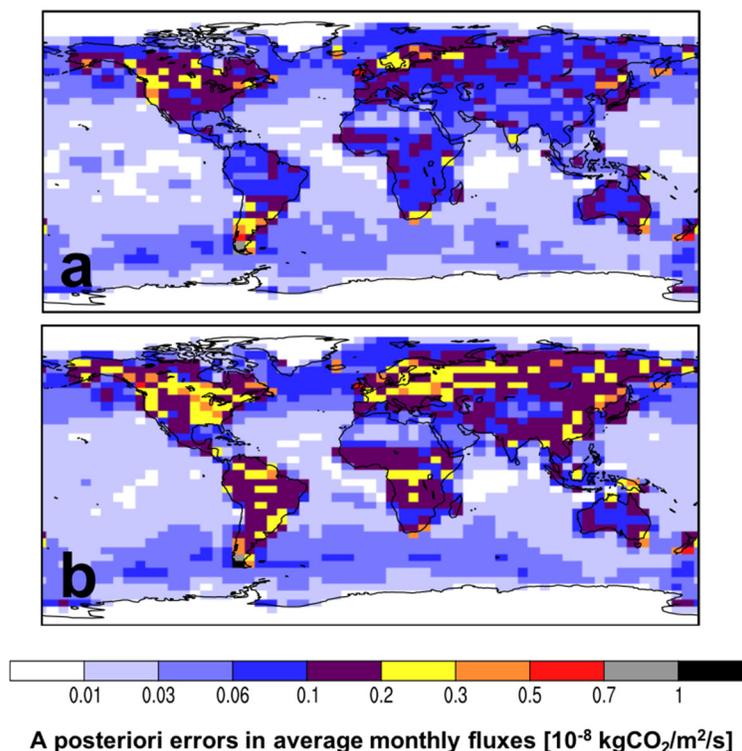
Figure 4-11 A posteriori estimation errors (1σ) in average monthly CO_2 flux from OSSEs (described in section 3.3.3) that predict the impact of observation errors from a) uncertainties in surface pressure (described in section 4.X), and b) random measurement errors from a notional ASCENDS instrument operating at 2.05 μm, assuming the 0.25 ppm nominal random error case. The pressure-based errors are relatively small compared to the already-low errors from the 0.25 ppm case, even in areas of complex terrain.

4.4   Summary

A baseline assessment of uncertainties in atmospheric state variables (vertical temperature, vertical moisture, and surface pressure), and their impact on a generic instrument implementation for a selected set of spectral lines/features is provided. This assessment offers a common parametric baseline that will evolve over time as the ASCENDS design matures, and will aid in instrument and mission definition, design and potential future source selection activities. It needs to be emphasized that this type of atmospheric state uncertainty analysis must be included as part of a total ASCENDS XCO$_2$ error budget assessment for any candidate instrument concept. In addition, these efforts have helped us to establish that the ASCENDS mission does not need to include a simultaneous O$_2$ lidar measurement of surface pressure, with its additional technical and cost challenges, to achieve high precision XCO$_2$ measurements globally. This topic may need to be revisited as requirements are refined on a regional basis, and weighted against future state of the art technological advances, e.g., updates to spectroscopic knowledge of O$_2$ and H$_2$O absorption, and the potential instrument noise characteristics of single-shot observations.

5. Technical Feasibility

5.1   Introduction – Lidar Measurements for the ASCENDS Mission

The lidar for the prospective ASCENDS mission uses the Integrated Path Differential Absorption (IPDA) approach to measure the column abundance of CO$_2$ and to derive the weighted column average dry air mixing ratio of CO$_2$ (XCO$_2$) in the lower atmosphere. Various IPDA lidar approaches may be used to sample a CO$_2$ line, measure range, measure CO$_2$ column optical depths, and then derive an estimate of XCO$_2$ using concurrent estimates of meteorological parameters with a spectroscopic analysis. The simplest approach to describe is shown in Figure 5-1 that uses a pulsed approach with the minimum of two wavelengths to sample the CO$_2$ absorption line. The IPDA lidar approach offers a number of unique and important capabilities for accurate column measurements of greenhouse gases. A summary is given in Table 5-1.
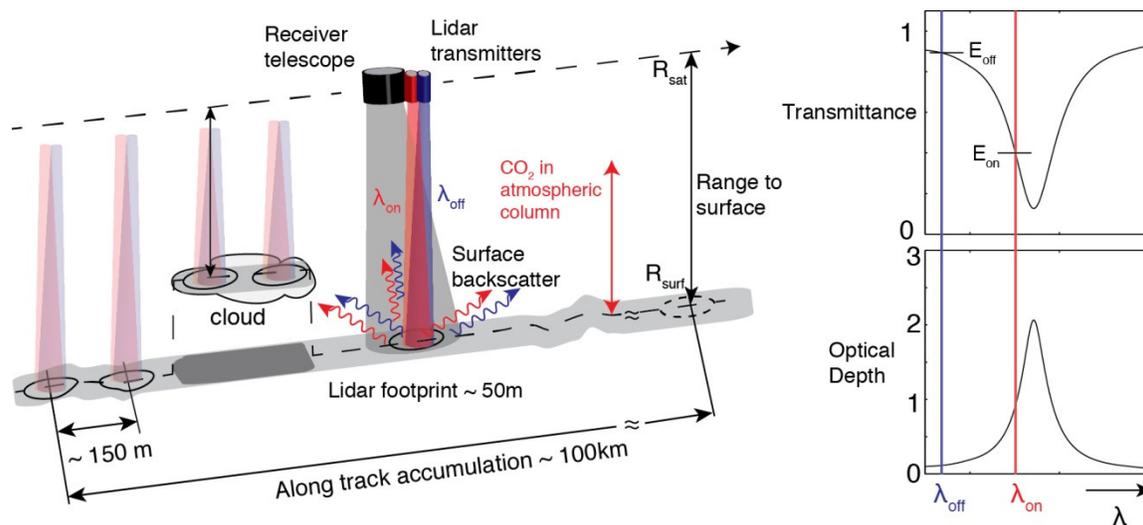
Figure 5-1 Illustration of one approach for an Integrated Path Differential Absorption (IPDA) measurement from space to scattering surfaces on or near the Earth's surface. This drawing is for the two-wavelength pulsed approach considered for the ESA A-SCOPE Mission. Several approaches for ASCENDS use more than two wavelengths to sample the lineshape to control biases and to gain some additional information on the vertical distribution of CO$_2$.

5.1.1   Overview of Measurement Approach

The pulsed two-wavelength lidar approach transmits two laser pulses of slightly different wavelengths in quick succession for every IPDA lidar measurement. Figure 5-1 shows two beams (red and blue) directed at nadir corresponding to the laser pulses tuned onto and off the CO$_2$ absorption line. They pass through the atmospheric column and are attenuated by an altitude-dependent CO$_2$ absorption, which is the product of the CO$_2$ absorption cross section and CO$_2$ number density at each altitude.. These pulses illuminate nearly the same area on the scattering surface, either the Earth's surface or cloud top. The light reflected by the surface passes back through the atmosphere with CO$_2$ absorption, and a small fraction of the light is collected by the receiver telescope. The lidar receiver measures the energies of the on- and off-line pulses (E_{on} and E_{off}) and the range to the scattering surface.

Figure 5-1 also shows a sketch of the shape of the integrated CO$_2$ line's transmission (top) and optical depth (bottom) when measured from space. The maximum CO$_2$ absorption occurs for

wavelengths tuned to the CO_2 line center. The wavelength of the laser's "on-line" pulse is usually selected to be offset from the peak of the CO_2 absorption line to provide enhanced sensitivity to CO_2 absorption in the lower atmosphere and is indicated by the red vertical line. The wavelength of the laser's "off-line" pulse, that undergoes minimal CO_2 absorption, is indicated by the blue line. The wavelengths λ_{on} and λ_{off} are sufficiently close that the scattering and absorption by atmospheric aerosols, clouds, and the illuminated scattering surface are the same for both.

Table 5-1 Unique and Important Capabilities of the ASCENDS Lidar

The light source (laser) is in the instrument measuring consistently in a nadir path. This enables day and night measurements at all latitudes in all seasons.
The measurements to the surface are range resolved. This allows accurate, bias-free column CO_2 measurements to the scattering surface through thin clouds and aerosol layers.
The lidar directly measures range, thus the estimates of the scattering surface elevation needed to infer CO_2 column mixing ratio are accurate and not impacted by height errors in DEM's, variable heights of trees and other above-surface scatterers, and/or reflectance variability within the footprint.
The laser footprint and spatial scale of sampling (~100 m) are small. This enables more frequent measurements to the surface in small gaps between optically thick clouds.
Many sources of potential bias are eliminated since the lidar interacts with the atmosphere and surface consistently in a nadir path. Other than causing signal attenuation, atmospheric aerosol scattering does not impact the lidar CO_2 measurement.
The laser's spectral width is a small fraction of the atmospheric CO_2 absorption linewidth, and it is tunable. Sampling the pressure-broadened CO_2 absorption line at an appropriate offset from its absorption line center enables preferential weighting to the CO_2 molecules in the lower troposphere, where the CO_2 source and sink "signals" are the strongest.
The absorption line can be sampled at a several different offsets from line center wavelength, enabling determination of column concentrations with separate weightings toward both the lower and upper troposphere.
The lidar samples only one selected atmospheric line instead of an entire band. This minimizes errors from interfering gas species. It also greatly reduces the quantity of accurate spectroscopic information needed, and so reduces the potential for spectroscopy-dependent errors.

The altitude-weighted CO_2 column abundance is calculated from the lidar's measurement of range to the surface and ratio of the energies in the on- and off-line return pulse signals. In the IPDA lidar designs considered for ASCENDS, averaging of multiple lidar pulses is planned, so the column abundance specification is for the average of measurements made (typically for 50-100 km) along the orbit's ground track. The column average mixing ratio (XCO_2) that is weighted over the altitude range of the lidar measurement is calculated using additional information about the density of dry air in the same measurement column.

In the original approach for ASCENDS, a simultaneous O_2 lidar measurement was included as part of the instrument to provide an estimate of the dry air column. The results of the initial O_2 lidar developments are summarized in Appendix F. As the ASCENDS definition activities progressed, a consensus developed that at the time of the mission, a state-of-the art atmospheric model analysis, evaluated at the location and time of the CO_2 lidar measurement, was likely to be sufficiently

accurate (see Section 4) to be used for a simpler, less technically challenging, and lower cost mission approach. The description in this section is based on that approach.

5.1.2   General Measurement Principle

The column averaged CO_2 mixing ratio measured from space across the lidar measurement range to the scattering surface can be calculated for the two-wavelength approach from (Browell et al., 2012)

$$X_{CO_2}(avg) = \frac{\int_{R_{surf}}^{R_{sat}} n_{CO2}(r)\left[\sigma_{on}(r) - \sigma_{off}(r)\right]dr}{\int_{R_{surf}}^{R_{sat}} n_{air}(r)\left[\sigma_{on}(r) - \sigma_{off}(r)\right]dr} \tag{5-1}$$

Here R_{surf} is the elevation of the scattering surface, R_{sat} is the elevation of the satellite, $n_{CO2}(r)$ is the altitude-dependent CO_2 number density, and $n_{air}(r)$ is the altitude-dependent dry air number density. At an elevation r, $n_{CO2}(r) = X_{CO2}(r)n_{air}(r)$ and the CO_2 line's altitude-dependent absorption cross-sections are $\sigma_{on}(r)$ and $\sigma_{off}(r)$ at the on- and off-line wavelengths respectively. Equation (5-1) assumes accurate knowledge of the CO_2 line shape and that there is no other absorption from other gas species (such as water vapor) at the CO_2 measurement wavelengths. If other gas species absorb there, then their additional absorption effects must be accounted for.

The lidar receiver measures the return pulse energies, E_{on} and E_{off} measured for the on- and off-line pulses reflected from the surface at elevation R_{surf}. The satellite's elevation (its distance from the Earth's center of mass) can be determined with meter-level or better accuracy by using an orbit model with inputs from the satellite's on-board Global Positioning System (GPS) receiver. Given a nadir pointed lidar's measurement of range R to the scattering surface, the elevation of the scattering surface is computed from

$$R_{surf} = R_{sat} - R \tag{5-2}$$

The total dry air column density to the scattering surface, n_{air}, is estimated by evaluating a sufficiently accurate atmospheric analysis at the lidar's spatial position and measurement time.

Because the width of the CO_2 line is broadened by atmospheric pressure, the line narrows at higher altitudes. This causes the off-set line's absorption cross section to decrease with increasing altitude. Equation (5-3) gives the measurement's weighting function, $W'(r)$, normalized to unit area, which is the measurement's relative sensitivity to CO_2 at different geometric altitudes.

$$W'(r) = \frac{n_{air}\left[\sigma_{on}(r) - \sigma_{off}(r)\right]}{\int_{R_{surf}}^{R_{sat}} n_{air}\left[\sigma_{on}(r) - \sigma_{off}(r)\right]dr} \tag{5-3}$$

Figure 5-2 shows an example of a CO$_2$ line's cross sectional shape and weighting function versus pressure altitude. The weighting function's dependence on altitude depends on the absorption line strength, the displacement of the "online" frequency from line center, and dry air density. Most candidate IPDA lidar approaches exploit the weighting function to enhance the column measurement's sensitivity in the lower atmosphere. By choosing a suitable λ_{on}, the laser signals are preferentially absorbed by the CO$_2$ molecules in the lower troposphere, where the ambient pressure is higher. This allows $W'(r)$ to be strongest in the lower troposphere. Thus, the lidar measurement can be more sensitive to the lower tropospheric CO$_2$ than that of a passive reflected solar instrument, by as much as a factor of two.

The one-way differential absorption optical depth (DAOD) measured by the lidar can be defined as

$$DAOD \equiv \frac{1}{2}\ln(E_{off}/E_{on}) \qquad\qquad\qquad (5\text{-}4)$$
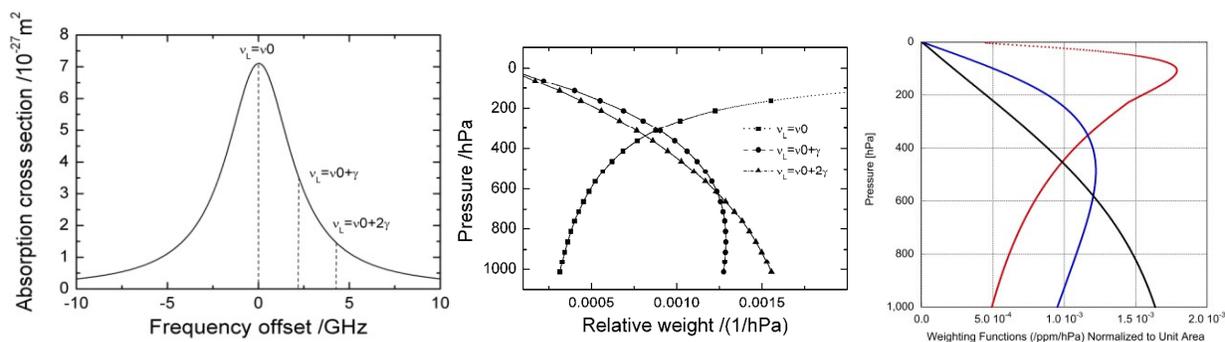
Figure 5-2 Absorption cross section and relative weight by pressure for an example CO$_2$ line. *(Left)* Example of the molecular absorption cross section of the 6348 cm^{-1} CO$_2$ line near 1575 nm, as function of frequency offset of the on-line laser frequency from line center for typical near surface conditions (T= 288 K and P = 1013 hPa). The dashed lines indicate the on-line laser frequency tuned off line center at one and two collisional halfwidths γ. As the atmospheric pressure decreases with increasing altitude, γ decreases and the CO$_2$ absorption line narrows. *(Middle)* Relative weight of the CO$_2$ column content as a function of pressure level for the same example on-line laser frequency positions (ν_L) with respect to the center of the absorption line (ν_0) (Ehret et al., 2008)). (*Right*) Weighting Functions calculated for some CO$_2$ line candidates for ASCENDS at different on-line wavelength offsets from line center (*Red* – 1572-nm line with 3-pm offset, *Blue* – 1572-nm line with 10-pm offset, *Black* – 2051-nm line with 42-nm offset). These are all normalized to unit area. Two or more on-line wavelengths may also be used to allow lidar retrievals to independently solve for XCO$_2$ values that weighted toward the upper as well as the lower troposphere.

The accurate measurements of XCO$_2$ needed for ASCENDS require accurate lidar measurements of *DAOD* and *R*, as well as knowledge of n_{air}(r) The conditions for measuring gas column densities to the Earth's surface from orbit can be complex. There can be variability in R_{surf} and surface reflectivity, as well as in the spatial coverage, altitude distribution and strength of cloud and aerosol scattering. Generally, there are potential error sources from the instrument, spectroscopy of the CO$_2$ line, and platform altitude and pointing angle (*measurement errors*) as well as potential errors from the knowledge of the parameters of the atmospheric column (*environmental errors*). All these factors must be considered in an ASCENDS lidar error budget for meeting the requirements for

measuring XCO_2. A major strength of the lidar approach is providing accurate and high-resolution measurements under widely varying conditions.

The various lidar approaches demonstrated as candidates for ASCENDS have used somewhat different methods for their DAOD measurements of CO_2. They have sampled different CO_2 lines, used different absorption line sampling strategies with different numbers of wavelength samples, and different ways of measuring the elevation of the scattering surface. All CO_2 lidar demonstrations to date have used estimated $n_{air}(r)$ using atmospheric models or in situ meteorological profiles. The details on their approaches are described in their respective sections. However, the operation of all the lidar candidates generally follow the measurement concept described above.

5.1.3   Importance of Range Measurements

The lidar's range measurements which link the backscattered online/offline signals with their round-trip time-of-flight, provides accurate determination of the column length and enables effective filtering of aerosols and optically thin clouds. It is well known that atmospheric scattering, if not accurately accounted for or eliminated, is a source of bias in passive optical measurements of CO_2 columns (see for example Aben et al., 2007). Another example is in Menzies et al. (2014), where a high-altitude cirrus layer having optical depth of 0.03 was shown to produce a bias of as much as ~10 ppmv.

Accurate measurements of the atmospheric column length to the scattering surface are also important. The weighting function for the CO_2 column measurement depends on the pressure of the scattering surface, which is derived from its elevation (SSE, scattering surface elevation) together with pressure surface data from atmospheric models. A small lidar footprint, or spatial sampling resolution element, has significant advantages when measuring over regions with varying topography and/or with tall trees, causing the range to vary significantly. There are also limitations to the use of a Digital Elevation Model (DEM). For example, the DEM from the Shuttle Radar Topography Mission (Farr et al., 2007) is not a sufficiently accurate indicator of the SSE over forests. Finally, it is important to note that the reflectance of surface materials may vary for different gas absorption bands.

5.1.4   Overview of Remainder of Measurement Section

The measurement group of the ASCENDS ad hoc science definition team (SDT) has developed a preliminary set of ten requirements for the lidar measurements on the ASCENDS Mission. They are described in Section 5.2. These requirements are the consensus view of the measurement group and are intended to be generic and independent of the measurement approach.

During the past decade, NASA has invested in the development of several different lidar approaches and technologies which are candidates for ASCENDS. With the support of the Earth Science Technology Office (ESTO), the ASCENDS ad hoc science definition activity, NASA centers, and some industry investments, the NASA lidar teams have made many advances in developing candidate lidar approaches, in demonstrating their measurement capabilities from aircraft, and in demonstrating data analysis (retrieval) approaches. Four of these are summarized in Section 5.3.

Although the airborne lidars have been quite valuable in demonstrating the capabilities of candidate approaches, an affordable space version requires additional technology development to allow similar measurements from orbit. The measurement group has analyzed the capabilities needed for

a space lidar and have made progress in addressing key technologies for it. This work is summarized in Section 5.6.

5.2   ASCENDS Lidar Measurement Requirements

The ASCENDS ad hoc SDT has developed a set of measurement requirements for the ASCENDS lidar based on the team's prior lidar experience as well as that gained from the numerous ASCENDS airborne campaigns and the modeling studies discussed previously in this report. These represent a consensus of the presently understood lidar measurement needs for the space mission. The requirements are also consistent with the mission simulation studies performed by Kawa et al. (2010) and Crowell et al. (2018).

The preliminary requirements are provided in this section with a justification for each. Each individual lidar requirement ("R-#") is stated subsequently, along with its rationale and a discussion of the relevant issues and questions. These requirements are intended to be independent of the individual lidar measurement approaches. It is expected that the requirements will be updated as the understanding of the mission's tradeoffs and the measurement characteristics improve.

The requirements take into account the high precision and high degree of accuracy (or low measurement bias) needed for the ASCENDS lidar. They also consider the complexity of making precise measurements of atmospheric gas columns when viewing the Earth from space. Some of the complicating factors include the widely varying reflectance and topographic heights of the Earth's land and ocean surfaces, the wide variety of cloud types, and the large variations in cloud and aerosol attenuation and scattering in the atmosphere. The physics of the IPDA lidar approach uniquely enables retrieving CO_2 mixing ratios with high precision and low bias in the midst of these complications. Several of the listed requirements relate to essential attributes of the lidar system that has these capabilities, as discussed briefly here. The requirements are summarized in Table 5-2, including one requirement that is applicable to the ground segment.

5.2.1   Discussion of Requirement Elements

The ad hoc SDT has summarized ten specific requirements for the ASCENDS lidar that are discussed in this section. Some of the requirements may need additional work to improve their definition, and those needs are summarized under the Discussion headings. To improve the accuracy of retrievals, the value of some parameters may need to be updated after launch by using calibration/validation (cal/val) campaigns and activities.

R-1: XCO₂ Random Error

Baseline: <0.3 ppm, for 10-sec averaging, over a surface with a lidar directional reflectance equivalent to the Railroad Valley, NV (RRV) surface, with clear atmosphere, and effective weighting function with over 50% of its response (or sensitivity) below 5 km.

Rationale: The Observational System Simulation Experiments (OSSE's) performed by the ASCENDS Modeling team (c.f., Section 3) indicate that 0.3-ppm XCO₂ precision for a 10-second average over a surface with a lidar directional reflectance equivalent to RRV, has sufficient precision to improve estimates of carbon fluxes.

Discussion: This requirement assumes that individual samples (or retrievals) obtained at ≥50 Hz are averaged over 10 seconds (70 km along track with no gaps), over a surface with a lidar directional reflectance or "backscatter" of $\beta = 0.176$ sr^{-1} (typical RRV playa value), with negligible atmospheric attenuation by clouds and aerosols. See R-3 for more discussion on surface reflectivity characteristics.

This requirement is weighting function dependent, i.e., the lower in altitude the weighting function is peaked; the greater the sensitivity to surfaces sources and sinks. See Section 3 for examples of this effect. The requirement is on XCO$_2$, and the apportionment of the errors/uncertainties in the estimate is not yet specified. Uncertainties in surface pressure, water vapor, and temperature profiles will contribute as discussed in Section 4. We estimate roughly half of the mission-required error budget is due to the lidar CO$_2$ column measurement error.

R-2: XCO$_2$ Biases

Baseline: The instrument must have sufficient stability so that "Residual biases" can be reduced over the first year of the mission by using additional instrument characterization & on-orbit calibrations and validations. Biases should be ≤0.3 ppm, one year after launch.

Rationale: Results from the Modeling team simulations summarized in Section 3.

Discussion: The main emphasis is on "residual spatially- or temporally-varying biases" (i.e., biases that are likely to vary over spatial and/or time scales which remain after measurement model corrections). Since the residuals will decrease as the on-orbit instrument calibration and retrieval algorithms improve during the mission (as for OCO-2) then logically targeted values can be larger earlier. Some plausible target values are ≤1.2 ppm pre-launch, ≤0.6 ppm 6 months after launch.

For passive sensors, clouds and variations in atmospheric scattering, and errors in estimating surface elevation all cause bias. These biases grow in cloudy scenes and with solar zenith angle and so are particularly troublesome in the tropics and at high latitudes. In contrast, the lidar in the ASCENDS mission carries its own laser source whose characteristics are carefully optimized to minimize bias in the XCO$_2$ measurements. The ASCENDS lidar approach also allows making measurements of the atmosphere with the same observing geometry regardless of latitude, sun angle and local time. This approach allows accurate measurements of XCO$_2$ to be made day and night, over ocean and land surfaces, at all latitudes at all times of year, and through optically thin clouds and aerosols.

Nonetheless controlling bias in lidar measurements of XCO$_2$ at the sub-ppm level is still challenging since small biases can be caused by several different factors. Some are varying surface reflectivity; path length uncertainties; low received signal levels due to aerosol/cloud scattering; calibration errors; changes in the instrument's thermal environment; uncompensated non-linearities in detector response; or errors or uncertainties in the spectroscopy of CO$_2$ or interfering gases. The ASCENDS airborne campaigns have demonstrated almost all of the lidar benefits listed above and have shown increasingly accurate measurements as the lidar instruments and their retrievals have been improved.

R-3: Return Signal Dynamic Range

Baseline: To provide global coverage, the lidar must make and record measurements to a wide variety of surface types and through atmospheres with some thin cloud and/or aerosol attenuation. These will present a wide range of signal strengths to the lidar receiver.

Calculations of return signal strength for candidate CO$_2$ lidar that measure in the 1570-nm and 2051-nm bands are summarized in two tables in Appendix E. These estimates are based on limiting cases with one-way extinction optical depth (OD) ≤ 1.0 at the weak return signal end of the range, and one-way OD ≤0.2 (1570 nm) or OD ≤0.1 (2051 nm) at the strong signal end. The upper limit cutoff for the signal is (about 3 times that from Railroad Valley) for measurements to smooth water surfaces (i.e., surface wind speed less than ~3 m/sec). The instrument XCO$_2$ measurement precision must meet or exceed the precision multiplier estimates shown in the last column of the tables in Appendix E for various signal measurement conditions. This includes allowing for noise from the detector and optical background.

The weakest signal case is observing a rough ocean through thin clouds (~3.5% of RRV) , and the strongest signal case is measuring to calm ocean through a clear sky (~300% of RRV). For measurements near 1570 nm, the total dynamic range (ratio of the strongest to weakest signal) is 86. For measurements near 2051 nm the weakest signal case is observing a rough ocean through thin clouds (~3.58% of RRV) , and the strongest signal case is measuring to calm ocean through a clear sky (~328% of RRV), so the total dynamic range is 123.

Rationale: ASCENDS must record data over a variety of surface types (including snow & water) and atmospheric transmissions to obtain globally distributed measurements (including high latitude winter).

R-4: Along Track Sampling Resolution

Baseline: ≤150 m, (≥50 Hz sampling). This sampling rate is driven by the need for measurements over cloudy atmospheres and over regions of rapidly changing surface topography & reflectance. The lidar measured parameters that need to be reported at this rate include the Mean CO$_2$ DAOD (or column density), Mean Range (or scattering surface elevation) in CO$_2$ wavelength region, Range Spread*.

Rationale: The ASCENDS capability in "seeing" through breaks in cloud cover diminishes with laser footprint sizes >150m. ASCENDS also needs to measure to terrain surfaces that rapidly vary in elevation and reflectance.   A smaller laser footprint reduces error in determination/assignment of "effective scattering surface elevation".

Discussion: This requirement relates to the maximum laser footprint size and along-track spatial scale of sampling. One driver for this requirement is to measure through scattered clouds. Estimates of cloud gap size were obtained from analyzing from laser altimeter measurements over Iowa during 2011 ASCENDS airborne campaign (Browell et al., 2012). More data from the 2011 airborne campaigns are also available. Over mountainous terrain the rapidly varying column length causes the measurement to degrade with poorer along-track resolution.

* See discussion of range spreading in R-7

R-5: Measurements through atmospheric scatter (thin clouds & aerosols)

Baseline: To ensure adequate coverage of the globe, the lidar DAOD and range measurements must be made through scattering & attenuating aerosol layers and partially transmissive cloud layers that together have a maximum OD of 1.0. The bias requirement (R-3) must be met under these conditions. The measurement precision is expected to degrade at the lower received signal levels as given in the last columns of the tables in Appendix E.

Rationale: An important benefit of ASCENDS is allowing accurate measurements in regions covered by thin clouds and aerosol layers. These are quite prevalent in the Earth's atmosphere. When these are present, the random errors in XCO$_2$ will increase due to their attenuation of the surface reflected signal. Extensive airborne measurements of aerosol layer optical properties indicate that atmospheric aerosol OD is <0.1 at 2051 nm and <0.2 at 1570 nm, even for dust layers from Asia and the Sahara that have been transported from their source regions (Winker et al., 2010). From these results we conclude that aerosol layers alone will not seriously impact ASCENDS global coverage.

R-6: Measurements over forests & over sloped or rough bare terrain

Baseline: Measurements meeting R-1 & R-2 over forests and over surfaces with height variations of up to 40 m over a horizontal distance of 150 m are required.

Rationale: Forests cover a large fraction of Earth's land surface and are an important part of carbon cycle. Simard et al., (2011) reported the spatially-resolved tree heights over the globe, based on analysis of Ice, Cloud and land Elevation Satellite (ICESat)/Geoscience Laser Altimeter System (GLAS) measurements. Their results showed maximum tree heights of ~40 m. The ASCENDS lidar also must measure over bare terrain, rough or sloped, whose surface has similar range spreading over 175-m distances.

R-7 : Range to Scattering Surface

The lidar must measure scattering surface elevation (SSE) to determine the atmospheric path length with sufficient resolution and accuracy to allow accurate computations of XCO$_2$. The requirements and rationale for precision and bias are summarized below. An along-track sampling resolution of 100-150 m also provides capability to take advantage of gaps in thick clouds to obtain CO$_2$ data in the lower troposphere to the surface. Requirements R-4 and R-5 are relevant to this capability.

R-7.1: Range (Scattering Surface Elevation) measurement: Precision

Baseline:

a. Mean Range measurement precision: Baseline: ≤20 m (at 50-Hz rate) for all cases included in the tables in Appendix E and range spreading cases in R-6, and $\leq$2 m for a 10-s average over a RRV equivalent surface.

b. The Lidar must report range relevant for the CO$_2$ measurement wavelength region, on the same spatial scale (see R-4).

c. Range Spread measurement: Baseline ≤20 m (at 50-Hz rate) for all cases included in the tables in Appendix E and range spreading cases in R-6, for the CO$_2$ wavelength region.

d. Rate of change in range: The lidar needs to accommodate changes in range of ≥5 km for adjacent footprints, to allow for measurements from cloud tops to the ground through holes in clouds.

e. Spacecraft radial orbit height**: <1 m, at a rate sufficient to model orbit to <1-m radial error

   Rationale: The rationale for measuring range at CO_2 lidar wavelengths is:

a.   Some surfaces (e.g., conifers with snow underneath) can have different average scattering surface elevations (SSE) at CO_2 and shorter wavelengths, due to the variability in snow reflectivity with wavelength. Snow is quite dark at the CO_2 wavelengths but is much brighter at shorter wavelengths nearer the visible. In this case, there is a difference in the return signal from the snow surface (CO_2 is dim, while the return made using shorter wavelengths is brighter). Consequently, the mean range (i.e., the SSE) at shorter wavelengths will be different when there are spatial variations in snow cover across the footprint). Reporting the SSE at CO_2 wavelengths is needed to accurately estimate CO_2 mixing ratios under these conditions.

b. In order to maximize the number of CO_2 retrievals over, e.g., patchy/broken cloud cover, range measurements are required at the 50-Hz reporting interval, with the precision requirement stated above. The 20-m uncertainty is equivalent to approximately 1 ppm of CO_2. This uncertainty should decrease with additional along-track samples, although the rate of decrease of the uncertainty depends on the cloud structure and the underlying surface topography.

c.   Some reflecting surfaces (i.e., trees) will have range spreads within the footprint that can be 20-40 m, and large surface slopes can occur over mountains. Range spread measurements at the 50-Hz sampling rate enable estimates of tree heights and slope magnitudes. Measuring range spread with above-stated precision at the CO_2 wavelength region enables allows minimizing bias over surfaces discussed in (a) above.

** The spacecraft's radial orbit height is also needed to compute the scattering surface elevation from the lidar measured range.

R-7.2: Range (SSE) measurements: Bias

a. *Baseline for ranging measurements:* ≤2 m per footprint for all cases included in the tables in Appendix E and satisfying R-4 for range spreading. The lidar must also report range at the CO_2 offline wavelengths, on the same spatial scale (see R-4).

   Rationale: The SSE needs to be measured for the CO_2 lidar wavelength at 50 Hz to minimize the bias inherent in rapidly changing terrain. Bias occurs under conditions described in R-7.1, due to spectrally varying reflectivity of various surface types. Large changes in, e.g., snow cover, can occur over distances of 150 m (the required sampling interval). Measurements are made though "holes" for conditions of patchy/broken cloud cover, creating rapid changes from cloud top to ground.

In addition, over hills/mountains large changes in elevation occur over km-scale distances. Due to the inherent reflectance weighting of the samples, correlations between elevation and surface type (and surface reflectivity) could produce bias if using km-scale averaging. Hence reporting the range to the SSE at 50-Hz rate, with sufficient precision (<20-m uncertainty) and low bias (<2 m) is required.

b. *Baseline for Spacecraft radial orbit height:* <1 m

Rationale: The spacecraft's radial orbit height needs to be known to compute the scattering surface elevation from the lidar-measured range.

R-8: Measurements over Cloud Tops and Decks

Baseline: "Report" measurements over optically-thick cloud tops that meet the other signal requirements. (i.e., roughness, signal strength, etc.).

Rationale: These measurements are expected to be useful for analysis, but currently it is judged that they do not have to be of the same measurement quality as those to the surface. Further studies are needed to better quantify the requirement.

Discussion: Initial airborne measurements made in 2014 over stratus cloud decks and broken cumulus clouds show useful XCO_2 values (Mao et al., 2018). Some improvement can be expected with additional algorithm development. Cloud tops are diffuse scatterers, and laser penetration depths may vary from ~10 m to >100 m; consequently, making accurate measurements over cloud decks is more difficult than for solid surfaces.

R-9: Uncertainty in Measurement Footprint's Surface Location

Baseline Knowledge: ~100 m; *Baseline Control:* ~500 m

Rationale: Measurement analysis requires knowledge of laser footprint locations for use in models, correlative measurements, control of systematic errors/biases due to terrain variability, above-ground variability, and effective use of digital elevation models (DEM's). The mission will also need control of measurement locations for effective calibration and validation (e.g., TCCON intercomparisons), which is related to R-10.

Discussion: This requirement applies to the CO_2 measurement beam. It is important to recognize that sharp transitions in reflectivity (e.g., land-to-water transitions) also must be accommodated in meeting the XCO_2 precision and bias requirements.

This requirement is also associated with accurate location of the measurement footprint on the surface for improved modeling accuracy. These numbers are consistent with maintaining the path length error (SSE estimate error) below a value that compromises the overall error budget. Studies using ASCENDS airborne lidar measurement indicate that slopes <15 degrees over 100-m scales occur with ~50% probability over mountains ranges such as the Sierra Nevada. Any aspect of ground spot location uncertainty that affects bias error should be derived from the bias requirement stated earlier. Knowledge of spatial location of the column end-point is more important for smaller-scale sources. Typical pointing knowledge for the requirements above is 200 µrad, or 40 arcsec.

R-10: Laser Beam Pointing Off-nadir Pointing and Limits

Baseline: Nadir angle offset: 6 - 20 mrad; Off nadir operating limits: <+/-15 degree of nadir

Rationale: Need to allow a pointing offset to limit the signal from specular scatterers. Also, a finite range of pointing angles away from nadir is needed over land areas to permit a useful frequency of pointing to TCCON (or other ground-based calibration) sites.

Discussion: This specifies how far away from the nadir-pointing angle that ASCENDS is required to measure. The ASCENDS lidar must be pointed slightly offset from local nadir, to allow measurements to smooth water and certain flat ice crystals, while avoiding the strongest part of the specular reflections from them. The results from ICESat indicate that the beam should be offset by >6 mrad from local nadir to limit the maximum signal to the detector. The maximum angle is uncertain but likely <20 mrad. The final operational angle may need to be determined when on-orbit.

The lidar also needs the capability to point to ground-based calibration sites like TCCON. The further off nadir, the more frequently ASCENDS can access (i.e., be "within range of") ground-based cal/val sites. In regular operation, ASCENDS will need to point off-nadir (cross-track) to locate footprints near ground-based calibration sites (e.g., TCCON). Calibration measurements are expected to be important to assess and minimize residual biases. It needs to be determined how frequently ASCENDS will be required to measure off nadir.

When pointed off-nadir, an additional complication for the CO$_2$ measurement is the Doppler shift. During those conditions, the Doppler effects from the spacecraft's velocity, Earth's rotation, and atmospheric winds may shift the frequency of the absorption line relative to the spacecraft and may possibly change the absorption line shape. Some contributors of Doppler shift (from spacecraft velocity and Earth's rotation) are predictable, and estimates of atmospheric wind velocity fields are available from atmospheric models.

Table 5-2 Summary of ASCENDS Measurement Requirements

R-1. **XCO₂ Random Error:** ≤0.3 ppm for 10-sec averaging, over a surface reflectance equivalent to Railroad Valley, NV and with over 50% of the CO_2 measurement sensitivity below 5 km.

R-2. **XCO₂ Biases:** ≤1.2 ppm pre-launch; ≤0.6 ppm 6 months after launch; ≤0.3 ppm one year after launch with gradual improvements resulting from on-orbit characterizations and calibrations.

R-3. **Return Signal Dynamic Range:** Measurements must be made over all global surface types and in presence of thin clouds and/or aerosol attenuation (see cloud/aerosol limits in **R-5**).

R-4. **Along-Track Sampling Resolution:** ≤150 m (≥50 Hz measurement rate) for range and CO_2 optical depth measurements between scattered clouds and over rapidly changing surface topography.

R-5. **Measurements through Atmospheric Scatter (Thin Clouds & Aerosols):** Lidar range and CO_2 measurements must be made through attenuating aerosol/cloud layers with optical depths of ≤1.0. The **R-2** bias requirement is maintained, but the **R-1** precision is relaxed due to signal attenuation.

R-6. **Measurements over Forests and Sloped/Rough Terrain:** Measurements must meet **R-1** & **R-2** over forests and surfaces with height variations of ≤40 m over horizontal distances of >150 m.

R-7. **Range to Scattering Surface:** Measure scattering surface elevation with ≤20-m precision and ≤2-m bias at 50 Hz to allow accurate computations of XCO₂ at that rate.

R-8. **Measurements over Cloud Tops and Decks:** Measurements from optically-thick cloud tops are to be reported but are not held to **R-1** or **R-2** standards.

R-9. **Uncertainty in Measurement Footprint Location:** Lidar nadir angle offset of 6-20 mrad with surface location control to ≤500 m and knowledge to ≤100 m.

R-10. **Laser Beam Pointing Off-Nadir Limits:** Up to +/- 15 deg. off-nadir for targeting measurement sites for calibration or science purposes.

5.3   Candidate Lidar Approaches and Measurement Demonstrations

During the past decade, NASA has invested in the development and demonstration of several different lidar approaches and technologies which are candidates for ASCENDS. With the support of ESTO, the ASCENDS science definition activity, and NASA Center and corporate investments, several NASA lidar teams have made substantial advances in developing suitable lidar techniques and instruments, demonstrating lidar capabilities from aircraft, improving the understanding of the characteristics needed in the measurements, and advancing the technologies needed for the space lidar.

The operating principles for different IPDA lidar approaches have been discussed in detail in many publications. Some examples in Ehret et al. (2008), Abshire et al. (2018a), Spiers et al. (2011a), Browell et al. (2012), Dobler et al. (2013), Menzies et al. (2014) and others. An analysis of signal to noise for candidate approaches is discussed in Sun and Abshire (2012). In this section we summarize NASA's experimental demonstrations and the results to date. Each candidate approach is described along with examples of atmospheric measurements from aircraft. Afterwards an overview of the summer 2017 ASCENDS/ABoVE campaign is included, along with references to early results. The results from developing two candidate Oxygen lidar approaches are summarized in Appendix F.

It is important to note that the airborne lidar measurements demonstrated to date were obtained with much smaller teams, more limited resources and less time than is available to develop a lidar for

space. Hence its logical to expect a lidar developed for space to perform better, to be much better calibrated and have smaller measurement biases.

5.3.1   The CO₂ Sounder Lidar and recent airborne measurements

The airborne CO_2 Sounder lidar was developed to demonstrate a pulsed multi-wavelength IPDA approach as a candidate for the ASCENDS mission. Its early configuration and performance are described in Riris et al. (2007), Abshire et al. (2010a), Abshire et al. (2010b), Amediek et al. (2013), and the results for the 2011 ASCENDS campaign are described in Abshire et al. (2013, 2014). A photograph of the airborne instrument is shown in Figure 5-3 and a diagram of the instrument configuration is shown in Figure 5-4. This summary provides an overview of the most recent version of the lidar and its measurements, and a more detailed description is given in Abshire et al. (2018a).

Figure 5-3 Photographs of the airborne CO_2 Sounder lidar inside the NASA DC-8 aircraft. *a)* The seed laser subsystem. *b)* The aircraft racks containing the laser power amplifiers and the lidar's detector subsystem. In the center, the lidar's transmitter and receiver telescope assembly is positioned over the nadir window in the aircraft fuselage. The optical pulses from the fiber amplifiers, and the received optical signals are coupled via fiber optics. *c)* The instrument operator's console, with the control computer screens folded away.
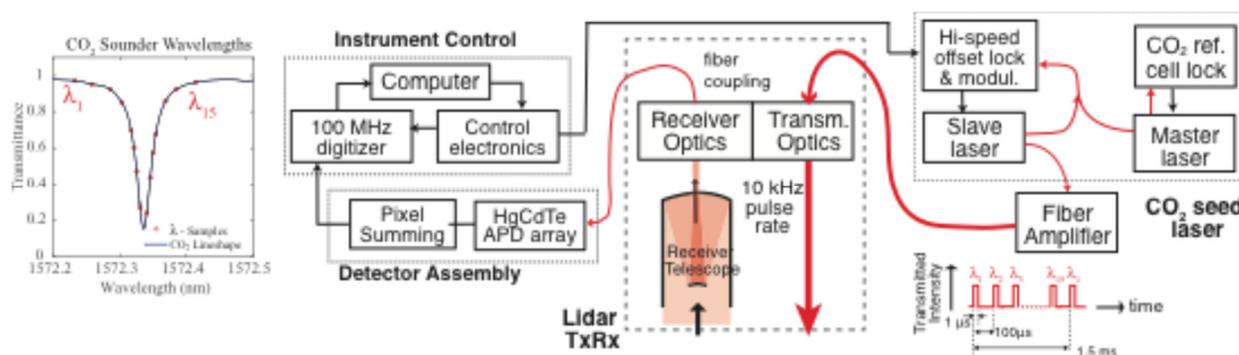
Figure 5-4 Instrument diagram for the 2014 and 2016 versions of the airborne CO_2 Sounder lidar. The seed laser subsystem produces laser pulse sequence that is repetitively stepped in wavelength across the CO_2 line. The wavelength of the master laser is locked to the center of the CO_2 absorption line. The slave laser is offset-frequency-locked to the master via an optical phase locked loop. The frequency offset is changed during the 99-µs between laser pulses based on a wavelength table. The slave laser's output is carved into 1-us wide pulses by a modulator and those are used as the input for the transmitter's fiber amplifiers that produce the transmitted laser pulse train. The direct detection receiver uses a mercury cadmium telluride (HgCdTe) Avalanche Photo Diode (APD) detector and an analog digitizer to record the backscatter profiles.

The CO_2 Sounder measurement samples a single CO_2 line in the 1570 nm band. The band has minimal interference from other atmospheric species like water vapor and has several temperature

79

insensitive lines. Although using other lines is also possible, the R16 line at 1572.335 nm has low temperature sensitivity, particularly in the lower atmosphere (Mao et al., 2007). The CO_2 Sounder approach samples the CO_2 line shape at multiple wavelengths, as shown in Figure 5-5. This provides several benefits including extracting line shape and some information on the vertical CO_2 distribution in the retrievals. It also allows solving for information such as line center wavelength, line width, and errors in the fits (Ramanathan et al., 2013). This approach also provides information that allows solving for several different environmental variables and instrument parameters, such as Doppler-shift and wavelength offsets, baseline tilts, and wavelength-dependent instrument transmission. This information allows minimizing bias in the retrievals. Performing retrievals in the presence of Doppler shifts allows measurements at off-nadir pointing angles and when pointing at ground targets. The pulsed approach also allows the simultaneous measurement of the backscatter profile and scattering surface height(s) in the same path.

Parameter	2016 values
CO_2 Line	R16, 6359.96 cm^{-1}
CO_2 line center wavelength	1572.335 nm
Laser min and max wavelengths	1572.228, 1572.390 nm
Laser pulse rate	10 kHz
# of wavelength samples	30 or 15
Laser scan rate of CO_2 line	300 or 600 Hz
Seed laser wavelength adj.	step locked
Wavelength change/ laser step	varied via program
Laser peak power, pulse width, pulse energy	25 watts, 1 μsec, 25 μJ
Laser divergence angle, linewidth	430 μrad, <4 MHz
Receiver Telescope type, diameter	Cassegrain, f/10, 20 cm
Receiver FOV diameter, optical transmission	500 μrad, 60%
Detector type	HgCdTe APD
Detector effective QE, Gain	70%, 300
Receiver signal processing	Analog detection & averaging
ADC sample time bin width	10 nsec
Receiver electronic bandwidth	7 MHz
Data recording rate, duty cycle	10 Hz, 90%

Figure 5-5 *(Upper Left)* Example of the CO_2 transmission line shape measured by the lidar from an altitude of 7.6 km when using 30 wavelength samples. The line shape samples from the lidar are the red dots. The line shape computed from the retrieval is shown as the black line. *(Lower left)* The ratio of the retrieved line shape and lidar retrievals with the red dots being the initial trial XCO_2 value of 400 ppm and the black dots and line being the final best fit retrieved XCO_2 value of 404 ppm. *(Right)* The parameters for the lidar used in the 2016 airborne campaign.

Several factors led to the choice of the pulsed approach and the laser pulse rate. Using lower pulse energies at higher pulse rates enables using a laser based on rugged and efficient fiber-laser technology. Using higher laser pulse rates allows using more averaging to reduce speckle noise. Using pulsed lasers also allows signal processing to isolate the signals from the primary scattering surface and to reject those from atmospheric backscatter. Hence it allows isolating the column measurement from potential bias errors. It also allows useful XCO_2 measurements to clouds tops and using a cloud-slicing approach to solve for XCO_2 in the boundary layer (Ramanathan et al., 2015; Mao et al., 2018). Isolating the surface signal via time gating also substantially improves the receiver's signal-to-noise ratio (SNR) by limiting the amount of noise from the detector and solar background.

5.3.1.1   CO₂ Sounder lidar used in 2014 and 2016 Airborne Campaigns

An earlier version of the lidar was used in the 2011 ASCENDS airborne campaign (Abshire et al., 2014) that had a similar basic design. Its receiver used a much less sensitive photomultiplier (PMT) detector. The 2014 and 2016 campaigns used the rapidly tunable step-locked seed laser described in (Numata et al., 2012). This sequentially wavelength-locked and -stepped the laser pulses across the 1572.33 nm CO_2 line in either 30 or 15 wavelength steps. For these campaigns the wavelength settings of the seed laser were also better optimized for measuring the CO_2 absorption lineshape. In the lidar receiver, the receiver's transmission was improved and used a much more sensitive 16-element HgCdTe avalanche photodiode (APD) detector whose analog output was recorded by an analog digitizer. In 2016 the laser's divergence and the receiver field of view (FOV) were also increased to reduce speckle noise. Finally, the retrieval algorithms and models that solve for range, for parameters that can cause offsets in the measurements and for XCO_2 were also updated. These changes considerably improved the lidar's measurement precision, stability and dynamic range, and reduced measurement bias. The parameters for lidar 2016 version are summarized in Figure 5-5.

5.3.1.2   Data Processing and XCO₂ Retrievals

Figure 5-5 shows the wavelength sampling of the CO_2 line shape used in 2016 campaigns. The retrieval algorithm approach is discussed in detail in (Abshire et al., 2018a; Ramanathan et al., 2018). First, the receiver backscatter profile at 10 Hz is averaged over 1-s and searched for pulse echoes with significant energy, such as those reflected from cloud tops or from the ground. The averaged pulse echo energies at each wavelength are then corrected for variation in transmission of the receiver's optical band-pass filter. This yields a first estimate of the lidar-sampled CO_2 transmission line shape. The 1-s averaged transmittances across the CO_2 absorption line are then converted into optical depth. Flight calibrations are constructed from a segment during Engineering Flights that had known atmospheric conditions and a vertical profile of CO_2 mixing ratio measured by the in situ sensor during the flight's spiral down maneuver. Radiative transfer calculations are used to predict the CO_2 transmission line shapes at different altitudes based on the in situ CO_2 measurements. This allows solving for and applying any further corrections needed to compensate for changes seen in flight, such as those in the wavelength dependence of the receiver optics. These final calibrations are then applied to all retrievals for the flights.

Line shape and fit: The retrievals utilize a CO_2 absorption line shape based on atmospheric state from an atmospheric model analysis. The aircraft altitude, measurement path angle and elevations of the significant scattering surfaces are determined from the aircraft GPS altitude, pitch and roll angles and the lidar-measured range. For the CO_2 line shape calculation, the algorithm used the spectroscopy database to calculate CO_2 optical depth and create Lookup Tables (LUTs). These are initially computed for a vertically uniform mixing ratio. The algorithm then retrieves the best-fit XCO_2 by comparing the line shapes to those calculated based on the LUT to the lidar measured line shape samples. The retrieval algorithm then solves for Doppler shift, baseline offset, slope, surface reflectance and XCO_2 by using a best fit of the lineshape to the data.

Weak Water Vapor Lines: There is a weak isotopic water vapor (HDO) absorption lines on the short wavelength shoulder of the 1572.335 nm CO_2 line, as well as one about 4 times weaker near 1572.389 nm. We found the HDO absorptions can bias the retrieved XCO_2 value by up to 2 ppm if these are not taken into account. Our laser settings assigned 1 or 2 wavelengths on the short wavelength HDO line to allow the retrievals to solve for the column water vapor concentration

(XHDO). The XHDO values are used in the forward calculations and then to improve the retrievals of XCO$_2$.

5.3.1.3 Measurement Examples from ASCENDS Airborne Campaigns

The airborne measurement examples that were analyzed in Abshire et al. (2018a) are summarized in Table 5-3. For each flight we compared lidar measurements of XCO$_2$ made during spiral down maneuvers to the surface with those computed from the Atmospheric Vertical Observations of Carbon Dioxide in the Earth's Troposphere (AVOCET) in situ sensor (Choi et al., 2008; Vay et al., 2003). Lidar measurements were made over low mountains covered by tall trees, desert areas with atmospheric haze, areas with growing crops, a transition area between high plateau and cropland, fresh cold snow, and in clear sky over desert. Spiral down maneuvers were made over most areas, allowing the lidar retrievals of XCO$_2$ to be compared to the column average from in situ sensors. A few examples are discussed below.

Table 5-3 Summary of 2014 and 2016 Campaign Flights and the Regions Studied

Flight Designation	Date	Location (in US)	Focus of Measurements	Aircraft Altitude Range (km)	Ave. Time per Measurement (sec)	Number of Lidar Measurements
2014 SF1	20-Aug-14	North CA Coastal Forests	Forests on low mountains	2.89 - 11.19	10	712
2014 SF2	22-Aug-14	Near Edwards AFB, CA	Desert through haze	3.50 - 11.25	10	446
2014 SF5	3-Sep-14	Eastern Iowa	XCO$_2$ over cropland	2.62 - 11.16	10	1010
2014 SF3G1	25-Aug-14	Colorado to Iowa (outbound)	East-West XCO$_2$ gradients	11.2	50	43
2014 SF3G2	25-Aug-14	Iowa to Colorado (return)	East-West XCO$_2$ gradients	5.6, 6.3, 10.8	50	67
2016 Desert	10-Feb-16	Edwards AFB, CA	Desert	3.59 - 12.60	1	1281
2016 Snow	11-Feb-16	Eastern Nevada	Recent cold snow	6.68 - 9.52	1	5893

2014 SF1: The focus of this flight was to make measurements over a forested region with tall trees and targeted the northern California coast. Most of the ground was covered by a forest covering hills and coastal mountains. A time series of the measurement results is shown in Figure 5-6. It shows the aircraft and ground elevations computed from range versus time as well as the lidar measured differential optical depths (DODs, measured from the peak to offline shoulder) and the retrieved values of XCO$_2$. In this and in similar figures, the scattering surface elevation is computed from the aircraft altitude, the off nadir beam angle, and the lidar measured slant range to the scattering surface.

2014 SF2: This flight targeted measurements over a desert region at the western edge of the Mohave Desert in California. Data from this flight are shown in Figure 5-7 including the spiral down over Edwards Air Force Base. This flight occurred during a period of widespread atmospheric haze at lower altitudes caused by smoke spreading from a wildfire in the nearby Sierra Nevada Mountains. Figure 5-7 shows a layer of haze from ~4km to the surface caused by smoke from the wildfire. The altitude profile of the lidar measurements is also shown, along with measurements from the in situ sensor. The results show there is very good agreement between the XCO_2 retrieved from the lidar and that computed from the in situ sensor, despite the thick haze layer.

2014 SF3: This was a flight from California to Iowa and back made in the afternoon and evening. These transits allowed assessing the lidar's capability to measure east-west gradients in XCO_2 on a near-continental scale. The ground track of the first segment was in Colorado and Nebraska during the west-to-east leg of the flight (Figure 5-8). The ground track of the second segment, in Iowa, Nebraska and Colorado, was during the east-to-west flight leg. The data points plotted in Figure 5-8 are lidar retrievals based on 50-s (~12 km along track) averaging. Both segments clearly show the gradual decrease of XCO_2 caused by increasing growing crop density (and CO_2 uptake) toward the eastern end of the flight legs in the Midwest US. The solid lines show the XCO_2 values computed from the NASA Parameterized Chemistry Transport Model (PCTM) (Kawa et al., 2004) for these tracks and times. Although there are offsets in the average values, there is good agreement between the E-W gradients measured by the lidar on the outbound flight segment and those from the model, as well as for the 6.3 km altitude leg of the return segment.
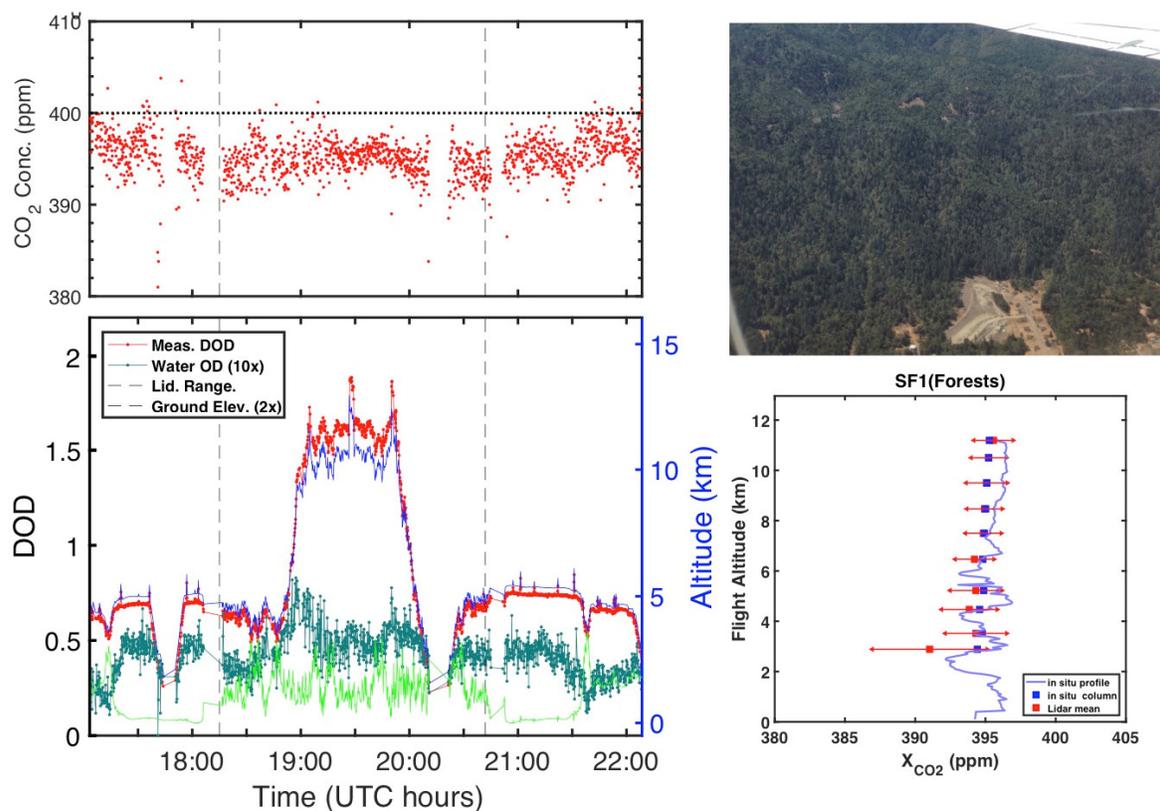
Figure 5-6 Lidar measurement and retrieval results from 2014 SF1 flight over the coastal redwood forests. *(Left Bottom)* time resolved results showing the lidar measured differential optical depth in red, the range to the surface in blue, and the computed elevation of the scattering surface in dark green. The upward spikes in the DOD and range are

from the banking of the aircraft during the corners of the box pattern. *(Left Top)* The retrieved XCO_2 values from the lidar measurements, with each dot made using 10 second averaging time. The measurements between the dashed lines are summarized in the lower right. *(Right Top)* Photo of the coastal redwood forests taken from the aircraft. *(Right bottom)* Summary plot of the in situ (blue) and retrievals from lidar measurements (red) versus altitude. The lidar results are for XCO_2 retrievals based on 10-s average from the altitude where the results are plotted, and the error bars are for 1 standard deviation. The XCO_2 computed from the in situ sensor from the plotted altitude to the ground are shown as the blue dots.

The 2016 campaign was a short (two flight) campaign flown during the local wintertime. The campaign objectives were to assess the performance of the 2016 version of the CO_2 Sounder lidar, to assess measurements made using fewer wavelength samples and with additional laser power, and to characterize the measurements made at low sun angles and darkness over fresh cold snow.

2016 Desert: This flight was near Edwards Air Force Base CA, which was the spiral down location. Figure 5-9 shows the altitude summary of the lidar measurements for the spiral down. The plot format is the same as for Figure 5-6, except that these measurements have 1-s averaging time. The smallest standard deviations for the 1-sec measurements were ~0.7 ppm for altitudes between 7-10 km, which is a factor of ~8 smaller than corresponding lidar measurements made in 2011. Figure 5-9 also plots the standard deviation of the 1-second lidar retrievals vs altitude, along with those computed from a statistical model of the lidar (Sun et al., 2017a). The altitude dependence of both plots shows the standard deviations increasing at lower altitudes due to decreasing optical depth of the CO_2 line, and at upper altitudes due to the lower lidar signal with increased CO_2 absorption. The plot also shows the standard deviations of the random error in the retrievals are about a factor of 1.4 higher than the lidar model. This increase may be caused by unmodeled variability in surface reflectivity or from an unmodeled noise source in the detector electronics.
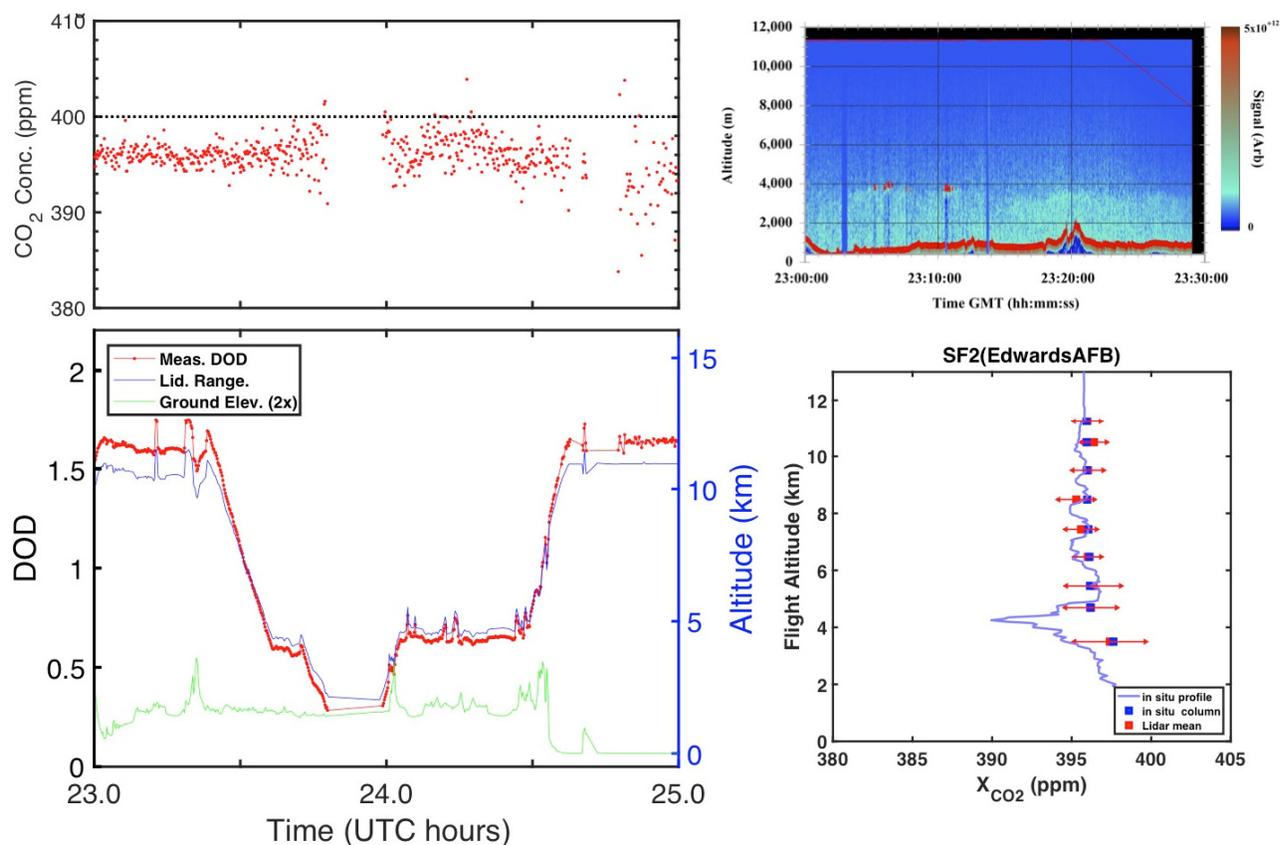
Figure 5-7 (*Left*) Lidar measurement and retrieval results from 2014 SF2 flight over Edwards AFB CA. From the ~11 km altitude, the aircraft flew a spiral down pattern to near the Edwards Dry Lake Bed. The plot format is the same as in **Figure 5-6**, and the retrieved XCO$_2$ values from the lidar measurements are made using 10-second averaging time. *(Right Top)* Time history of the range resolved backscatter for the off-line wavelengths recorded on this flight before the spiral down maneuver. The plot shows enhanced scattering from haze in the boundary layer. The aircraft altitude is the thin red line at the top of the plot. *(Right bottom)* Summary of the in situ (blue) CO$_2$ measurements and the XCO$_2$ retrievals from lidar measurement (red) versus altitude for the segment shown. The lidar results are for XCO$_2$ retrievals based on 10-s average and the plot format is the same as **Figure 5-6**.
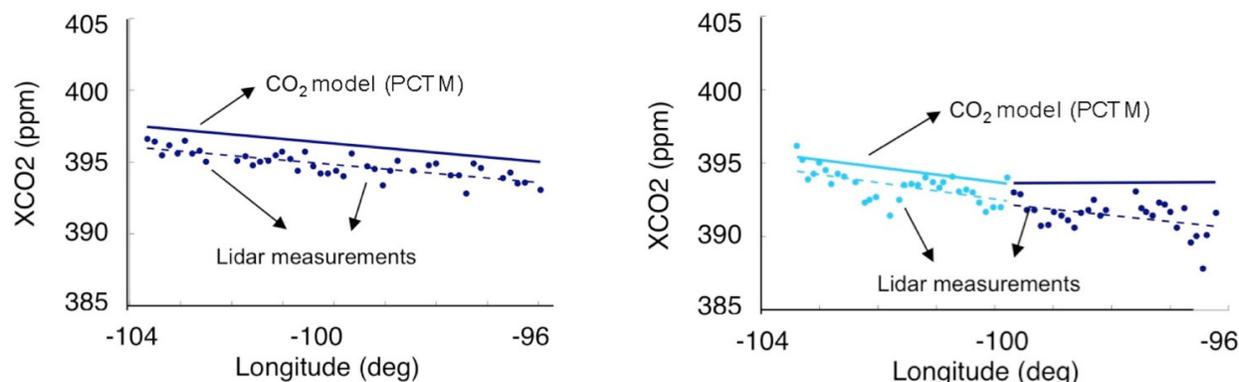
Figure 5-8 Retrieved XCO_2 from lidar measurements vs longitude for the transit flights to/from Colorado to Iowa on 2014 SF3 on Aug. 25, 2014. *(Left)* Outbound leg (West to East flight direction, SF3G1, measured from 11.2 km altitude) and *(Right)* Return flight leg (East to West flight direction, Iowa approaching Colorado, with dark blue points measured from 5.6 km altitude and light blue points from 6.3 km altitude). The measurements shown are for retrievals using 50-s data averages. The solid lines show the XCO_2 values computed from the PCTM atmospheric model for that location and these times.
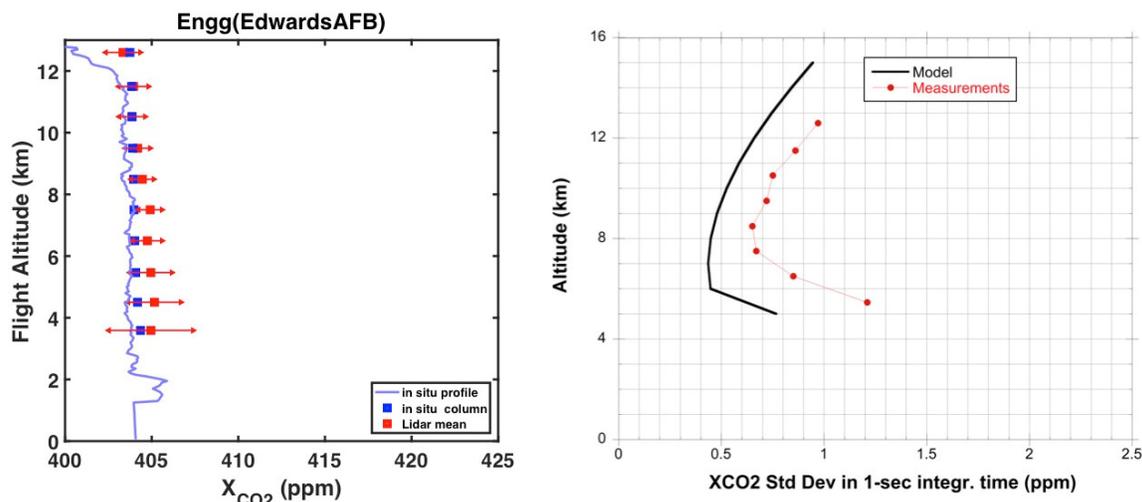
Figure 5-9 *(Left)* Plot of the measurements made during the spiral down segment of the 2016 desert flight over Edwards AFB CA. The XCO_2 retrievals from the lidar measurements are shown (in red) from the plotted altitude to the surface, the in situ CO_2 concentration measurements (blue line) and the XCO_2 computed from the in situ CO_2 readings from the plotted altitude to the surface (blue dots). *(Right)* Plot of the standard deviation of the XCO_2 retrievals from the lidar measurements (red) using 1-s integration time, showing best resolution near 8 km altitude. The solid black line is the standard deviations computed from a statistical model of the lidar measurement.

The retrieval results show the lidar worked well during both 2014 and 2016 campaigns (Figure 5-10). The 2016 airborne results were best due to the higher receiver optical transmission and the reduced speckle noise. The retrievals from the 2016 measurements made over desert surfaces from a 10 km altitude with 1 second averaging time consistently had a standard deviation of ~0.8 ppm, while those with 10-s averaging time had precision of 0.3 ppm. This is a five-fold improvement in precision over measurements made in 2011 (Abshire et al., 2014), where the agreement between the lidar and in situ values of XCO_2 were <1.4 ppm. The higher precision in 2016 also allows a more careful comparison of differences in lidar measured XCO_2 values to those computed from the column averaged in situ sensor. In most cases, the agreement of average XCO_2 computed from the

lidar to that computed from the in situ sensor was better than 1 ppm. The flights and height-resolved measurement statistics from the 2014 and 2016 airborne campaigns have been summarized in Abshire et al. (2018a). A presentation of initial CO_2 Sounder results from the 2017 ASCENDS airborne campaign is also available (Abshire et al., 2018b).
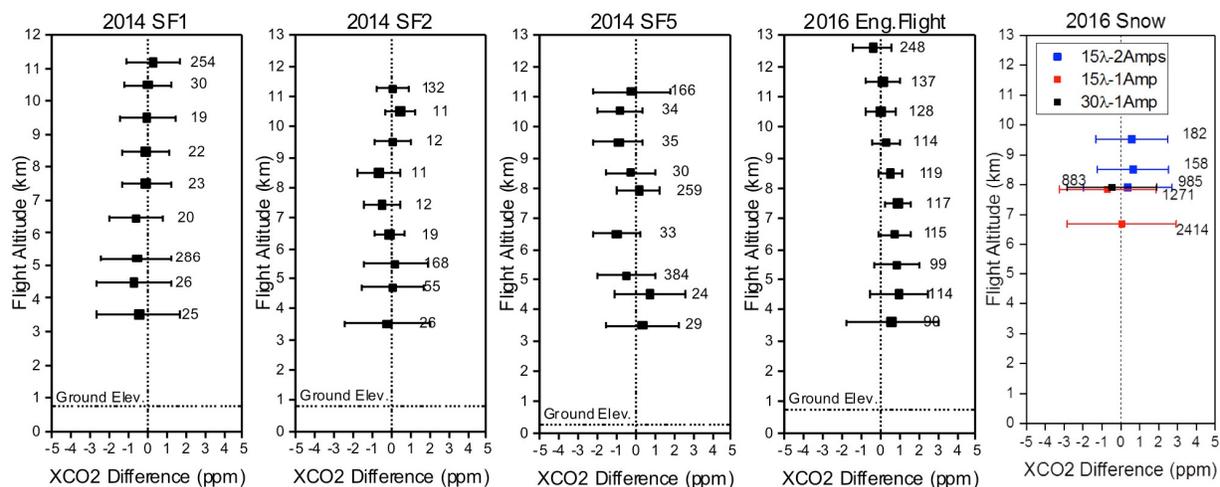
Figure 5-10 Summary of the CO_2 Sounder Lidar retrieval results from the 2014 and 2016 flights, plotted from the values summarized in (Abshire 2018a). The dots are the mean value of the XCO_2 from the lidar minus that computed from the in situ sensor. They are plotted at the altitude from which they were measured, and the average ground elevations are also shown. The 2014 statistics are from data using10-s averaging and the 2016 measurements used 1-s averaging. The error bars are those of the lidar data set, and the numbers shown are the number of lidar observations in that set. There were three different settings used in the lidar for the 2016 snow flight, and their results are plotted in different colors.

5.3.1.4 Measurements to Cloud Tops and Partial Column Retrievals

Analysis of airborne CO_2 Sounder measurements to cloud tops was reported in (Mao et al. 2018). The airborne measurements were made during the 2011, 2013 and 2014 ASCENDS campaigns. The laser pulses reflected from cloud tops had sufficient energy to allow clear identification of CO_2 line shapes and retrievals of XCO_2 from the aircraft to cloud tops >90% of the time. Retrievals from the CO_2 measurements to cloud tops had minimal bias but larger standard deviations compared to those made to the ground. When used with nearby full-column measurements to ground, the CO_2 measurements to cloud tops were shown to be useful to estimate the partial-column CO_2 concentration below clouds, which should lead to better estimates of surface carbon sources and sinks. This capability of the CO_2 Sounder measurements provides a new benefit for future airborne and space missions.

5.3.1.5 CO_2 Sounder Summary

An improved CO_2 Sounder lidar was demonstrated during the ASCENDS 2014 and 2016 airborne campaigns. The changes included incorporating a rapidly wavelength tunable, step-locked seed laser in the transmitter, using a much more sensitive HgCdTe APD detector, and using an analog digitizer with faster readout time in the receiver.

The flights were made from 3-12 km aircraft altitudes, and the results are compared to the XCO_2 values computed from an airborne in situ sensor. The 2014 results show significantly better performance than previous and include measurement of horizontal gradients in XCO_2 made over

the US Midwest that agree with chemistry transport models. The results from the 2016 airborne lidar retrievals show precisions of ~0.7 parts per million (ppm) with 1 second averaging over desert surfaces, which is an eight-fold improvement compared to corresponding measurements made in 2011. The results from both campaigns showed the mean values of XCO_2 retrieved from the lidar consistently agreed with those based on the in-situ sensor to within 1 ppm. The improved precision and accuracy demonstrated in the 2014 and 2016 flights advance the technique's readiness for a space and should benefit future airborne science campaigns.

5.3.2   The Intensity-Modulated Continuous-Wave (IM-CW) Laser Absorption Spectrometer for XCO₂

The NASA Langley Research Center (LaRC) in collaboration with Harris Corp. (previously ITT Exelis) has been developing and testing advanced lidar technologies for application to the ASCENDS space mission. The critical aspect of these activities is the development of a prototype Intensity-Modulated Continuous-Wave (IM-CW) Laser Absorption Spectrometer (LAS) for high-precision, column averaged CO_2 mixing ratio (XCO_2) measurements using the Integrated Path Differential Absorption (IPDA) approach. Airborne flight campaigns demonstrate that the CO_2 measurements of current IM-CW LAS systems meet the accuracy and precision requirements of the ASCENDS mission. Also, model simulations have shown that this IM-CW LAS technology and approach can be used for the ASCENDS space mission to reach its science goals.

The first IM-CW LAS system, the Multifunctional Fiber Laser Lidar (MFLL) developed by Harris (Dobbs et al., 2007, 2008; Dobler et al., 2013), demonstrated the capability of CO_2 column measurements from several aircraft under a variety of atmospheric and surface conditions (Browell et al., 2008, 2009b, 2010, 2012; Dobler et al., 2013; Lin et al. 2015). Extensive demonstrations of the capability of column CO_2 measurements have also been conducted in the laboratory and over a horizontal ground test range. The MFLL CO_2 column measurements over desert and vegetated surfaces during those technology demonstration flight campaigns are found to agree with those calculated from surface reflectance models and in-situ profile measurements of atmospheric meteorological parameters and CO_2 mixing ratios to within an average XCO_2 value of 0.17% or ~0.65 ppmv. An XCO_2 measurement precision of ~0.3 ppmv for a 10-s average over these surfaces has also been achieved (Browell et al., 2009b; Dobler et al., 2013). Beyond these technology flight demonstrations, MFLL is also a key instrument of the Atmospheric Carbon and Transport – America (ACT-America) Project (https://act-america.larc.nasa.gov), which is a NASA Earth Venture Suborbital Mission. During field campaigns of ACT-America, XCO_2 measurements with high signal-to-noise ratios (SNRs) of >120 at 10 Hz sampling rate, resulted in a similar precision to those found during technology demonstration flights. Stable, accurate XCO_2 measurements with systematic variations of <0.3 ppm compared to in-situ measurements for extensive flight periods over generally-uniform environments were observed (Lin et al., 2017).

Recently, NASA Langley with support from Harris has also been developing an advanced IM-CW laser absorption spectrometer, the ASCENDS CarbonHawk Experiment Simulator (ACES), to demonstrate advanced technologies critical for developing a spaceborne instrument with lower platform consumption of size, mass, and power, and with improved performance (Campbell et al. 2014a, b, c, d; Obland et al., 2017). Current field experiments during ASCENDS and ACT-America flight campaigns have shown encouraging results in ranging and XCO_2 measurements.

5.3.2.1   Basic Characteristics of IM-CW LAS System

The CO$_2$ lidar discussed here is based on the airborne prototype LAS system, MFLL (Dobbs et al., 2007, 2008; Dobler et al., 2013; Lin et al., 2013). Figure 5-11 shows the lidar design. Key improvements in the ACES instrumentation design include the use of multiple amplifiers and an extra transmitted-power-monitor downstream of the amplifiers, which is used as an additional external transmitted power reference to complement the power-fiber-tap inside the amplifier.
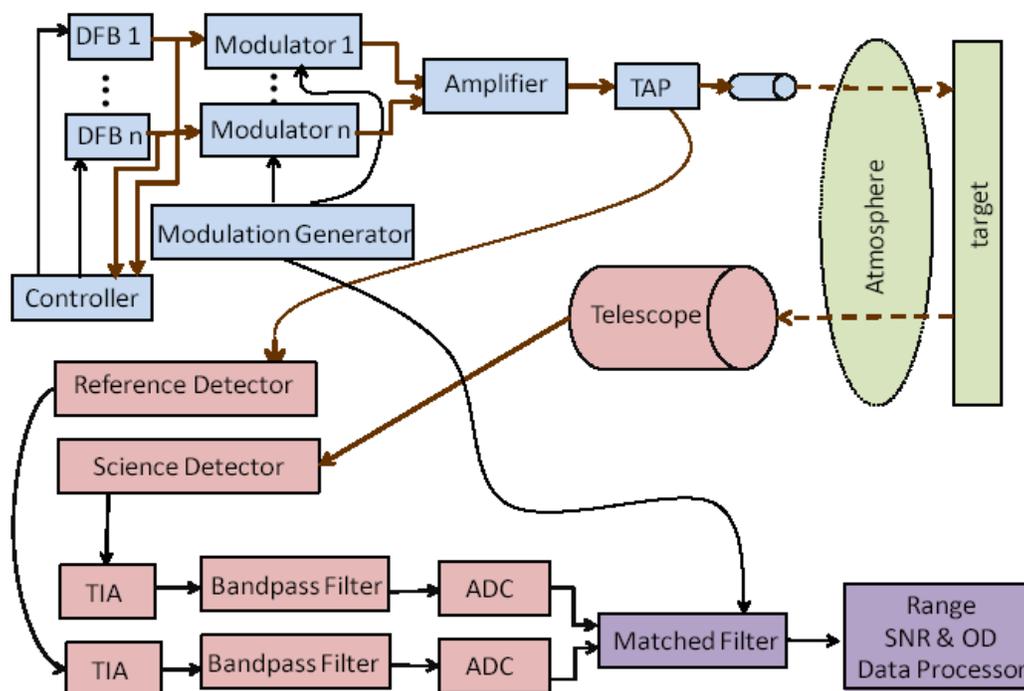
Figure 5-11 Architecture of the airborne MFLL lidar (Lin et al., 2013).

The LAS system incorporates a laser transmitter, a receiving telescope, a data acquisition system, and a signal-processing unit. The lidar transmitter uses a 5-W Erbium-Doped Fiber Amplifier (EDFA) and has one laser wavelength positioned at the center of the CO$_2$ absorption line at 1571.112 nm ("online") and two other laser wavelengths in the distant wings of the absorption line at offsets of ±50 pm ("offlines") for the CO$_2$ IPDA measurements (Figure 5-12). All CO$_2$ wavelengths were selected to simultaneously minimize water vapor and other trace gas interference and to maximize the signal-to-noise ratio (SNR) of the differential absorption optical depth (DAOD) measurements (Ismail and Browell, 1989; Remsberg and Gordley, 1978). Other considerations in the laser line selection include the altitude-dependent gas absorption weighting function; the DAOD sensitivity to knowledge of the laser wavelength and line-width; and the wavelength stability of the laser spectra (Menzies and Tratt, 2003; Ehret et al., 2008; Kameyama et al., 2011; Lin et al., 2013).
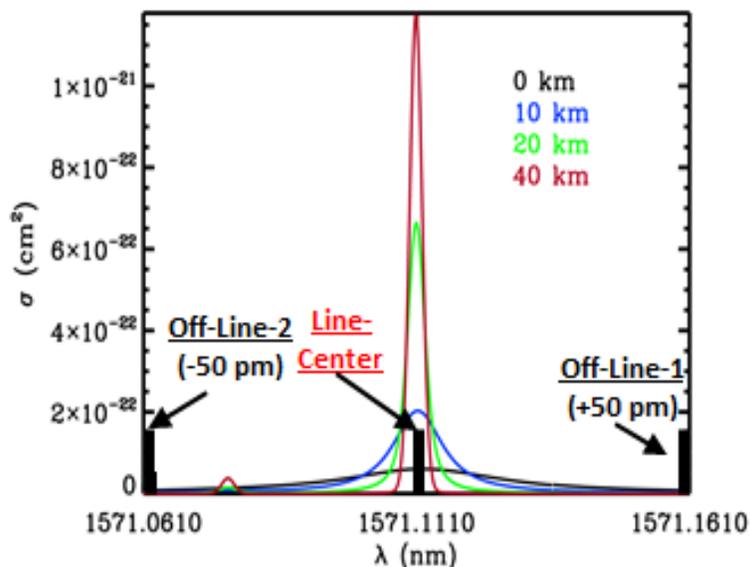
Figure 5-12 The wavelength sampling approach for the airborne MFLL lidar and the altitude dependence of the CO$_2$ absorption cross section (σ).

An essential capability to achieve high accuracy XCO$_2$ measurements is to apply a range-encoded intensity-modulation technique to the IM-CW lidar system for CO$_2$ column measurements and range determination. The use of range encoding with a phase-sensitive detection subsystem clearly discriminates the magnitude and timing/range of laser signals reflected from the surface against those from other intermediate backscatters. A commonly used technique in the detection subsystem for the signal discrimination is a matched filter that correlates the range-encoded modulation waveforms with the recorded signals. Figure 5-13 illustrates the modeled capability of a range-encoded IM system using a swept frequency technique with three measurement channels (c.f., Lin et al., 2013). The illustration is for an idealized case of a target at 12-km range with an intermediate backscatterer at 6 km to represent the presence of an intervening cloud/aerosol layer. Fractional intensity units are used as the return power is normalized by the output power. The sampling rate, swept frequency bandwidth of the IM waveform, and unambiguous range (UR) are set to be 2 megahertz (MHz), 500 kilohertz (kHz), and 15 km, respectively, which are consistent with the current airborne systems.
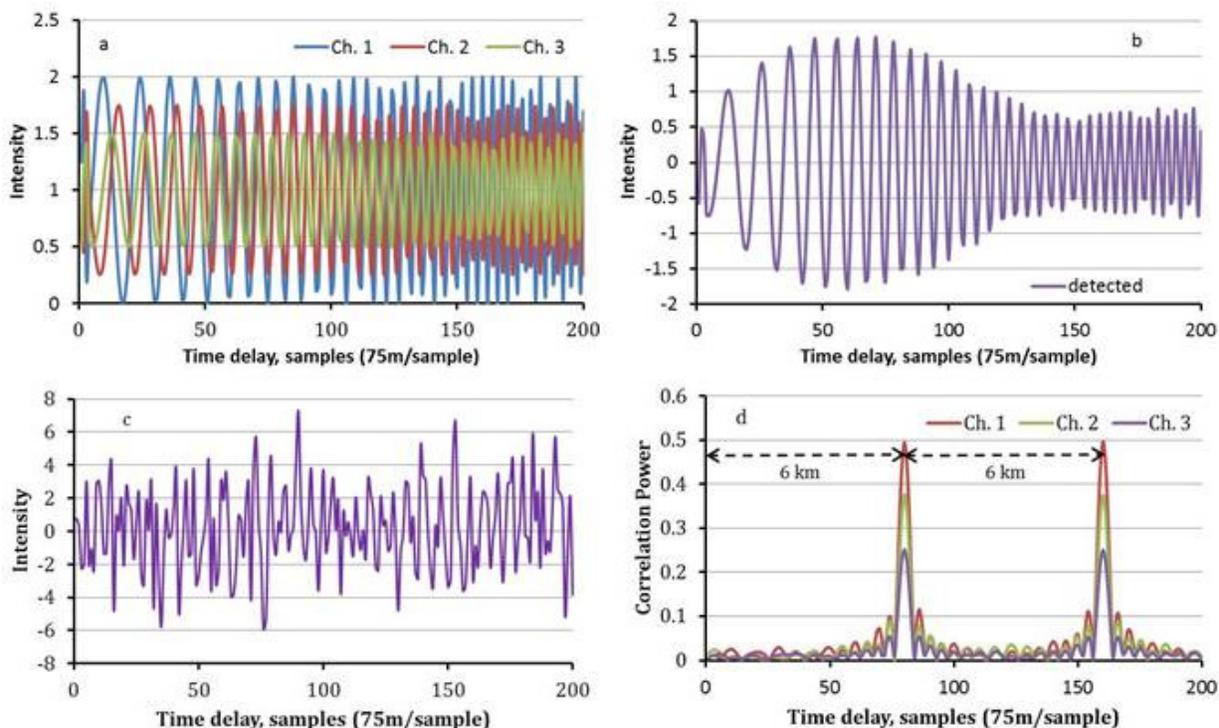
Figure 5-13 Simulated sample laser signals detected by MFLL. a) Range-encoded lidar signals from the target without noise for individual channels coming onto the detector; b) The intensity modulated lidar signals of the three channels produce a single time series at the detector; c) Recorded lidar return, which is a combination of lidar signals from the target and intermediate backscatterer as well as all noise sources; d) Lidar signal power as a function of range obtained by the correlation of the matched filter of the lidar system (Lin et al., 2013).

In Figure 5-13, panel a shows the individual laser signals that are combined to yield the modulated signal shown in panel b. The beat frequencies among the three channels are shown in the variations of the signal power with the time delay due to the IM scheme used. The detector receives the combined signal, including noise, and this is then passed through an electronic bandpass filter to reduce background noise and to avoid spectral aliasing. The bandpass filter also removes the DC component of the signal. To show the importance of intermediate scatterers, the received signal power from the intermediate scatterer is assumed to be equal to that of the target, and the noise level is as high as the return signal power from both scatterers. Compared to candidate IM waveforms (panels a & b), the signature of the received signal (panel c) appears be very weak due to 3 channel signal mixing, a combination of signals from the target and intermediate backscatterers with different time delays, and noise. Even in this case, the matched filter technique with 0.1-s integration period clearly demonstrates the capabilities of detecting weak target signals and minimizing the effects of intermediate scatterers and noise. The outputs of the matched filter show two distinct correlation peaks corresponding to the target and intermediate scatterer (panel d). The wider the IM bandwidth, the narrower the peaks and the easier to differentiate between two closely spaced scattering objects. Besides the detection of target signals, panel (d) also illustrates that the target range can be estimated by measuring the time delay of the peak power of the target or intermediate reflection. The range capability and CO$_2$ column measurements to both surface and cloud tops under cloudy conditions are illustrated by this figure.

Figure 5-14 Photograph of the MFLL mounted inside the NASA DC-8 aircraft (Dobler et al., 2013).

A photograph of the MFLL lidar onboard the NASA DC-8 aircraft is shown in Figure 5-14. The onboard data processing and onboard display unit, detection system, and CO_2 transmitter subsystems are located at the front. The telescope and transmit optics are housed under the black laser curtain. Table 5-4 lists the key parameters of the lidar system. The CO_2 lidar has been implemented using IM-CW techniques that include sine wave and rolling tone frequencies, and more recently using swept-frequency and pseudorandom number (PN) code modulation approaches. The swept-frequency and PN code IM techniques provide ranging capabilities to discriminate surface returns from cloud and aerosol returns. After the receiver and data acquisition subsystems record lidar return signals, a matched filter correlates the transmitted IM waveforms with the received IM waveforms reflected from the surface and clouds. The location and magnitude of correlation peak power values are estimated from the matched filter output. The peak magnitudes of individual channels are proportional to the powers received for their corresponding channels and used in the retrievals of CO_2 columns. This leads to the calculation of the CO_2 DAOD value, while the location of the correlation peaks is used to determine the range. Because of the sampling rate limit, sampled maximum power values may not be located exactly at the correlation peaks. Thus, a technique of fitting the correlation function with multiple sampled points is used to find the power and range (Harrison et al. 2014). From flight campaigns and range testing, the accuracy and precision of the calculated range was found to be better than 3 m (Dobler et al., 2013; Lin et al., 2013, Harrison et al. 2014): equivalent to a XCO_2 error of about 0.12 ppmv. Recently, the determination of peak power and its location has been significantly improved by applying a super-resolution algorithm developed by NASA Langley for IM-CW lidar signals (Campbell et al., 2014a, b, c, d). Generally, when repeatedly measuring a scattering surface (500 measurements used here, for example) with independent phase information, the lidar return power and the range from the lidar to the scattering surface can be determined much more accurately than when using a single measurement. The unique character of this algorithm is that the interpolation is conducted within the frequency domain instead of the time (or space) domain, which significantly reduces computational burden in data processing using convolution, deconvolution, and interpolation, and enables fast and accurate estimations of lidar return power and range.

Table 5-4 Airborne MFLL Lidar Parameters

Airborne MFLL Lidar Parameters	
Seed laser type:	DFB diode laser
Line width	<6 MHz each wavelength
Side mode suppression	Ratio > 45 dB
CO_2 lines: (vacuum)	1.571112 µm (On), 1.571061 µm (Off 1), 1.571161 µm (Off 2)
Modulator:	Semiconductor Optical Amplifier
Modulation type:	Intensity-modulated continuous-wave (IM-CW)
Optical amplifier:	EDFA
Output power:	5 Watts
Optical bandpass filter:	2.4 nm
Telescope	Cassegrain, 8 in. diameter.
Receiver optical throughput	8.5%
Detectors	DRS HgCdTe APD gain: ~940; Excess noise factor ~1.3, 77 K
Transimpedance amplifier	Gain: 10^6
Sample rate of digitizer	2 MHz
Encoding scheme:	Swept-frequency; ~350 ± 250 kHz;
Unambiguous range:	15 km (or 200 samples); 30 km (or 400 samples)
Laser divergence angle:	190 urad (half angle)
Receiver FOV:	240 urad (half angle)
Receiver duty cycle:	100%
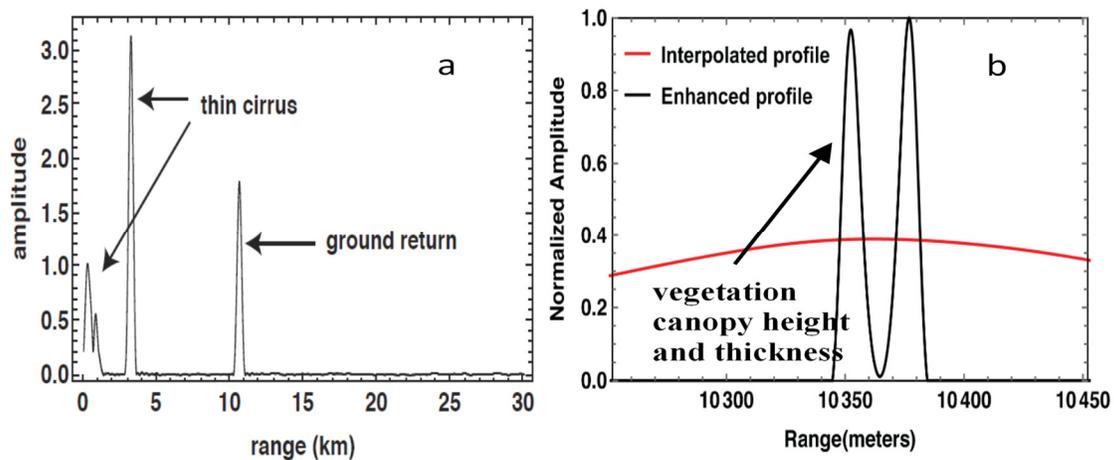
Figure 5-15 Examples of IMCW lidar range measurements: (a) thin clouds; (b) vegetation canopy (Campbell et al., 2014d).

Figure 5-15 shows examples of IM-CW lidar range measurements for (a) thin cirrus cloud and (b) forest land surface cases. Multiple cirrus layers were found underneath the lidar (and aircraft) for this thin cirrus case. Lidar return signals from the ground were still discernible, which enabled

XCO$_2$ retrievals in the presence of thin cirrus (Campbell et al., 2014d). The advantage of the super-resolution algorithm is reflected in the forest case, where both canopy top and ground surface could be identified with 24-m separation due to both fine horizontal resolution (or footprint) of the lidar system and high range resolution of the algorithm (Campbell et., 2014c). Details on the instrument and data processing can be found in Dobler et al. (2013), Lin et al. (2013, 2015) and Campbell et al. (2014a, b, c, d).

5.3.2.2 Approach for Determining CO₂ Column Differential Absorption Optical Depth

To evaluate the accuracy and precision of the MFLL remotely-sensed CO$_2$ column measurements, the actual CO$_2$ DAOD values are needed as a reference. These DAOD values are derived based on the knowledge of the in-situ observed vertical profiles of CO$_2$ mixing ratios and meteorological parameters; the altitude- and meteorologically-dependent spectroscopy of CO$_2$ and interfering gases, such as water vapor; the path length from the aircraft to the surface; and the off-nadir pointing of the laser beam (Browell et al., 2008, 2009b, 2010, 2012; Dobler et al., 2013; Lin et al., 2013, 2015). High-quality in-situ measurements of CO$_2$ (Choi et al., 2008; Vay et al., 2003), temperature (T), pressure (P), and relative humidity (q) profiles were obtained from onboard instruments during aircraft spirals and collocated, contemporaneous radiosonde launches. A pulsed laser altimeter was also included as a part of the MFLL suite of subsystems to make an independent measurement of the range to the surface and cloud tops for validation of the IM-CW range measurement. A GPS receiver and the aircraft navigation system provided additional aircraft information including latitude, longitude, altitude, and attitude. Comparisons of MFLL and in-situ-derived DAOD values were typically limited to a horizontal distance of less than 10 km from the aircraft spiral and radiosonde locations. When multiple in-situ spirals were conducted during a flight, the spiral data corresponding to the closest MFLL overpass time was used.

5.3.2.3 Airborne CO₂ Column Measurements

The LaRC ASCENDS team conducted 13 flight campaigns using the NASA UC-12 and DC-8 aircraft since May 2005 to evaluate the capability of obtaining remote CO$_2$ column measurements for the ASCENDS mission. Accurate CO$_2$ column measurements have been demonstrated in these flights.   Figure 5-16 shows two comparison examples of 1-s average MFLL CO$_2$ DAOD measurements and in-situ-derived (modeled) values in drastically different geographic regions.
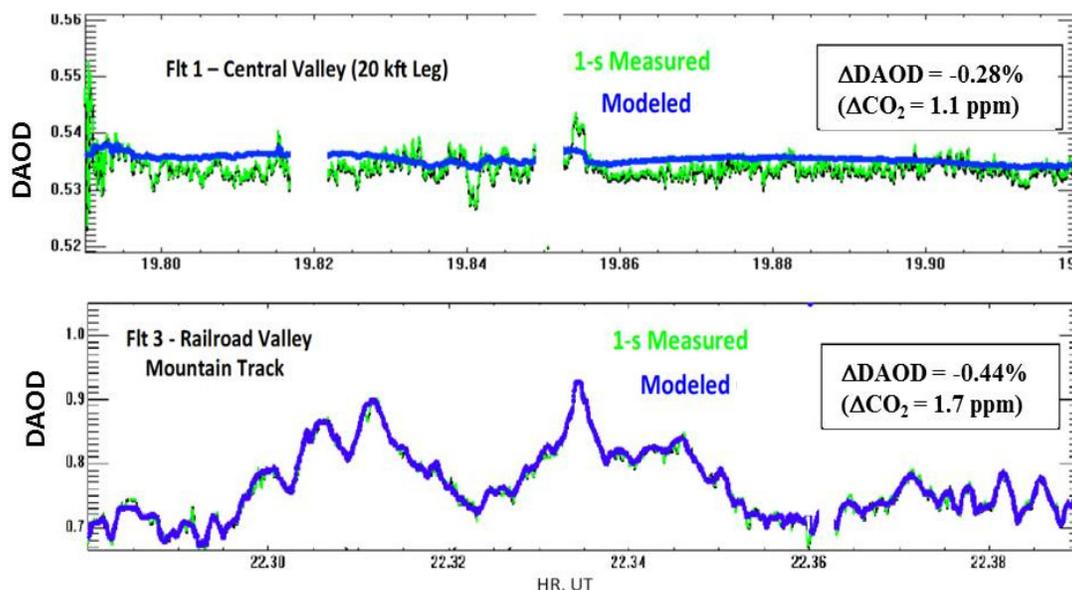
Figure 5-16 Comparison of measured and in-situ/modeled CO_2 DAODs for flights over Central Valley, CA (top) and the Rocky Mountains (bottom) in route to Railroad Valley, NV (Dobler et al. 2013).

The top panel of Figure 5-16 shows the CO_2 measurements on a constant altitude flight leg over the Central Valley, CA in comparison to modeled DAOD values derived from in-situ CO_2 data from a DC-8 spiral at the center of the leg and radiosonde data obtained within about 1 hour of the over-flight. The small variations in the in-situ-derived (i.e., model-calculated) DAOD across the flight leg were due to small changes in the range from the aircraft to the surface. The resulting difference of 1-s averages between the measured and modeled DAOD values on the Central Valley flight leg was found to be -0.28% or the equivalent of ~1.1 ppmv. The bottom panel shows the DAOD comparison while transiting across the Rocky Mountains. The in-situ data (spiral and radiosonde) came from Railroad Valley, NV, and the variation in DAOD values across the mountains was almost entirely due to surface elevation changes as the aircraft was at a constant altitude. The comparison of 1-s measured and modeled DAOD values demonstrated a high level of agreement (ΔDAOD = -0.44% or ~1.7 ppmv) even when one expects some change in CO_2 across the mountains that could not be captured in the modeled DAOD due to the lack of in-situ data. Flight tests of the current LAS instrument have demonstrated very high-precision CO_2 DAOD measurements (SNR_{DAOD} >1800) with a 10-s averaging interval (Browell et al., 2012; Dobler et al., 2013). This provides a foundation to consider the space-based XCO_2 measurements to meet the ASCENDS random error requirement (0.3 ppm).
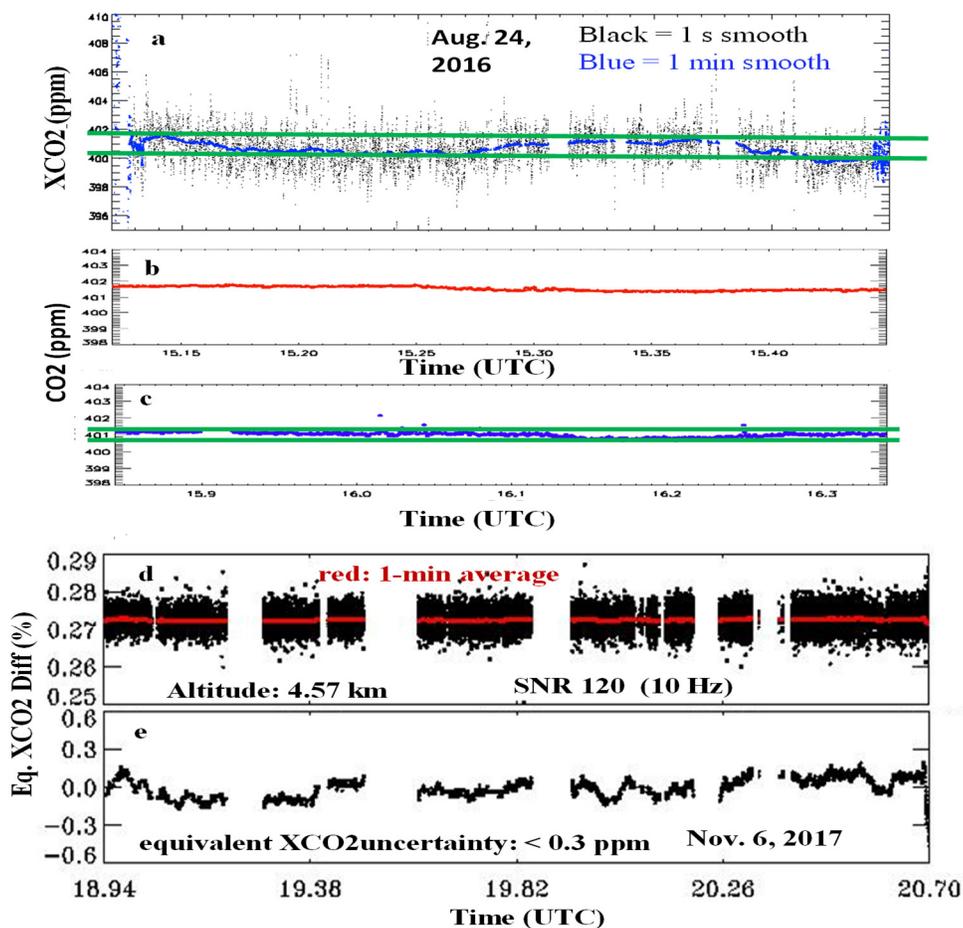
Figure 5-17 Lidar XCO_2 measurements over Gulf of Mexico and comparison with in-situ observations for Aug. 24, 2016 (a, b, c) and Nov. 6, 2017 cases (d, e): Lidar XCO_2 for 1-s (black) and 10-s (blue) averages (a); C-130 (b) and B-200 (c) in-situ CO_2 measurements. Green lines in (a) and (c) bound the measurement variability. Lidar measured 10 Hz (black) and 1-s averaged (red) data of CO_2 DAOD (d). Equivalent XCO_2 uncertainty (e, in percentage) of 1-s DAOD measurements in (d).

Based on the ASCENDS flight campaign demonstrations, the MFLL was selected to participate in the NASA ACT-America Project for intensive CO_2 column measurements over the eastern US to evaluate XCO_2 spatial variations under different meteorological conditions and assess small scale-XCO_2 variations in OCO-2 satellite retrievals. The ACT-America project provides further opportunity for extensive IM-CW LAS technology development and carbon science applications in field campaigns. Figure 5-17 shows two MFLL flights over the Gulf of Mexico during ACT-America field campaigns, within a generally uniform CO_2 environment, which were selected for testing the instrument's stability, precision and accuracy. On the Aug. 24, 2016 flight, the observed XCO_2 changes were within about 0.5 ppm (a), slightly larger than in-situ observed variations (~0.3 ppm) obtained by in situ instruments on the C-130 flying with the lidar (b) and B-200 within planetary boundary layer (PBL, c). For the Nov. 6, 2017 case, the short-term performance is promising with a SNR of 120 for 10-Hz DAOD data (d) and equivalent XCO_2 uncertainty <0.3 ppm at 1-minute time scales at an altitude of 4.57 km (e). The stability, precision, and accuracy of XCO_2 were also found to be within 0.3 ppm at 1-hour time scales.

A comparison of airborne lidar partial column XCO_2 measurements with OCO-2 retrievals based on the August 27, 2016 OCO-2 under flight during ACT-America is shown in Figure 5-18. The upper air contribution of CO_2 on OCO-2 observations is removed using the Copernicus Atmosphere Monitoring Service (CAMS) model. Besides the MFLL and OCO-2 remote sensing XCO_2 retrievals, other XCO_2 estimates are also plotted in the figure: CO_2 atmospheric curtains of in-situ aircraft measurements, and several different chemical-transport model results. Consistent XCO_2 retrievals from MFLL and OCO-2 were reported by Bell et al. (2018).
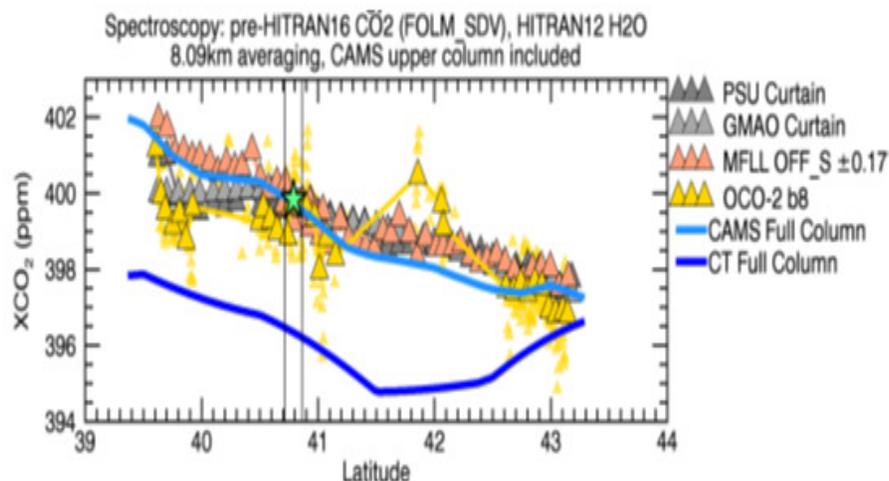
Figure 5-18 XCO_2 Comparison of the OCO-2 under flight on July 27, 2016 for OCO-2 (yellow), MFLL (orange), in-situ observations, and various model results. Partial column CO_2 retrievals are shown except Copernicus Atmosphere Monitoring Service (CAMS) (light blue line) and Carbon Tracker (CT) (dark blue line) modeling results. Dark and light grey triangles are from atmospheric curtains of aircraft measurements constructed by Penn State University (PSU) and the Global Modeling and Assimilation Office (GMAO) model, respectively. The star is the in-situ estimate based on the aircraft spiral of the flight.

5.3.2.4   Surface Reflectance, Cloud Discrimination, and Range Measurements

Since variations in surface types and reflectance can significantly affect lidar return power and thus CO_2 column retrievals, different surface conditions were analyzed from MFLL flight data. For farm fields and deserts, moderate to high reflectance values were observed, and strong signals for CO_2 column retrievals were received. For some surfaces, especially snow, ice, and rough water, very low reflectance was expected and observed. From MFLL data, the measured surface reflectance of snow and ice was as low as about 0.02/sr. Fresh snow (less than 1-2 days old) was found to have even significantly lower reflectance (about ~0.01/sr). Even in these low reflectance cases, MFLL received enough backscattered signal for CO_2 column retrievals from 12 km altitudes. The surface reflectance for completely snow-covered terrain was found to be relatively homogeneous, however the magnitude of the surface reflectivity for both snow-covered mountainous and farmland terrain was observed to vary by more than an order of magnitude over distances of less than 10-20 meters from the nominal snow and ice surface reflectance values.

In addition to surface types, the presence of thin clouds, aerosol layers, and thick low level clouds are important factors that can affect the accuracy of CO_2 column measurements. Thin cirrus clouds introduce multiple lidar returns and reduce returned signal power from the surface. As mentioned previously, the capability for detection of surface returns in the presence of intervening cloud

returns is achieved using the swept frequency or PN code IM-CW approaches. Thick low clouds may block lidar signals reaching the ground and increase uncertainty for column CO_2 measurements. Since lidar systems have small footprints, they can measure the lidar returns from low clouds and even the ground between broken clouds. Thus, both partial column CO_2 to cloud tops and full column CO_2 to ground can be retrieved from CO_2 lidar measurements, though the uncertainty levels of these retrievals to cloud tops can be higher.

Atmospheric profiles for a thin cirrus cloud case were obtained over an arid/semi-arid region around 1600 Local Time (LT) on 22 February 2013 (0000 Universal Time (UT) on 23 February 2013) near Blythe, California (Lin et al., 2015). The atmospheric profiles of CO_2 concentration, temperature, pressure, and humidity were measured by in situ instruments onboard the NASA DC-8 aircraft during an aircraft spiral at the center of the leg. This and a second case discussed next both showed significant horizontal CO_2 variations (several ppm), which would introduce uncertainties in the comparison of lidar and in situ CO_2 measurements. The in-situ measured CO_2 profile indicated that PBL CO_2 values below about 3.5 km were significantly higher than those in the free troposphere, which started at about 400 ppm in the PBL and decreased with increasing altitude to about 393 ppm at 12 km. The high-altitude leg of this flight was at an altitude of about 12.2 km, and the extended thin cirrus clouds were observed just below the aircraft.

Both online and offline channels clearly showed the thin cirrus clouds just below the aircraft (range close to zero). Higher power returns from the clouds observed by the online channel compared to the offline channel resulted from higher transmitted power at the online wavelength in order to offset the reduction in SNR due to CO_2 absorption (Dobler et al., 2013; Lin et al., 2013). The range to the extended thin cirrus layer was nearly constant, indicating the height uniformity of these thin clouds. There were some changes in the range to the surface, which resulted from small changes in the surface topography. For this cloud case, our calculation of cloud optical depth based on offline lidar backscatter returns indicated that the cirrus cloud, as expected, was indeed very thin with an averaged cloud optical depth (one-way) of about 0.158 (Lin et al. 2015). The variability in the optical depth of these cirrus clouds was very large with values ranging from near zero to as large as 0.8 with a median of 0.135. The higher the cloud optical depth, the stronger the potential impact of the cloud on CO_2 estimates.

The retrieved DAOD of CO_2 column to the ground and its equivalent XCO_2 values are shown in Figure 5-19. The mean difference in DAOD retrievals between cloudy and clear conditions (a) is about -0.20%, which corresponds to an equivalent XCO_2 difference of -0.7 ppm (b). For airborne CO_2 column measurements, the thin clouds are very close to the sensor and their returns are significant compared with surface returns (due to the signal dependence on range^{-2}). While for space CO_2 lidar case, the ranges from space to the cirrus and surface are nearly the same, and the power returns from the cirrus would be much weaker than those from surface. Thus, the difference in the CO_2 column measurements between clear and cirrus cases would be much smaller (within 0.02% for cloud optical depth ~0.16) as shown by space modeling studies (Lin et al., 2013).
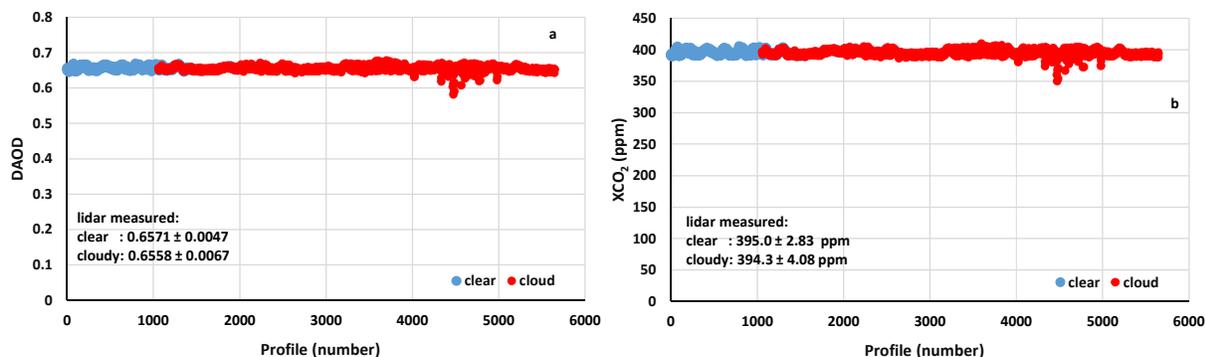
Figure 5-19 Plotted are DAOD (a) of CO$_2$ column to the ground and its equivalent XCO$_2$ (b) values with 0.1-s integration of lidar measurements for both clear (blue points) and cloudy (red points) conditions (Lin et al., 2015).

Data for a thick, low cloud case were obtained over an agriculturally vegetated area in the vicinity of West Branch, Iowa on 10 August 2011 during the ASCENDS 2011 summer flight campaign (Lin et al., 2015). In situ measured CO$_2$ profiles indicated free tropospheric CO$_2$ values were generally >385 ppm, slowly increasing with altitude, and reached about 392 ppm at 12 to 13 km. The low CO$_2$ (~365 ppm) values in the PBL below ~2 km reflected the CO$_2$ drawdown due to the active agriculture growing season, especially for corn, during the period of this flight campaign. Multiple layers of clouds from high thin cirrus and scattered mid-level clouds to thick low-level fair weather cumulus clouds were observed during this flight. These complicated environments of different kinds of clouds increase uncertainties in atmospheric CO$_2$ column retrievals compared to those with clear scenes.

The range (a) and DAOD (b) estimates for the flight at 12.5 km are shown in Figure 5-20. These ranges to the surface (blue points) or clouds (red points) were very similar for individual measurements, which was a result of generally a level flight attitude, a flat surface, and similar cloud heights. The rms error of the range estimates was generally within 3 meters using correlation function peak fitting technique (Harrison et al., 2014). DAOD retrievals showed consistent high precision results although variations in DAOD retrievals to cumulus cloud tops were much larger than those to the surface owing to smaller DAOD values, extended backscatter sources and weaker lidar power returns from the clouds. The estimated reflectance of thick boundary layer clouds was basically slightly higher than 0.01 sr^{-1} which was only about 1/10 of the reflectance of vegetated surface. The variations in the cloud structure, cloud top height, and particle size distribution may also affect the precision of the CO$_2$ measurements.
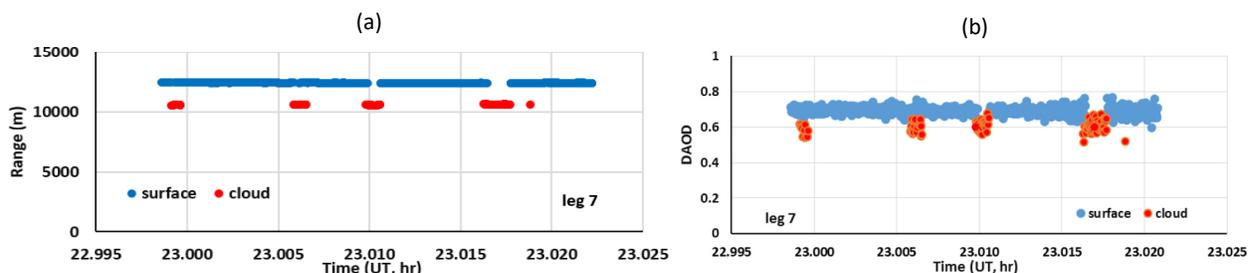
Figure 5-20 Plotted are range (a) and DAOD (b) to the ground of 0.1-s integration of lidar measurements for clear (blue) and low cloud (red) conditions (Lin et al., 2015).

Finally, the LaRC team conducted a comprehensive MFLL ground test on an 860-m horizontal test range at NASA LaRC during July-August 2012 (Lin et al., 2013). Several surface targets with different reflectivities were tested and calibrated. Very good agreement between model predictions and LAS signal measurements for the tested albedos was obtained, which significantly contributes to the evaluation capabilities for space missions (Lin et al., 2013).

5.3.2.5   Near-term Plans

The key areas for the LaRC team near-term measurement development and demonstration plan include maturing low-mass, high-power high-efficiency lasers, optical receiver subsystems, and electronics required for the ASCENDS space mission via the ACES instrument (Obland et al., 2012, 2013, 2017) and further demonstration of the capabilities of CO_2 column measurements in various environmental conditions. The LaRC team is close to achieving the laser power required for the space mission through the ACES program and has developed an achievable path to meet the ASCENDS mission requirements. The CO_2 measurement accuracy and precision over low reflectance rough ocean surfaces and the length of integration period to increase SNR_{DAOD} to required levels were also tested through ocean flights during ACT-America field campaigns. The accuracy and systematic errors in the retrievals of CO_2 column amounts from low and high thin clouds will be assessed using current ACT-America and future flight campaign data sets.

5.3.3   Continuous Wave CO_2 Laser Absorption Spectrometer (LAS)

A team at JPL developed an airborne CO_2 Laser Absorption Spectrometer (JPL CO_2LAS) in the 2002-2006 time frame to demonstrate the airborne IPDA lidar technique as a stepping stone to a capability for global measurements of CO_2 concentrations from space.   The first airborne measurements were conducted in summer, 2006 on a Twin Otter aircraft. The JPL CO_2LAS has flown on the NASA DC-8 since summer, 2010. This instrument utilizes the 2.05µm CO_2 band, which has a band-strength nearly an order of magnitude larger than the 1.57 µm band. This enables probing CO_2 at frequencies suitably displaced from line center such that the IPDA measurement preferentially weights the lower tropospheric CO_2, while maintaining a differential absorption optical depth (DAOD) at its optimum value for maximizing the DAOD signal (Bruneau et al., 2006) and simultaneously minimizing the impacts of sources of bias. The instrument uses a heterodyne detection receiver, which provides efficient photon detection.

5.3.3.1   JPL CO_2 LAS Instrument Description and Data Processing

The CO_2 LAS instrument was developed jointly by JPL and Coherent Technologies, Inc. (later Lockheed Martin Coherent Technologies) (Spiers et al., 2002; Spiers et al., 2011a). The lidar consists of five key subsystems: (1) the optical assembly, (2) the control electronics unit, (3) the control software unit, (4) the thermal management assembly, and (5) the signal processing / data acquisition electronics. In operation, the optical assembly is completely autonomous, no adjustments are required. The optics alignment has not been adjusted since the instrument integration and tested in 2004.

The CO_2 LAS transceiver approach utilizes heterodyne detection, implementing a narrow bandwidth receiver, with frequency-stabilized narrow-linewidth laser transmitters and local oscillators. The lasers are diode-pumped Thulium/Holmium (Tm/Ho)-doped Yttrium Lithium Fluoride (YLF) crystal lasers (McGuckin and Menzies, 1992), that emit in the 2.05 µm spectral region. The transceiver consists of two separate transmit/receive channels for the on-line and off-

line measurements. The off-axis beam expanding telescopes for each channel are identical in size and configuration. The transmitter frequencies are stabilized with respect to a selected CO_2 absorption line. Each channel has a dedicated heterodyne detector, and a continuous-wave (cw) single frequency laser which acts both as the transmit laser and the local oscillator for heterodyne detection of the return signal. The transceiver also includes a separate low-power cw laser that provides a reference for frequency offset-locking of the on-line and off-line lasers.

A comprehensive study of candidate CO_2 absorption lines was conducted considering (1) minimizing interference from water vapor lines, (2) minimizing susceptibility to atmospheric temperature profile uncertainty, (3) optimizing line strength (Menzies and Tratt, 2003). The R(30) line of the (2001)III ← (0000) band, with line center at 4875.749 cm^{-1}, was selected based on this evaluation. The choice of R(30) as the optimum line in the 2.05-μm band has been validated in recent more comprehensive wavelength optimization studies (Caron and Durand, 2009). The instrument contains an onboard low pressure CO_2 gas absorption cell for locking the reference laser to the CO_2 R(30) line. The on-line laser is tunable over a range of several Gigahertz (GHz) with respect to the fixed reference laser frequency. A few mW from the on-line laser is tapped off to act as the local oscillator (LO) for heterodyne detection of the return on-line signal. The offline laser channel configuration is similar.

Offset locking is accomplished using wide-band photomixers that monitor the beat frequencies between the outputs of the on-line and off-line lasers with respect to the reference laser. Dating from the time of first integrated performance tests, the on-line and off-line lasers have been tuned to the same offset frequencies with respect to the CO_2 R(30) line center, namely +4.00 GHz and -15.72 GHz respectively.

A frequency offset is required between the return signals and their corresponding local oscillators for heterodyne detection. By pointing the transmit beams at a known offset from nadir, the return signals are Doppler shifted by the aircraft velocity, eliminating the need for a frequency shifting device in the instrument. The aircraft pitch angle adds to the fixed off-nadir pointing angle and is taken into account both in mounting hardware and retrieval software.

The transceiver assembly is mounted to a 2-sided optical bench, with custom-designed mounts for the optical components. This optical bench is edge-mounted to a base plate, as pictured in Figure 5-21 (a). In operational configuration, the optical bench is in a near-vertical plane, and a cover is fastened to the base plate. Thus, the assembly is contained within an enclosure with electrical feed-throughs and optical windows (Figure 5-21 (b)). The baseplate/enclosure assembly includes vibration isolation. With the cover in place, the transceiver subsystem is ready to be mounted to an aircraft interface frame. In the DC-8, it is mounted in the rear cargo bay.

The key airborne LAS instrument parameters are summarized in Table 5-5 below.

(a)   (b)
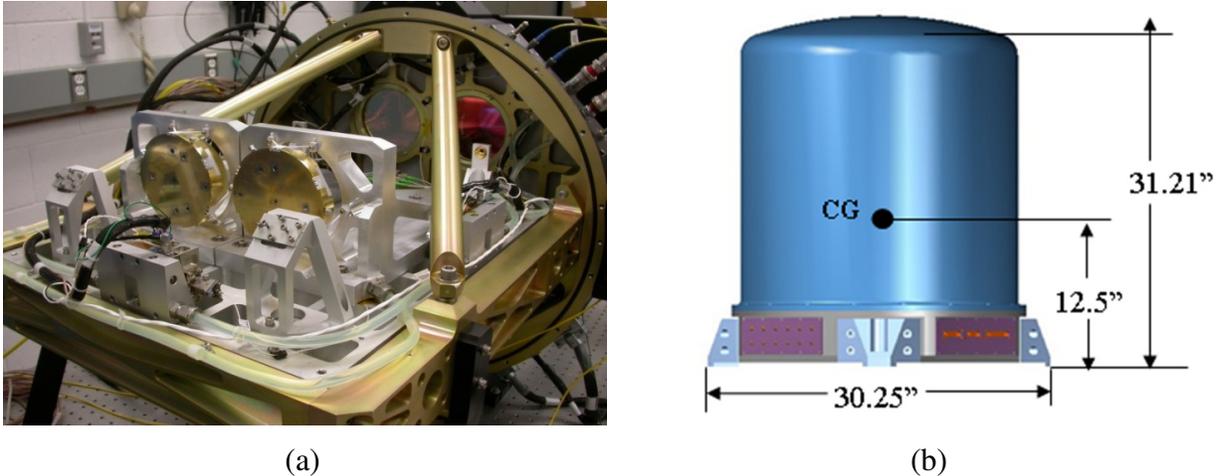
Figure 5-21 (a) LAS with optical bench horizontal, telescope side up, base plate in background. (b) LAS transceiver in hermetically sealed enclosure.

5.3.3.2   Signal Processing and Data Analysis

A description of the CO_2 retrieval algorithm is published in Jacob et al. (2018). The approach to data analysis and CO_2 retrieval is as follows. The LAS on-line and off-line signals are sampled, stored, and processed to calculate for various atmospheric layers the values of:

$$ln\,(P_{off}/P_{on}) = (2\,DAOD) \qquad\qquad (5\text{-}5)$$

P_{off} and P_{on} are the estimates of return power at the off-line and on-line frequencies, properly normalized by the transmitted laser powers at these two frequencies. These results, derived from the measurements, are compared with forward model predictions of *DAOD*. Prior to 2014 the LBLRTM (Line-By-Line Radiative Transfer Model) provided by the Atmospheric and Environmental Research Inc. (AER) was used in the forward model. This was replaced by AER's MonoRTM due to its improved handling of pressure broadening of CO_2 lines due to water vapor. The spectroscopic line database input to these models is based on HITRAN 2012, with improved H_2O line parameters in the 5 cm^{-1} region centered at 4875.5 cm^{-1}. The forward model also includes the atmospheric meteorological data needed to provide the altitude-dependent weighting function. The on-board GPS system provides the aircraft position knowledge (including altitude with respect to the geoid). Lacking an on-board co-aligned laser altimeter, the surface elevation is obtained using the Shuttle Radar Topography Mission (SRTM) digital elevation database along with the laser pointing angle, updated at 10 Hz rate.

The CO_2 retrievals are aggregated at 0.5 to 5 sec intervals depending on the flight altitude and the 2 μm surface reflectance. The sampling of the offline and online signal power is normally at 30 Hz (33 msec intervals). Laser range to ground averages over the 0.5 to 5 sec intervals are critical inputs to the forward model. In averaging range, the variation of 2 μm surface reflectance within these intervals must be accounted for. Using the offline signal power as a proxy for reflectance, we compute offline power at the 33 ms intervals, subsample SRTM elevation at that same rate, and compute a "reflectance weighted" average elevation with the weights given by the subsample offline power estimates.

Table 5-5 JPL Airborne LAS Instrument Parameters

Parameter	Value
CO_2 line center frequency	4875.749 cm^{-1}
JPL LAS ON frequency JPL LAS OFF frequency	4875.882 cm^{-1} 4875.225 cm^{-1}
Laser output power	100 mW
Transmit/Receive Telescope apertures	10 cm diameter
Receiver FOV (diffraction limited)	60 μrad
Photomixer type	InGaAs
Receiver heterodyne frequency window	9-21 MHz
Signal Digitization	16 bits / 60 MHz

The normalized return signal power values are determined as follows. The Intermediate Frequency (IF) photomixer signals from the on-line and off-line channels are amplified and are bandwidth limited to a nominal 9-21 MHz window. The signals from each channel are digitized with a 60 Msamples/sec, 16-bit digitizer. The samples are transformed into the spectral domain using a Fast Fourier Transform (FFT) operation followed by conversion to periodograms. The return power is proportional to the size of the signal in the frequency space of the periodogram. On-line and off-line signal power calculations are performed, followed by normalization steps to account for variations in slant path length between instrument and footprint on the surface, small variations in laser power, or other small drifts in overall system gain. System stability is quantified through the use of "validation" data collection periods, when an on-board backscattering validator subsystem is inserted into the instrument field-of-view, intercepting the transmitter beams.

5.3.3.3   Cloud Detection and Filtering

To obtain adequate coverage, (weighted) column CO_2 mole fractions must be collected in the presence of broken clouds. Clouds in the FOV reduce the path length, and if not recognized, bias the CO_2 retrieval. In cases of scattered cloud cover, breaks or holes permit soundings down to the surface some fraction of the time. The small transmitter footprint of the lidar provides a capability to acquire retrievals in such circumstances. If the lidar provides time-of-flight to the backscatter source (e.g. a range-gated pulsed system, or a Frequency-Modulated/Continuous Wave (FM/CW) system), any sources of backscatter other than that which occurs at the expected delay time corresponding to range to the surface can be set aside or filtered out. With the current implementation of our airborne lidar, we do not have this capability. However, we do employ alternative methods to detect and filter out the backscatter signals from clouds in the FOV (field of view). The following methods are very effective in identifying a large variety of clouds.

- Heterodyne detection provides capability to see both intensity and spectral properties of backscatter signal;

- Cloud motion provides a discriminating tool, both broadening and shifting the backscatter signal in the spectral/frequency domain;

- Clouds in FOV also cause shortening of atmospheric sounding path length – reduced values of retrieved CO_2 column.

These provide the basis for the algorithm's cloud filtering. The spectral broadening of the heterodyne signal is typical of backscatter from cumulus and stratocumulus (Menzies et al., 2014).

5.3.3.4   CO₂ Retrieval in Vicinity of an Urban Area (Summer 2014 campaign)

The map in Figure 5-22 shows the CO_2 weighted column mixing ratio retrieved for a box pattern flown at an altitude of about 16 kft above Indianapolis, Indiana (IN). This was on 9/3/2014 during the morning commuter period with heavy traffic emissions as well as stationary source emissions. The wind speed of about 6 m/s and direction, indicated by the yellow arrow, are derived from GEOS5/MERRA and NOAA's Indiana Flux Study (INFlux) HALO Doppler wind lidar.

The observed CO_2 plume downwind of the urban area, along with the prevailing wind speed and direction, enables determination of emission rate. The plume exhibits an average increase of about 2.5 ppm over the baseline CO_2 level across an along-track segment of about 25 km length. Considering the prevailing wind direction perpendicular to the flight track in the lowest 2 km of the atmosphere, and a simple box model between the aircraft altitude and the surface modified by the weighting function, this corresponds to an emission rate of approximately 12×10^5 kg C hr^{-1}. In comparison, estimates from the Open-source Data Inventory for Anthropogenic CO_2 (ODIAC) with hourly scaling factors from the Carbon Dioxide Information Analysis Center (CDIAC) predict a mid-day emission rate of 8×10^5 kg C hr^{-1} upwind of the flight segment. Likely factors that contribute to the difference in the retrieved emission rate and the ODIAC prediction are the use of the simple box model with the relatively coarse 25 km horizontal resolution of MERRA, and the application of the diurnal scaling factors to ODIAC that exhibit just a single mid-day peak and might not accurately capture the impact of the urban commuter traffic patterns. The smaller CO_2 plume observed in the vicinity of I-865 to the northwest of Indianapolis is consistent with the emission model assuming the plume is caused by ~12 km of upwind on-road emissions due to relatively constant traffic along that corridor during the morning commute period.
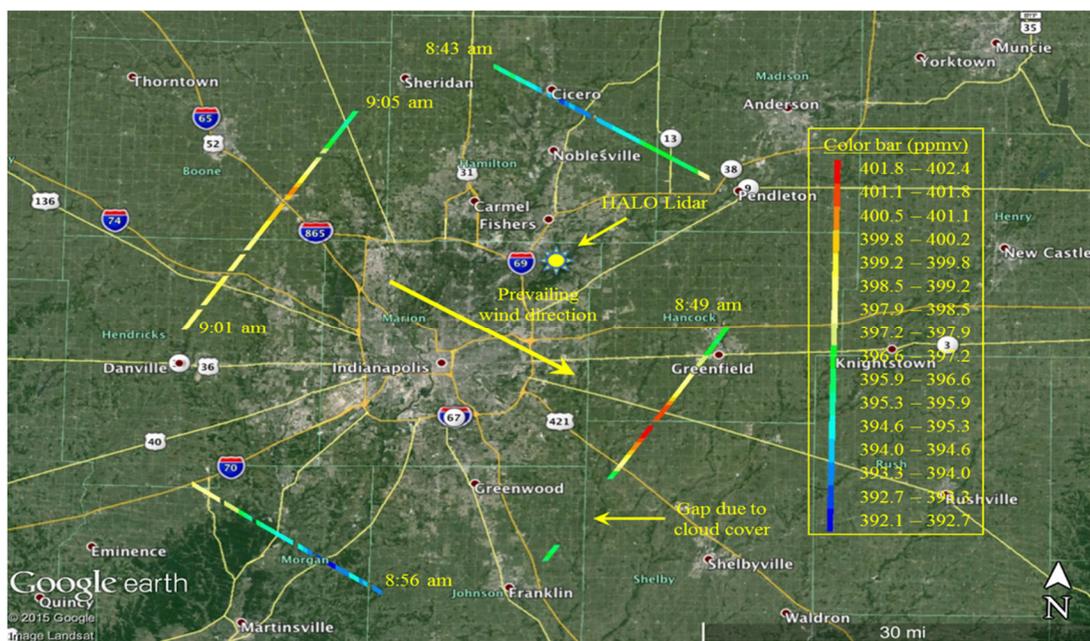
Figure 5-22 Retrieval of CO$_2$ weighted column mixing ratio along box pattern flown around Indianapolis, IN on 9/3/2014.

5.3.3.5   Observation of CO₂ Drawdown (Summer 2011 campaign)

The August 10, 2011 flight's primary objective was the upper Midwest, arriving over the target area (Iowa) near mid-day, with the expectation that CO$_2$ drawdown in the boundary layer would be observed due to the photosynthetic assimilation by crops over this large-scale agricultural region. The flight to the Midwest included a long transit at fixed pressure altitude starting near Denver, Colorado (CO) and continuing to the vicinity of the West Branch Iowa (WBI) Tower in Iowa. We encountered clear atmosphere over the Denver area, with scattered fair weather cumulus appearing over the eastern Colorado plains. Cloud fraction steadily increased as the flight ground track moved into Nebraska.

The JPL LAS data clearly indicated a steady decrease in CO$_2$ weighted column mole fraction (or mixing ratio) en route to Iowa beginning with the overflight of the Eastern Colorado high plains (Spiers et al., 2011b; Spiers et al., 2012; Menzies et al., 2014). The observed weighted-column CO$_2$ mixing ratio is shown in Figure 5-23. The SRTM DEM data were used to obtain the along-track elevation. The atmospheric meteorological data that were incorporated into our retrieval algorithm came from the MERRA (Modern Era Retrospective Analysis for Research and Applications) products available from the NASA Goddard Space Flight Center GMAO (Global Modeling and Assimilation Office) (Reinecker et al., 2011).

The record shown in Figure 5-23 starts a few km south of the Denver International Airport, and the distance covered from left to right is 340 km. The averaging corresponds to about 4 km along-track resolution for the plotted data. The flight altitude CO$_2$ readings from the in situ Picarro instrument measurements trended lower over a narrow range from approximately 389.5 to 387.5 ppmv during the period of time plotted. Nadir camera imagery shows a transition to agricultural activity (occasional crop circles) beginning at 20.02 UTC, with increasing land use for agricultural activity occurring as the ground track continues eastward. Crossing into Nebraska occurred near 20:13

105

UTC. Gaps in the data are due to presence of clouds. The ground track is in the middle of Nebraska at the end of the plotted data. By this time the cumulus coverage had increased, with corresponding decrease in the durations of the clear air gaps between clouds, precluding the continuation of high precision retrievals. The conclusion that the observed steady decrease in column CO_2 abundance is due to drawdown is supported by later measurements in Iowa during a traverse over the West Branch Iowa (WBI) tower at 10 km altitude, where in situ vertical profile data obtained near the WBI tower from the on-board Picarro instrument indicated boundary layer CO_2 mole fraction values ~365 ppm, and free troposphere values averaging 382 ppm. Mid-day CO_2 levels in this region during early August are among the lowest in North America due to strong uptake by corn and other crops (Denning et al., 1996; Miles et al., 2012).
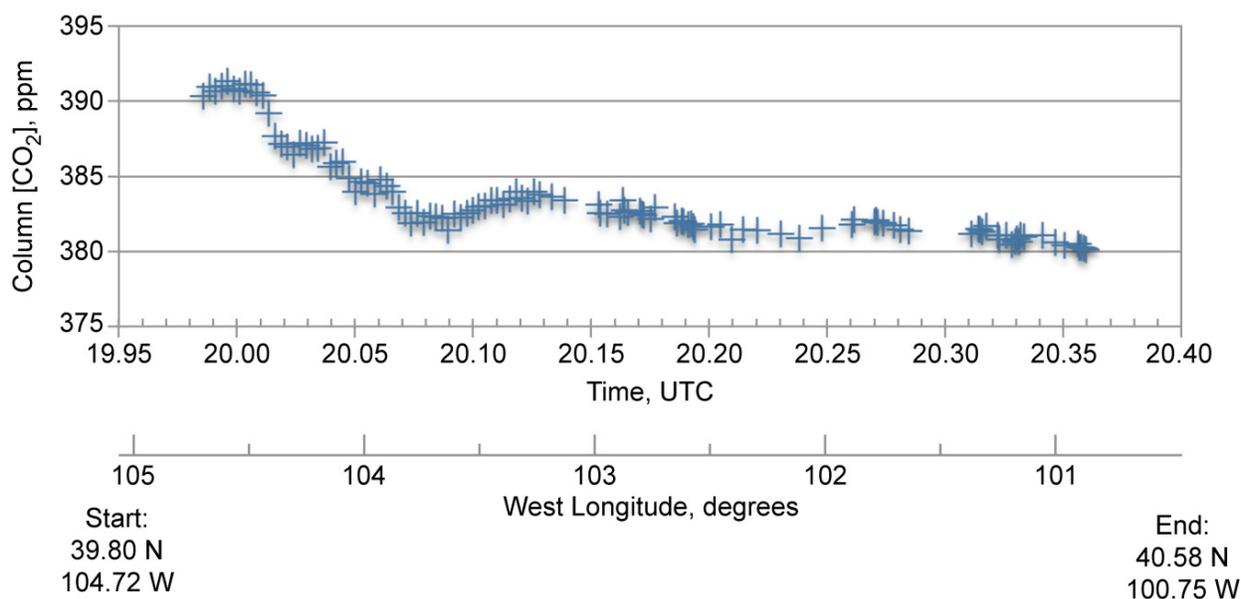
Figure 5-23 LAS weighted column CO_2 mole fraction retrievals during flight over Central US. The segment from Denver, Colorado vicinity to middle of Nebraska, was flown on August 10, 2011. (Locations: 39.80 N / 104.72 W at 19.98 UTC; 40.58 N / 100.75 W at 20.37 UTC. Distance travelled: 310 km.) The 1-sigma precision level for this retrieval is equivalent to 1.1 ppm. The steady decrease in column CO_2 is due to mid-day drawdown in the atmospheric boundary layer.

5.3.3.6 Quantification of Power Plant CO₂ Emission Rate

On August 9, 2011, the DC-8 flew a northward flight segment at 15,000 foot pressure altitude whose ground track was downwind of the 4-Corners Power Plant, located in San Juan County, New Mexico (36.690 N, 108.483 W). The JPL LAS data indicated multiple spatially distinct plumes emanating from the power plant complex (Spiers et al., 2012; Menzies et al., 2014). The ground track was within a few hundred meters of the plant site. The plant has five coal-fired units, with spacing such that the emissions appear to originate from three sources. The source encountered first during this flight leg (leftmost in Figure 5-24) is the tall stack. Figure 5-25 is a plot of the weighted column CO_2 mole fraction during the pass, with variable along-track resolution. The along-track resolution is 15 m during the 1-km segment immediately downwind of the plant.

A simple box model estimate of the power plant CO_2 emission rate during the mid-day time of this flight leg can be made by calculating the CO_2 mass crossing a plane of height equal to the aircraft

height above ground (3135 m) and ground track segment length of 1.0 km for which the mole fraction is above the background value. The speed of the wind carrying the CO_2 plume across the plane at this time, 2.15 m s^{-1}, is obtained from the MERRA reanalysis. The atmospheric temperature in the lowest MERRA layer at this time was 299 K. Taking the weighting function into account, and assuming the plume is within the first 200 m above the surface, where the weighting function is nearly constant, a source of 470 kg s^{-1} emission rate is derived, based on the observed integrated weighted column increment (Menzies et al., 2014).

Figure 5-24 Four-Corners Power Plant, New Mexico, U.S showing 3 main clusters of stacks. From left to right, starting with the tall stack (cluster #1): Clusters #1 - #2 separation ~400 m; Clusters #2 - #3 separation ~150-200 m.

The Four Corners Power Plant complex emits in the neighborhood of 14 x 10^6 metric tons of CO_2 annually, according to a 2011 study prepared by RMT, Inc. for the California Public Utilities Commission (RMT, 2011). This corresponds to an average CO_2 emission of 440 kg s^{-1}. We have a measurement that corresponds closely with the average emission rate. This demonstrates the potential capability of the IPDA measurement method.
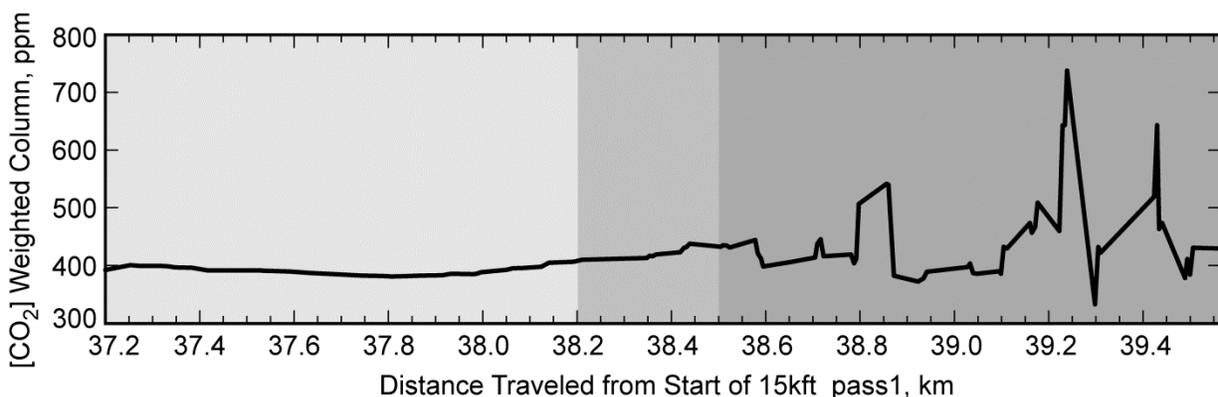
Figure 5-25 Weighted column CO_2 retrievals during flyby of the Four-Corners Power Plant at 15 kft pressure altitude along a south-to-north track and a few hundred meters downwind. The shading corresponds to three spatial resolution segments: (1) 37.2 – 38.2: 150 m along track resolution; (2) 38.2 – 38.5: 50 m resolution; (3) 38.5 – 39.5: 15 m resolution.

5.3.3.7   CO₂ Retrievals over Snow-Covered Surfaces

Assessment of the capability to retrieve CO_2 weighted column mole fraction over snow-covered surfaces is important in ASCENDS planning.   Snow reflectance at the 1.57 and 2.05 µm wavelengths is relatively low (Aoki et al., 2000), but quantitative values of lidar directional reflectance at these wavelengths did not exist prior to the ASCENDS campaigns of 2011 and 2013. These campaigns offered the opportunity to measure reflectances of a variety of snow-covered surfaces. The basis of our 2.05 µm snow reflectance derivation is the linkage that we have to ocean surface reflectance as measured over the clear Pacific Ocean off the coast of California.   The CALIPSO mission provides by far the largest study of lidar backscatter from the ocean surface, and we rely on data from Hu et al. (2008) for determination of the surface directional reflectance (backscatter) over this region of the Pacific Ocean, given the estimated surface wind. Comparisons were made of range-corrected off-line return signals from the Pacific Ocean flight and the 8/07/2011 flight over the snow-capped British Columbia coastal mountains. The LAS instrument radiometric stability is good to within 10% from flight-to-flight, and flight-to-flight and in-flight variations are monitored with the internal Validator. This allowed the determination of surface reflectance during the flight segment over the British Columbia (BC) coastal mountains, as in Figure 5-26. In this case the snow backscatter averaged over the ground track is ~0.012 sr⁻¹ (Menzies et al., 2014).
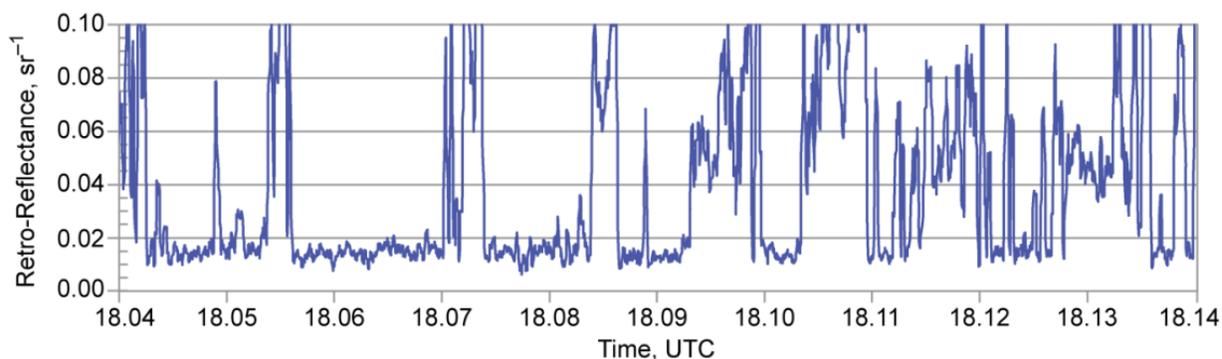
Figure 5-26 LAS measured surface reflectance during a portion of the "snowline out" flight segment over the British Columbia Coastal Mountains, August 7, 2011 at 2.05 µm wavelength (in units of sr-1). Snow covered areas (low backscatter) were mixed with patches of bare rock, dirt, alpine flora (high backscatter). Time duration from left to right: 0.1 hr (6 min).

Snow-covered terrain was also encountered on the March 7, 2013 flight to the upper Midwest. The low reflectance over snow-covered land was often interrupted by road crossings, structures, and patches of bare land that show larger reflectances. We found during this flight and the March 5 flight that targeted the Colorado Rocky Mountains a range of values for snow reflectance (i.e., lidar directional reflectance), with values at the 2.05 µm lidar wavelength from 0.07 to 0.2 sr⁻¹. (Spiers et al., 2016).

The flights of the JPL CO_2 Laser Absorption Spectrometer have enabled us to assess and demonstrate the performance of a 2.05 µm IPDA lidar using a heterodyne detection receiver to obtain CO_2 retrievals for a variety of atmospheric and surface conditions. Measurements made during a mid-day flight over the US Upper Midwest clearly indicate that we can observe the CO_2 drawdown due to photosynthesis at the surface. Measurements made in the vicinity of the Four Corners power plant demonstrate the capability to resolve the plumes with high spatial resolution and estimate the source emission rate. We demonstrated the capability to measure CO_2 over snow-

covered surfaces in the Upper Mid-West during winter, 2013, and we observed CO_2 bulges/plumes that appear to be associated with developed areas that were encountered along the flight tracks. The 2-μm weighting function, which gives added weight to the atmospheric boundary layer (ABL), enables enhanced sensitivity to sources and sinks that alter the CO_2 mole fraction in the ABL.

5.3.4   Pulsed 2-μm CO₂ IPDA Lidar

Pulsed 2-μm lasers have narrow linewidths and can have high energies that make them well suited as transmitters for CO_2 IPDA lidar. The strong 2.0-μm CO_2 lines have low temperature sensitivity with weighting functions that can be strongly peaked near the surface. NASA Langley Research Center (LaRC) has been involved for over 20 years in developing pulsed 2-μm lasers and lidar technologies (Singh et al., 2015a). Recently we have applied them to the measurement objectives of ASCENDS (Koch et al., 2008; Refaat et al., 2010, 2011, 2015a, 2016a; Yu et al., 2003, 2012, 2017). This section describes the development of ground-based Differential Absorption Lidar (DIAL) and airborne IPDA lidar systems for CO_2 measurements using the 2-μm wavelength.

5.3.4.1   Single-Pulse 2-μm CO₂ DIAL Demonstration

Range resolved CO_2 DIAL measurements, using single-pulse 2-μm laser, have been demonstrated using both heterodyne and direct detection approaches (Koch et al., 2008; Refaat et al., 2010, 2011). For these initial demonstrations, the wavelength of the output laser pulses alternated between on-line and off-line positions at a 5-10 Hz rate. Using heterodyne detection, CO_2 DIAL measurements were attempted with a 90 mJ, 140 ns, 5 Hz pulsed Ho:Tm:LuLiF laser transmitter (Koch et al., 2008). The laser used a wavelength controller to precisely tune and lock the operating wavelength at any desired offset, up to 2.9 GHz, from the center of the R22 CO_2 absorption line. Once detuned from the line center, the laser wavelength is actively locked to keep the wavelength within 1.9 MHz. The laser transmitter was used with a coherent heterodyne receiver for measurements of CO_2 concentration using aerosol backscatter.

Detector technology usually limits the CO_2 DIAL profiling capability at 2-μm. Therefore, 2-μm phototransistors have been developed and integrated for the first time in lidar applications and, using direct detection, another 2-μm CO_2 DIAL system was developed at NASA LaRC using the same transmitter (Refaat et al., 2010, 2011). Field experiments were conducted at West Branch, Iowa, for evaluating the system for CO_2 measurement by comparing with NOAA in-situ sensors located on the WBI tower at 31, 99 and 379 m altitudes. Results demonstrated the capabilities of the DIAL system in profiling atmospheric CO_2 using the 2-μm wavelength with both range resolved and integrated column content (Refaat et al., 2010).

The results from single-pulse 2-μm DIAL experiments highlight several desirable improvements to enhance their CO_2 measurement capability. First, the selected CO_2 R22 absorption line demonstrated high water vapor interference that coexists at the same operating wavelength. Operating on the CO_2 R30 line potentially increases the lidar sensitivity while reducing the impact of water vapor interference and temperature sensitivity. In addition, operating with single-pulse, 5-Hz transmitter, causes a 200 ms separation period between the on-line and off-line pulse, which results in inconsistent atmospheric sampling volume between the two wavelengths. This led to the development of the higher pulse rate double-pulse 2-μm laser transmitter. In the double-pulse

operation, two pulses are generated with two different wavelengths. Thus, only one laser is required to generate the on-line and off-line pulses for DIAL/IPDA profile or column measurement of CO_2.

5.3.4.2   Airborne Double-Pulse CO₂ IPDA Lidar

Because it relies on strong reflection from hard targets, the IPDA lidar approach provides higher signal-to-noise ratio measurement compared to the range-resolved DIAL that depends on atmospheric backscatter signals. Double-pulsed 2-μm lasers have been demonstrated with energy as high as 600 mJ and up to 10-Hz repetition rate (Yu et al., 2003). The double-pulse CO_2 IPDA laser transmitter is based on Ho:Tm:YLF high-energy 2-μm pulsed laser technology. This laser is side pumped using diode arrays at 792 nm. The laser configuration is capable of generating two pulses, separated by 150 to 200 μs, with 100-mJ and 30-mJ energies at 10 Hz. For airborne applications, double-pulse operation allows maximizing the overlap between the on-line and off-line footprint on the ground resulting in sampling the same atmospheric volume. This feature enhances the IPDA measurement by reducing sampling error. The design of the double-pulse laser transmitter includes fixed off-line and tunable on-line wavelengths. A wavelength control unit adjusts and locks the wavelength of the on-line pulse using injection seeding in reference to a gas cell. Changing the on-line wavelength setting results in changing the column weighting function. Therefore, tuning the transmitter weights the CO_2 column measurement toward the surface, within the boundary layer or lower troposphere (Refaat et al., 2016a; Singh et al., 2017b). The pulses are transmitted coaxially with the receiver telescope.

The receiver telescope is a custom designed Newtonian with 0.4-m diameter hyperbolic aluminum primary mirror. The primary focuses the return radiation on to a 300-μm spot diameter. This is compatible with the sensitive area of extended-range InGaAs pin photodiode detectors. An aft-optics assembly is used to split the telescope return into high and low signals channels (10-90%) to two detection channels. A detector and a commercial trans-impedance amplifier form a detection channel. After amplification, the lidar signals were digitized and stored using a data acquisition unit. The data acquisition unit is based on two 200-MHz, 12-bit digitizers, for the lidar return and a 500-MHz 10 bit digitizer for the laser energy monitor (Refaat et al., 2015a). The design of the 2-μm double-pulse IPDA lidar is compatible with a small research aircraft such as the NASA B-200. The mechanical design of the system is compact to allow aircraft integration, along with any other supporting instrumentation, including a CO_2 validation sensor. Figure 5-27 shows the design concept of the transmitter-telescope-receiver integrated structure of the CO_2 IPDA lidar, as well as system installation inside the B-200 aircraft. The integration includes an optical port modified and installed to accept the lidar system (Singh et al., 2014).
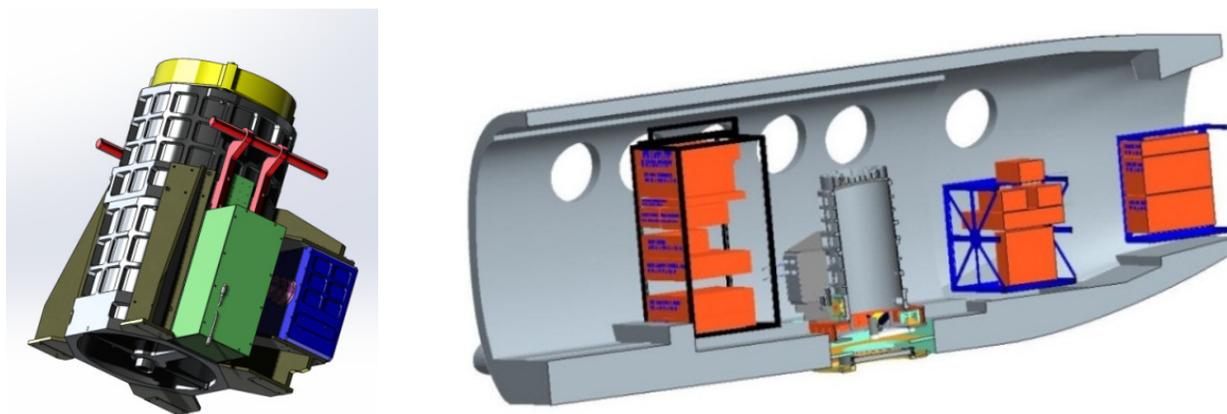
Figure 5-27 (Left) Illustration of 2-μm, double-pulsed IPDA lidar for airborne CO_2 measurements. (Right) Integration of the lidar instrument inside the NASA B-200 aircraft.

The 2-μm double-pulse IPDA lidar airborne testing was conducted during ten daytime flights, spanning more than 27 hours, during March 20, 2014 through April 10, 2014. Testing included different operating and environmental conditions, such as different flight altitudes, and different ground target conditions including vegetation, soil, ocean, snow and sand, and different cloud conditions (Singh et al., 2014; Refaat et al., 2016a, 2018). On April 5, 2014, the NASA B-200 flight coincided with a NOAA in situ air sampling flight. The IPDA lidar sampled the same geographical location as the NOAA flask samples over the Atlantic Ocean off the east shore of New Jersey (NJ). NOAA Earth System Research Laboratory provided the CO_2 air sampling data, which were used to predict the IPDA lidar measurements and to evaluate measurement sensitivity and bias errors. Figure 5-28 compares the CO_2 differential optical depths, obtained from the IPDA lidar measurements and modelled using NOAA data. The IPDA signals and their variation with altitude compare well with predicted model results. IPDA CO_2 column measurement compares well for different altitudes. In addition, off-line testing was conducted to evaluate the IPDA systematic and random errors. Analysis shows an altitude-independent differential optical depth offset of 0.0769. This compares well with the predicted value of 0.0761. With a 10-s shot average, CO_2 differential optical depth measurement of 1.0054±0.0103 was retrieved from 6-km altitude and 4-GHz on-line operation. As compared to CO_2 weighted-average column dry-air volume mixing ratio of 404.08 ppm, derived from air sampling, IPDA measurement resulted in a value of 405.22±4.15 ppm with 1.02% uncertainty and 0.28% bias. IPDA ranging resulted in a measurement uncertainty of <3 m (Refaat et al., 2016a).
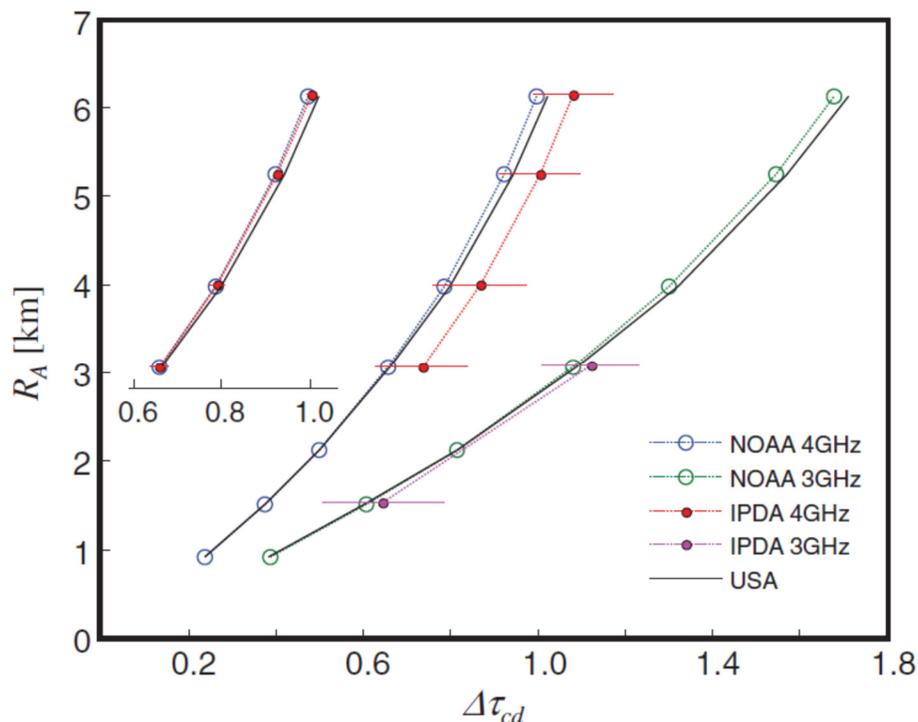
Figure 5-28 Comparison between the 2-μm double-pulse IPDA lidar CO_2 differential optical depth measurement and simulation conducted through NOAA flask sample data at different altitudes and operating conditions. Results indicate the agreement of both profiles with a consistent instrument systematic error of 0.0769 for the 4 GHz data, which is corrected in the inset of the figure. The horizontal lines mark the per-shot sensitivity limits for each measurement and the 100 shots (10 s) averaged for the inset.

5.3.4.3 Airborne Triple-Pulse CO₂ and H₂O IPDA Lidar

Through support from the NASA ESTO Office, a 2-μm triple-pulse IPDA was developed at LaRC (Refaat et al., 2015a; Singh et al., 2017b). Through wavelength tuning, this triple-pulse IPDA allows simultaneous and independent measurement of water vapor (H_2O) and CO_2 differential optical depths from an aircraft. This system is an upgrade to the 2-μm CO_2 double-pulse IPDA lidar. The main upgrade was in the 2-μm laser transmitter. The triple-pulse IPDA lidar is a direct detection system based on a state-of-the-art high repetition rate (50 Hz), high-energy (80 mJ), triple-pulse, 2-μm laser transmitter. The three pulses are separated by 150 to 200 μs and are injection seeded with three different wavelengths. The laser crystal used for this design is a co-doped Ho:Tm:YLF, which exhibit a long fluorescence lifetime. The long lifetime allows the generation of a burst of Q-switched pulses using a single pump pulse. The crystal is pumped using 792 nm laser diode laser. For operation at 50 Hz pulse rate, a trade was made to achieve lower thermal load at the expense of laser performance, in terms of doping concentration and output energy splitting between the pulses. The oscillator is a 1-m long ring cavity using 6 mirrors. One of the mirrors is mounted on a piezo-electric transducer to adjust the resonator length for injection seeding operation. Double-end pump configuration was achieved by dividing and routing the pump radiation toward

two crystals. Operating the laser with multiple pulses has several advantages including raising the overall efficiency and reducing the thermal load (Petros et al., 2018).

The 2-μm triple-pulse IPDA lidar requires three stable wavelengths that have narrow line width and high spectral purity. The seed source is based on distributed feedback semiconductor laser diode, operating at a single wavelength with narrow line width (Bagheri et al., 2015). Pound-Drever-Hall technique is used for locking the seed laser using a CO_2 reference cell. This results in less than ±650 kHz jitter (Refaat et al., 2016a). An electro-optics modulator is used to generate three wavelengths, that are referenced to the CO_2 R30 line center-locked wavelength. Focusing on simultaneous and independent H_2O and CO_2 measurement condition, the selected wavelengths correspond to 32, 6 and 16 GHz frequency offsets from the R30 line-center. The three frequencies are switched, to seed the oscillator within each pulse, using ramp and fire technique through the piezo-electric transducer.

The triple-pulse IPDA receiver is based on that of the double-pulse lidar. Updates include incorporating a HgCdTe electron-initiated avalanche photodiode (e-APD) detector array to the low signal channel. This was achieved by focusing the radiation on a multi-mode fiber that is routed to e-APD enclosure. The e-APD is configured in a 4×4 array with 80-μm square pixel element. The output of each pixel can be selectively added to produce a single summation signal. For this IPDA the return signal is focused on the center 2×2 pixels. The detector operates at a temperature of 77 K. Using high bias reduces the detector's average NEP to 1.4 fW/Hz$^{1/2}$ per pixel, with 6 MHz electronic bandwidth. The e-APD detection system was developed by Goddard Space Flight Center (GSFC) and was utilized for lidar applications at 1.6-μm (Beck et al., 2014; Sun et al., 2017b).

The data acquisition system uses two 2-channel, 12 bit, 1 GS/s digitizers. One digitizer is assigned for transmitted energy monitors and the other is for the lidar returns. The transmitted pulses are acquired using two detectors the first detector is an InGaAs pin detector for energy monitoring and the second is a fast photo-electro-magnetic (PEM) detector for monitoring the seeding performance. Data acquisition software allows real-time monitoring and processing of the IPDA signals (Singh et al., 2017b; Petros et al., 2018).

Ground and airborne testing of the 2-μm triple-pulse IPDA lidar airborne was conducted during December 2017 through March 2018. The primary objective of the ground test was to integrate the various sub-systems of the IPDA and align the instrument. This was done in a mobile lidar trailer. The lidar is mounted in a nadir configuration, with a 0.6 m diameter mirror set at 45° that steers the beam for horizontal operation toward calibrated targets (900 m). The primary product of the IPDA lidar is the optical depth, which is listed in Table 5-6. The table shows the results of a 2.5 minute record (7500 shots) with equal pulse energy distribution of 11 mJ for all three pulses. The listed column average dry mixing ratios were obtained from the IPDA measurements and meteorological data obtained from the Chemistry and Physics Atmospheric Boundary Layer Experiment (CAPABLE) site. (Singh et al., 2014). The IPDA lidar was integrated into the NASA B-200.

Table 5-6 Summary of the 2-μm Triple-Pulse IPDA Lidar Ground Testing Conducted at LaRC

	CO₂	*H₂O*
Differential Optical Depth		
Single shot	0.0955 ± 0.0215	0.1408 ± 0.0361
50 shots	0.0986 ± 0.0049	0.1384 ± 0.0182
500 shots	0.0987 ± 0.0015	0.1382 ± 0.0134
Met. Model	0.1045 ± 0.0001	0.1759 ± 0.0005
US Standard	0.1029	0.1866
Column Dry-air Mixing Ratio		
Single shot	392.3 ± 71.9	5057.8 ± 1398.8
50 shots	436.9 ± 19.8	5037.1 ± 673.2
500 shots	425.9 ± 6.0	5353.2 ± 496.6
Met. Model	422.0 ± 0.4	6481.9 ± 17.5
US Standard	422.0*	7750.0

Figure 5-29 shows the IPDA lidar integrated inside the aircraft. The main objective of the airborne testing was to demonstrate the IPDA capability to measure two different atmospheric species using a single instrument. Four flights were conducted for various objectives. The first flight was to verify instrument performance using the highest altitude. The second flight was conducted over ocean targeting clear, broken cloud and cloudy conditions. The third flight was coordinated with NOAA and university of Maryland. The fourth flight was conducted over power plant during day and night. The instrument performance met the design objectives, demonstrating the measurements of CO_2 and H_2O simultaneously and independently from an airborne platform.

 Table 5-7 lists a summary of airborne data sample, shown in Figure 5-30, that was obtained from 7.7 km altitude while flying off the coast of Cape May, NJ.

Figure 5-29 Photographs of the 2-μm triple-pulse IPDA lidar integrated inside the NASA B-200 aircraft.

Table 5-7 Summary of the 2-μm Triple-Pulse IPDA Lidar Airborne Record Shown in Figure 5-30 That Was Conducted at 7.7 km Altitude

	Differential Optical Depth	
	CO₂	*H₂O*
Single shot	0.3692 ± 0.1609	0.1709 ± 0.2124
50 shots	0.3724 ± 0.0224	0.1840 ± 0.0284
500 shots	0.3704 ± 0.0079	0.1864 ± 0.0124
Met. Model	0.4026	0.1853
US Standard	0.3895	0.5623
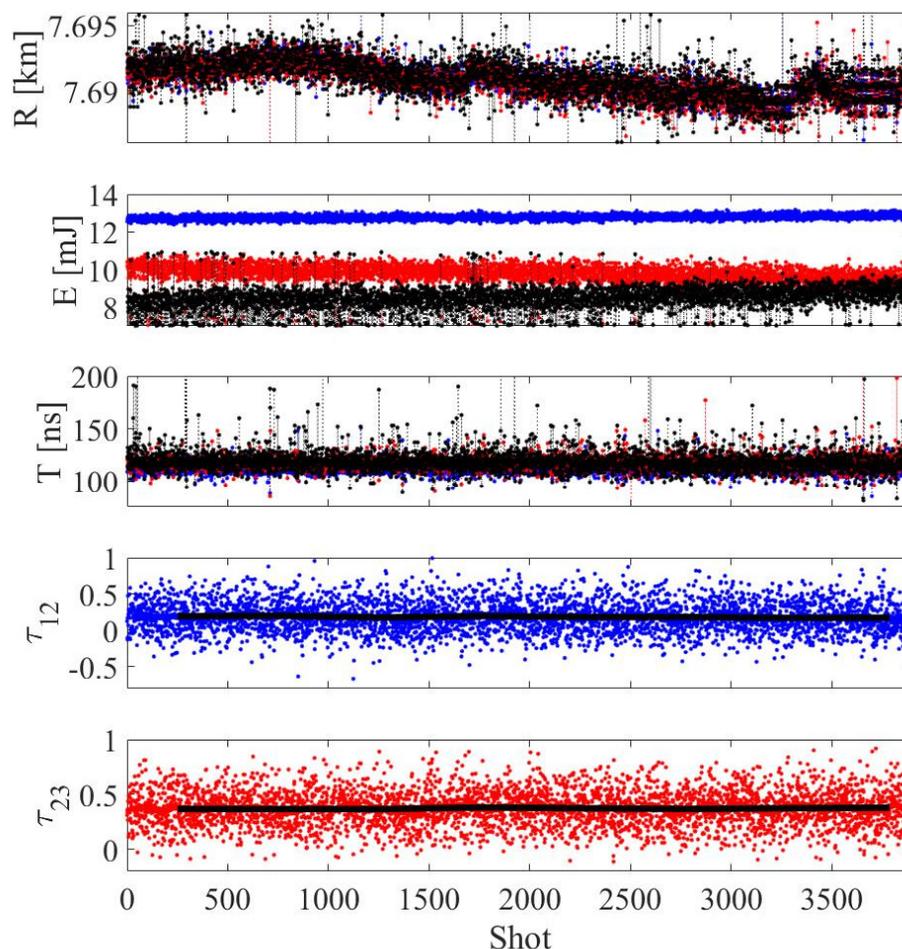
Figure 5-30 Sample of airborne 2-µm triple-pulse IPDA lidar measurements. Measurements include range, R, energy, E, and return pulse width, T in the top three plots, in which color arrangements are blue, red and black for the first, second and third pulses, respectively. Bottom two plots show simultaneous, single-shot H_2O (τ_{12}, blue dots) and CO_2 (τ_{23}, red dots) differential optical depth measurements from the NASA B-200 aircraft. The IPDA lidar operated from 7.7 km altitude over the ocean, east from Cape May, NJ, on February 27, 2018. The solid black curves show 10 second (500 shot) average of the data.

5.4   The 2017 ASCENDS Airborne campaign

The CO_2 Sounder and ACES lidar teams participated in the 2017 ASCENDS airborne campaign. This campaign was flown on the NASA DC-8 in late July and early August 2017 and was planned in coordination with the NASA Arctic-Boreal Vulnerability Experiment (ABoVE) 2017 field campaign. The airborne campaign objectives were to assess the accuracy of airborne IPDA lidar measurements of CO_2 column concentrations (XCO_2), and to extend these lidar measurements to the ABoVE study area in the North American Arctic and over the Arctic Ocean. Eight flights were conducted with XCO_2 measurements from the CO_2 Sounder and the ACES lidar along with in-situ CO_2 measurements made at the aircraft with the AVOCET and Picarro instruments. During the campaign forty-seven spiral-down maneuvers were conducted over locations in California, Nebraska, North Dakota, the Northwest Territories Canada and over Alaska, and the return flight

from Alaska, to Washington, Oregon, Nevada and California. The flight path and campaign summary are shown in Figure 5-31. Since each spiral maneuver allowed comparing the retrievals of XCO_2 from the lidar against those computed from in-situ measured CO_2, this campaign allowed an unprecedented opportunity to assess the lidar measurements of XCO_2 over a diverse set of conditions, including those the North American Arctic, and produced extensive data sets. The southbound transit flight also allowed lidar measurements to the wind-blown ocean surface. Some early results from analyzing the CO_2 Sounder lidar measurements are given in Abshire et al. (2018b) and Allan et al. (2018), and those from analyzing the ACES lidar measurements are given in Meadows et al. (2018) and Obland et al. (2018). These analyses are continuing.

Dates	Name	Duration (hrs)	# Spirals/Descents
20-Jul	Engineering	4.4	3
21-Jul	Calibration	5.6	10
27-Jul	Northbound science/transit	9.4	4
31-Jul	Western NWT	8	6
2-Aug	Northern NWT	6.6	4
5-Aug	South-Central Alaska	6.2	5
6-Aug	Central Alaska	7	7
8-Aug	Southbound science/transit	8.1	8
8	Totals:	55.3	47
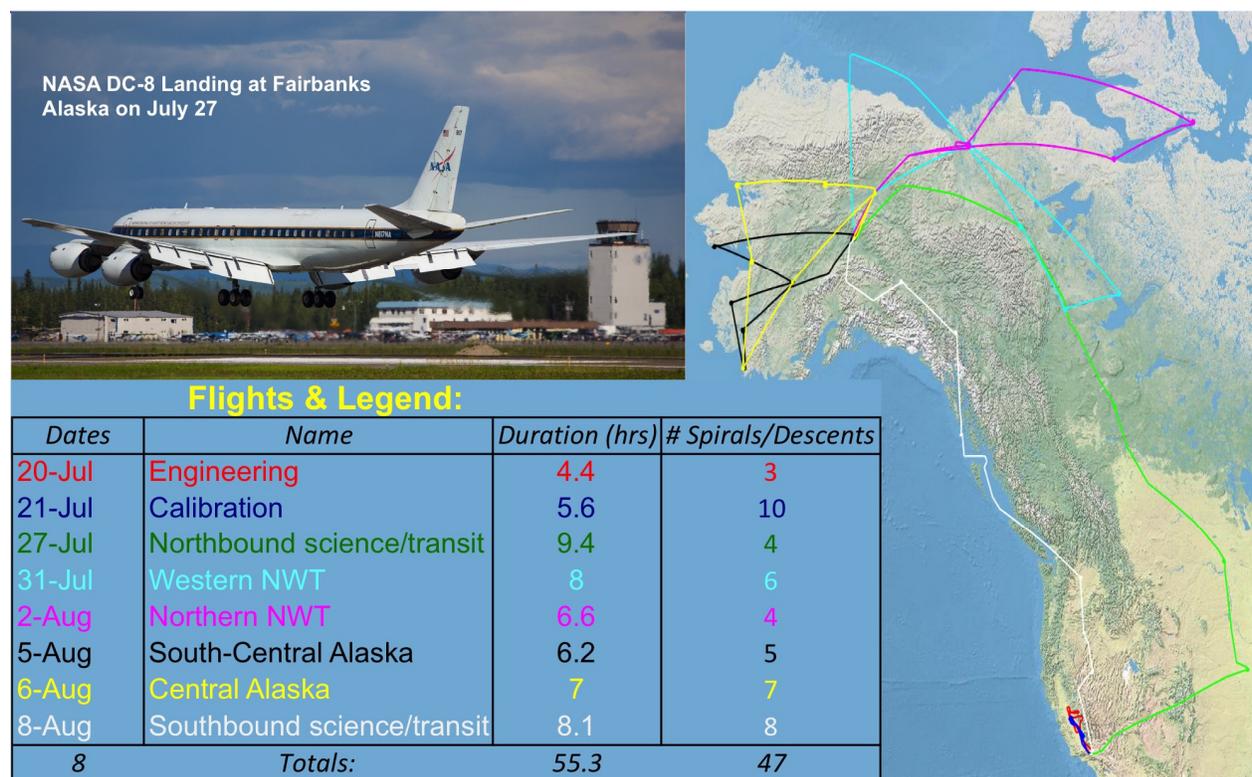
Figure 5-31 Map of the ground track for the 2017 ASCENDS Airborne campaign and a summary of the dates, locations, durations and number of spirals or in-line descents of each flight.

5.5   Recommendations for Further Airborne Activity

The airborne lidar campaigns have provided important opportunities to demonstrate the performance of candidate lidar techniques for ASCENDS. This was valuable given the wide variety of combinations of atmospheric scattering and extinction and surface backscatter and morphology where CO_2 measurements must be made. As stated in the introduction, ASCENDS has several fundamentally new and important capabilities for measuring XCO_2. The airborne campaigns have allowed demonstrations of those capabilities and performance assessments. With each successive campaign, the instruments, data analysis approaches and CO_2 retrieval algorithms improved. Measurements have been demonstrated over a wide variety of land, snow-covered and ocean surfaces, during conditions with cloud cover and with broken clouds, and under day and night conditions. Since these have been representative of key conditions for a space mission, the

campaigns have allowed assessment and improvements of how the candidate lidar techniques will work from space. This section highlights some remaining benefits for additional airborne campaigns and measurements.

First, it is important to further demonstrate the capabilities of airborne CO_2 IPDA lidars to provide measurements related to the determination of CO_2 fluxes from both natural and anthropogenic sources. Additional measurements over the Arctic at different times of year are of considerable interest. Other logical candidates are CO_2 fluxes from large areas of rapidly growing cropland in the summertime, and CO_2 emissions from cities. Airborne campaigns that target these types of measurements are important as initial demonstrations of ASCENDS-type measurements to address local and regional scale questions about carbon exchange between the surface and atmosphere.

Second, it will be valuable to further compare airborne lidar measurements of CO_2 with those from passive satellite instruments. Some initial attempts at these comparisons have been made with GOSAT and OCO-2, e.g., within the NASA ACT-America airborne project (see Bell et al., 2018). Continuing these comparisons under a variety of conditions should be quite valuable and informative. Lidar cal/val would also include comparisons with on-board in situ CO_2 data made during spirals down to and within the boundary layer. Methods for modeling the CO_2 column above the aircraft (~10-12 km) also need to be considered.

Finally, it is desirable to improve the fidelity of the lidar measurement models used in initial space mission simulations (Kawa et al., 2010; Crowell et al., 2018). These have been quite useful to examine the requirements analysis for the mission, to initiate simulations of flux retrievals, and to assess the impacts of random and bias errors in the lidar measurements. It is also desirable to expand the simulations to include range and CO_2 column measurement to the tops of certain types of optically opaque clouds, such as marine stratus and fair weather cumulus.

5.6   Technology Developments Needed for an ASCENDS Space Lidar

Many important capabilities for ASCENDS have been demonstrated by several of the airborne lidar teams. These include CO_2 column absorption and range measurements with high precisions and low biases over a wide variety of surface types, and measurements over a wide range of altitudes. Some measurements have been demonstrated to cloud tops and through thin clouds. Several teams have demonstrated accurate retrievals of CO_2 mixing ratios based on the airborne lidar data in comparison with in situ data. Almost all measurement results have been presented at conferences and most have been published in peer-reviewed journals. This work has greatly improved the science definition team's understanding of the capabilities needed from space for ASCENDS and represents significant progress toward meeting the demands of the space mission. However, this work has also identified key challenges that must be addressed to meet the requirements of the ASCENDS mission. Some specific improvements needed in technology are summarized below.

5.6.1   Generic Needs for Up-Scaling Existing Airborne Lidars as "Bridge" to Space

For space use, a lidar has additional technical and engineering challenges beyond those for aircraft. These include: (1) a much longer range to the scattering surface (typically 400 km for space vs $\leq$12 km for airborne). This significantly increases the loss from photon scattering to the receiver (typically a factor of $\geq$1000), which must be overcome by higher laser power and a larger receiver telescope. (2) A much faster along track velocity (7 km/sec vs 0.25 km/sec) which increases the rate of reflectance variability. (3) A larger spot diameter (typically 100 m vs ~5 m) on the surface, which can increase range spreading. (4) The need to withstand the launch vibration and the vacuum

and radiation environment of space. (5) The instrument technology and components also must be designed for at least 3-5 years of continuous operation.

The airborne lidar candidates need further investments to attain a high technical readiness for space. The largest common factor is the need for improvement of the product of laser power and telescope area to overcome the signal loss due to increased range. Direct detection lidar can benefit by using a larger diameter telescope, but the laser power still must be increased significantly, typically by a factor of 10-100, over current airborne instruments. The highest common need is for a laser, that meets all other requirements and that also has the needed power for space. The selected approach needs to have a viable technical path to achieve these ends in a robust and mechanically rugged design that can be shown to have long unattended lifetime and also can withstand the radiation and vacuum environment of space. The individual teams have addressed the scaling of their approaches to space, and their approaches and progress are summarized below.

5.6.2   Scaling the CO₂ Sounder Lidar to Space

The CO₂ Sounder team has made considerable progress in advancing its approach for use in space since the 2015 Ascends White Paper. A block diagram of the space lidar approach is shown in Figure 5-32. This approach has been proven in the airborne campaigns, and the space version allows for measurements from orbit by using adding laser power amplifier stages to increase the transmitted pulse energy and by using a larger diameter receiver telescope.
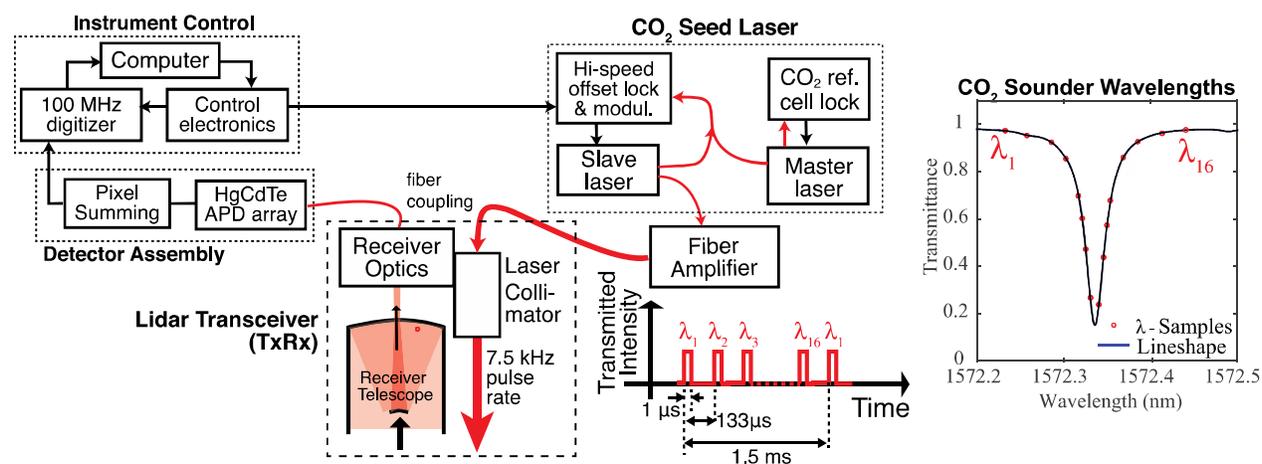
Figure 5-32 Block diagram of the space lidar instrument and its wavelength-stepped laser pulse-train.The pulsed laser measurements are made of shape of the at 1572.33 nm CO₂ line and of backscatter profiles. The laser backscatter is collected by a common 1-m telescope and detected by a HgCdTe APD. The insets show the laser-sampled line shape and the wavelength-stepped laser pulse-train used to measure it.

Similar to the airborne version, the seed lasers for space are rapidly switched from 16 fixed-locked wavelengths points. This produces a repeating wavelength-stepped pulse train every 2.1 msec. At 7.5-kHz pulse rate, the pulses are separated by 133 µsec, which permits them to clear the bottom 20 km of the atmosphere to minimize crosstalk from cloud scattering. At the spacecraft velocity the ~60-m diameter laser spots on the surface move ~0.9 m for each wavelength step, resulting in highly overlapped footprints. The team has developed and demonstrated these key technologies

needed for a space instrument. This approach can meet the ASCENDS random error requirements by using a 1-m diameter receiver telescope. Some views of preliminary instrument layout for space are shown in Figure 5-33.
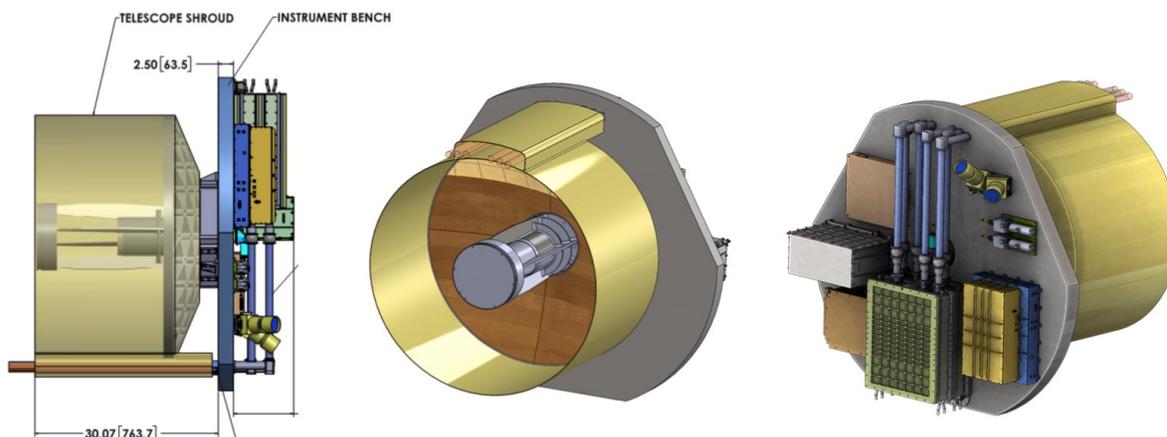
Figure 5-33 Preliminary layouts for a space version of the CO_2 Sounder lidar that uses a 1-m diameter Be receiver telescope, like that used in NASA's ICSat/GLAS and Calipso lidar. The configuration uses a single optical bench , with the lidar components mounted on the side opposite the receiver telescope. The largest box (with the tubes) is that for the laser amplifier, with others for the laser stages (described below) and absorption cell, the detector assembly, the electronics box and the power supply, and two small star cameras. The star camera light baffles are not shown and the layout is not yet optimized.

Since 2015, the CO_2 Sounder team has also improved its model to predict measurement performance based on work from the airborne instrument. This model analyzes the signal, noise, and uncertainty in gas concentrations by calculating the average number of signal photons, solar background photons, speckle noise and detector noise observed over each 1-μsec pulse interval. The model was first used for performance of the airborne CO_2 sounder measurements in 2014, and the results for the 2016 spiral over Edwards are shown in Figure 5-34 and in (Abshire et al., 2018a).

The results show the measured XCO_2 errors were close to the model for measurements at altitudes >6 km. At lower altitudes, the measurement errors increased because of the low CO_2 absorption, more contribution from the surface variability and from reducing the laser power to prevent receiver saturation. Overall, the random error from the measurements agree well with the performance model, but are a factor of 1.4 larger (Sun et al., 2017a). The larger errors may be caused by unmodeled surface reflectance variation during the receiver integration time, and by unmodeled instrument noise sources.

The same measurement model can be used to predict the performance of the space version of the CO_2 Sounder lidar. Figure 5-34 shows the expected measurement performance along with the instrument and measurement parameters. The calculations show that the random errors in the retrievals are primarily limited by the shot noise of the detected signal photons on the absorption line, although for brighter surfaces speckle noise is also a factor. Results show that for desert surfaces the model predicted random error is ~0.5 ppm for 1-sec averaging time. If this is increased

by x1.4 to follow the results from the airborne lidar, this results in 0.7 ppm (1-sec) random error, better than the 1 ppm (1-sec) requirement.
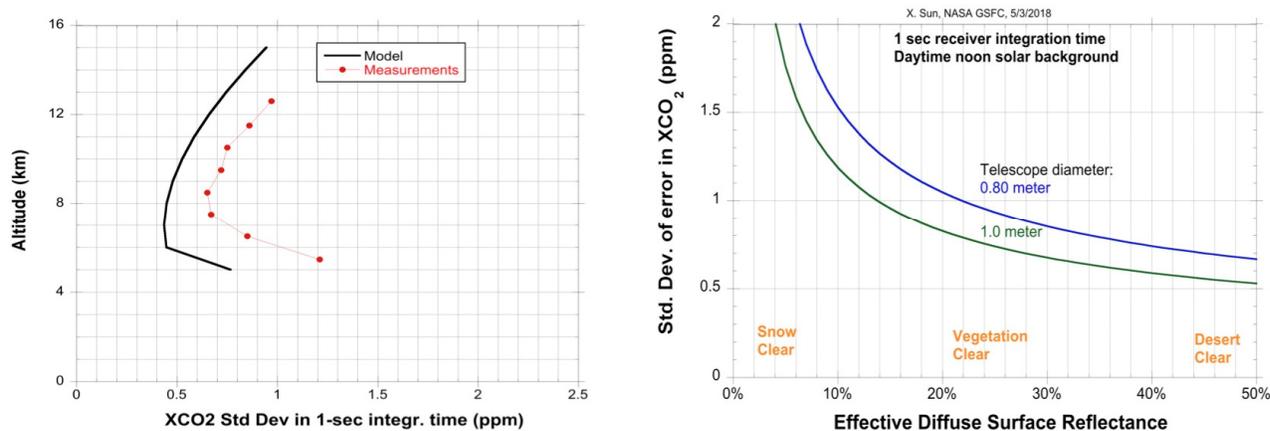
Parameter	Value		Parameter	Value		Parameter	Value
Orbit Altitude	400 km		Laser wavelengths/scan	16		Receiver optical transmission	50%
Laser pulse energy	2.67 mJ		Off-line atmosphere trans.	70%		Detector effective QE	67%
Laser pulse rate	7.5 kHz		Surface reflectivity	varies		Detector APD gain	500
Laser pulse width	1.0 usec		Telescope diameter	0.8 and 1.0 m		Detector dark current	5 fA
Laser divergence	150 urad		Telescope FOV	225 urad		Detector bandwidth	~ 6.5 MHz

Figure 5-34   *(Left top)* Comparison of the predicted XCO₂ error and the measurements for the 2016 airborne measurements over Edwards CA that used 1-sec averaging.   *(Right top)* Predicted XCO₂ error of the CO₂ Sounder model versus surface reflectivity for 1-sec averaging, with parameters scaled to space. The effective diffuse surface reflectivity (i.e., reflectivity with enhancement factor) for RRV is 55%. The ASCENDS simulation studies show the global average value effective diffuse reflectivity is ~16%. *(Bottom)* Some parameters used in the space calculation.

5.6.2.1 Space Technology for the CO₂ Sounder

Laser Transmitter – The CO₂ Sounder approach uses a master-oscillator power-amplifier (MOPA) approach for the laser (Yu et al., 2015, Stephen et al., 2018). This approach is modular and flexible, and it leverages the lower power stages that have already been demonstrated in airborne campaigns. The power increase needed for space is achieved by adding power amplifiers to the prior stages, and so that the space laser is an incremental step rather than a new development. The laser is all fiber coupled, except for free-space output beams, and is rugged.

The diode seed lasers for the CO₂ wavelengths are highly developed, and have been space qualified. The seed module, shown in Figure 5-35 uses two diode lasers. One is a wavelength reference that is locked to the peak of the CO₂ line. A ruggedized 10-m path length Herriott cell filled with CO₂ serves as an absolute wavelength standard (Numata et al., 2011) . A quickly tunable slave-laser is offset-locked to the reference laser via programmable offset frequencies. Repetitively stepping through a table of frequencies between pulses causes the slave to emit very accurately tuned laser output across the CO₂ absorption line (Numata et al., 2012).
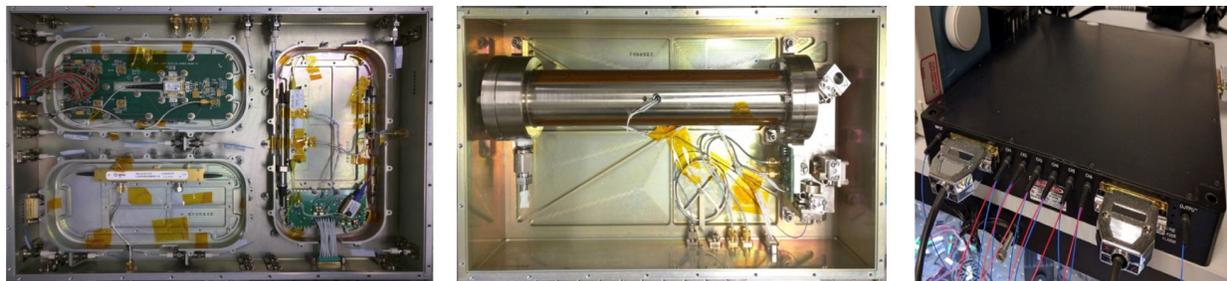
Figure 5-35 *(Left)* Photo of the completed seed laser module with reference laser, tunable laser and Mach-Zehnder modulator shown. *(Middle)* Photo of the Herriot cell filled with CO_2 gas with integration optics in a ruggedized package to lock the reference laser to an absolute wavelength standard. Gas cell module dimensions are 25.5-cm x 12.5-cm x 10-cm. *(Right)* Photo of the engineering model of the preamplifier.

The pre-amplifier module was developed by NuPhoton, Inc. It has a single input and six parallel output signals. It increases the pulse energy in each of the six channels to ~2.5 uJ/pulse. The packaging is compact and includes drive and control electronics. It has undergone vibration tests and a preliminary vacuum bake-out procedure with no changes in performance.

Laser power amplifiers - The final amplifier stages increase the total output energy to 2.7 mJ/pulse, the energy needed for space. The approach, shown in Figure 5-36 uses 6 very large mode area (VLMA) Erbium-doped (Er) fiber amplifiers (Nicholson et al., 2016) in parallel. The light is collimated as it exits the fiber and all six beams are co-aligned to illuminate the same spot on the Earth's surface. The power amplifier fibers are pumped at 1480 nm using a fiber Raman laser. Presently each module has a single Raman laser that pumps two amplifiers. The power amplifiers use VLMA fiber as gain stages. Their large mode field allows each fiber amplifier to produce the needed ~450W peak optical power. Since the VLMA fiber requires a large bend radius, the fiber is mounted in a spiral pattern. Two smaller fiber spools are used for the Raman pump. Two power amplifier stages are packaged in each module presently, although using 3 stages per module is also viable. Three complete two-fiber modules capable of the full power required for space are now under development.
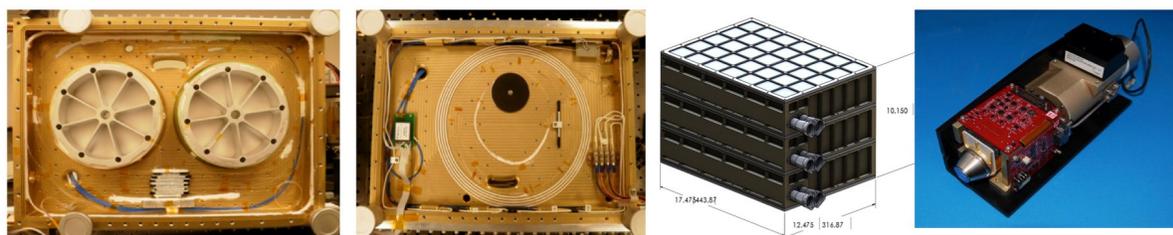
Figure 5-36 *(Two left figures)* Photos of the interior of the prototype VLMA fiber laser power amplifier. The left photo shows the two spools of the Raman pump fiber laser. The other fiber components are in the lower center of the photo. The right photo shows the top half of the box with the VLMA fiber spiral. The white fiber potting material makes the spiral groove easy to visualize. The dual output power amplifier module dimensions are 44 x 32 x 9-cm. *(Middle)* Drawing of the stack of 3 laser amplifier assemblies containing the 6 parallel laser outputs that are coaligned. When summed on the ground spot, the total pulse energy is 2.7 mJ. *(Right)* Photograph of a DRS 16-element HgCdTe APD detector inside the Integrated Detector Cooler Assembly (IDCA). This is 20 cm long and was developed as a 2U payload for a CubeSat in the ESTO InVest-12 program. The unit passed environmental tests at NASA Goddard in 2017.

As of mid-July 2018, the engineering models of the laser seed module and cell, pre-amplifier module, and the power amplifier module have all been built and have passed vibration testing. Thermal vacuum testing is ongoing now. The performance achieved meets the requirements for a space laser transmitter.

Receiver telescope and detectors –The present plan uses a 1-m diameter Be receiver telescope, like those used on the ICESat/GLAS and Calipso missions. The lidar detector will utilize the DRS HgCdTe e-APD (Beck et al., 2013) shown in Figure 5-36. This detector has gain >500, effective Quantum Efficiency (QE) >70% from 0.5 to 4 μm, and a NEP <0.4 fW/ $Hz^{1/2}$ (Sun et al. 2017b). Tests show the detector is tolerant to the expected space radiation (Sun et al., 2018a), and a detector cooler assembly has passed space environmental tests (Sun et al, 2018b).

5.6.3   Scaling the Airborne IM-CW Lidar to Space

The LaRC ASCENDS team has developed a measurement model for the IM-CW lidar and CO_2 measurement simulations (Lin et al., 2013). Such models are essential for the improvement of LAS systems and the prediction of the performance of space CO_2 measurements for future space missions. Validation tests show excellent agreements of simulated results with ground-based and airborne LAS measurements (Lin et al., 2013). The simulations show a potential for the ASCENDS mission using technologies that currently exist or are expected to be available within the next few years. The studied spaceborne IM-CW LAS instrument will achieve root-mean-square errors of CO_2 column measurements for surfaces similar to the playa of Railroad Valley, NV within 0.25 ppm for 10-s averages (Lin et al., 2013). Figure 5-37 illustrates the basic structure of the space LAS instrument which is expected to have a system architecture similar to that of the airborne LAS instrument.
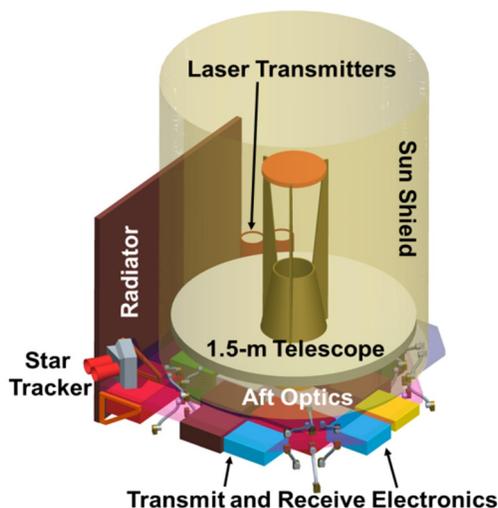
Figure 5-37 Concept for a space-based IM-CW LAS lidar.

Compared to the airborne lidar, the main changes for space are using two sideline wavelengths with one at +3-pm offset from the CO_2 absorption line center (called Side-1) and the other at +10-pm offset (called Side-2); increasing the total transmitted laser output power to 42 W; increasing the

telescope diameter to 1.5 m; reducing the receiver optical bandpass filter bandwidth to 0.5 nm full-width and half magnitude; and reducing the laser half-angle divergence to 50 μrad (Lin et al., 2013). The receiver's field-of-view (FOV) will be set to be 33% larger than that of the laser divergence, and the optical throughput is expected to be >0.65. The sideline wavelengths are selected to have more sensitivity to CO_2 absorption across the mid to lower troposphere (lower-altitude weighting function), where most of the CO_2 flux exchange with ecosystems and transport within the atmosphere take place.

5.6.3.1 Model and Simulations for LAS Space Lidar

The performance of the space lidar for CO_2 measurements was simulated using a model developed by Lin et al. (2013). This model for the lidar and its measurement environment are important to guide improvements of LAS systems and allows for predictions of CO_2 measurements for future space missions. The model accounts for the physics and characteristics of the instruments and their related measurement environments. The model results are presented statistically from simulation ensembles that include noise sources and uncertainties related to the LAS instruments and the CO_2 measurement environment. The characteristics of simulated LAS systems are based on existing technologies and their implementation in existing systems.

The modeled lidar is assumed to be an IM-CW LAS system such as the Multifunctional Fiber Laser Lidar (MFLL) operating in the 1.57-μm CO_2 absorption band. Environmental effects due to variations in atmospheric CO_2, solar radiation, turbulence, surface reflectance, and aerosols and thin clouds are also included in the model. The simulated results show excellent agreement with measurements (Lin et al., 2013). Figure 5-38 shows an example of the comparison of model-simulated results with instrument measurements for the Railroad Valley playa flight on 3 August 2011 at 6.1-km altitude. The differences in CO_2 DAOD between model results and observations are very small, clearly demonstrating the capability of the model to estimate the performance of LAS systems and their CO_2 column measurements.
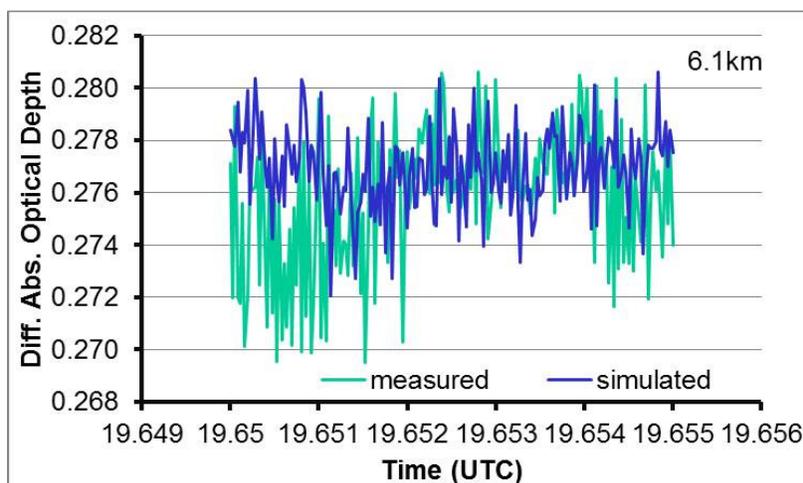
Figure 5-38 Comparison of simulated results of DAODs with observations for the Railroad Valley 6.1-km flight on 3 August 2011 (Lin et al. 2013).

For the ASCENDS space mission, the assumptions are a sun-synchronous, dawn/dusk orbit (Ehret et al., 2008) with an altitude of 390 km. Under clear conditions, simulations show that the precision of the DAOD measurements for surfaces similar to the playa of Railroad Valley, NV (reflectance 0.176 sr^{-1}) will be better than 0.05% (~0.2 ppm) for 10-s averages (c.f., Figure 5-39).
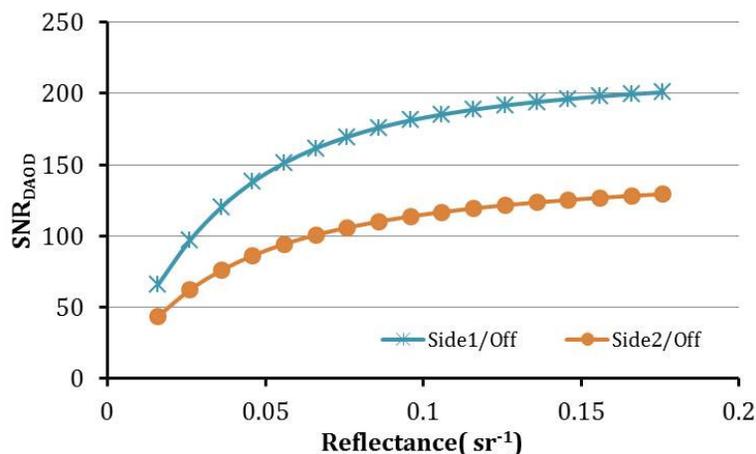
Figure 5-39 10Hz SNR_{DAOD} for a space IM-CW LAS for a range of surface reflectance (Lin et al. 2013).

For other types of surfaces such as low-reflectivity snow and ice surfaces, the precision will be within 0.23%. Including measurements through thin clouds with optical depths up to 1, the CO_2 SNR_{DAOD} measurements with 0.1-s integration period for surfaces similar to that of Railroad Valley, NV will be greater than 94 and 65 for Side-1 and Side-2, respectively (Figure 5-40).
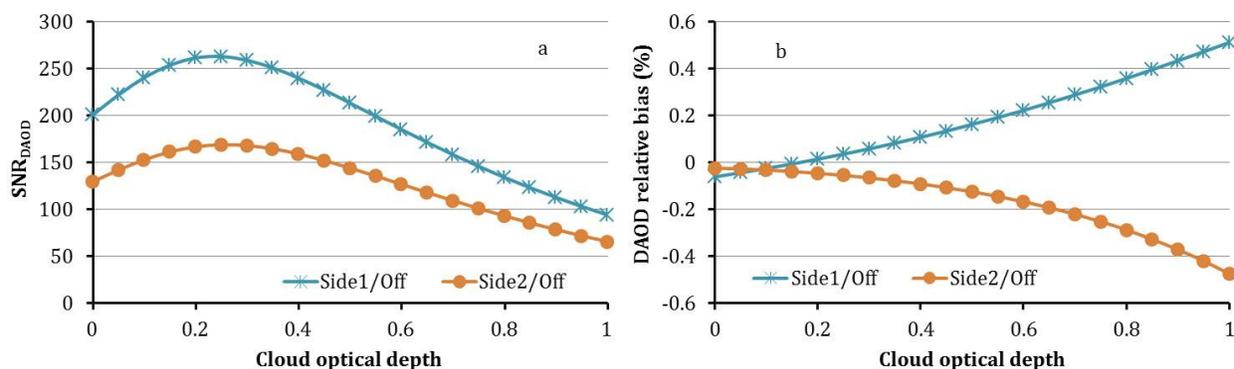
Figure 5-40 10Hz results for a space lidar under thin cirrus conditions. The CO_2 SNR_{DAOD} (a) and bias (b) are calculated for surfaces similar to Railroad Valley, NV (Lin et al., 2013).

The CO_2 column bias errors introduced by the thin clouds are $\leq$0.1% for cloud optical depth $\leq$0.4, but they could reach ~0.5% for more optically thick clouds with optical depths up to 1 (Figure 5-40b). When the cloud and surface ranges and scattering amplitudes are obtained from the analysis of matched filter outputs, the cloud bias errors can be further reduced as seen from the compensating feature of the bias errors between the retrievals of the two sidelines (Figure 5-40b). Other simulation studies indicate that the present IM-CW LAS concept for space can provide ASCENDS-required

125

CO_2 measurements from not only the dawn/dusk orbit but also other Low Earth Orbits (LEOs) such as sun-synchronous, day/night orbits, maximizing the flexibility of the space instrumentation to various CO_2 measurement needs.

5.6.3.2 Technology Development for IM-CW Space Lidar

Several of the technologies that are critical for achieving a measurement of XCO_2 from a space-based lidar have been and will continue to be tested using the LaRC ACES instrument. First, space mission design studies have shown that 42 W of transmitted power is required for the space-based measurement (Lin et al., 2013), and ACES is currently transmitting 30 W of CW power using three 10-W commercially-available erbium-doped fiber amplifiers. LaRC has worked with Fibertek, Inc., to build a 20-W amplifier, which has been demonstrated in the laboratory and will be incorporated into the airborne instrument for further testing. Combining multiple 20-W amplifiers will achieve the transmitted power that is required for the space-based measurement, and further increases in power are expected to continue in the future as commercial products continue to advance. Regardless, the transmitted power requirement is readily achievable. The DRS HgCdTe detector that has been used for some ACES test flights, as well as in other airborne instruments, will provide the necessary sensitivity for XCO_2 measurements from space.

Additional technology efforts needed for space CO_2 lidar applications includes space qualification testing of individual components and the entire lidar instrument for vibration, acceleration, thermal heat change, and space radiation. Although the LaRC team feels confident about the space application of the lidar design, these tests will significantly reduce risks for space flight.

5.6.4 Scaling the Pulsed 2-μm Lidar to Space and Future Plans

The 2-μm triple-pulse IPDA lidar operated well on ground and in the aircraft environment, demonstrating simultaneous and independent CO_2 and H_2O measurements, along with precise range (0.2 m) measurements. System tuning, characterization, and testing are in progress for performance optimization. A technology development roadmap over the next decade is shown in Figure 5-41. The next steps are: 1) Focusing on CO_2 through instrument optimization and testing for high accuracy measurements from ground and B-200 aircraft. 2) Participating in field experiments for validating the CO_2 measurements using in-situ sensors and full diagnosis of systematic and random errors. 3) Participation in science measurement campaigns, and validation of satellite CO_2 measurements from OCO-2 and GOSAT. 4) Meeting one of the objectives of Earth Science and Applications from Space (ESAS) 2017 of "quantifying the fluxes of CO_2 and CH_4 globally at spatial scales of 100-500 km and monthly temporal resolution with uncertainty <25% between land ecosystems and atmosphere and between ocean ecosystems and atmosphere" National Research Council's (NRC, 2017). This is one of the objectives an Explorer class mission identified by the ESAS 2017 recommendation that could be accomplished under the NASA Earth Venture Instrument (EVI) program in the 2026-2028 timeframe from the ISS platform. This will also allow maturation of the IPDA for operation on a free-flyer science mission with potential international collaboration in the future (Singh et al., 2018).
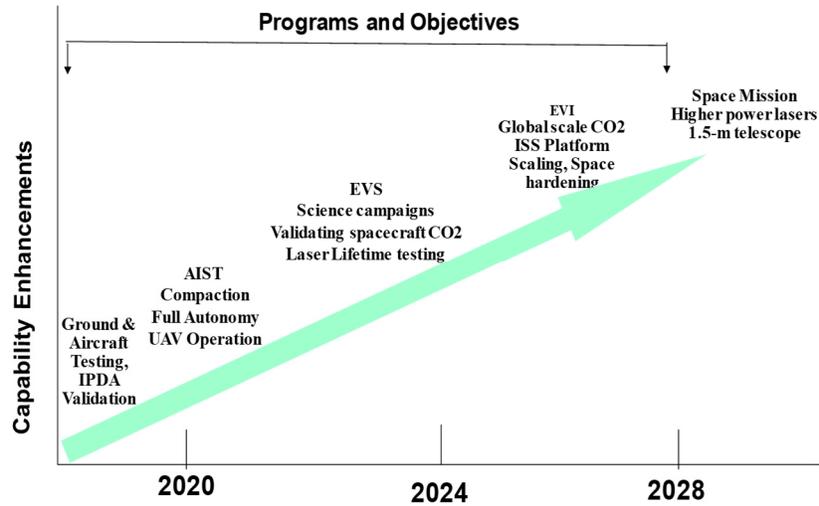
Figure 5-41 Projected triple-pulse, 2-μm IPDA lidar technology development roadmap for lidar measurements of carbon dioxide from space.

The performance of the triple-pulse IPDA lidar in simulating CO_2 space-based measurements at 2-μm was calculated by assuming 400 km altitude dawn-dusk orbit, a US Standard atmospheric model and a RRV surface reflectivity. Analysis of both random errors associated with IPDA, and systematic errors from atmospheric and instrument biases were estimated (Singh et al., 2017a). Residual systematic errors in CO_2 measurement arise due to uncertainties in the knowledge of atmospheric and the IPDA instrument capabilities. The estimated CO_2 differential optical depth error from atmospheric effects include uncertainties in temperature ($\pm0.5°K$), pressure (±100 Pa), relative humidity ($\pm10\%$) and H_2O interference. A normally distributed random number generator was used to simulate the variability of these fields to evaluate the systematic error. CO_2 differential optical depth bias errors resulting from the IPDA transmitter uncertainties including on- and off-line laser position jitters (±650 kHz) and laser spectral profiles were also estimated as shown in Figure 5-42.
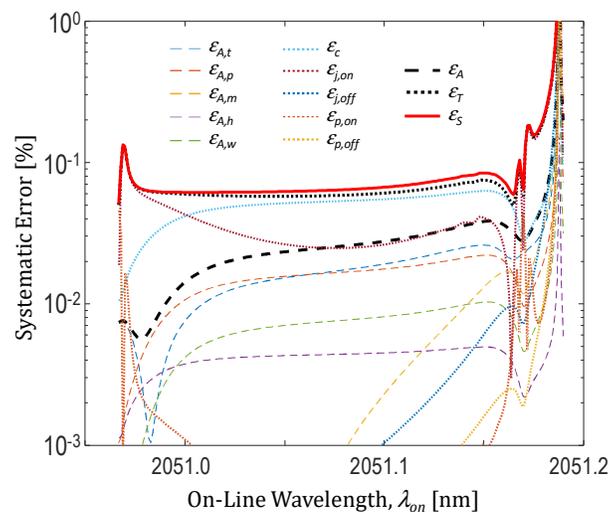
Figure 5-42 Systematic errors variation with on-line wavelength. Simulated IPDA systematic error, ε_S, is the sum of the atmospheric error, ε_A, and IPDA transmitter error, ε_T. Atmospheric error includes temperature, $\varepsilon_{A,t}$, pressure, $\varepsilon_{A,p}$,

molecular interference, $\varepsilon_{A,m}$, relative humidity, $\varepsilon_{A,h}$, and water vapor broadening, $\varepsilon_{SA,w}$. Transmitter error includes laser jitters , ε_j, and line profiles, ε_p, for both the on and on-line wavelengths.

Random errors for the combination of 50, 15, and 5 mJ on- and off-line energies and total errors are shown in Figure 5-43, assuming single-pixel alignment of the e-APD detection system. Measurements with two weighting functions, at 50 Hz each, with the triple pulse system can be accomplished using two on-lines and a common off-line. The near optimum random error for each pair is <0.12% (<0.5 ppm), and the residual systematic error is <0.07% (0.3 ppm). With 10 MHz detection bandwidth, surface ranging with an uncertainty of <3 m can be achieved as demonstrated from earlier airborne flights (Singh et al., 2017b).
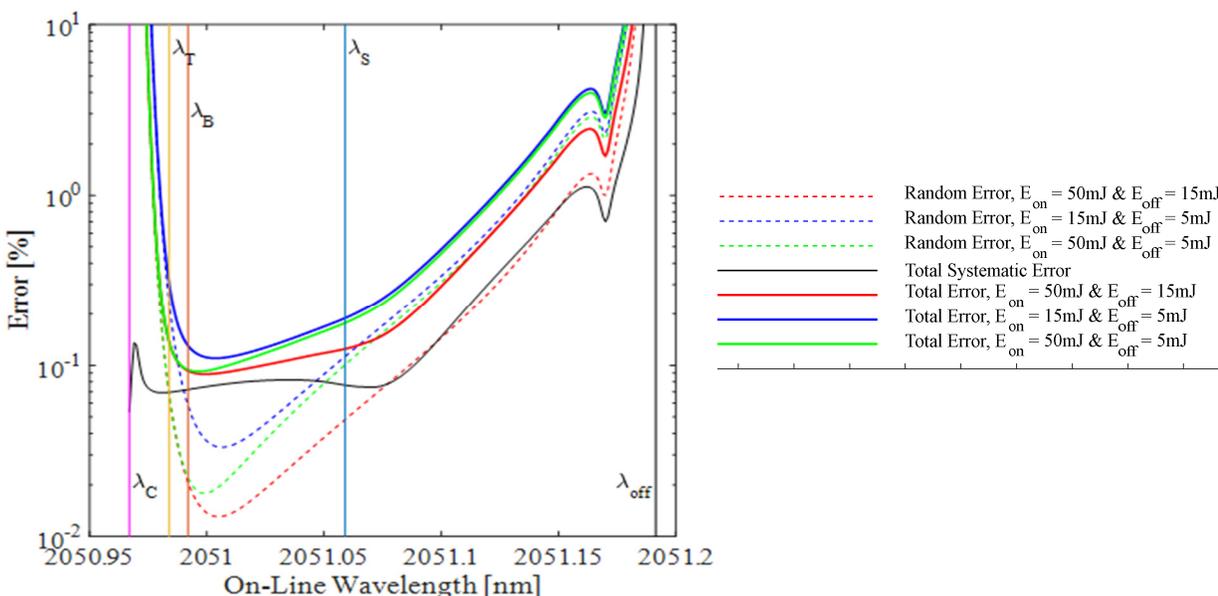
Figure 5-43 Random errors variation with on-line wavelength obtained using different on and off-line transmitted energy combinations. Total error for CO₂ measurement using the 2-μm IPDA lidar is obtained by adding random and total systematic errors.

The 2-μm triple-pulse IPDA space-based measurements can be optimized by tuning on-lines depending upon ground target scenarios, environment and science objectives using adaptive targeting. This was demonstrated using the double-pulse IPDA lidar, where the on-line was varied from 1 to 6 GHz away from the R30 line center. With the same instrument, another demonstration of the technique was conducted to perform off-off-line testing, in which the on-line wavelength was tuned to exactly match the off-line. The 2 μm IPDA lidar triple-pulse capability allows simultaneous and independent measurement of CO₂ using two different weighting functions. For example, weighting function selection allows measuring CO₂ concentration near the surface for studying source and sink interactions. With the same off-line, the third pulse can be tuned to a different weighting function that is optimized for tropospheric measurements. Both measurements can be targeted simultaneously for studying the CO₂ exchange and transport. On the other hand, the triple-pulse capability can be used to independently measure CO₂ and H₂O column amounts. Having one laser delivering, nearly simultaneously, three pulses at different frequencies eliminates the

complexity of three different lasers. This helps reduce the mass, size, and power consumption of the instrument, while increasing the efficiency. Measurements with adaptive targeting would be a valuable tool for a space mission (Singh et al., 2017b).

5.7   Summary

During the period of the ASCENDS mission preformulation development, the measurement group made great progress in developing lidar measurement approaches, demonstrating the lidar measurements and developing technology for a space mission. The group developed a consensus set of ten requirements for the lidar measurements on the ASCENDS Mission. These are consistent with the results of the modeling activity, are generic and independent of the measurement approach. As part of this activity, NASA invested in the development of four different lidar approaches and technologies that can be considered candidates for ASCENDS. The NASA lidar teams made many advances in developing candidate lidar and data analysis approaches. They have also demonstrating their measurement capabilities in ASCENDS airborne campaigns under a wide variety of conditions and have demonstrated data analysis (retrieval) approaches. The results from all ASCENDS campaigns have been presented at conferences and all but the most recent campaign have been published in journals. The measurement group has also analyzed the capabilities needed for a space mission for three of the lidar approaches. Several approaches appear to be strong candidates for a near-term space mission.

6. Mission Design

6.1 Introduction

In 2012, NASA's Earth Science Division (ESD) requested that the Earth Systematic Mission Program Office (ESMPO) perform a mission study to determine the feasibility of accommodating a conceptual ASCENDS instrument on commercially available spacecraft buses as well as the feasibility of flying a conceptual observatory on an Evolved Expendable Launch Vehicle (EELV) and in a Dual Spacecraft System (DSS) configuration. The study team was made up of representatives from the ESMPO, the Goddard Space Flight Center (GSFC), the Jet Propulsion Laboratory (JPL) and the Langley Research Center (LaRC). The mission study covered eight areas and includes assessments in the areas of mass, power, mechanical/thermal interface, volumetric, attitude determination and control (AD&CS), telecom, mission operations, and de-orbit considerations. Assessments captured design requirements, assumption, design rationale, design risks, and the report summarized the finding and results. Some values for key parameters are listed in Table 6-1, Table 6-2, and Table 6-3. The final report by Hyon et al. (2012) documented the results and findings of the assessments, summarized those results and findings, and provided recommendations for future studies. These are also summarized in the Section 6 of the ASCENDS White Paper (Jucks et al., 2015).

Throughout the report, Ball's BCP 2000 (Ball Aerospace Commercial Platform 2000) bus was used as an example of a spacecraft appropriate for supporting the ASCENDS mission. Buses from other manufacturers, including Boeing, Lockheed Martin, Northrop Grumman, Orbital Dulles and Orbital Gilbert are also considered to be quite capable of supporting the ASCENDS mission. The Figure 6-1 depicts one of the spacecraft configurations with hosted payload and the ASCENDS instrument.

By 2018, the ASCENDS measurement team had matured their measurement approaches and instrument approaches for space. The changes were based on improvements to the measurement requirements as well as on the new OSSE studies and analyses performed by the modeling teams. One example was using modeling for the dry air column that allowed deleting the need for the oxygen lidar channel. Other changes were based on maturing some key laser and detector technologies used in the instruments. These allowed for more accurate estimates of the parameters shown in Table 6-3. As discussed in Section 5, further progress in reducing individual instrument sizes and input power summarized in Table 6-3 (including increasing laser efficiency and mass reduction) may allow compatibility with the new small satellite and launch options. Thus, if these trends continue, it may be possible that an updated ASCENDS mission concept might fit under an Explorer Class Mission in the future.

Table 6-1 Mission and Launch Parameters

Parameter	ASCENDS Generic Payload 2 from August 2015	ASCENDS Lidar Payload - July 2018
Mission Parameters:		
Measurement	CO₂ and altimetry	CO₂ and altimetry
Launch Requirements:		
Nominal Orbit	Sun-sync, ~noon crossing	Sun-sync, ~noon crossing
Altitude (Km)	~450 km ± TBD km	~450 km ± TBD km
Inclination	Polar	Polar
Design Operational Life	3 yrs with propellant for 6 yrs	3 yrs with propellant for 6 yrs
Current Best Estimate (CBE) Instrument Size (m)	<2.5 tall x 1.5 x 1.5	<1.6 tall x 1.3 x 1.3

Table 6-2 Spacecraft and Operation Parameters

Parameter	ASCENDS Generic Payload 2 from August 2015	ASCENDS Lidar Payload - July 2018
Science and C&D Handling:		
Average Science Data Rate (Mbps)	20	10
Maximum Science Data Rate (Mbps)	-	-
Instrument Housekeeping Telemetry		
Instrument Housekeeping Telemetry Data Rate (Mbps)	0.1	0.1
Onboard Data Storage (Gbits/day)	~1750/day	~1000/day
Attitude Control:		
Pointing Knowledge	5 arc sec	10 arc sec
Pointing Control	20 arc sec	50 arc sec
Jitter	0.4 arc sec over 4 ms and 5 arc sec over 20 ms	1 arc sec over 4 ms and 10 arc sec over 20 ms
Attitude Control Subsystem (ACS):		
Global Positioning System (GPS) Receiver	YES	YES
Post Processing GPS onboard knowledge	-	-
Star Trackers	YES	YES
Major Maneuvers	Yaw flip as required; calibration as required; on orbit stability after maneuvers	Yaw flip as required; calibration as required; on orbit stability after maneuvers
Propulsion	Required for orbit maintenance.	Required for orbit maintenance.
Design	Standard biprop or monoprop blowdown	Standard biprop or monoprop blowdown
Observatory Environmental & Facility (driven by Instrument):		
NASA Risk Classification	Sensor: C Platform: B	Sensor: C Platform: B
Electromagnetic Interference / Electromagnetic Compatibility (EMI/EMC)	Per MIL-STD-461C, tailored as required	Per MIL-STD-461C, tailored as required
Vibe	GEVS for Atlas & F9 LV	General Environmental Verification Specification (GEVS) for Atlas & F9 LV
Thermal Vacuum (TVAC)	YES	YES
Radiation	Meet orbit levels	Meet orbit levels
Cleanroom Class	As required	As required
Special Facility Needs	Per instrument type	Per instrument type
Mission Operations:		
S/C ballistic coefficient	2.2	2.2
Cross-sectional area	19.1 m^2	<15 m^2

Table 6-3 Instrument Parameters

Parameter	ASCENDS Generic Payload 2 from August 2015	ASCENDS Lidar Payload - July 2018
Instrument Mass:		
Total Instrument Mass Allocation (CBE+Margin, kg)	<400	<350 with instrument radiator ~280 without radiator
Instrument Power:		
Total Instrument Power Allocation (CBE+Margin, W)	<750	~700
Mechanical Interface:		
Mechanical Interface, e.g., kinematic, planar, etc.	Instrument to I/F panel - Kinematic	Instrument to I/F panel - Kinematic
Interface Panel or hard mount to bus	I/F panel	I/F panel
Field of View (FOV)	<1.5° about nadir	<1.0° about nadir
Instrument Thermal Requirement:		
Thermally isolated	YES	YES
Thermal FOV	Based on instrument thermal requirements	Based on instrument thermal requirements
Cryo Cooler	Will be provided as part of the ASCENDS instrument	None required
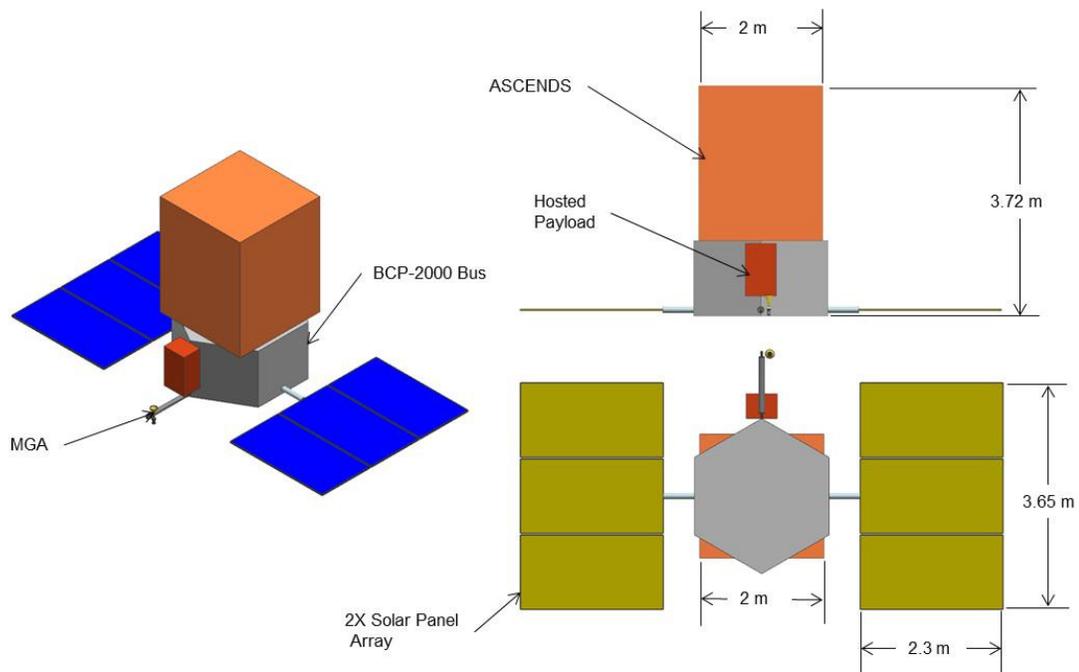
Figure 6-1 Drawings from the 2012 study showing a hosted payload volume mounted to the top of the spacecraft bus.

> **The previous study showed that there are many commercial buses that are compatible with existing lidar concepts for the Falcon 9 or Atlas V launch vehicles. With the new CO$_2$ lidar payload, there are smaller and more cost effective spacecraft buses and launch options available.**

6.2   Summary of Assessment

6.2.1   Summary

A preliminary study of the ASCENDS Mission design has been published in the report by Hyon et al. (2012). Although a variety of potential spacecraft buses had been included in the sections on volumetric assessment of accommodating the ASCENDS instrument, the Ball BCP2000 bus has been assumed as the baseline for the sections on power, mechanical/thermal, AD&CS, and telecom assessment. The design assessments were developed based on a preliminary design from Ball, as enhanced via a JPL Team X study conducted in June 2012.

Since 2015, work by the measurement team has reduced the size and power of the generic lidar instrument and eliminated the Oxygen channel. With these changes, the mission team has begun to explore new spacecraft and launch options in order to fit under the new Explorer-Class mission cost cap, which is $350 million. New secondary spacecraft options offer up to 200 watts for payload power and up to 150 Kg of payload mass. Examples include, but are not limited to, Ball's BCP – 100, Airbus/OneWeb bus, and SSL (formerly SS/L, Space Systems/Loral) Skybox bus. Smallsats allow to use a smaller launch vehicle or a secondary launch. Also, EELV Secondary Payload Adapter (ESPA) Grande has been used as a spacecraft (e.g., Lunar Crater Observation and Sensing Satellite (LCROSS) and DSX (originally Deployable Structures Experiment) http://space.skyrocket.de/doc_sdat/dsx.htm) in order to take advantage of secondary launch options, whose costs range from $20 million – $32 million. However, the ESPA Grande spacecraft cost could vary from tens of millions to over $100 million depending on a power, downlink, and pointing required for the payload.

SpaceX and United Launch Alliance (ULA), offer the secondary launch integration and ESPA-based spacecraft. In addition, there are also commercial Auxiliary Payload Integration Contractors (APICs) like Spaceflight Industries, Adaptive Launch Solutions (ALS), TriSept, etc. who can manage the payload integration. Furthermore, SpaceX reusable Falcon 9 and Blue Origin's New Glenn launch vehicle continue to be a cost-effective alternative, and it is possible that the launch cost could be under $60 million in near future.

The results of this study are that multiple commercially available spacecraft buses will be available to accommodate an ASCENDS instrument in the future with the parameters used in this study when allowing for minor mission-specific modifications. As spacecraft offer more capabilities and if the ASCENDS lidar can be further reduced in size and power, these new trends in spacecraft and launch options may allow it to fit under the Explorer class mission.

6.2.2   Recommendations for Future Studies

In addition to the studies mentioned above, the trade studies listed below are recommended in order to be ready for an Announcement of Opportunity for an Explorer-Class mission.

1. Determination of risk classification for the Mission (instrument and spacecraft)

2. Evaluating orbit altitudes from 350 – 450 km and impact on the mission

3. Examination of the lidar technology trade space to further reduce instrument size and power

4. Orbital debris assessment to determine if a controlled re-entry will be required

5. Investigations to determine if the instrument resolution needs to change to accommodate relaxed control on orbit and/or spacecraft attitude.

6.2.3   Recommendation for an Implementation Schedule

With a notional launch date of no earlier than 2025, a mission implementation duration of 5.5 years is recommended between start of Phase A to launch. Since there is no specific operational requirement for the Explorer class mission, we assume that it would be a Class C mission. From the past mission implementations of this class of missions, it is reasonable to have this phase duration with sufficient reserves to control risks. As a result, the project Preliminary Design Review (PDR) can occur as late as 5 years before the launch and Mission Concept Review (MCR) will occur 2 years before PDR.

Table 6-4 provides a notional schedule of mission implementation, where Fiscal Year (FY) N denotes the first year of Phase A. Establishment of a science working group will occur 3 years before Phase A. The level 1 mission requirements will be finalized 1 year before Phase A, and the level 2 mission requirements will be finalized by MCR.

Table 6-4 Notional Schedule of Mission Implementation

7. Summary

Globally-distributed atmospheric CO_2 measurements are essential for understanding the Earth's carbon cycle and its interactions with the climate. A critical remote sensing challenge is to provide atmospheric CO_2 measurements with sufficient coverage, accuracy and sampling frequency to allow the locations and magnitudes of CO_2 sources and sinks to be inferred from the small changes they cause in atmospheric CO_2 concentrations.

Two satellite missions have been deployed for several years to specifically measure atmospheric CO_2 using passive spectrometers: Japan Aerospace Exploration Agency's (JAXA's) GOSAT satellite and NASA's OCO-2 mission. The contributions of these passive missions towards understanding the global carbon cycle have been significant. However, these passive approaches have inherent limitations in coverage, since favorable conditions require sunlit scenes, free of clouds, with low scattering, and with accurate estimates of surface elevation within their footprint. There are many important regions for carbon cycle and climate studies where favorable conditions seldom occur. For passive sensors, atmospheric conditions such as clouds and variations in scattering, coupled with surface elevation errors (which change the length of the measurement path) can cause bias. These biases increase for cloudy scenes and/or vary with solar zenith angle and are particularly prevalent in the tropics and at high latitudes. The sparse coverage at high latitudes is a particularly serious limitation.

In contrast, the ASCENDS mission carries its own laser source whose characteristics are carefully optimized for these measurements. This approach allows simultaneous measurements of CO_2 column absorption and range to be taken day and night, over ocean and land surfaces, at all latitudes at all times of year, and through optically-thin clouds and aerosols. The lidar approach also allows altitude-weighted measurements with enhanced sensitivity to CO_2 in the lower troposphere, where the CO_2 concentrations respond more strongly to surface fluxes. Because the lidar has a small FOV and is nadir-pointed, it can see through gaps in clouds. The ASCENDS capabilities will enable more frequent observations of critical Arctic and tropical regions and the Southern Ocean, especially in the wintertime, when the ocean is otherwise inaccessible to passive measurements. Since ASCENDS can make measurements regardless of sun angle and local time, various non-sun-synchronous orbits also can be considered to provide additional information about the diurnal cycle of flux.

NASA organized the ASCENDS ad hoc Science Definition Team to lead the mission definition activities. Their work has focused on developing the mission's science and measurement objectives, conducting science mission modeling studies, and carrying out initial engineering studies of spacecraft concepts.

Observing System Simulation Experiments (OSSEs) were conducted to assess the characteristics of the CO_2 fluxes that can be inferred from space-based lidar measurements with various candidate levels of measurement precision and accuracy. A variety of modeling approaches were employed that allowed cross-checking the findings from individual models. The mission simulation analysis has identified some mission science tradeoffs and led to the formulation of an initial set of ASCENDS measurement requirements. The OSSE results primarily show: 1) ASCENDS will resolve statistically significant differences in total column CO_2 concentrations, resulting from foreseeable changes in surface flux over the entire globe, including over high latitudes throughout the year; 2) ASCENDS will enable improved estimation of carbon fluxes with reduced uncertainty at global to regional scales; and 3) ASCENDS data, with lower systematic errors and improved

spatial and temporal coverage, will constrain surface fluxes significantly better than passive sensors such as GOSAT and OCO-2.

The largest fraction of the ASCENDS work involved developing and demonstrating candidate lidar approaches in airborne campaigns. Two candidate techniques, using direct-detection lidar approaches that measure both range and CO_2, have been demonstrated using an absorption line near 1570 nm. Two other approaches have demonstrated measurements of CO_2 using a line near 2051 nm: a CW heterodyne approach and a pulsed direct-detection approach that measures both range and CO_2 absorption using the same line. NASA's Earth Science Technology Office has supported the development of the key lidar technologies. All approaches made substantial progress during the ASCENDS definition activity and a number of papers have been published reporting precise airborne lidar measurements of XCO_2 with low bias under a variety of measurement conditions.

Preliminary instrument and space mission engineering studies also have been conducted on generic lidar candidate instruments that are suitable for the mission. The payload parameters fit comfortably with a medium-sized spacecraft bus to be flown in a polar ~400 km altitude orbit. No significant engineering issues were identified during this stage of the mission definition.

Recently, however, the NRC 2017 Decadal Survey for Earth Science and Applications from Space (NASEM, 2018) recommended that future NASA greenhouse gas missions compete within the lower-NASA-cost Explorer Mission Category. This creates new affordability challenges for an ASCENDS-like mission to fit into the assigned NASA cost cap. This consideration will need to be factored into technology developments, science mission objectives and possible international collaborations to meet the important mission goals.

A number of activities are recommended to carry forward a possible ASCENDS development in the future. These are summarized below and listed in priority order in each focus area.

Modeling Activities:

- *Further define the role of an ASCENDS-like mission in a future international greenhouse gas constellation combining active and passive space measurements to obtain robust estimates of carbon fluxes and budgets at a wide range of spatiotemporal scales.*
- *Test the possible benefit of updated ASCENDS performance for diurnal information by examining dawn/dusk and precessing orbits.*
- *Examine the advantages of vertical profile information from ASCENDS measurements above cloud tops and with multi-layer CO_2 retrievals.*

Atmospheric Analyses Activities:

- *Expand the baseline analysis of the impact of surface and upper-air meteorological uncertainties for different ASCENDS instrument and retrieval approaches to include improved statistical metrics for uniform analysis and comparisons.*
- *Update the representative data sets of observed and modeled atmospheric state parameters for use in assessment of proposed instrument performance. Data sets should ideally include new data that are not represented by current observations particularly in the Southern Ocean and polar environments.*

Airborne Lidar Measurement and Application Activities:

- *Conduct additional measurement campaigns over the Arctic at different times of year.*

- *Demonstrate CO_2 flux determinations based on the airborne lidar data. Some important investigations include measuring CO_2 fluxes from the Arctic and from the tropics, from large areas of rapidly growing crops in the summertime, as well as CO_2 emissions from urban areas.*
- *Compare airborne lidar and satellite CO_2 column measurements under a variety of atmospheric conditions and surface types.*
- *Improve the fidelity of numerical simulations of space lidar measurements for the ASCENDS mission to include updated lidar measurement models and measurements to the tops of clouds where appropriate.*

Lidar Technology Development Activities:

- *Demonstrate the laser powers needed to meet the required performance for the ASCENDS mission, while maintaining the other required laser properties.*
- *Explore lidar technologies that might enable lower cost ASCENDS mission approaches.*
- *Conduct further lidar instrument and mission studies to update technical and cost tradeoffs.*

Mission Planning Activities:

- *Explore international partnerships to potentially enable an ASCENDS-like mission within NASA's Explorer Class funding limits.*
- *Assess instrument accommodations for an ASCENDS-like mission option that might be flown as one or more secondary payloads.*

This ASCENDS definition study has shown that an orbiting IPDA lidar will allow CO_2 measurements to be made over a much wider variety of conditions than is possible with passive sensors. These more accurate measurements, with lower bias and wider spatial and diurnal coverage, are key to addressing important questions about the locations, strengths and evolution of the regional CO_2 fluxes needed for climate modeling.

Appendices

A. References

[ACOS B2.10 REF] ACOS Level 2 Standard Product: Data User's Guide, v3.4, (2013). *CO₂ Virtual Science Data Environment*. Retrieved from: https://co2.jpl.nasa.gov/static/docs/v3.4_DataUsersGuide-RevB_131028.pdf

[Anon, n.d.] Anon. (n.d.). Standard atmospheric lapse rate. *National Oceanic and Atmospheric Administration (NOAA), NASA, United States Air Force.* Retrieved from: http://ntrs.nasa.gov/archive/nasa/casi.ntrs.nasa.gov/19770009539.pdf

 [Aben et al., 2007] Aben, I., O. Hasekamp and W. Hartmann, (2007, April 3). Uncertainties in the space-based measurements of CO₂ columns due to scattering in the Earth's atmosphere. *J. Quant. Spectrosc. Radiat. Transfer, Vol. 104* (Issue 3), pp. 450-459

[Abshire et al., 2005] Abshire J. B., X. Sun, H. Riris, J. M. Sirota, J. F. McGarry, S. Palm, D. Yi and P. Liiva, (2005, November). Geoscience Laser Altimeter System (GLAS) on the ICESat Mission: On-orbit measurement performance. *Geophys. Res. Lett., Vol. 32* (Issue 21). L21S02. DOI: 10.1029/2005GL024028

[Abshire et al., 2008] Abshire, J. B., H. Riris, G. Allan, S. Kawa, J. Mao, E. Wilson, M. Stephen, M. Krainak, X. Sun and C. Weaver, (2008). Laser sounder approach for global measurements of tropospheric CO₂ mixing ratio from space. 24th International Laser Radar Conference, Boulder, Colorado.

[Abshire et al., 2010a] Abshire, J. B., H. Riris, G. R. Allan, C. J. Weaver, J. Mao, X. Sun, W. E. Hasselbrack, … and E. V. Browell, (2010, November 2). A lidar approach to measure CO₂ concentrations from space for the ASCENDS Mission. *Proc. SPIE Vol. 7832, Lidar Technologies, Techniques, and Measurements for Atmospheric Remote Sensing VI,* paper 78320D. Retrieved from: http://dx.doi.org/10.1117/12.868567. DOI: 10.1117/12.868567

[Abshire et al., 2010b] Abshire, J. B., H. Riris, G. R. Allan, C. J. Weaver, J. Mao, X. Sun, W. E. Hasselbrack, S. R. Kawa, and S. Biraud, (2010, November). Pulsed airborne lidar measurements of atmospheric CO₂ column absorption. *Tellus B, Vol. 62 (Issue 5)*, pp. 770-783. DOI: 10.1111/j.1600-0889.2010.00502.x

[Abshire et al., 2011] Abshire, J. B., H. Riris, G. R. Allan, C. J. Weaver, J. Mao, X. Sun, W. E. Hasselbrack, M. Rodriguez, and E. V. Browell, (2011). Pulsed airborne lidar measurements of CO₂ column absorption. 2011 Earth Science Technology Forum (ESTF2011), Pasadena, CA, June 21-23, 2011, NASA ESTO ESTF-2011 Conference. Avail from: http://esto.nasa.gov/conferences/estf2011/papers/Abshire_ESTF2011.pdf

[Abshire et al., 2013] Abshire, J. B., H. Riris, C. J. Weaver, J. Mao, G. R. Allan, W. E. Hasselbrack and E.V. Browell, (2013). Airborne measurements of CO₂ column absorption and range using a pulsed direct-detection integrated path differential absorption lidar. *Appl. Opt., Vol. 52 (Issue 19)*, pp. 4446-4461

[Abshire et al., 2014] Abshire, J.B., A. Ramanathan, H. Riris, J. Mao, G.R. Allan, W.E. Hasselbrack, C.J. Weaver, and E.V. Browell, (2014). Airborne Measurements of CO₂

Column Concentration and Range Using a Pulsed Direct-Detection IPDA Lidar. *Remote Sensing* **2014**, *Vol. 6 (Issue 1),* pp. 443-469. DOI:10.3390/rs6010443

[Abshire et al., 2017] Abshire, J.B., H. Riris, G. R. Allan, J. Mao, W. E. Hasselbrack, K. Numata, J. Chen, R. Kawa, J. P. DiGangi, and Y. Choi, (2017). Pulsed Lidar Measurements of CO_2 Column Concentrations in the 2017 ASCENDS Airborne Campaign and Comparison with In-Situ Measurements, *Fall 2017 American Geophysical Union (AGU) Meeting Abstracts,* Paper A21M-03, December 2017.

[Abshire et al., 2018a] Abshire, J.B., A.R. Ramanathan, H. Riris, G.R. Allan, X. Sun, W.E. Hasselbrack, J. Mao, S. Wu, J. Chen, K. Numata, S.R. Kawa, M.Y.M. Yang, and J.DiGangi, (2018). Airborne measurements of CO_2 column concentrations made with a pulsed IPDA lidar using a multiple-wavelength-locked laser and HgCdTe APD detector. *Atmos. Meas. Tech. Vol. 11,* pp. 2001-2025. https://doi.org/10.5194/amt-11-2001-2018

[Abshire et al., 2018b] Abshire, J.B., H. Riris, G. R. Allan, J. Mao, W. E. Hasselbrack, K. Numata, J. Chen, R. Kawa, J. DiGangi, and M. Stephen, (2018). Pulsed Lidar Measurements of CO_2 Column Concentrations in the 2017 ASCENDS Airborne Campaign, and beyond. Paper 6.12, presented at the *14th International Workshop on Greenhouse Gas Measurements from Space* (IWGGMS-2018), Toronto, Canada, May 8 – 10, 2018. Available from: https://iwggms14.physics.utoronto.ca/documents/128/6.12_CO2SounderIWGGMS14.pdf

[Allan et al., 2008] Allan, G.R., H. Riris, J.B. Abshire, X. Sun; E. Wilson, J. F. Burris, and M. A. Krainak, (2008, March). Laser Sounder for Active Remote Sensing Measurements of CO_2 Concentrations. *Proceedings of Aerospace Conference, 2008 IEEE*, pp. 1-7. DOI: 10.1109/AERO.2008.4526387

[Allan et al., 2017] Allan, G. R., M. A. Stephen, A. Yu, J. B. Abshire, S. Wu, J. Chen, and K. Numata, (2017). Optimizing Output Power through Temporal Pulse Shaping. In *Conference on Lasers and Electro-Optics*, OSA Technical Digest (online), (Optical Society of America, 2017), paper JTu5A.87. https://doi.org/10.1364/CLEO_AT.2017.JTu5A.87, (2017).

[Allan et al., 2018] Allan, G. R., J. B. Abshire, H. Riris, J. Mao, W. E. Hasselbrack, K. Numata, J. Chen, R. Kawa, M. Rodriguez, and M. Stephen, (2018). Lidar measurements of CO_2 column concentrations in the Arctic region of North America from the ASCENDS 2017 airborne campaign. *Proc. SPIE 10779, Lidar Remote Sensing for Environmental Monitoring XVI,* 1077906 (24 October 2018).

[Amediek et al., 2008] Amediek, A., A. Fix, M. Wirth and G. Ehret, (2008). Development of an OPO system at 1.57 μm for integrated path DIAL measurement of atmospheric carbon dioxide. *Applied Physics B, 92,* pp. 295.

[Amediek et al., 2009] Amediek, A., A. Fix, G. Ehret, J. Caron, and Y. Durand, (2009). Airborne lidar reflectance measurements at 1.57 μm in support of the A-SCOPE mission for atmospheric CO_2. *Atmos. Meas. Tech., Volume 2, Issue 2,* pp. 755-772. https://doi.org/10.5194/amt-2-755-2009

[Amediek et al., 2013] Amediek, A., X. Sun, and J. B. Abshire, (2013, May). Analysis of Range Measurements From a Pulsed Airborne CO_2 Integrated Path Differential Absorption Lidar. *IEEE Transactions on Geoscience and Remote Sensing, Vol. 51* (Issue 5), pp. 2498-2504. DOI: 10.1109/TGRS.2012.2216884

[Amediek et al., 2017] Amediek, A., G. Ehret, A. Fix, M. Wirth, C. Büdenbender, M. Quatrevalet, C. Kiemle, and C. Gerbig, (2017). CHARM-F-a new airborne integrated-path differential-absorption lidar for carbon dioxide and methane observations: measurement performance and quantification of strong point source emissions. *Applied Optics, Vol. 56*, Issue 18, pp. 5182-5197 (2017), https://doi.org/10.1364/AO.56.005182

[Andres et al., 2011] Andres, R. J., J. S. Gregg, L. Losey, G. Marland, and T. A. Boden, (2011, July), Monthly, global emissions of carbon dioxide from fossil fuel consumption. *Tellus B, Vol. 63* (Issue 3), pp. 309-327.. DOI: 10.1111/j.1600-0889.2011.00530.x

[Andres et al., 2012] Andres, R. J., T. A Boden, F.-M. Bréon, P. Ciais, S. Davis, D. Erickson, J. S. Gregg, … and K. Treanton, (2012). A synthesis of carbon dioxide emissions from fossil-fuel combustion. *Biogeosciences Discuss, Vol. 9,* pp. 1299-1376. DOI: 10.5194/bgd-9-1299-2012

[Aoki et al., 2000] Aoki, T., T. Aoki, M. Fukabori, A. Hachikubo, Y. Tachibana, and F. Nishio, (2000). Effects of snow physical parameters on spectral albedo and bidirectional reflectance of snow surface. *J. Geophys. Res.: Atomospheres, Vol. 105 (Issue D8)*, pp. 10219-10236. DOI: 10.1029/1999JD901122

[Archer et al., 2009] Archer, D., M. Eby, V. Brovkin, A. Ridgwell, L. Cao, U. Mikolajewicz, K. Caldeira, … and K. Tokos, (2009, May). Atmospheric Lifetime of Fossil Fuel Carbon Dioxide. *Annual Review of Earth and Planetary Sciences, Vol. 37,* pp. 117 -134.

[Badger et al., 2013] Badger, M. P. S., D. N. Schmidt, A. Mackensen, and R. D. Pancost, (2013, October 28). High-resolution alkenone palaeobarometry indicates relatively stable pCO_2 during the Pliocene (3.3–2.8 Ma). *Phil. Trans. R. Soc. A, Vol. 371.*

[Bagheri et al., 2015] Bagheri, M., G. Spiers, C. Frez, S. Forouhar, and F. Aflatouni, (2015). Linewidth Measurement of Distributed-Feedback Semiconductor Lasers Operating Near 2.05 μm. *IEEE Photonics Technology. Letters, Vol. 27, Issue 18,* pp. 1934–1937, Sept. 15, 2015.

[Baker et al., 2006] Baker, D. F., S. C. Doney, and D. S. Schimel, (2006, November). Variational data assimilation for atmospheric CO_2. *Tellus Series B Chemical and Physical Meteorology, Vol. 58* (Issue 5), pp. 359-365.

[Baker et al., 2008] Baker, I.T., L. Prihodko, A.S. Denning, M. Goulden, S. Miller, and H.R. da Rocha, (2008, March). Seasonal drought stress in the Amazon: Reconciling models and observations. *Journal of Geophysical Research: Biogeosciences (2005–2012), Vol. 113,* (Issue G1). G00B01, DOI: 10.1029/2007JG000644

[Baker et al., 2010] Baker, D. F., H. Bösch, S. C. Doney, D. O'Brien, and D. S. Schimel, (2010). Carbon source/sink information provided by column CO_2 measurements from the Orbiting Carbon Observatory, *Atmos. Chem. Phys., Volume 10, Issue 9,* pp. 4145-4165, https://doi.org/10.5194/acp-10-4145-2010

[Ballantyne et al., 2012] Ballantyne, A. P., C.B. Alden, J.B. Miller, P.P. Tans, and J.W.C. White, (2012, August 2). Increase in observed net carbon dioxide uptake by land and oceans during the past 50 years. *Nature 488,* pp.70-72. DOI: 10.1038/nature11299

[Barton and Scott, 1986] Barton, I. J., and J. C. Scott, (1986). Remote measurement of surface pressure using the oxygen A-band of absorption. *Appl. Opt., Vol. 25, Issue 19,* pp. 3502-3507 (1986), https://doi.org/10.1364/AO.25.003502

[Basu et al., 2013] Basu, S., S. Guerlet, A. Butz, S. Houweling, O. Hasekamp, I. Aben, P. Krummel, … and D. Worthy, (2013). Global CO_2 fluxes estimated from GOSAT retrievals of total column CO_2. *Atmospheric Chemistry and Physics, 13,* pp. 8695–8717. DOI: 10.5194/acp-13-8695-2013

[Basu et al., 2018] Basu, S., D. F. Baker, F. Chevallier, P. K. Patra, J. Liu, and J. B. Miller, (2018). The impact of transport model differences on CO_2 surface flux estimates from OCO-2 retrievals of column average CO_2. *Atmos. Chem. Phys., Vol. 18, Issue 10,* pp. 7189-7215, https://doi.org/10.5194/acp-18-7189-2018, 2018.

[Bey et al., 2001] Bey, I., D. J. Jacob, R. M. Yantosca, J. A. Logan, B. D. Field, A. M. Fiore, Q. Li, H. Y. Liu, L. J. Mickley, and M. G. Schultz, (2001). Global modeling of tropospheric chemistry with assimilated meteorology: Model description and evaluation. *Journal Of Geophysical Research, Vol. 106, No. D19*, pp. 23073-23095, October 16, 2001.

[Beck et al., 2011] Beck, J.D., R. Scritchfield, P. Mitra, W. Sullivan III, A.D. Gleckler, R. Strittmatter and R.J. Martin, (2011, May 12). Linear-mode photon counting with the noiseless gain HgCdTe e-APD. *Proc. SPIE 8033, Advanced Photon Counting Techniques V,* 80330N. DOI: 10.1117/12.886161

[Beck et al., 2013] Beck, J., J. McCurdy, M. Skokan, C. Kamilar, R. Scritchfield, T. Welch, P. Mitra, X. Sun, J. Abshire, and K. Reiff, (2013, May 21). A highly sensitive multi-element HgCdTe e-APD detector for IPDA lidar applications. *Proc. SPIE 8739, Sensors and Systems for Space Applications VI, 87390V*. Retrieved from: http://dx.doi.org/10.1117/12.2018083. DOI: 10.1117/12.2018083

[Beck et al., 2014] Beck, J., T. Welch, P. Mitra, K. Reiff, X. Sun, and J. Abshire, (2014). A Highly Sensitive Multi-element HgCdTe e-APD Detector for IPDA Lidar Applications. *Journal of Electronic Materials, Volume 43, Issue 8*, pp. 2970-2977, August 2014, First Online: 10-May-2014. https://doi.org/10.1007/s11664-014-3164-8

[Beer et al., 2010] Beer, C., M. Reichstein, E. Tomelleri, P. Ciais, M. Jung, N. Carvalhais, C. Rodenbeck, M. A. Arain, D. Baldocchi, G. B. Bonan, A. Bondeau, A. Cescatti, G. Lasslop, A. Lindroth, M. Lomas, S. Luyssaert, H. Margolis, K. W. Oleson, O. Roupsard, E. Veenendaal, N. Viovy, C. Williams, F. I. Woodward, and D. Papale, (2010). Terrestrial Gross Carbon Dioxide Uptake: Global Distribution and Covariation with Climate. *Science, Volume 329, Issue 5993*, pp. 834-83, 13 August 2010, doi: 10.1126/science.1184984

[Belikov et al., 2014] Belikov, D.A., A. Bril, S. Maksyutov, S. Oshchepkov, T. Saeki, H. Takagi, Y. Yoshida, … and T. Yokota, (2014). Column-averaged CO_2 concentrations in the subarctic from GOSAT retrievals and NIES transport model simulations *Polar Science*. Retrieved from: http://dx.doi.org/10.1016/j.polar.2014.02.002

[Boden et al., 2013] Boden, T.A., G. Marland, and R.J. Andres, (2013). Global, Regional, and National Fossil-Fuel CO_2 Emissions. *Carbon Dioxide Information Analysis Center*, Oak Ridge National Laboratory, U.S. Department of Energy, Oak Ridge, Tenn., U.S.A. doi 10.3334/CDIAC/00001_V2013

[Boden et al., 2017] Boden, T.A., G. Marland, and R.J. Andres, (2017). Global, Regional, and National Fossil-Fuel CO$_2$ Emissions. *Carbon Dioxide Information Analysis Center*, Oak Ridge National Laboratory, U.S. Department of Energy, Oak Ridge, Tenn., U.S.A. doi 10.3334/CDIAC/00001_V2017

[Bell et al., 2018] Bell, E., C. O'Dell, E. Browell, B. Lin, S. Kooi, J. Dobler, and K. Davis, (2018). Evaluation of OCO-2 Small-Scale Variability Using Lidar and In Situ CO 2 Observations from the ACT-America Campaign. *14th International Workshop on Greenhouse Gas Measurements from Space* (IWGGMS-2018), Toronto, Canada, May 8 – 10, 2018.

[Bösch et al., 2011] Bösch, H., D. Baker, B. Connor, D. Crisp and C. Miller, (2011). Global Characterization of CO$_2$ Column Retrievals from Shortwave-Infrared Satellite Observations of the Orbiting Carbon Observatory-2 Mission. *Remote Sens., Vol. 3 (Issue 2)*, pp. 270-304. DOI: 10.3390/rs3020270, 2011

[Bovensmann et al., 2010] Bovensmann, H., M. Buchwitz, J. P. Burrows, M. Reuter, T. Krings, K. Gerilowski, O. Schneising, J. Heymann, A. Tretner, and J. Erzinger, (2010). A remote sensing technique for global monitoring of power plant CO$_2$ emissions from space and related applications. *Atmos. Meas. Tech., 3,* pp. 781–811. DOI: 10.5194/amt-3-781-2010

[Bréon et al., 2002] Bréon, F.M., F. Maignan, M. Leroy, and I. Grant, (2002). Analysis of hot spot directional signatures measured from space. *J. Geophys. Res., Vol. 107* (Issue 16), pp. 4282-4296.

[Browell et al., 2008] Browell, E. V., M. E. Dobbs, J. Dobler, S. Kooi, Y. Choi, F. W. Harrison, B. Moore III, and T. S. Zaccheo, (2008). Airborne demonstration of 1.57-micron laser absorption spectrometer for atmospheric CO$_2$ measurements. *Proc. of 24th International Laser Radar Conference, S06P-13,* Boulder, CO, June 23-27, 2008.

[Browell et al., 2009a] Browell, E. V., M. E. Dobbs, J. Dobler, S. Kooi, Y. Choi, F. W. Harrison, B. Moore III, and T. S. Zaccheo, (2009). First Airborne Laser Remote Measurements of Atmospheric Carbon Dioxide. Presented at *Fourth Symposium on Lidar Atmospheric Applications, Proc. 89th AMS Annual Meetin*g, Phoenix, Arizona, January 11-15, 2009.

[Browell et al., 2009b] Browell, E. V., M. E. Dobbs, J. Dobler, S. Kooi, Y. Choi, F. W. Harrison, B. Moore III, and T. S. Zaccheo, (2009). First airborne laser remote measurements of atmospheric CO$_2$ for future active sensing of CO$_2$ from Space. Presented at the *Proceedings of the 8th International Carbon Dioxide Conference,* Jena, Germany, 13–18 September 2009.

[Browell et al., 2010] Browell, E.V., J. Dobler, S. Kooi, Y. Choi, F.W. Harrison, B. Moore III, and T. Scott Zaccheo, (2010). Airborne Validation of Laser Remote Measurements of Atmospheric Carbon Dioxide. *Proc., 25th International Laser Radar Conference 2010, S6O-03*, St. Petersburg, Russia, July 5-9, 2010 (ILRC 25).

[Browell et al., 2011] Browell, E.V., J.T. Dobler, S.A. Kooi, M.A. Fenn, Y. Choi, S.A. Vay, F.W. Harrison, and B. Moore, (2011). Airborne laser CO$_2$ column measurements: Evaluation of precision and accuracy under wide range of conditions. Presented at the *Fall AGU Meeting*, San Francisco, California, 5–9 December 2011.

[Browell et al., 2012] Browell, E.V., J.T. Dobler, S.A. Kooi, M.A. Fenn, Y. Choi, S.A. Vay, F. W. Harrison, and B. Moore III, (2012). Airborne Validation of Laser CO₂ and O₂ Column Measurements. *Proc. 92ⁿᵈ AMS Annual Meeting,* New Orleans, LA, January 22-26, 2012.

[Bruneau et al., 2006] Bruneau, D., F. Gibert, P.H. Flamant and J. Pelon, (2006). Complementary study of differential absorption lidar optimization in direct and heterodyne detections. *Appl. Opt., Vol. 45* (Issue 20)*,* pp. 4898-4908.

[Buchwitz et al., 2017] Buchwitz, M., M. Reuter, O. Schneising, W. Hewson, R.G. Detmers, H. Boesch, O.P. Hasekamp, I. Aben, H. Bovensmann, J. P. Burrows, A. Butz, F. Chevallier, B. Dils, C. Frankenberg, J. Heymann, G. Lichtenberg, M. De Mazière, J. Notholt, R. Parker, T. Warneke, C. Zehner, D. W. T. Griffith, N. M. Deutscher, A. Kuze, H. Suto, D. Wunch, (2017). Global satellite observations of column-averaged carbon dioxide and methane: The GHG-CCI XCO₂ and XCH₄ CRDP3 data set. *Remote Sensing of Environment, Vol. 203*, pp. 276-295, 2017, doi: 10.1016/j.rse.2016.12.027

[Camacho-de Coca et al., 2004] Camacho-de Coca, F., F.M. Bréon, M. Leroy, and F.J. Garcia-Haro, (2004). Airborne measurement of hot spot reflectance signatures, *Remote Sens. Environ., Vol. 90 (Issue 1)*, pp. 63-75.

[Campbell et al., 2014a] Campbell, J.F., B. Lin, and A. Nehrir, (2014). Advanced sine wave modulation of continuous wave laser system for atmospheric CO₂ differential absorption measurements. *Applied Optics, Volume 53 (Issue 5)*, pp. 816-829.
Retrieved from: http://www.opticsinfobase.org/ao/abstract.cfm?URI=ao-53-5-816

[Campbell et al., 2014b] Campbell, J. F., B. Lin, A. R. Nehrir, F.W. Harrison, and M. D. Obland, (2014). High Resolution CW Lidar Altimetry using Repeating Intensity-Modulated Waveforms and Fourier Transform Reordering*, Opt. Letters, Vol. 39, Issue 20,* pp. 6078-6081, 2014. https://doi.org/10.1364/OL.39.006078

[Campbell et al., 2014c] Campbell, J., B. Lin, A. Nehrir, F.W. Harrison, M. D. Obland, (2014). Binary phase shift keying on orthogonal carriers for multi-channel CO₂ absorption measurements in the presence of thin clouds. *Optics Express, Vol. 22, Suppl. 6*: A1634 – A1640, October 2014. DOI:10.1364/OE.22.0A1634

[Campbell et al., 2014d] Campbell, J., B. Lin, A. Nehrir, F.W. Harrison, and M. Obland, (2014). Super-resolution technique for CW lidar using Fourier transform reordering and Richardson–Lucy deconvolution. *Optics Letters, Vol. 39, Issue 24*, pp. 6981-6984.

[Caron and Durand, 2009] Caron, J., and Y. Durand, (2009). Operating wavelengths optimization for a spaceborne lidar measuring atmospheric CO₂. *Appl. Opt., Vol. 48* (Issue 28)*,* pp. 5413-5422.

[Chatterjee et al., 2017] Chatterjee, A., M. M. Gierach, A. J. Sutton, R. A. Feely, D. Crisp, A. Eldering, M. R. Gunson, C. W. O'Dell, B. B. Stephens, and D. Schimel, (2017). Influence of El Niño on atmospheric CO₂ over the tropical Pacific Ocean: Findings from NASA's OCO-2 mission. *Science Vol. 358, Issue 6360,* eaam5776, 2017. DOI: 10.1126/science.aam5776

[J. R. Chen, et al., 2012] Chen, J. R., K. Numata, and S. T. Wu, (2012). Error reduction methods for integrated-path differential-absorption lidar measurements. *Optics Express, Vol. 20, Issue 14,* pp. 15589-15609. Retrieved from: https://doi.org/10.1364/OE.20.015589

[J. R. Chen, et al., 2014] Chen, J. R., K. Numata, and S. T. Wu, (2014). Error reduction in retrievals of atmospheric species from symmetrically measured lidar sounding absorption spectra. *Optics Express, Vol. 22, Issue 21,* pp. 26055-26075. Retrieved from: https://doi.org/10.1364/OE.22.026055

[Y. Chen, et al., 2006] Chen, Y., S. Sun-Mack, R. F. Arduini, and P. Minnis, (2006). Clear-sky and surface narrowbandalbedo variations derived from VIRS and MODIS data. *Proc. AMS 12th Conf. Atmos. Radiation,* Madison, WI, July 10-14, CD-ROM, 5.6.

[Chevallier et al., 2007] Chevallier, F., F.-M. Bréon, and P. J. Rayner, (2007). Contribution of the Orbiting Carbon Observatory to the estimation of CO₂ sources and sinks: Theoretical study in a variational data assimilation framework. *J. Geophys. Res., 112,* D09307, DOI: 10.1029/2006JD007375

[Chevallier et al., 2009] Chevallier, F., S. Maksyutov, P. Bousquet, F. M. Bréon, R. Saito, Y. Yoshida, and T. Yokota, (2009). On the accuracy of the CO₂ surface fluxes to be estimated from the GOSAT observations. *Geophys. Res. Lett., Vol. 36,* L19807. DOI: 10.1029/2009GL040108

[Chevallier et al., 2014] Chevallier, F., P. I. Palmer, L. Feng, H. Boesch, C. W. O'Dell, and P. Bousquet, (2014). Toward robust and consistent regional CO₂ flux estimates from in situ and spaceborne measurements of atmospheric CO₂. *Geophys. Res. Lett*., *Vol. 41 (Issue 3)*, pp. 1065–1070. DOI: 10.1002/2013GL058772

[Choi et al., 2008]   Choi, Y., S. A. Vay, K. P. Vadrevu, A. J. Soja, J–H Woo, S. R. Nolf, G. W. Sachse, … and H. E. Fuelberg, (2008). Characteristics of the atmospheric CO₂ signal as observed over the conterminous United States during INTEX NA (Intercontinental Chemical Transport Experiment-North America). *J. Geophys. Res., Vol. 113 (Issue D7)*, 2008. D07301, DOI: 10.1029/2007JD008899

[Ciais et al., 2010] Ciais, P., J. G. Canadell, S. Luyssaert, F. Chevallier, A. Shvidenko, Z. Poussi, M. Jonas, P. Peylin, A. W. King, E.-D. Schulze, S. Piao, C. Rödenbeck, W. Peters, and F.-M. Bréon, (2010, October). Can we reconcile atmospheric estimates of the Northern terrestrial carbon sink with land-based accounting? *Current Opinion in Environmental Sustainability, Vol. 2 (Issue 4),* pp. 225-230.

[Ciais et al., 2013] Ciais, P., C. Sabine, G. Bala, L. Bopp, V. Brovkin, J. Canadell, A. Chhabra, R. DeFries, J. Galloway, M. Heimann, C. Jones, C. Le Quéré, R.B. Myneni, S. Piao and P. Thornton, (2013). Carbon and Other Biogeochemical Cycles. In: *Climate Change 2013: The Physical Science Basis. Contribution of Working Group I to the Fifth Assessment Report of the Intergovernmental Panel on Climate Change* [Stocker, T.F., D. Qin, G.-K. Plattner, M. Tignor, S.K. Allen, J. Boschung, A. Nauels, Y. Xia, V. Bex and P.M. Midgley (eds.)]. Cambridge University Press, Cambridge, United Kingdom and New York, NY, USA.

[Clough et al., 1992] Clough, S. A., M. J. Iacono, and J. Moncet, (1992). Line-by-line calculations of atmospheric fluxes and cooling rates: Application to water vapor. *J. Geophys. Res. Atmos.*

Vol. 97, Issue D14, pp. 15761-715785, 20 October 1992. https://doi.org/10.1029/92JD01419

[Clough and Iacono, 1995] Clough, S. A., and M. J. Iacono, (1995). Line-by-line calculation of atmospheric fluxes and cooling rates: 2. Application to carbon dioxide, ozone, methane, nitrous oxide and the halocarbons. *J. of Geophys. Res., Vol. 100 (Issue D8)*, pp. 16519-16535, 20 August 1995. DOI: 10.1029/95JD01386

[Clough et al., 2005] Clough, S.A., M. W. Shephard, E.J. Mlawer, J.S. Delamere, M.J. Iacono, K. Cady-Pereira, S. Boukabara, and P.D. Brown, (2005, March). Atmospheric radiative transfer modeling: a summary of the AER codes. Short Communication. *J. Quant. Spectrosc. Radiat. Transfer, Vol. 91* (Issue 2), pp.233-244.

[Conway et al., 1994] Conway, T. J., P. P. Tans, L. S. Waterman, K. W. Thoning, D. R. Kitzis, K. A. Masarie, and N. Zhang, (1994). Evidence for interannual variability of the carbon cycle from the National Oceanic and Atmospheric Administration/Climate Monitoring and Diagnostics Laboratory Global Air Sampling Network. *J. Geophys. Res., Vol. 99,* (Issue D11), pp. 22831–22855. DOI: 10.1029/94JD01951

[Conway et al., 2009] Conway, T.J., P.M. Lang, and K.A. Masarie, (2009, July 15). Atmospheric Carbon Dioxide Dry Air Mole Fractions from the NOAA ESRL Carbon Cycle Cooperative Global Air Sampling Network, 1968-2008., Version: 2009-07-15. Retrieved from: ftp://cdiac.ornl.gov/pub/ndp005/README_flask_co2.html

[Creeden et al., 2008] Creeden D., M. Jiang, P. A. Budni, P. A. Ketteridge, S. D. Setzler, Y. E. Young, J. C. McCarthy, P. G. Schunemann, T. M. Pollak, P. Tayebati, and E. P. Chicklis, (2008, April 14). Thulium fiber laser-pumped mid-IR OPO. *SPIE Proc., Vol. 6952.* DOI: 10.1117/12.775196

[Crisp et al., 2012] Crisp, D., B. M. Fisher, C. O'Dell, C. Frankenberg, R. Basilio, H. Bösch, L. R. Brown, … and Y. L. Yung, (2012). The ACOS CO₂ retrieval algorithm -- Part II: Global X$_{CO2}$ data characterization. (2012). *Atmos. Meas. Tech., Vol. 5,* pp. 687–707. DOI: 10.5194/amt-5-687-2012

[Crowell et al., 2015] Crowell, S., P. Rayner, S. Zaccheo, and B. Moore, (2015). Impacts of Atmospheric State Uncertainty on O₂ Measurement Requirements for the ASCENDS Mission. *Atmospheric Measurement Techniques Vol. 8, Issue 7,* pp. 2685-2697, 2015. DOI:10.5194/amt-8-2685-2015

[Crowell et al., 2018] Crowell, S. M. R., S. R. Kawa, E. V. Browell, D. M. Hammerling, B. Moore, K. Schaefer, and S. C. Doney, (2018). On the Ability of Space-Based Passive and Active Remote Sensing Observations of CO₂ to Detect Flux Perturbations to the Carbon Cycle. *Journal of Geophysical Research: Atmospheres, Vol. 123, Issue 2*, pp. 1460–1477. https://doi.org/10.1002/2017JD027836

[Davis and Grainger, 2003] Davis, and C. A. Grainger, (2003). A near-field tool for simulating the upstream influence of atmospheric observations: The Stochastic Time-Inverted Lagrangian Transport (STILT) model, *Geophys. Res., Vol. 108* (D16), pp. 4493. DOI: 10.1029/2002JD003161

[Dee et al., 2011] Dee, D.P., S. M. Uppala, A. J. Simmons, P. Berrisford, P. Poli, S. Kobayashi, U. Andrae, … and F. Vitart, (2011, April 28). The ERA-Interim reanalysis: configuration and

performance of the data assimilation system. *Quarterly Journal of the Royal Meteorological Society, Vol. 137* (Issue 656)*,* pp.553-597. DOI: 10.1002/qj.828. Retrieved from http://onlinelibrary.wiley.com/doi/10.1002/qj.828/abstract

[DeFries et al., 2002] DeFries, R.S., R. A. Houghton, M. C. Hansen, C. B. Field, D. Skole, and J. Townshend, (2002). Carbon emissions from tropical deforestation and regrowth based on satellite observations for the 1980s and 1990s. *Proc. Natl. Acad. Sci., Vol. 99* (No. 22), pp.14256-14261. DOI: 10.1073/pnas.182560099

[Denning et al., 1996] Denning, A.S., G.J. Collatz, C. Zhang, D.A. Randall, J.A. Berry, P.J. Sellers, G.D. Colello, and D.A. Dazlich, (1996, September). Simulations of terrestrial carbon metabolism and atmospheric CO_2 in a general circulation model, Part 1: Surface carbon fluxes. *Tellus B*, *Vol. 48 (Issue 4),* pp. 521-542. DOI: 10.1034/j.1600-0889.1996.t01-2-00009.x

[Deng, et al., 2014] Deng, F., D. B. A. Jones, D. K. Henze, N. Bousserez, K. W. Bowman, J. B. Fisher, R. Nassar, … T. Warneke, (2014, April 11). Inferring regional sources and sinks of atmospheric CO2 from GOSAT XCO_2 data. *Atmos. Chem. Phys., Vol. 14,* pp. 3703–3727. DOI: 10.5194/acp-14-3703-2014

[Devi et al., 2007a] Malathy Devi, V., D. C. Benner, L. R. Brown, C. E. Miller, and R. A. Toth, (2007). Line mixing and speed dependence in CO_2 at 6348cm^{-1}: Positions, intensities, and air- and self-broadening derived with constrained multispectrum analysis. *Journal of Molecular Spectroscopy*, *Vol. 242* (Issue 2), pp. 90-117. Retrieved from http://adsabs.harvard.edu/abs/2007JMoSp.242.90M

[Devi et al., 2007b] Malathy Devi, V., D. C. Benner, L. R. Brown, C. E. Miller, and R. A. Toth, (2007, September). Line mixing and speed dependence in CO_2 at 6227.9cm^{-1}: Constrained multispectrum analysis of intensities and line shapes in the 30013←00001 band. *Journal of Molecular Spectroscopy, Vol. 245* (Issue 1), pp.52-80. Retrieved from http://www.sciencedirect.com/science/article/pii/S0022285207001300

[Disney et al., 2009] Disney, M. I., P. E. Lewis, M. Bouvet, A Prieto-Blanco, and S. Hancock. (2009). Quantifying surface reflectivity for spaceborne lidar via two independent methods, *IEEE Trans. on Geoscience and Remote Sensing, Vol. 47,* pp. 3262-3271. DOI:10.1109/TGRS.2009.2019268

[Dlugokencky et al., 2013] Dlugokencky, E.J., P.M. Lang, K.A. Masarie, A.M. Crotwell, and M.J. Crotwell, (2013). Atmospheric Carbon Dioxide Dry Air Mole Fractions from the NOAA ESRL Carbon Cycle Cooperative Global Air Sampling Network, 1968-2012, Version: 2013-08-28. Retrieved from: ftp://aftp.cmdl.noaa.gov/data/trace_gases/co2/flask/surface/

[Dlugokencky and Tans, 2018] Dlugokencky, E., and P. P. Tans, Globally averaged marine surface annual mean data. National Oceanic & Atmospheric Administration, Earth System Research Laboratory (NOAA/ESRL). Accessed 09/06/2018. Retrieved from: www.esrl.noaa.gov/gmd/ccgg/trends/

[Dobbs et al., 2007] Dobbs, M., W. Sharp, and J. Jenny, (2007). A Sinusoidal Modulated-CW Integrated Path Differential Absorption LIDAR for Mapping Sources and Sinks of Carbon Dioxide from Space. *Proc. 14th Coherent Laser Radar Conference 2007*, Snowmass, CO, July 8-13, 2007.

[Dobbs et al., 2008] Dobbs, M., J. Dobler, M. Braun, D. McGregor, J. Overbeck, B. Moore III, E. Browell, and T. S. Zaccheo, (2008). A Modulated CW Fiber Laser-Lidar Suite for the ASCENDS Mission. *Proc. 24th International Laser Radar Conference, S01O-04,* Boulder, CO, June 23-27, 2008.

[Dobler et al., 2011a] Dobler, J. T., J. Nagel, V. Temyanko, B. Karpowicz, S. Zaccheo, and M. Braun, (2011). Fiber Raman Amplifier Development for Laser Absorption Spectroscopy Measurements of Atmospheric Oxygen near 1.26 Micron. *The 2011 Earth Science Technology Forum (ESTF2011),* Pasadena, CA, June 21-23, 2011. Retrieved from: http://esto.nasa.gov/conferences/estf2011/papers/Dobler_ESTF2011.pdf

[Dobler et al., 2011b] Dobler, J.T., J. Nagel, V. Temyanko, B. Karpowicz, and T. S. Zaccheo, (2011). Lidar Measurements of Atmospheric Oxygen Using a 1.27-Micron Raman Amplifier. In *CLEO: 2011 – Laser Applications to Photonic Applications*, OSA Technical Digest (CD) (Optical Society of America, 2011), paper JTuE1. https://doi.org/10.1364/CLEO_AT.2011.JTuE1

[Dobler et al., 2013] Dobler, J. T., F. W. Harrison, E. V. Browell, B. Lin, D. McGregor, S. Kooi, Y. Choi, and S. Ismail, (2013). Atmospheric CO_2 column measurements with an airborne intensity-modulated continuous-wave 1.57 μm fiber laser lidar. *Applied Optics, Vol. 52 (Issue 12)*, pp. 2874-2892. Retrieved from: http://dx.doi.org/10.1364/AO.52.002874

[Doney et al., 2006] Doney, S.C., K. Lindsay, I. Fung and J. John, (2006, July). Natural Variability in a Stable, 1000-Yr Global Coupled Climate-Carbon Cycle Simulation. *J. Climate, Vol. 19 (Issue 13)* pp. 3033-3054.

[Doney et al., 2009] Doney, S. C., I. Lima, R. A. Feely, D.M. Glover, K. Lindsay, N.Mahowald, J. K. Moore, and R. Wanninkhof, (2009, April). Mechanisms governing interannual variability in upper-ocean inorganic carbon system and air-sea CO_2 fluxes: Physical climate and atmospheric dust. *Deep Sea Res., Part II,* Vol. 56 (Issues 8–10), pp. 640–655. DOI: 10.1016/j.dsr2.2008.12.006

[DTC, n.d.] Developmental Testbed Center (DTC), (n. d.). *Model evaluation tools* [Data file]. Retrieved from: http://www.dtcenter.org/met/users/downloads/observation_data.php

[Dufour and Bréon, 2003] Dufour, E. and F.-M. Bréon, (2003). Spaceborne Estimate of Atmospheric CO_2 Column by Use of the Differential Absorption Method: Error Analysis. *Applied Optics, Vol. 42* (Issue 18), pp. 3595-3609. Retrieved from: http://dx.doi.org/10.1364/AO.42.003595

[Dumont et al., 2010] Dumont, M., O. Brissaud, G. Picard, B. Schmitt, J.-C. Gallet, and Y. Arnaud, (2010). High-accuracy measurements of snow bidirectional reflectance distribution function at visible and NIR wavelengths -- comparison with modeling results. *Atmos. Chem, Phys., Vol. 10,* pp. 2507-2520. www.atmos-chem-phys.net/10/2507/2010/

[Duren and Miller, 2012] Duren, R. M. and C. E. Miller, (2012, August). Measuring the carbon emissions of megacities. *Nature Climate Change, Vol. 2,* pp. 560–562. DOI: 10.1038/ nclimate1629

[Ehrenreich et al., 2010] Ehrenreich T., R. Leveille, I. Majid, K. Tankala, G. Rines, and P. Moulton, (2010, January 28). 1-kW, All-Glass Tm:fiber Laser. *SPIE Photonics West, 2010: LASE, Fiber Lasers VII: Technology, Systems, and Applications, Conference 7580, Session 16: Late Breaking News.* Retrieved from:

http://www.qpeak.com/Meetings/PW%202010%201kW%20Tm_fiber%20laser.pdf

[Ehret et al., 2008] Ehret, G., C. Kiemle, M. Wirth, A. Amediek, A. Fix, and S. Houweling, (2008). Space-borne remote sensing of CO_2, CH_4, and N_2O by integrated path differential absorption lidar: a sensitivity analysis. *Appl. Phys. B 90,* pp. 593–608. DOI: 10.1007/s00340-007-2892-3

[Eldering, et al., 2017] Eldering, A., C. W. O'Dell, P.O. Wennberg, D. Crisp, M.R. Gunson, C. Viatte, C. Avis, A. Braverman, R. Castano, A. Chang, L. Chapsky, C. Cheng, B. Connor, L. Dang, G. Doran, B.Fisher, C. Frankenberg, D. Fu, R. Granat, J. Hobbs, R. A. M. Lee, L. Mandrake, J. McDuffie, C. E. Miller, V. Myers, V. Natraj, D. O'Brien, G. B. Osterman, F. Oyafuso, V. H. Payne, H. R. Pollock, I. Polonsky, C. M. Roehl, R. Rosenberg, F. Schwandner, M. Smyth, V. Tang, T.E. Taylor, C. To, D. Wunch, and J. Yoshimizu, (2017). The Orbiting Carbon Observatory-2: first 18 months of science data products. *Atmos. Meas. Tech., 10,* pp. 549-563, https://doi.org/10.5194/amt-10-549-2017

[Engelen et al., 2002] Engelen, R. J., A. S. Denning, K. R. Gurney, and TransCom3 modelers, (2002). On error estimation in atmospheric CO_2 inversions. *J. Geophys. Res., Vol. 107* (Issue D22), pp. 4635. DOI: 10.1029/2002JD002195

[Enting, 2002] Enting, I.G, (2002). *Inverse Problems in Atmospheric Constituent Transport.* Cambridge University Press, Cambridge.

[EPA, 2010] Environmental Protection Agency, (2010, April 15). *Inventory of U.S. Greenhouse Gas Emissions and Sinks: 1990 – 2008,* pp. 407. Retrieved from: http://www.epa.gov/climatechange/Downloads/ghgemissions/508_Complete_GHG_1990 _2008.pdf

[ESA, 2008] European Space Agency (ESA), (2008, November). *A-SCOPE (Advanced Space Carbon and Climate Observation of Planet Earth) Mission Assessment report,* Chapter 4. Retrieved from: http://esamultimedia.esa.int/docs/SP1313-1_ASCOPE.pdf

[Etheridge et al., 1996] Etheridge, D. M., L. P. Steele, R. L. Langenfelds, R. J. Francey, J, -M. Barnola, and V.I. Morgan, (1996). Natural and anthropogenic changes in atmospheric CO_2 over the last 1000 years from air in Antarctic ice and firn. *Journal of Geophysical Research*, *Vol. 101, Issue D2,* pp. 4115-4128, https://doi.org/10.1029/95JD03410

[Etheridge et al., 1998] Etheridge, D. M., L. P. Steele, R. J. Francey, and R. L. Langenfelds, (1998). Atmospheric methane between 1000 AD and present: Evidence of anthropogenic emissions and climatic variability. *Journal of Geophysical Research-Atmospheres*, *Vol. 103, Issue D13,* pp. 15979-15993, https://doi.org/10.1029/98JD00923

[Evensen, 2004] Evensen, G, (2004). Sampling strategies and square root analysis schemes for the EnKF. *Ocean Dynamics,Vol.* 54, pp. 539-560. DOI: 10.1007/s10236-004-0099-2

[Fan et al., 1998] Fan, S., M. Gloor, J. Mahlman, S. Pacala, J. Sarmiento, T. Takahashi, and P. Tans. (1998, October 16). A Large Terrestrial Carbon Sink in North America Implied by Atmospheric and Oceanic Carbon Dioxide Data and Models. *Science, Vol. 282* (No. 5388), pp. 442-446. DOI: 10.1126/science.282.5388.442

[Farr et al., 2007] Farr, T. G., , P. A. Rosen, E. Caro, R. Crippen, R. Duren, S. Hensley, M. Kobrick, M. Paller, E. Rodriguez, L. Roth, D. Seal, S. Shaffer, J. Shimada, J. Umland, M. Werner,

M. Oskin, D. Burbank, and D. Alsdorf, (2007). The Shuttle Radar Topography Mission. *Rev. Geophys., Vol. 45, Issue 2*, RG2004, doi:10.1029/2005RG000183 (2007)

[Fix et al., 2011] Fix, A., C. Büdenbender, M. Wirth, M. Quatrevalet, A. Amediek, C. Kiemle, and G. Ehret (2011). Optical parametric oscillators and amplifiers for airborne and spaceborne active remote sensing of CO_2 and CH_4. *Proceedings SPIE 8182, Lidar Technologies, Techniques, and Measurements for Atmospheric Remote Sensing VII; 818206 (2011)* https://doi.org/10.1117/12.898412   Event: SPIE Remote Sensing, 2011, Prague, Czech Republic

[Fix et al., 2015] Fix, A., A. Amediek, C. Büdenbender, G. Ehret, G., M. Quatrevalet, M. Wirth, J. Löhring, R. Kasemann, J. Klein, H.-D. Hoffmann, and V. Klein, (2015). Development and First Results of a new Near-IR Airborne Greenhouse Gas Lidar. *Advanced Solid State Lasers 2015,* Berlin Germany, 4–9 October 2015, (Optical Society of America 2015), paper ATh1A-2. https://doi.org/10.1364/ASSL.2015.ATh1A.2

[Frankenberg et al., 2011a] Frankenberg, C., A. Butz, and G. C. Toon, (2011). Disentangling chlorophyll fluorescence from atmospheric scattering effects in O_2 A-band spectra of reflected sun-light. *Geophys. Res. Lett. Vol. 38, Issue 3,* 2011a. doi:10.1029/2010GL045896

[Frankenberg et al., 2011b] Frankenberg, C., J. B. Fisher, J. Worden, G. Badgley, S. S. Saatchi, J.-E. Lee, G. C. Toon, A. Butz, M. Jung, A. Kuze, and T. Yokota, (2011). New global observations of the terrestrial carbon cycle from GOSAT: Patterns of plant fluorescence with gross primary productivity. *Geophysical Research Letters Vol. 38, Issue 17*. doi:10.1029/2011GL048738

[Friedlingstein et al., 2006] Friedlingstein P., P. Cox, R. Betts, L. Bopp, W. von Bloh W, V. Brovkin, …. C. Yoshikawa, and N. Zeng, (2006). Climate-Carbon Cycle Feedback Analysis: Results from the C^4MIP Model Intercomparison. *Journal of Climate. Vol. 19*, pp. 3337–3353, July 2006, doi.org/10.1175/JCLI3800.1

[Geibel et al., 2012] Geibel, M. C., J. Messerschmidt, C. Gerbig, T. Blumenstock, H. Chen, F. Hase, O. Kolle, … and D. G. Feist, (2012). Calibration of column-averaged CH_4 over European TCCON FTS sites with airborne in-situ measurements. *Atmos. Chem. Phys., Vol. 12,* pp. 8763–8775. DOI: 10.5194/acp-12-8763-2012

[Gelaro et al., 2017] Gelaro, R., W. McCarty, M. J. Suárez, R. Todling, A. Molod, L. Takacs, C. A. Randles, A. Darmenov, M. G. Bosilovich, R. Reichle, K. Wargan, L. Coy, R. Cullather, C. Draper, S. Akella, V. Buchard, A. Conaty, A M. da Silva, W. Gu, G. Kim, R. Koster, R. Lucchesi, D. Merkova, J. E. Nielsen, G. Partyka, S. Pawson, W. Putman, M. Rienecker, S. D. Schubert, M. Sienkiewicz, and B. Zhao, (2017, July) The Modern-Era Retrospective Analysis for Research and Applications, Version 2 (MERRA-2). *Journal of Climate , Vol. 30 (Number 14)*, pp. 5419-5454, DOI: 10.1175/JCLI-D-16-0758.1

[Georgieva et al., 2006] Georgieva E.M., E. L. Wilson, M. Miodek, and W.S. Heaps. (2006, November). Total column oxygen detection using a Fabry-Perot interferometer. *Optical Engineering, Vol. 45* (Issue 11), pp. 115001. DOI: 10.1117/1.2387878

[Georgieva et al., 2008] Georgieva E.M., W. S. Heaps, and E. L. Wilson, (2008, October), Differential Radiometers Using Fabry-Perot Interferometric Technique for Remote Sensing of Greenhouse Gases. *IEEE Transactions on Geoscience and Remote Sensing (TGARS), Vol. 46* (Issue 10), pp. 3115-3122. DOI: 10.1109/TGRS.2008.921570

[Gibert et al., 2006] Gibert F., P. Flamant, D. Bruneau and C. Loth, (2006). Two-micrometer heterodyne differential absorption lidar measurements of the atmospheric CO_2 mixing ratio in the boundary layer. *Applied Optics, Vol. 45*, pp. 4448.

[Goodno et al., 2009] Goodno G.D., L. D. Book, and J. E. Rothenberg, (2009). Low-phase-noise, single-frequency, single-mode 608 W thulium fiber amplifier. *Opt. Lett. Vol. 34* (Issue 8), pp. 1204-1206.

[Gordon et al., 2017] Gordon, I. E., L. S. Rothman, C. Hill, R. V. Kochanov, Y. Tan, P. F. Bernath, M. Birk, V. Boudon, A. Campargue, K. V. Chance, B. J. Drouin, J. –M. Flaud, R. R. Gamache, J. T. Hodges, D. Jacquemart, V. I. Perevalov, A. Perrin, K. P. Shine, M. –A. H. Smith, J. Tennyson, G. C. Toon, H. Tran, … and E. J. Zak, (2017, December). The HITRAN2016 molecular spectroscopic database. *Journal of Quantitative Spectroscopy and Radiative Transfer, Vol 203, pp. 3-69.* DOI: 10.1016/j.jqsrt.2017.06.038.

[Gourdji et al., 2012] Gourdji, S. M., K. L. Mueller, V. Yadav, D. N. Huntzinger, A. E. Andrews, M. Trudeau, G. Petron, … and A. M. Michalak, (2012). North American CO_2 exchange: intercomparison of modeled estimates with results from a fine-scale atmospheric inversion, *Biogeosciences*, *Vol. 9,* pp. 457–475. DOI: 10.5194/bgd-8-6775-2011

[Guan et al., 2012] Guan, D., Z. Liu, Y. Geng, S. Lindner, and K. Hubacek. (2012). The gigatonne gap in China/'s carbon dioxide inventories. *Nature Climate Change, Vol. 2* (Issue 9), *pp.* 672-675. DOI: 10.1038/nclimate1560

[Guanter et al., 2012] Guanter, L., C. Frankenberg, A. Dudhia, P. E. Lewis, J. Gómez-Dans, A. Kuze, H. Suto, and R. G. Grainger, (2012). Retrieval and global assessment of terrestrial chlorophyll fluorescence from GOSAT space measurements. *Remote Sensing of Environment Vol. 121,* pp. 236–251, June 2012. doi:10.1016/j.rse.2012.02.006

[Guerlet et al., 2013] Guerlet, S., S. Basu, A. Butz, M. Krol, P. Hahne, S. Houweling, O. P. Hasekamp, and I. Aben, (2013). Reduced carbon uptake during the 2010 Northern Hemisphere summer from GOSAT. *Geophysical Research Letters, Vol. 40* (Issue 10), pp. 2378–2383. DOI: 10.1002/grl.50402

[Gurney et al., 2002] Gurney, K.R., R.M. Law, A.S. Denning, P.J. Rayner, D. Baker, P. Bousquet,... C.W. Yuen, (2002). Towards robust regional estimates of CO_2 sources and sinks using atmospheric transport models. *Nature, 415(6872)*, pp. 626-630. DOI: 10.1038/415626a

[Gurney et al., 2009] Gurney, K. R., D. L. Mendoza, Y. Zhou, M. L. Fischer, C.C. Miller, S. Geethakumar, and S. de la Rue du Can. (2009). High Resolution Fossil Fuel Combustion CO_2 Emission Fluxes for the United States. *Environmental Science & Technology, Vol. 43 (Issue 14)*, pp. 5535-5541. DOI: 10.1021/es900806c

[Hakkarainen et al., 2016] Hakkarainen, J., I. Ialongo, and J. Tamminen, (2016). Direct space-based observations of anthropogenic CO_2 emission areas from OCO-2. *Geophysical Research Letters, Vol. 43 Issue 21*, pp. 11400-11406, doi: 10.1002/2016GL070885

[Hammerling et al., 2012a] Hammerling, D.M., A.M. Michalak, and S.R. Kawa. (2012). Mapping of CO_2 at high spatiotemporal resolution using satellite observations: Global distributions from OCO-2. *J. Geophys. Res., Vol. 117 (Issue D6).* DOI: 10.1029/2011JD017015

[Hammerling et al., 2012b]   Hammerling, D. M., A. M. Michalak, C. O'Dell, and S. R. Kawa (2012). Global CO_2 distributions over land from the Greenhouse Gases Observing Satellite (GOSAT). *Geophys. Res. Lett., Vol. 39 (Issue 8)*. DOI: 10.1029/2012GL051203

[Hammerling et al., 2015] Hammerling, D. M., S. R. Kawa, K. Schaefer, S. Doney, A. M. Michalak. (2015). Detectability of CO_2 flux signals by a space-based lidar mission, *J. Geophys. Res. Atmos.*, *Vol. 120 (Issue 5)*, pp. 1794–1807. DOI: 10.1002/2014JD022483

[Hapke, 1986] Hapke, B., Bidirectional Reflectance Spectroscopy: 4. The extinction coefficient and opposition effect. *Icarus Vol. 67,* pp. 264-280. DOI:10.1016/0019-1035(86)90108-9

[Hapke et al., 1996] Hapke, B., D. DiMucci, R. Nelson, and W. Smythe. (1996). The cause of the hot spot in vegetation canopies and soils: shadow-hiding versus coherent backscatter. *Remote Sens. Environ., Vol.58*, pp. 63-68.

[Harrison et al., 2014] Harrison, F. W., B. Lin, S. Ismail, A. R. Nehrir, J. T. Dobler, E. V. Browell, S. A. Kooi, J. F. Campbell, M. D. Obland, M. M. Yang, and B. Meadows, (2014). Advancements in Algorithms for the Retrieval of CO_2 Column Amount and Path Length Using an Intensity-Modulated Continuous-Wave Lidar. *2014 American Geophysical Union, Fall Meeting*, abstract id. A43C-3285, San Francisco, CA, 15-19 December 2014, 2014AGUFM.A43C3285H

[Heaps et al., 2008] Heaps, W.S., E.L. Wilson, and E.M. Georgieva. (2008, September). Precision Measurement of Atmospheric Trace Constituents Using a Compact Fabry-Perot Radiometer. *International Journal of High Speed Electronics and Systems (IJHSES), Vol. 18* (Issue 3), pp. 601. DOI: 10.1142/S0129156408005606

[Heymann et al., 2017] Heymann, J., M. Reuter, M. Buchwitz, O. Schneising, H. Bovensmann, J. P. Burrows, S. Massart, J. W. Kaiser, and D. Crisp, (2017). CO_2 emission of Indonesian fires in 2015 estimated from satellite-derived atmospheric CO_2 concentrations. *Geophysical Research Letters, Vol. 44, Issue 3,* pp. 1537–1544. doi: 10.1002/2016GL072042

[Hintze, et al., 1998] Hintze, J. L. and R. D. Nelson. (1998). Violin plots: a box plot-density trace synergism. *The American Statistician*, *Vol. 52* (Issue 2), pp. 181-4. Retrieved from: http://www.jstor.org/discover/10.2307/2685478?uid=16777912&uid=3739560&uid=2&uid=3&uid=16752808&uid=67&uid=62&uid=3739256&sid=21106108757843

[Houghton, 1999] Houghton, R. A. (1999, April). The annual net flux of carbon to the atmosphere from changes in land use 1850–1990, *Tellus B, Vol. 51* (Issue 2), pp. 298–313. DOI: 10.1034/j.1600-0889.1999.00013.x

[Houghton, 2003] Houghton, R. A. (2003, April). Revised estimates of the annual net flux of carbon to the atmosphere from changes in land use and land management 1850-2000. *Tellus B, Vol. 55* (Issue 2), pp. 378-390. DOI: 10.1034/j.1600-0889.2003.01450.x

[Houweling et al., 2004] Houweling, S., F. M. Breon, I. Aben, C. Rödenbeck, M. Gloor, M. Heimann and P. Ciais. (2004). Inverse modeling of CO_2 sources and sinks using satellite data: A synthetic inter-comparison of measurement techniques and their performance as a function of space and time. *Atmos. Chem. Phys., Vol. 4,* pp. 523-548.

[Hu et al., 2008] Hu, Y., K. Stamnes, M. Vaughan, J. Pelon, C. Weimer, D. Wu, M.Cisewski, W. Sun, P. Yang, B. Lin, A. Omar, D. Flittner, C. Hostetler, C. Trepte, D. Winker, G. Gibson, and M. Santa-Maria. (2008). Sea surface wind speed estimation from space-based lidar

measurements. *Atmos. Chem. Phys., Vol. 8,* pp. 2771-2793 and 3593-3601. DOI: 10.5194/acp-8-3593-2008 and www.atmos-chem-phys-discuss.net/8/2771/2008/.

[Hudson et al., 2006] Hudson, S. R., S. G. Warren, R. E. Brandt, T. C. Grenfell, and D. Six. (2006). Spectral bidirectional reflectance of Antarctic snow: Measurements and parameterization. *J. Geophys. Res., Vol. 111,* D18106, doi:10.1029/2006JD007290

[Hungershoefer et al., 2010] Hungershoefer, K., F.-M. Breon, P. Peylin, F. Chevallier, P. Rayner, A. Klonecki, S. Houweling, and J. Marshall. (2010). Evaluation of various observing systems for the global monitoring of CO₂ surface fluxes. *Atmospheric Chemistry and Physics, Vol. 10* (Issue 21), pp.10503–10520. DOI: 10.5194/acp-10-10503-2010

[Hyon et al., 2012] Hyon, J., K. Anderson, B. Bienstock, G. Andrew, M. DiJoseph, J. Demsey, C. Jones (2012, August). ASCENDS Mission Study Summary. *NASA SER-SE-001, Vol. 1.0.*

[Ingmann et al., 2008] Ingmann P., P. Bensi, Y. Durand, A. Griva, and P. Clissold. (2008, November). A-Scope – advanced space carbon and climate observation of planet earth. *ESA Report for Assessment.* SP-1313/1. ISBN 978-92-9221-406-7, ISSN 0379-6566

[Inoue et al., 2013] Inoue, M., I. Morino, O. Uchino, Y. Miyamoto, Y. Yoshida, T. Yokota, T. Machida, … and P. K. Patra. (2013). Validation of XCO₂ derived from SWIR spectra of GOSAT TANSO-FTS with aircraft measurement data. *Atmos. Chem. Phys., Vol. 13,* pp. 9771-9788. DOI: 10.5194/acp-13-9771-2013

[IPCC, 2007] IPCC. (2007, September 19-21). Towards new scenarios for analysis of emissions, climate change, impacts, and response strategies. Intergovernmental Panel on Climate Change Report, IPPC Expert Meeting Report. Noordwijkerhout, The Netherlands. Retrieved from: http://www.ipcc.ch/pdf/supporting-material/expert-meeting-report-scenarios.pdf

[IPCC, 2007] Core Writing Team, Pachauri, R.K and Reisinger, A. (eds.) (2007). Synthesis report. Contribution of working groups I, II and III to the fourth .assessment report of the intergovernmental panel on climate change. *Climate Change 2007, IPCC*, Geneva, Switzerland, pp. 104.

[IPCC, 2013] Stocker, T.F., D. Qin, G.-K. Plattner, M. Tignor, S.K. Allen, J. Boschung, A. Nauels, Y. Xia, V. Bex and P.M. Midgley (eds.). (2013). The Physical Science Basis. Contribution of Working Group I to the Fifth Assessment Report of the Intergovernmental Panel on Climate Change. *Climate Change 2013,* Cambridge University Press, Cambridge, United Kingdom and New York, NY, USA, 1535 pp. DOI: 10.1017/CBO9781107415324

[IPCC, 2014] Intergovernmental Panel on Climate Change. *Climate Change 2014–Impacts, Adaptation and Vulnerability: Regional Aspects*, (Cambridge Univ. Press, Cambridge, U. K. and New York, 2014).

[Irvine and Pollack, 1968] Irvine, W.M. and J.B. Pollack. (1968). Infrared optical properties of water and ice spheres. *Icarus, Vol. 8,* pp. 324-360.

[Ismail and Browell, 1989] Ismail, S., and E. V. Browell, (1989). Airborne and spaceborne lidar measurements of water vapor profiles: a sensitivity analysis. *Applied Optics, Vol. 28, Issue 17*, pp. 3603-3615, 1989. https://doi.org/10.1364/AO.28.003603

[Ishii et al., 2008] Ishii, S., K. Mizutani, H. Fukuoka, T. Ishikawa, H. Iwai, P. Baron, J. Mendrok, … and T. Itabe. (2008). "Development of 2 micron coherent differential absorption lidar," *24th International Laser Radar Conference,* Boulder, Colorado.

[Jackson, 2004] Jackson, S.D. (2004, January 2004). Cross relaxation and energy transfer upconversion processes relevant to the functioning of 2 μm Tm^{3+}-doped silica fibre lasers. *Optics Communications Vol. 230* (Issues 1-3), pp.197-203. DOI: 10.1016/j.optcom.2003.11.045

[Jacob et al., 2018] Jacob, J. C., R. T. Menzies, and G. D. Spiers, (2018). Data Processing and Analysis Approach to Retrieve Carbon Dioxide Weighted Column Mixing Ratio and 2-Micron Reflectance with an Airborne Laser Absorption Spectrometer, to appear in *IEEE Transactions on Geoscience and Remote Sensing*, accepted June 2018. IEEE Open Access pre-publication available at: http://doi.org/10.1109/TGRS.2018.2863711

[Janssens-Maenhout et al., 2017] Janssens-Maenhout, G., M. Crippa, D. Guizzardi, M. Muntean, E. Schaaf, F. Dentener, P. Bergamaschi, V. Pagliari, J.G.J. Olivier, J.A.H.W. Peters, J.A. van Aardenne, S. Monni, U. Doering, and A.M.R. Petrescu, (2017). EDGAR v4.3.2 Global Atlas of the three major Greenhouse Gas Emissions for the period 1970–2012. *Earth Syst. Sci. Data Discuss.*, doi: 10.5194/essd-2017-79

[Joiner et al., 2011] Joiner, J., Y. Yoshida, A.P. Vasilkov, Y. Yoshida, L. A. Corp, and E. M. Middleton, (2011). First observations of global and seasonal terrestrial chlorophyll fluorescence from space. *Biogeosciences Volume. 8, Issue 3*, pp. 637-651, https://doi.org/10.5194/bg-8-637-2011

[Joiner et al., 2012] Joiner, J., Y. Yoshida, A.P. Vasilkov, E.M. Middleton, P.K.E. Campbell, A. Kuze, L.A. Corp, (2012). Filling-in of near-infrared solar lines by terrestrial fluorescence and other geophysical effects: simulations and space-based observations from SCIAMACHY and GOSAT. *Atmos. Meas. Tech. Vol. 5, Issue 4,* pp. 809–829, https://doi.org/10.5194/amt-5-809-2012

[Jones et al., 2013] Jones C., E. Robertson, V. Arora, P. Friedlingstein, E. Shevliakova, L. Bopp, V. Brovkin, T. Hajima, E. Kato, M. Kawamiya, S. Liddicoat, K. Lindsay, C. H. Reick, C. Roelandt, J. Segschneider, and J. Tjiputra, (2013). Twenty-First-Century Compatible CO_2 Emissions and Airborne Fraction Simulated by CMIP5 Earth System Models under Four Representative Concentration Pathways. *Journal of Climate, Vol. 26,* pp. 4398–4413, doi:10.1175/JCLI-D-12-00554.1

[Jucks et al., 2015] Jucks, K. W., S. Neeck, J. B. Abshire, D. F. Baker, E. V. Browell, A. Chatterjee, D. Crisp, S. M. Crowell, S. Denning, D. Hammerling, F. Harrison, J. J. Hyon, S. R. Kawa, B. Lin, B. L. Meadows, R. T. Menzies, A. Michalak, B. Moore, K. E. Murray, L. E. Ott, P. Rayner, O. I. Rodriguez, A. Schuh, Y. Shiga, G. D. Spiers, J. S. Wang, and T. S. Zaccheo, (2015). Active Sensing of CO_2 Emissions over Nights, Days, and Seasons (ASCENDS) Mission, Science Mission Definition Study, (August 19, 2015). Available at: https://cce.nasa.gov/ascends_2015/ASCENDSFinalDraft81915.pdf

[Kameyama et al., 2011] Kameyama, S., M. Imaki,1 Y. Hirano, S. Ueno, S. Kawakami, D. Sakaizawa, T. Kimura and M. Nakajima, (2011). Feasibility study on 1:6 μm continuous-wave modulation laser absorption spectrometer system for measurement of global CO_2

concentration from a satellite. *Appl. Opt., Vol. 50 (Issue 14),* pp. 2055-2068 (2011). https://doi.org/10.1364/AO.50.002055

[Kaminski et al., 2001] Kaminski, T., P. J. Rayner, M. Heimann, and I. G. Enting. (2001, March 16). On aggregation errors in atmospheric transport inversions. *Journal of Geophys. Res., Vol. 106* (Issue D5), pp. 4703–4715. DOI: 10.1029/2000JD900581

[Kaasalainen et al., 2006] Kaasalainen, S., M. Kaasalainan, T. Mielonen, J. Suomalainen, J.I. Peltoniemi, and J. Naranen. (2006). Optical properties of snow in backscatter, *J. Glaciology, Vol. 52*, pp. 574-584.

[Kawa et al., 2004] Kawa, S. R., D. J. Erickson III, S. Pawson, and Z. Zhu. (2004). Global CO₂ transport simulations using meteorological data from the NASA data assimilation system. *J. Geophys. Res., Vol.109 (Issue D18).* DOI: 10.1029/2004JD004554

[Kawa et al., 2010] Kawa, S. R., J. Mao, J. B. Abshire, G. J. Collatz, X. Sun and C. J. Weaver. (2010, November). Simulation studies for a space-based CO₂ lidar mission. *Tellus B, Vol. 62 (Issue 5)*, pp.759-769. DOI: 10.1111/j.1600-0889.2010.00486.x

[Keeling, 1960] Keeling, C. D. (1960). The concentration and isotopic abundances of carbon dioxide in the atmosphere. *Tellus, Vol. 12 (Issue 2),* pp. 200-203. DOI: 10.1111/j.2153-3490.1960.tb01300.x

 [Keeling, 1995] Keeling, Ralph F., (1995). The atmospheric oxygen cycle: The oxygen isotopes of atmospheric CO₂ and O₂ and the O₂/N₂ ratio. *Reviews of Geophysics Volume 33, Issue S2*, pp. 1253-1262, (1995). https://doi.org/10.1029/95RG00438

[Keppel-Aleks et al., 2012] Keppel-Aleks, G., P. O. Wennberg, R. A. Washenfelder, D. Wunch, T. Schneider, G. C. Toon, R. J. Andres, … and S. C. Wofsy (2012). The imprint of surface fluxes and transport on variations in total column carbon dioxide. *Biogeosciences, Vol. 9*, pp. 875-891. DOI: 10.5194/bg-9-875-2012

[Kiemle et al., 2011] Kiemle, C., M. Quatrevalet, G. Ehret, A. Amediek, A. Fix, and M. Wirth, (2011). Sensitivity studies for a space-based methane lidar mission. *Atmospheric Measurement Techniques Vol. 4, Issue 10,* pp. 2195-2211 (2011).

[Kiemle et al., 2014] Kiemle, C, S. R. Kawa, M. Quatrevalet, E. V. Browell. (2014). Performance simulations for a spaceborne methane lidar mission. *J Geophys Res Atmos*, *Vol. 119* (Issue 7), pp. 4365–79. Retrieved from: http://dx.doi.org/10.1002/2013JD021253

[Koch et al., 2008] Koch G. J., J. Y. Beyon, F. Gibert, B. W. Barnes, S. Ismail, M. Petros, P. J. Petzar, J. Yu, E. Modlin, K. Davis and U. N. Singh, (2008). Side-line tunable laser transmitter for differential absorption lidar measurements of CO₂: design and application to atmospheric measurements. *Applied Optics, Vol. 47 (Issue 7)*, pp. 944-956, 2008.

[Korb and Weng, 1983] Korb, C.L. and C. Y. Weng, (1983). Differential absorption lidar technique for measurement of the atmospheric pressure profile. *Applied Optics, 22(23),* pp. 3759-3770, December 1983.

[Krol et al., 2005] Krol, M., S. Houweling, B. Bregman, M. van den Broek, A. Segers, P. van Velthoven, W. Peters, F. Dentener, and P. Bergamaschi, (2005).The two-way nested global chemistry-transport zoom model TM5: algorithm and applications. *Atmos. Chem. Phys., Vol. 5, Issue 2,* pp. 417-432, https://doi.org/10.5194/acp-5-417-2005

[Kulawik et al., 2015] Kulawik, S., D. Wunch, C. O'Dell, C. Frankenberg, A. R. Jacobson, M. Reuter, T. Oda, and C. Miller. (2015). Consistent evaluation of GOSAT, SCIAMACHY, CarbonTracker, and MACC through comparisons to TCCON. *Atmos. Chem. Phys. Disc*.

[Kulawik et al., 2016] Kulawik, S., D. Wunch, C. O'Dell, C. Frankenberg, M. Reuter, T. Oda, … and J. Wolf, (2016). Consistent evaluation of ACOS-GOSAT, BESD-SCIAMACHY, CARBONTRACKER, and MACC through comparisons to TCCON. *Atmospheric Measurement Techniques, Vol. 9, Issue 2,* pp. 683–709. https://doi.org/10.5194/amt-9-683-2016

[Kulawik et al., 2018] Kulawik, S., S. Crowell, C. W. O'Dell, G. B. Osterman, P. O. Wennberg, D. Wunch, C. M. Roehl, N. M. Deutscher, M. Kiel, D. W.T. Griffith, et al., Characterization of OCO-2 biases and errors for flux estimates, manuscript in preparation 2018.

[Kuze et al., 2011] Kuze, A., D. M. O'Brien, T. E. Taylor, J. O. Day, C. W. O'Dell, F. Kataoka, M. Yoshida, … and H. Suto. (2011). Vicarious Calibration of the GOSAT Sensors Using the Railroad Valley Desert Playa. *IEEE Trans. on Geoscience and Remote Sensing*, *Vol. 49, Issue 5,* pp. 1781-1795. DOI: 10.1109/TGRS.2010.2089527

[Lamouroux et al., 2010] Lamouroux, J., H. Tran, A. L. Laraia, R. R. Gamache, L. S. Rothman, I. E. Gordon, and J. M. Hartmann, (2010). Updated database plus software for line-mixing in CO_2 infrared spectra and their test using laboratory spectra in the 1.5–2.3 um region*, JQSRT, 111*, pp. 2321-2331, doi:10.1016/j.jqsrt.2010.03.006, 2010.

[Lancaster et al., 2005] Lancaster, R. S., J. D. Spinhirne, and S. P. Palm. (2005). *Geophys. Res. Lett.,* Vol. 32, L22S10. DOI: 10.1029/2005GL023732

[Larsson et al., 2006] Larsson, H., O. Steinvall, T. Chevalier, and F. Gustafsson. (2006). Characterizing laser radar snow reflection for the wavelengths 0.9 and 1.5 µm. *Optical Eng., Vol. 45,* pp. 116201-1-11. doi:10.1117/1.2386026

[Lawrence, 2011] Lawrence, James. (2011). Differential absorption lidar for the total column measurement of atmospheric CO_2 from space. *Department of Physics and Astronomy Dissertation*, University of Leicester. Retrieved from: http://hdl.handle.net/2381/10379

[Lemke et al., 2007] Lemke, P., J. Ren, R. B. Alley, I. Allison, J. Carrasco, G. Flato, Y. Fujii, … and T. Zhang. (2007). Observations: changes in snow, ice and frozen ground. *Climate Change 2007: the physical science basis; summary for policymakers, technical summary and frequently asked questions. Part of the Working Group I contribution to the Fourth Assessment Report of the Intergovernmental Panel on Climate Change.* Cambridge Univ. Press, Cambridge, UK. *ISBN: 92-9169-121-6.*

[Le Quéré et al., 2009] Le Quéré, C., M. R. Raupach, J G. Canadell, G. Marland, L. Bopp, P. Ciais, T. J. Conway, … and F. I. Woodward. (2009). Trends in the sources and sinks of carbon dioxide. *Nature Geosci., Vol. 2,* pp. 831-836. DOI: 10.1038/ngeo689

[Le Quéré et al., 2013] Le Quéré, C., G. P. Peters, R. J. Andres, R. M. Andrew, T. Boden, P. Ciais, P. Friedlingstein, … and C. Yue. (2013). Global carbon budget 2013. *Earth System Science Data Discussions*, *Vol. 6,* pp. 689-760. Retrieved from: http://www.earth-syst-sci-data-discuss.net/6/689/2013, DOI: 10.5194/essdd-6-689-2013

[Le Quéré et al., 2017] Le Quéré, C., R. M. Andrew, P. Friedlingstein, S. Sitch, J. Pongratz, A. C. Manning, J. I. Korsbakken, G. P. Peters, J. G. Canadell, R. B. Jackson, T. A. Boden, P. P. Tans, O. D. Andrews, V. K. Arora, D. C. E. Bakker, L. Barbero, … , A. J. Wiltshire, S. Zaehle, and D. Zhu, (2017). Global Carbon Budget 2017, *Earth System Science Data Discussions,* pp. 1-79, doi: 10.5194/essd-2017-123

[Le Quéré et al., 2018] Le Quéré, C., R. M. Andrew, P. Friedlingstein, S. Sitch, J. Pongratz, A. C. Manning, J. I. Korsbakken, G. P. Peters, J. G. Canadell, R. B. Jackson, T. A. Boden, P. P. Tans, O. D. Andrews, V. K. Arora, D. C. E. Bakker, L. Barbero, … , A. J. Wiltshire, S. Zaehle, and D. Zhu, (2018). Global Carbon Budget 2017, *Earth System Science Data, Vol. 10, Issue 1*, pp. 405-448, 2018, https://doi.org/10.5194/essd-10-405-2018

[Lin et al., 2003] Lin, J. C., C. Gerbig, S. C. Wofsy, A. E. Andrews, B. C. Daube, K. J. Davis, and C. A. Grainger. (2003, August 19). A near-field tool for simulating the upstream influence of atmospheric observations: the stochastic time-inverted lagrangian transport (stilt) model. *Journal of Geophysical Research: Atmospheres, Vol. 108 (Issue D16),* pp. 10001-10021. DOI: 10.1029/2002JD003161

[Lin et al., 2013] Lin, B., S. Ismail, F. W. Harrison, E. V. Browell, A. R. Nehrir, J. Dobler, B. Moore, T. Refaat and S. A. Kooi, (2013). Modeling of intensity-modulated continuous-wave laser absorption spectrometer systems for atmospheric CO_2 column measurements. *Applied Optics, Vol. 52 (Issue 29),* pp. 7062-7077, 2013.

[Lin et al., 2015] Lin, B., A. Nehrir, F. Harrison, E. Browell, S. Ismail, M. Obland, J. Campbell, J. Dobler, B. Meadows, T. Fan, and S. Kooi, (2015). Atmospheric CO_2 column measurements in cloudy conditions using intensity-modulated continuous-wave lidar at 1.57 micron. *Optics Express, Vol. 23, No. 11,* DOI:10.1364/OE.23.00A582, A582 – A593, 1 June 2015.

[Lin et al., 2017] Lin, B., E. Browell, S. Kooi, J. Dobler, J. Campbell, T. Fan, S. Pal, C. O'Dell, M. Obland, W. Erxleben, D. McGregor, I. Gordon, R. Kochanov, J. DiGangi, K. Davis, and Y. Choi, (2017). Assessment of MFLL column CO_2 measurements obtained during the ACT-America field campaigns. *2017 American Geophysical Union Fall Meeting*, AGU, New Orleans, LA, December 2017. Biblio. Code: 2017AGUFM.A23C2352L

[Liu et al., 2017] Liu, J., K. W. Bowman, D. S. Schimel, N. C. Parazoo, Z. Jiang, M. Lee, A. A. Bloom, D. Wunch, C. Frankenberg, Y. Sun, C.W. O'Dell, K. R. Gurney, D. Menemenlis, M. Gierach, D. Crisp, and A. Eldering, (2017). Contrasting carbon cycle responses of the tropical continents to the 2015–2016 El Niño. *Science Vol. 358, Issue 6360, eaam5690* (2017). doi: 10.1126/science.aam5690

[Long et al., 2010] Long D. A., D.K. Havey, M. Okumura, C.E. Miller, and J.T. Hodges, (2010). O_2 A-band line parameters to support atmospheric remote sensing. *J. of Quant. Spectr. Rad. Transfer, Vol. 111 (Issue 14)*, pp. 2021-2036, 2010.

[Long et al., 2011] Long, D. A., K. Bielska, D. Lisak, D. K. Havey, M. Okumura, C. E. Miller, and J. T. Hodges. (2011). The air-broadened, near-infrared CO_2 line shape in the spectrally isolated regime: Evidence of simultaneous Dicke narrowing and speed dependence, *Journal of Chemical Physics, Volume. 135,* 064308. Retrieved from: http://dx.doi.org/10.1063/1.3624527

[Long and Hodges, 2012] Long, D.A., and J. T. Hodges, (2012). On spectroscopic models of the O$_2$ *A*-band and their impact upon atmospheric retrievals. *J. Geophys. Res., 117,* D12309, doi:10.1029/2012JD017807.

[Lüthi et al., 2008] Lüthi, D., M. Le Floch, B. Bereiter, T. Blunier, J.-M. Barnola, U. Siegenthaler, D. Raynaud, … and T. F. Stocker (2008). High-resolution carbon dioxide concentration record 650,000-800,000 years before present. *Nature 453*, pp. 379-382. DOI: 10.1038/nature06949

[Mao and Kawa, 2004] Mao, J. and S. R. Kawa, (2004). Sensitivity studies for space-based measurement of atmospheric total column carbon dioxide by reflected sunlight. *Applied Optics, Vol. 43 (Issue 4)*, pp. 914-927, 2004.

[Mao et al., 2007] Mao, J., S. R. Kawa, J. B. Abshire and H. Riris. (2007). Sensitivity studies for a space-based CO$_2$ laser sounder. *Eos Trans., Vol 88 (Issue 52), AGU 2007 Fall Meeting,* Suppl. Abstract A13D-1500. 2007AGUFM.A13D1500M

[Mao et al., 2013] Mao, J., A. Ramanathan, M. Rodriguez, G. R. Allan, W. Hasselbrack, J. B. Abshire, H. Riris, … and E. V. Browell. (2013). Retrieval of Vertical Structure of Atmospheric CO$_2$ Concentration from Airborne Lidar Measurements during the 2011 and 2013 ASCENDS Science Campaigns. 2*013 Fall AGU Meeting,* San Francisco, December 9-13, 2013, Paper A23H-03.

[Mao et al., 2018] Mao, J., A. Ramanathan, J. B. Abshire, S. R. Kawa, H. Riris, G. R. Allan, M. Rodriguez, W. E. Hasselbrack, X. Sun, K. Numata, J. Chen, Y. Choi, and M. Y. M. Yang, (2018). Measurement of atmospheric CO$_2$ column concentrations to cloud tops with a pulsed multi-wavelength airborne lidar. *Atmos. Meas. Tech., Vol. 11, Issue 1*, pp. 127-140, https://doi.org/10.5194/amt-11-127-2018

[Marland et al., 2009] Marland, G., K. Hamal and M. Jonas. (2009). How uncertain are estimates of CO$_2$ emissions? *J. Ind. Ecol., Vol. 13,* pp. 4-7. DOI: 10.1111/j.1530-9290.2009.00108.x

[McGuckin and Menzies, 1992] McGuckin B.T. and R.T. Menzies. (1992). Efficient CW diode-pumped tm,ho:ylf laser with tunability near 2.06 µm. *IEEE J. Quantum Electronics*, *Vol. 28,* pp. 1025-1028.

[Meadows et al., 2018] Meadows, B., B. Lin, M. D. Obland, W. Carrion, J. Hicks, J. Sparrow, J. Campbell, S. Kooi, T. Fan, E. V. Browell, J. Dobler, J. DiGangi, (2018). Airborne CO$_2$ Lidar Measurements for the Atmospheric Carbon and Transport – America (ACT-America) Project and the ASCENDS 2017 Field Campaign. *14th International Workshop on Greenhouse Gas Measurements from Space (IWGGMS-14)*, Toronto, Canada, 8-10 May, 2018.

[Measures, 1992] Measures, R. (1992, January 1). Laser remote sensing: fundamentals and applications, *Krieger Publishing Company,* New York.

[Menzies et al., 1998] Menzies, R.T., D. M. Tratt, and W. H. Hunt. (1998). Lidar in-space technology experiment measurements of sea surface directional reflectance and the link to surface wind speed. *Appl. Opt, Vol. 37* (Issue 24), pp. 5550-5558.

[Menzies and Tratt, 2003] Menzies, R. T., and D. M. Tratt, (2003). Differential laser absorption spectrometry for global profiling of tropospheric carbon dioxide: selection of optimum

sounding frequencies for high-precision measurements. *Appl. Opt., Vol. 42 (Issue 33),* pp. 6569-6577. Retrieved from: http://dx.doi.org/10.1364/AO.42.006569

[Menzies and Spiers, 2008] R. Menzies and G. Spiers. (2008). Airborne laser absorption spectrometer for IPDA measurement of atmospheric effects on attainable precision and a technique for cloud and aerosol filtering. 24th International Laser Radar Conference, Boulder, Colorado.

[Menzies et al., 2014] Menzies, R.T., G.D. Spiers, and J. Jacob. (2014, February). Airborne laser absorption spectrometer measurements of atmospheric CO_2 column mole fractions: Source and sink detection and environmental impacts on retrievals. *Journal of Atmospheric and Oceanic Technology, Vol. 31,* pp. 404–421. DOI: http://dx.doi.org/10.1175/JTECH-D-13-00128.1

[Meredith et al., 2012] Meredith, M. P., A. C. N. Garabato, A. M. Hogg, and R. Farneti. (2012, January). Sensitivity of the Overturning Circulation in the Southern Ocean to Decadal Changes in Wind Forcing. *J.Climate, Vol. 25 (Issue 1)*, pp. 99-110.

[MERRA, 1979-Present] MERRA. (1979-Present). *Modern Era-Retrospective Analysis for Research and Applications* [Data file]. Retrieved from: http://gmao.gsfc.nasa.gov/research/merra/intro.php and http://disc.sci.gsfc.nasa.gov/daac-bin/FTPSubset.pl

[Messerschmidt et al., 2013] Messerschmidt, J., N. Parazoo, D. Wunch, N.M. Deutscher, C. Roehl, T. Warneke, and P. O. Wennberg. (2013). Evaluation of seasonal atmosphere–biosphere exchange estimations with TCCON measurements. *Atmos. Chem. Phys., Vol. 13,* pp. 5103-5115. DOI: 10.5194/acp-13-5103-2013

[Michalak et al., 2004] Michalak, A.M., L. Bruhwiler, and P.P. Tans. (2004, July 27). A geostatistical approach to surface flux estimation of atmospheric trace gases. *Journal of Geophysical Research, Vol. 109 (Issue D14), D14109.* DOI: 10.1029/2003JD004422

[Miles et al., 2012] Miles, N.L., S.J. Richardson, K.J. Davis, T. Lauvaux, A.E. Andrews, T.O. West, V. Bandaru, and E.R. Crosson. (2012). Large amplitude spatial and temporal gradients in atmospheric boundary layer CO_2 mole fractions detected with a tower-based network in the U.S. upper Midwest. *J. Geoophys. Res., Vol. 117,* G01019. DOI: 10.1029/2011JG001781

[Miller et al., 2007] Miller, C.E., D. Crisp, P. L. DeCola, S. C. Olsen, J. T. Randerson, A. M. Michalak, A. Alkhaled, … and R. M. Law. (2007, May 27). Precision requirements for space-based XCO_2 data. *J. Geophys. Res.-Atmos., Vol. 112 (Issue D10)*, D10314. DOI: 10.1029/2006JD007659

[Miller et al., 2018] Miller, S. M., A. M. Michalak, V. Yadav, and J. M. Tadić, (2018). Characterizing biospheric carbon balance using CO_2 observations from the OCO-2 satellite. *Atmos. Chem. Phys., Vol. 18, Issue 9,* pp. 6785-6799, https://doi.org/10.5194/acp-18-6785-2018, 2018.

[Mitchell and O'Brien, 1987] Mitchell, R. M., and D. M. O'Brien, (1987). Error estimate for passive satellite measurements of surface pressure using absorption in the A band of oxygen. *J. Atmos. Sci.*, **44**, 1981-1991, (1987).

[Najjar et al., 2007] Najjar, R.G., X. Jin, F. Louanchi, O. Aumont, K. Caldeira, S. C. Doney, J.-C. Dutay, … and A. Yool. (2007, September). Impact of circulation on export production,

dissolved organic matter, and dissolved oxygen in the ocean: Results from phase ii of the ocean carbon-cycle model intercomparison project (OCMIP-2). *Global Biogeochem. Cy., Vol. 21* (Issue 3), GB3007. DOI: 10.1029/2006GB002857

[NASA, 2008] NASA. (2008). Active sensing of CO_2 emission over nights, days, and seasons (ASCENDS) mission. *NASA Science Definition and Planning Workshop Report,* University of Michigan in Ann Arbor, Michigan, July 23-25, 2008. Retrieved from: http://cce.nasa.gov/ascends/12-30-08%20ASCENDS_Workshop_Report%20clean.pdf

[NASA, 2008] NASA Science Definition and Planning Workshop Report for ASCENDS Mission. (2008). University of Michigan in Ann Arbor, Michigan. Retrieved from: http://decadal.gsfc.nasa.gov/documents/12-30-08-ASCENDS_Workshop.pdf

[NASA, 2015] NASA ASCENDS Mission ad-hoc Science Definition Team, 2015 ASCENDS Mission White Paper, available from: https://cce.nasa.gov/ascends_2015/ASCENDSFinalDraft81915.pdf

[NASA Goddard, n.d.] NASA Goddard Space Flight Center. CO_2 sounder. *Papers, Posters, and Related Studies.* Retrieved from: http://ssed.gsfc.nasa.gov/co2sounder/

[NASEM, 2018] National Academies of Sciences, Engineering, and Medicine (2018). *Thriving on Our Changing Planet: A Decadal Strategy for Earth Observation from Space.* Washington, DC: The National Academies Press. https://doi.org/10.17226/24938, Updated on 1/19/2018 to include missing pages in Appendix B.

[Nassar et al., 2017] Nassar, R., T. G. Hill, C. A. McLinden, D. Wunch, D.B.A. Jones, and D. Crisp, (2017). Quantifying CO_2 Emissions From Individual Power Plants From Space. *Geophysical Research Letters, Vol. 44, Issue 19,* pp. 10045-10053 (2017). doi: 10.1002/2017GL074702

[Nayar and Oren, 1995] Nayar, S.K., and M. Oren, (1995). Generalization of the Lambertian Model and Implications for Machine Vision. *International Journal on Computer Vision, Vol. 14, No. 3,* pp. 227-251, Apr. 1995.

[NCDC, n.d.] NCDC. (n.d.). *NCDC's* Integrated *Surface Database (ISD)* [Data file]. Retrieved from: http://www.ncdc.noaa.gov/oa/climate/isd/index.php

[NCDC, n.d. b] NCDC. (n.d.). *NCDC's NOMADS* [Data file]. Retrieved from: ftp://nomads.ncdc.noaa.gov

[NCEP, n.d. c] *NCEP. (n.d.). PREPBUFR Usage* [Data file]. Retrieved from: http://www.emc.ncep.noaa.gov/mmb/data_processing/prepbufr.doc

[Nehrkorn et al., 2010] Nehrkorn, T., J. Eluszkiewicz, S. C. Wofsy, J. C. Lin, C. Gerbig, M. Longo, and S. Freitas. (2010). Coupled weather research and forecasting -- stochastic time-inverted Lagrangian transport (WRF-STILT) model. *Meteor. Atmos. Phys., Vol. 107* (Issues 1-2), pp. 51–64.

[Nicholson et al., 2016] Nicholson, J. W., A. DeSantolo, M. F. Yan, P. Wisk, B. Mangan, G. Puc, A. W. Yu, and M. A. Stephen, (2016). High energy, 1572.3 nm pulses for CO_2 LIDAR from a polarization-maintaining, very-large-mode-area, Er-doped fiber amplifier. *Optics Express, Vol. 24, Issue 17,* pp. 19961-19968 (2016). https://doi.org/10.1364/OE.24.019961

[Nicodemus et al., 1977] Nicodemus, F.E., J.C. Richmond, J.J. Hsia, I.W. Ginsburg, and T.

Limperis. (1977). Geometrical Considerations and Nomenclature for Reflectance. *National Bureau of Standards. U.S. Monograph 160.*

[NOAA, 2003] NOAA, Washington, D.C. (2003, November). The GFS Atmospheric Model, *NCEP Office Note 422*, Environmental Modeling Center. Retrieved from: http://search.usa.gov/search?affiliate=nws.noaa.gov&v%3Aproject=firstgov&query=The+GFS+Atmospheric+Model%2C+NCEP+Office+Note+422

[NOAA, 2017] NOAA, Office of the Federal Coordinator for Meteorology (OFCM), Washington, D.C. (2017), *Surface Weather Observations and Reports*. [Online]: https://www.ofcm.gov/publications/fmh/FMH1/FMH1_2017.pdf

[NOAA, n.d.] NOAA. (n.d.). *NOAA's ESRL's archive*. [Data file]. Retrieved from: http://www.esrl.noaa.gov/raobs/intl/ and http://www.esrl.noaa.gov/raobs/   or http://www.esrl.noaa.gov/raobs/General_Information.html

[NRC, 2007] National Research Council (2007). *Earth Science and Applications from Space: National Imperatives for the Next Decade and Beyond*. Washington, DC: The National Academies Press. https://doi.org/10.17226/11820

[NRC, 2013] National Research Council (2013). *Abrupt Impacts of Climate Change: Anticipating Surprises. Committee on Understanding and Monitoring Abrupt Climate Change and its Impacts.* US National Research Council, National Academies Press, Washington, DC.

[NRC, 2017] The 2017-2027 NRC Decadal Survey for Earth Science and Applications from Space (ESAS 2017) will help shape science priorities and guide agency investments into the next decade. The survey, sponsored by NASA, NOAA, and the USGS, is driven by input from the scientific community and policy experts.

[Numata et al., 2011] Numata, K., J. R. Chen, S. T. Wu, J. B. Abshire, and M. A. Krainak, (2011). Frequency stabilization of distributed-feedback laser diodes at 1572 nm for lidar measurements of atmospheric carbon dioxide, *Applied Optics Vol. 50, Issue 7,* pp. 1047–1056 (2011). https://doi.org/10.1364/AO.50.001047

[Numata et al., 2012] Numata, K., J. R. Chen and S. T. Wu, (2012). Precision and fast wavelength tuning of a dynamically phase-locked widely-tunable laser. *Optics Express, Vol. 20 (Issue 13)*, pp. 14234-14243. http://dx.doi.org/10.1364/OE.20.014234

[Obland et al., 2012] Obland, M. D., N. S. Prasad, F. W. Harrison, E. V. Browell, S. Ismail, J. T. Dobler, B. Moore, … and W. Welch, (2012). ACES: the ASCENDS carbonhawk experiment simulator. *2012 American Geophysical Union Fall Meeting*, San Francisco, CA, December 3-7, 2012. Paper A53H-0230.

[Obland et al., 2013] Obland, M. D., C. Antill, E. V. Browell, J. F. Campbell, S. Chen, C. Cleckner, M. S. Dijoseph, … and W. Welch, (2013). Technology advancement for the ASCENDS mission using the ASCENDS carbonhawk experiment simulator (ACES), *2013 American Geophysical Union Fall Meeting,* San Francisco, CA, December 9-13, 2013, Paper A13C-0212.

[Obland et al., 2017] Obland, M., J. Campbell, S. Kooi, T. Fan, W. Carrion, J. Hicks, B. Lin, A. Nehrir, E. Browell, B. Meadows, and K. Davis, (2017). Technology Advancements for Active Remote Sensing of Carbon Dioxide from Space using the Active Sensing of CO₂ Emissions over Nights, Days, and Seasons (ASCENDS) CarbonHawk Experiment

Simulator. *28th International Laser-Radar Conference*, Bucharest, Romania, June 25-30, 2017.

[Obland et al., 2018] Obland, M. D., A. M. Corbett, B. Lin, B. Meadows, J. F. Campbell, S. Kooi, T. Fan, W. Carrion, J. Hicks, J. Sparrow, E. V. Browell, J. Dobler, and J. DiGangi, (2018). Advancements towards active remote sensing of CO_2 from space using intensity-modulated, continuous-Wave (IM-CW) lidar. *Proc. SPIE 10785, Sensors, Systems, and Next-Generation Satellites XXII,* 1078509 (25 September 2018), Berlin, Germany; doi: 10.1117/12.2325816

[O'Brien and Rayner, 2002] O'Brien, D. M. and Rayner, P. J. (2002). Global observations of the carbon budget 2. CO_2 column from differential absorption of reflected sunlight in the 1.61 μm band of CO_2. *J. Geophys. Res., Vol. 107*, ACH6-1. DOI: 10.1029/2001JD000617

[Oda and Maksyutov, 2011] Oda, T., and S. Maksyutov, (2011). A very high-resolution (1 km×1 km) global fossil fuel CO_2 emission inventory derived using a point source database and satellite observations of nighttime lights. *Atmos. Chem. Phys., Vol. 11,* pp. 543-556. https://doi.org/10.5194/acp-11-543-2011

[O'Dell et al., 2012] O'Dell, C. W., B. Connor, H. Bösch, D. O'Brien, C. Frankenberg, R. Castano, M. Christi, D., … and D. Wunch. (2012). The ACOS CO_2 retrieval algorithm – Part 1: Description and validation against synthetic observations. *Atmos. Meas. Tech., Vol. 5,* pp. 99–121. DOI: 10.5194/amt-5-99-2012

[O'Dell et al., 2018] O'Dell, C. W., A. Eldering, P. O. Wennberg, D. Crisp, M. R. Gunson, B. Fisher, C. Frankenberg, M. Kiel, H. Lindqvist, L. Mandrake, … and V. A. Velazco, (2018). Improved Retrievals of Carbon Dioxide from the Orbiting Carbon Observatory-2 with the version 8 ACOS algorithm. Atmos. Meas. Tech. Discuss., https://doi.org/10.5194/amt-2018-257 Manuscript under review for journal *Atmospheric Measurement Techniques*, 2018.

[Olivier et al., 2012] Olivier, J. G., J. A. Peters and G. Janssens-Maenhout. (2012). Trends in global CO_2 emissions 2012 report. *PBL Netherlands Environmental Assessment Agency; Ispra: Joint Research Centre,* The Hague, The Netherlands.

[Oren et al., 2001] Oren, R., D.S. Ellsworth, K. H. Johnsen, N. Phillips, B. E. Ewers, C. Maler, K.V. R. Schafer, … and G. G. Katul. (2001), Soil fertility limits carbon seqestration by forest ecosystems in a CO_2-enriched atmosphere. *Nature* Vol. 411, pp. 469-472. DOI: 10.1038/35078064

[Ott et al., 2015] Ott, L., S. Pawson, J. Collatz, W. Gregg, D. Menemenlis, H. Brix, C. Rousseaux, K. Bowman, J. Liu, A. Eldering, M. Gunson, and S. R. Kawa, (2015). Assessing the magnitude of CO_2 flux uncertainty in atmospheric CO_2 records using products from NASA's Carbon Monitoring Flux Pilot Project. *J. Geophys. Res. - Atmos, Vol. 120, Issue 2,* pp. 734-765. doi: 10.1002/2014JD022411

[Ott et al., 2017] Ott, L., P. J. Sellers, D. Schimel, B. Moore III, C. O'Dell, S. Crowell, S. R. Kawa, S. Pawson, A. Chatterjee, D. F. Baker, and A. E. Schuh, (2017). NASA's Carbon Cycle OSSE Initiative - Informing future space-based observing strategies through advanced modeling and data assimilation. *2017 American Geophysical Union Fall Meeting, AGU,* New Orleans, LA, December 2017. Biblio. Code: 017AGUFMGC51C0817O. http://adsabs.harvard.edu/abs/2017AGUFMGC51C0817O

[Pan et al., 2011] Pan Y., Birdsey R.A., Fang J., et al. (2011). A large and persistent carbon sink in the world's forests. *Science, Vol. 333 (No. 6045).* pp. 988-993. DOI: 10.1126/science.1201609

[Parazoo et al., 2016] Parazoo, N. C., R. Commane, S. C. Wofsy, C. D. Koven, C. Sweeney, D. M. Lawrence, J. Lindaas, R. Y. Chang, and C. E. Miller, (2016). Detecting regional patterns of changing CO_2 flux in Alaska. *Proceedings of the National Academy of Sciences of the United States of America, Vol. 113(28),* pp. 7733-7738, doi: 10.1073/pnas.1601085113. https://doi.org/10.1073/pnas.1601085113

[Patra et al., 2017] Patra, P.K., D. Crisp, J.W. Kaiser, D. Wunch, T. Saeki, K. Ichii, T. Sekiya, P.O. Wennberg, D.G. Feist, D.F. Pollard, D.W.T. Griffith, V.A. Velazco, M. De Maziere, M.K. Sha, C. Roehl, A. Chatterjee, and K. Ishijima, (2017). The Orbiting Carbon Observatory (OCO-2) tracks 2-3 peta-gram increase in carbon release to the atmosphere during the 2014-2016 El Niño. *Nature Scientific Reports, 7(1).* 13567, December 2017. doi:10.1038/s41598-017-13459-0

[Payne, 2017] Payne, V. (2017, Aug) OCO (Orbiting Carbon Observatory) -2 : ABSCO User Guide Jet Propulsion Laboratory Publication Retrieved from: https://docserver.gesdisc.eosdis.nasa.gov/public/project/OCO/ABSCO_UsersGuide_20170724_corr2_v5.0.pdf

[Peters et al., 2010] Peters, W., M. C. Krol, G. R. Van Der Werf, S. Houweling, C. D. Jones, J. Hughes, K. Schaefer, … and P. P. Tans. (2010). Seven years of recent European net terrestrial carbon dioxide exchange constrained by atmospheric observations. *Global Change Biology, Vol. 16* (Issue 4)*,* pp. 1317-1337. DOI: 10.1111/j.1365-2486.2009.02078.x

[Peters et al., 2011] Peters, G. P., G. Marland, C. L. Quéré, T. Boden, J. G. Canadell, and M. R. Raupach, (2011). Rapid Growth in CO_2 Emissions after the 2008-2009 Global Financial Crisis. *Nature Climate Change, Vol. 2, Issue 1*, pp. 2-4. December, 2011. DOI: 10.1038/nclimate1332

[Peters et al., 2012] Peters, G. P., S.J. Davis, and R. Andrew, (2012). A synthesis of carbon in international trade. *Biogeosciences, Vol. 9*, pp. 3247-3276. doi:10.5194/bg-9-3247-2012

[Petros et al., 2018] M. Petros, T. Refaat, U. Singh, J. Yu, C. Antill, R. Remus, B. Taylor, T. Wong, K. Reithmaier, J. Lee, S. Ismail, and K. Davis, (2018). Development of an advanced two-micron triple-pulse IPDA lidar for carbon dioxide and water vapor measurements. EPJ Web of Conferences 176, 01009 (2018), *28th International Laser Radar Conference, ILRC 2017*, Bucharest, Romania, June 25-30, 2017. Published April 13 2018.

[Picarro, Inc.] Picarro, Inc., 480 Oakmead Parkway, Sunnyvale, CA 94085, USA.

[Pillai et al., 2010] Pillai, D., C. Gerbig, J. Marshall, R. Ahmadov, R. Kretschmer, T. Koch, and U. Karstens, (2010). High resolution modeling of CO_2 over Europe: implications for representation errors of satellite retrievals. *Atmos. Chem. Phys., Vol. 10,* pp. 83–94. DOI: 10.5194/acp-10-83-2010

[Poulter et al., 2011] Poulter, B., D.C. Frank, E.L. Hodson, and N.E. Zimmermann, (2011). Impacts of land cover and climate data selection on understanding terrestrial carbon dynamics and the CO_2 airborne fraction. *Biogeosciences, 8*, pp. 2027-2036, https://doi.org/10.5194/bg-8-2027-2011

[Raab and Tward, 2010] Raab, J., and E. Tward. (2010, September). Northrop Grumman Aerospace Systems cryocooler overview. *Cryogenics, Volume 50* (Issue 9), pp. 572-581. ISSN 0011-2275. DOI: 10.1016/j.cryogenics.2010.02.009

[Ramanathan et al., 2013] Ramanathan, A., J. Mao, G. R. Allan, H. Riris, C. J. Weaver, W. E. Hasselbrack, E. V. Browell, and J. B. Abshire, (2013). Spectroscopic measurements of a CO_2 absorption line in an open vertical path using an airborne lidar. *Applied Physics Letters, Vol. 103 (Issue 21),* 214102. DOI: http://dx.doi.org/10.1063/1.4832616

[Ramanathan et al., 2015] Ramanathan, A. K., J. Mao, J. B. Abshire, and G. R. Allan, (2015). Remote sensing measurements of the CO_2 mixing ratio in the planetary boundary layer using cloud slicing with airborne lidar. *Geophys. Res. Lett., Vol.42 (6),* 2055–2062, DOI: 10.1002/2014GL062749

[Ramanathan et al., 2018] Ramanathan, A. K., H. M. Nguyen, X. Sun, J. Mao, J. B. Abshire, J. M. Hobbs, and A. J. Braverman. (2018) A Singular Value Decomposition framework for retrievals with vertical distribution information from greenhouse gas column absorption spectroscopy measurements, *Atmos. Meas. Tech. Discuss.,* https://www.atmos-meas-tech-discuss.net/amt-2018-14/, in review, 2018.

[Randerson et al., 1997] Randerson, J.T., M.V. Thompson, T. J. Conway, I. Y. Fung and C. B. Field. (1997, December). The contribution of terrestrial sources and sinks to trends in the seasonal cycle of atmospheric carbon dioxide. *Global Biogeochem. Cy., Vol. 11* (Issue 4), pp. 535-560. DOI: 10.1029/97GB02268

[Rayner and O'Brien, 2001] Rayner, P.J. and D. M. O'Brien, (2001). The utility of remotely sensed CO_2 concentration data in surface source inversions. *Geophysical Research Letters, Vol. 28, Issue 1*, pp. 175-178, https//doi.org/10.1029/2000GL011912

[Rayner et al., 2002] Rayner, P. J., R. M. Law, D. M. O'Brien, T. M. Butler, and A. C. Dilley. (2002). Global observations of the carbon budget - 3. Initial assessment of the impact of satellite orbit, scan geometry, and cloud on measuring C0₂ from space. *Journal of Geophysical Research-Atmospheres, Vol. 107* (Issue D21). DOI: l0.1029/2001JD000618

[Rayner et al., 2010] Rayner, P. J., M. R. Raupach, M. Paget, P. Peylin, and E. Koffi. (2010). A new global gridded data set of CO_2 emissions from fossil fuel combustion: Methodology and evaluation. *J. Geophys. Res., Vol. 115,* D19306, DOI: 10.1029/2009JD013439

[Refaat et al., 2010] Refaat, T. F., S. Ismail, G. J. Koch, L. Diaz, K. Davis, and M. Rubio, (2010). Field Testing of a Two-Micron DIAL System for Profiling Atmospheric Carbon Dioxide. *25th International Laser Radar Conference,* 5-9 Jul. 2010, St. Petersburg, Russia.

[Refaat et al., 2011] Refaat, T. F., S. Ismail, G. J. Koch, M. Rubio, T. L. Mack, A. Notari, J. E. Collins, J. Lewis, R. De Young, Y. Choi, N. Abedin and U. N. Singh. (2011, January). Backscatter 2-µm Lidar Validation for Atmospheric CO_2 Differential Absorption Lidar Applications. *IEEE Transaction on Geoscience and Remote Sensing, Vol. 49 (Issue 1)* pp. 572-580. DOI: 10.1109/TGRS.2010.2055874

[Refaat et al., 2013] Refaat, T. F., S. Ismail, A. R. Nehrir, J. W. Hair, J. H. Crawford, I. Leifer, and T. Shuman, (2013). Performance evaluation of a 1.6-µm methane DIAL system from ground, aircraft and UAV platforms. *Optics Express, Vol.21(Issue 25),* pp. 30415-30432 (2013).

[Refaat et al., 2015a] Refaat, T., U. Singh, J. Yu, M. Petros, S. Ismail, M. Kavaya, and K. Davis, (2015). Evaluation of an airborne triple-pulsed 2 μm IPDA lidar for simultaneous and independent atmospheric water vapor and carbon dioxide measurements. *Applied Optics, Vol. 54(Issue 6),* pp.1387-1398 (2015). https://doi.org/10.1364/AO.54.001387

[Refaat et al., 2015b] Refaat, T., U. Singh, M. Petros, R. Remus, and J. Yu, (2015). Self-calibration and laser energy monitor validations for a double-pulsed 2-μm CO₂ integrated path differential absorption lidar application. *Applied Optics, Vol. 54(Issue 24),* pp. 7240-7251 (2015). https://doi.org/10.1364/AO.54.007240

[Refaat et al., 2016a] T. Refaat, U. Singh, J. Yu, M. Petros, R. Remus, and S. Ismail, (2016). Double-pulse 2-μm integrated path differential absorption lidar airborne validation for atmospheric carbon dioxide measurement. *Applied Optics, Vol. 55(Issue 15),* pp. 4232-4246 (2016). https://doi.org/10.1364/AO.55.004232

[Refaat et al., 2016b] T. Refaat, M. Petros, C. Antill, U. Singh and J. Yu, (2016). Wavelength locking to CO₂ absorption line-center for 2-μm pulsed IPDA lidar application. *Proceedings of SPIE Vol. 9879,* Lidar Remote Sensing for Environmental Monitoring XV, 987904 (5 May 2016); doi: 10.1117/12.2224950

[Refaat et al., 2018] Refaat, T., U. Singh, J. Yu, M. Petros, R. Remus, and S. Ismail, (2018). Airborne Two-Micron Double-Pulse IPDA Lidar Validation for Carbon Dioxide Measurements Over Land. EPJ Web of Conferences 176, 05001 (2018), *28th International Laser Radar Conference, ILRC 2017*, Bucharest, Romania, June 25-30, 2017. Published April 13 2018.

[Remsberg and Gordley, 1978] Remsberg, E. E., and L. L. Gordley. (1978). Analysis of differential absorption lidar from the Space Shuttle. *Appl. Opt. Vol. 17 (Issue 4)*, pp. 624-630. Retrieved from: http://dx.doi.org/10.1364/AO.17.000624

[Reuter et al, 2014] Reuter, M., M. Buchwitz, M. Hilker, J. Heymann, O. Schneising, D. Pillai, H. Bovensmann, J.P. Burrows, H. Bösch, R. Parker, A. Butz, O. Hasekamp, C.W. O'Dell, Y. Yoshida, C. Gerbig, T. Nehrkorn, N.M. Deutscher, T. Warneke, J. Notholt, F. Hase, R. Kivi, R. Sussmann, T. Machida, H. Matsueda, and Y. Sawa, (2014). Satellite-inferred European carbon sink larger than expected. *Atmospheric Chemistry and Physics, 14*, pp. 13739-13753, https://doi.org/10.5194/acp-14-13739-2014

[Rienecker et al., 2011] Rienecker, M. M., M. J. Suarez, R. Gelaro. R. Todling, J. Bacmeister, E. Liu, M. G. Bosilovich, … and J. Woollen, (2011, July). MERRA: NASA's Modern-Era Retrospective Analysis for Research and Applications. *Journal of Climate, Vol. 24 (Issue 14),* pp.3624-3648. Retrieved from: http://journals.ametsoc.org/doi/abs/10.1175/jcli-d-11-00015.1

[Riris et al., 2007] Riris, H., J. Abshire, G. Allan, J. Burris, J. Chen, S. Kawa, J.-P. Mao, … and E. Wilson. (2007, October 3). A laser sounder for measuring atmospheric trace gases from space. *Proc. of SPIE Vol. 6750, Lidar Technologies, Techniques, and Measurements for Atmospheric Remote Sensing III,* 67500U. DOI: 10.1117/12.737607

[Riris et al., 2011] Riris, H., M. D. Rodriguez, G. R. Allan, W. E. Hasselbrack, M. A. Stephen, and J. B. Abshire. (2011, September 13). Airborne lidar measurements of atmospheric pressure

made using the oxygen A-band. *Proc. SPIE 8159, Lidar Remote Sensing for Environmental Monitoring XII, 815909.* DOI: 10.1117/12.892021

[Riris et al., 2013] Riris, H., M. Rodriguez, G. Allen, W. Hasselbrack, J. Mao, M. Stephen, and J. Abshire, (2013). Pulsed airborne lidar measurements of atmospheric optical depth using the Oxygen A-band at 765 nm. *Applied Optics Vol. 52, Issue 25,* pp. 6369-6382 (2013). https://doi.org/10.1364/AO.52.006369

[Riris et al., 2017] Riris, H., K. Numata, S. Wu, B. Gonzalez, M. Rodriguez, S. Scott, S. Kawa, and J. Mao, (2017). Methane optical density measurements with an integrated path differential absorption lidar from an airborne platform. *J. Appl. Remote Sens.,* **11**(3), 034001 (July 2017). DOI: 10.1117/1.JRS.11.034001

[RMT, 2011] RMT, Inc. (2011). *Four Corners Generating Station Project.* Retrieved from: http://www.cpuc.ca.gov/environment/info/mha/fourcorners/images/FourCorners_Sept2011web.pdf

[Rothman et al., 2009] Rothman, L. S., I. E. Gordon, A. Barbe, D.C. Benner, P.F. Bernath, M. Birk, V. Boudon, L. R. Brown, A. Campargue, J.-P. Champion, K. Chance, …and J. Vander Auwera, (2009). The HITRAN 2008 molecular spectroscopic database. *Journal of Quantitative Spectroscopy and Radiative Transfer, Vol. 110* (Issues 9-10), pp.533-72, Retrieved from: DOI: 10.1016/j.jqsrt.2009.02.013
http://adsabs.harvard.edu/abs/2009JQSRT.110.533R

[Rothman et al., 2013] Rothman, L. S., I. E. Gordon, Y. Babikov, A. Barbe, D. C. Benner, P.F. Bernath, M. Birk, L. Bizzocchi, V. Boudon, … and G.Wagner. (2013). The HITRAN 2012 molecular spectroscopic database. *Journal of Quantitative Spectroscopy and Radiative Transfer, Vol. 130,* pp.4-50. Retrieved from:
https://www.cfa.harvard.edu/hitran/Download/HITRAN2012.pdf

[Saha et al., 2010] Saha, S., S. Moorthi, H.-L. Pan, X. Wu, J. Wang , S. Nadiga, P. Tripp, R. … and M. Goldberg. (2010). The NCEP Climate Forecast System Reanalysis. *Bulletin of the American Meteorological Society*, *Volume 91* (Issue 8), pp.1015-57. Retrieved from: http://www.sciencedirect.com /science/article/pii/S0022407309000727

[Sakaizawa et al., 2008] D. Sakaizawa, C. Nagasawa, M. Abo, Y. Shibata, and T. Nagai. (2008). Development of a 1.6 μm CO_2 DIAL transmitter using OPM-OPO. *24th International Laser Radar Conference*.

[Salstein et al., 2008] Salstein, D.A., R.M. Ponte, and K. Cady-Pereira. (2008). Uncertainties in atmospheric surface pressure fields from global analyses. *Journal of Geophysical Research: Atmospheres, Vol. 113 (Issue D14)*, Retrieved from:
http://onlinelibrary.wiley.com/doi/10.1029/2007JD009531/abstract.
DOI: 10.1029/2007JD009531

[Sarmiento et al., 2002] Sarmiento, J. L. and N. Gruber. (2002). Sinks for Anthropogenic Carbon. *Physics Today*, Vol. 55 (Issue 8), pp.30-36.

[Schaefer et al., 2011] Schaefer, K., T. Zhang, L. Bruhwiler, and A. P. Barrett. (2011). Amount and timing of permafrost carbon release in response to climate warming. *Tellus B, Vol. 63 (Issue 2),* pp. 165-180. DOI: 10.1111/j.1600-0889.2011.00527.x

[Schneising et al., 2013] Schneising, O., J. Heymann, M. Buchwitz, M. Reuter, H. Bovensmann, and J. P. Burrows, (2013). Anthropogenic carbon dioxide source areas observed from space: assessment of regional enhancements and trends. *Atmospheric Chemistry and Physics, 13*, pp. 2445–2454, doi:10.5194/acp-13- 2445-2013

[Schwandner et al., 2017] Schwandner, F.M., M.R. Gunson, C.E. Miller, S.A. Carn, A. Eldering, T. Krings, K.R. Verhulst, D.S. Schimel, H.M. Nguyen, D. Crisp, C.W. O'Dell, G.B. Osterman, L.T. Iraci, and J.R. Podolske, (2017). Spaceborne detection of localized carbon dioxide sources. *Science Vol. 358, Issue 6360, eaam5782,* doi: 10.1126/science.aam5782

[Schwemmer et al., 1987] Schwemmer, G.K., M. Dombrowski, C. L. Korb, J. Milrod, H. Walden, and R. H. Kagann, (1987). A lidar system for measuring atmospheric pressure and temperature profiles. *Review of scientific instruments, Vol. 58 (Issue 12),* 2226 (1987). https://doi.org/10.1063/1.1139327

[Sellers et al., 2018] Sellers, P. J., D. S. Schimel, B. Moore III, J. Liu, and A. Eldering, (2018). Observing carbon cycle–climate feedbacks from space. *Proceedings of the National Academy of Science of the United States of America, 115(31)*, pp. 7860–7868. doi: 10.1073/pnas.1716613115. https://doi.org/10.1073/pnas.1716613115

[Sharp et al., 2014] Sharp, W.E., T. S. Zaccheo, E.V. Browell, S. Ismail, J.T. Dobler and E.J. Llewellyn (2014), Impact of ambient O₂ (a¹Δ_g) on satellite-based laser remote sensing of O₂ columns using absorption lines in the 1.27 µm region, *Journal of Geophysical Research: Atmospheres, 119,* pp. 7757-7772, doi:10.1002/2013JD021324, June 27, 2014.

[Shiga et al, 2014] Shiga, Y. P., A. M. Michalak, S. M. Gourdji, K. L. Mueller, and V. Yadav. (2014). Detecting fossil fuel emissions patterns from sub-continental regions using North American in-situ CO₂ measurements. *Geophys. Res. Lett.*, 2014GL059684. DOI: 10.1002/2014GL059684

[Simard, et al., 2011] Simard, M., N. Pinto, J. B. Fisher, and A. Baccini. (2011). Mapping forest canopy height globally with spaceborne lidar. *J. Geophys. Res., Vol. 116,* G04021. DOI: 10.1029/2011JG001708

[Singer, 1968] Singer, S.F., (1968). Measurement of atmospheric surface pressure with a satellite-borne laser. *Applied Optics, Vol. 7 (Issue 6),* pp. 1125-1127 (1968). https://doi.org/10.1364/AO.7.001125

[Singh et al., 2013] Singh, U. N., J. Yu, M. Petros, T. Refaat, and K. Reithmaier. (2013, September 17). Development of a pulsed 2-micron integrated path differential absorption lidar for CO₂ measurement. *Proceeding of SPIE. Vol. 8872, Lidar Remote Sensing for Environmental Monitoring XIV, 887209.* San Diego, CA, DOI: 10.1117/12.2028245

[Singh et al., 2014] Singh U., J. Yu, M. Petros, T. Refaat, R. Remus, J. Fay and K. Reithmaier, (2014). Airborne 2-micron double-pulsed integrated path differential absorption lidar for column CO₂ measurement. *Proceedings Volume 9246, Lidar Technologies, Techniques, and Measurements for Atmospheric Remote Sensing X*, 924602 (2014) https://doi.org/10.1117/12.2069670, Amsterdam, Netherlands, 23 October 2014.

[Singh et al., 2015a] Singh, U., B. Walsh, J. Yu, M. Petros, M. Kavaya, T. Refaat, and N. Barnes, (2015). Twenty years of Tm:Ho:YLF and LuLiF laser development for global wind and

carbon dioxide active remote sensing. *Optical Materials Express, Vol. 5(Issue 4),* pp. 827-837 (19 March 2015). https://doi.org/10.1364/OME.5.000827

[Singh et al., 2015b] Singh, U., T. Refaat, J. Yu, M. Petros, and R. Remus, (2015). Double-pulsed 2-μm lidar validation for atmospheric CO_2 measurements. In *Proc. SPIE 9645, Lidar Technologies, Techniques, and Measurements for Atmospheric Remote Sensing XI, 964502* (20 October 2015). doi: 10.1117/12.2196489

[Singh et al., 2017a] Singh, U., T. Refaat, S. Ismail, K. Davis, S. Kawa, R. Menzies, and M. Petros, (2017). Feasibility study of a space-based high pulse energy 2 μm CO_2 IPDA lidar. *Applied Optics, Volume 56 (Issue 23)*, pp. 6531-6547 (10 August 2017). https://doi.org/10.1364/AO.56.006531

[Singh et al., 2017b] Singh, U., M. Petros, T. Refaat, J. Yu, C. Antill, B. Taylor, S. Bowen, A. Welters, R. Remus, T. Wong, K. Reithmaier, J. Lee, and S. Ismail, (2017). Progress on development of an airborne two-micron IPDA lidar for water vapor and carbon dioxide column measurements. *Proc. SPIE 10406, Lidar Remote Sensing for Environmental Monitoring 2017, 1040603* (7 September 2017). doi: 10.1117/12.2276206

[Singh et al., 2018] Singh, U., T. Refaat, M. Petros, and S. Ismail, (2018). Evaluation of 2-μm Pulsed Integrated Path Differential Absorption Lidar for Carbon Dioxide Measurement—Technology Developments, Measurements, and Path to Space. *IEEE Journal of Selected Topics in Applied Earth Observations and Remote Sensing, Vol. 11(Issue 6),* pp. 2059-2067 (2018). DOI: 10.1109/JSTARS.2017.2777453

[Sitch et al., 2003] Sitch, S., B. Smith, I.C. Prentice, A. Arneth, A. Bondeau, W. Cramer, J.O. Kaplan, … and S. Venevsky. (2003). Evaluation of ecosystem dynamics, plant geography and terrestrial carbon cycling in the LPJ dynamic global vegetation model. *Global Change Biology, Vol 9* (Issue 2), pp. 161-185.

[Skamarock et al., 2008] Skamarock, W. C. and J. B. Klemp. (2008, March). A time-split nonhydrostatic atmospheric model for weather research and forecasting applications. *J. Comput. Phys., Vol. 227* (Issue 7), pp. 3465–3485.

[SOCCR, 2007] SOCCR, (2007). The First State of the Carbon Cycle Report (SOCCR): The North American Carbon Budget and Implications for the Global Carbon Cycle. A Report by the U.S. Climate Change Science Program and the Subcommittee on Global Change Research [King, A.W., L. Dilling, G.P. Zimmerman, D.M. Fairman, R.A. Houghton, G. Marland, A.Z. Rose, and T.J. Wilbanks (eds.)]. National Oceanic and Atmospheric Administration, National Climatic Data Center, Asheville, NC, USA, 242 pages. http://cdiac.ess-dive.lbl.gov/SOCCR/final.html

[Solomon et al., 2007] Solomon, S., Qin, D., Manning, M., Chen, Z., Marquis, M., Averyt, K., M.Tignor and Miller, H., ed. (2007). IPCC, 2007: Climate Change 2007: The Physical Science Basis. *Contribution of Working Group I to the Fourth Assessment Report of the Intergovernmental Panel on Climate Change.* Cambridge, United Kingdom and New York, NY, USA.

[Spiers et al., 2002] Spiers, G.D., R.T. Menzies, D.M. Tratt, and M. Phillips. (2002). The Laser Absorption Spectrometer for Carbon Dioxide Sink and Source Detection. Proceedings of the Second Annual Earth Science Technology Conference, Greenbelt, MD.

[Spiers et al., 2011a] Spiers, G.D., R.T. Menzies, J. Jacob, L.E. Christensen, M.W. Phillips, Y. Choi, and E.V. Browell, (2011). Atmospheric CO_2 measurements with a 2 µm airborne laser absorption spectrometer employing coherent detection. *Appl. Opt. Vol. 50 (Issue 14)*, pp. 2098-2111 (2011).

[Spiers et al., 2011b] Spiers, G.D., R.T. Menzies, and J.C. Jacob, (2011). CO_2 Mixing Ratio Retrievals from JPL Airborne Laser Absorption Spectrometer Flight Campaigns in 2010-11. 2011 AGU Fall Meeting, Paper A21D-0105.

[Spiers et al., 2012] Spiers, G.D., R.T. Menzies, J.C. Jacob, and S. Geier. (2012). The Remote Measurement of Carbon Dioxide by the CO₂LAS Instrument during the 2011 ASCENDS Field Campaign. 2012 AGU Fall Meeting, Paper, A51H-04.

[Spiers et al., 2013] Spiers, G. D., R.T. Menzies, J. Jacob, J.B. Abshire, H. Riris, M.M. Yang, Y. Choi, and B.L. Meadows. (2013). Recent measurement results from the Carbon Dioxide Laser Absorption Spectrometer for the ASCENDS Mission. 2013 AGU Fall Meeting, Paper A23H-02.

[Spiers et al., 2016] Spiers, G.D., R.T. Menzies, and J.C. Jacob, (2016). Lidar reflectance from snow at 2.05 μm wavelength as measured by the JPL Airborne Laser Absorption Spectrometer, *Appl. Opt. Vol. 55, Issue 8*, pp. 1978-1986 (2016), https://doi.org/10.1364/AO.55.001978

[Stephen et al., 2007] Stephen, M., M. Krainak, H. Riris and G. R. Allan. (2007, August). Narrowband, tunable, frequency-doubled, erbium-doped fiber-amplified transmitter. *Optics Letters, Vol. 32* (No. 15), pp. 2073-2075.

[Stephen et al., 2017] Stephen, M.; A. Yu, J. Chen, K. Numata, J. Nicholson, A. Hariharan, S. Wu, G. Allan, B. Gonzales, L. Han, W. Hasselbrack, M. Rodriguez, W. Mamakos, M. Fahey, and J. Abshire, (2017). Fiber-based, trace-gas, laser transmitter technology development for space. *NASA 2017 ESTF Conference, 2017,* available at: https://esto.nasa.gov/forum/estf2017/presentations/Stephen_Yu_A5P2_ESTF2017.pdf

[Stephen et al., 2018] Stephen, M., A. Yu, J. Chen, K. Numata, S. Wu, B. Gonzales, L. Han, M. Fahey, M. Plants, M. Rodriguez, G. Allan, J. Abshire, J. Nicholson, A. Hariharan, W. Mamakos, and B. Bean, (2018). Fiber-based laser MOPA transmitter packaging for space environment. *Proc. SPIE Vol. 10513, Components and Packaging for Laser Systems IV, 1051308* (20 Feb 2018). doi: 10.1117/12.2290720; https://doi.org/10.1117/12.2290720

[Stohl, 1998] Stohl, A. (1998). Computation, accuracy and applications of trajectories – A review and bibliography. *Atmos. Environ., Vol. 32* (Issue 6), pp. 947–966.

[Sun et al., 2010] Sun, B., A. Reale, D. J. Seidel, and D. C. Hunt. (2010). Comparing radiosonde and COSMIC atmospheric profile data to quantify differences among radiosonde types and the effects of imperfect collocation on comparison statistics. *J. Geophys. Res.: Atmospheres, Vol. 115* (Issue D23), D23104. DOI: 10.1029/2010JD014457

[Sun and Abshire, 2012] X. Sun and J. B. Abshire, (2012). Comparison of IPDA lidar receiver sensitivity for coherent detection and for direct detection using sine-wave and pulsed modulation. *Opt. Express, Vol. 20 (Issue 19),* pp. 21291-21304. Retrieved from: http://dx.doi.org/10.1364/OE.20.021291

[Sun et al., 2013] Sun, X., J.B. Abshire, J.F. McGarry, G.A. Neumann, J.C. Smith, J.F. Cavanaugh, D. J. Harding, … and M.T. Zuber. (2013, June). Space lidar developed at the nasa goddard space flight center - the first 20 years. *IEEE Journal of Selected Topics in Applied Earth Observations and Remote Sensing, Vol.6* (No. 3), pp. 1660-1675. DOI: 10.1109/JSTARS.2013.2259578

[Sun et al., 2017a] Sun, X.; J. Abshire, A. Ramanathan, H. Riris, G. Allan, W. Hasselbrack, J. Mao, and M. Stephen, (2017). Advances in the CO₂ Sounder Lidar for Measurements from Aircraft and in Scaling for Space. Presented at *NASA 2017 Earth Science Technology Forum (ESTF) Conference, 2017,* Pasadena CA, June 2017. Abstract available at: https://esto.nasa.gov/forum/estf2017/abstracts/Sun_Abshire.htm Presentation available at: https://esto.nasa.gov/forum/estf2017/presentations/Sun_Abshire_A5P5_ESTF2017.pdf

[Sun et al., 2017b] Sun, X., J. B. Abshire, J. D. Beck, P. Mitra, K. Reiff, and G.Yang, (2017). HgCdTe avalanche photodiode detectors for airborne and spaceborne lidar at infrared wavelengths. *Optics Express, Volume 25 (No.14),* pp. 16589-16602 (10 July 2017). https://doi.org/10.1364/OE.25.016589

[Sun et al., 2018a] Sun, X, J. Abshire, M. Krainak, W. Lu, J. Beck, W. Sullivan, P. Mitra, D. Rawlings, R. Fields, D. Hinkley, B. Hirasuna, (2018). Single photon HgCdTe avalanche photodiode and integrated detector cooler assemblies for space lidar applications," *Proc. SPIE 10659, Advanced Photon Counting Techniques XII,* 106590C (14 May 2018), doi: 10.1117/12.2305017; https://doi.org/10.1117/12.2305017

[Sun et al., 2018b] Sun, X, J. B. Abshire, J.-M. Lauenstein, W. Sullivan, J. Beck, and J. E. Hubbs, (2018). Evaluation of space radiation effects on HgCdTe avalanche photodiode arrays for Lidar applications. *Proc. SPIE 10624, Infrared Technology and Applications XLIV,* 106240G (31 May 2018). DOI: 10.1117/12.2304601

[Takahashi et al., 1999] Takahashi, T., R. H. Wanninkhof, R A. Feely, R. F. Weiss, D. W. Chipman, N. Bates, J. Olafsson, C. Sabine, and S.C. Sutherland. (1999). Net sea-air CO₂ flux over the global oceans: an improved estimate based on the sea-air pCO₂ difference. Proceedings of the 2nd International Symposium: CO₂ in the Oceans, the 12th Global Environmental Tsukuba, 18-22 January 1999, Tsukuba Center of Institutes.

[Takahashi et al., 2002] Takahashi, T., S. C. Sutherland, C. Sweeney, A. Poisson, N. Metzl, B. Tilbrook, N. Bates, … and Y. Nojiri. (2002). Global sea-air CO₂ flux based on climatological surface ocean *p*CO₂, and seasonal biological and temperature effects. *Deep-Sea Res.Part II: Topical Studies in Oceanography, Vol.49* (Issues 9-10), pp.1601-1622.

[Takahashi et al., 2009] Takahashi, T., S. C. Sutherland, R. Wanninkhof, C. Sweeney, R. A. Feely, D. W. Chipman, B. Hales, … and N. R. Bates. (2009). Climatological mean and decadal changes in surface ocean pCO₂, and net sea-air CO₂ flux over the global oceans, *Deep Sea Res., Part II, Vol. 56,* pp. 554–577. Retrieved from: http://cdiac.ornl.gov/oceans/LDEO_Underway_Database/air_sea_flux_2010.html. DOI: 10.1016/j.dsr2.2008.12.009

[Tans and Keeling, n.d.] Tans, P., and R. Keeling. (n. d.). Trends in Atmospheric Carbon Dioxide. *National Oceanic & Atmosphere Administration, Earth System Research Laboratory (NOAA/ESRL).* Retrieved from: http://www.esrl.noaa.gov/gmd/ccgg/trends/

[Tans et al., 1990] Tans, P. P., I. Y. Fung, and T. Takahashi. (1990), Observational Constraints on the Global Atmospheric CO₂ Budget. *Science, Vol. 247,* pp.1431-1438.

[Tarnocai et al., 2009] Tarnocai, C., J.G. Canadell, E.A.G. Schuur, P. Kuhry, G. Mazhitova and S. Zimov. (2009). Soil organic carbon pools in the northern circumpolar permafrost region. *Global Biogeochemical Cycles, Vol 23* (Issue 2)*,* GB2023. DOI: 10.1029/ 2008GB003327

[Taylor et al., 2016] Taylor, T.E., C.W. O'Dell, C. Frankenberg, P.T. Partain, H.Q. Cronk, A. Savtchenko, R.R. Nelson, E.J. Rosenthal, A.Y. Chang, B. Fisher, G.B. Osterman, R.H. Pollock, D. Crisp, A. Eldering, and M.R. Gunson, (2016). Orbiting Carbon Observatory-2 (OCO-2) cloud screening algorithms: validation against collocated MODIS and CALIOP data. *Atmos. Meas. Tech., Vol. 9, Issue 3,* pp. 973-989, https://doi.org/10.5194/amt-9-973-2016

[Tippett et al., 2003] Tippett, M. K., J. L. Anderson, C. H. Bishop, T. M. Hamill, T. M. and J. S. Whitaker. (2003, July). Ensemble Square Root Filters*. *Monthly Weather Review, Vol. 131 (Issue 7),* pp.1485-1490.

[Tran et al., 2006] Tran, H., C. Boulet, and J.-M. Hartmann, (2006, August). Line mixing and collision-induced absorption by oxygen in the A band: Laboratory measurements, model, and tools for atmospheric spectra computations. *J. of Geophysical Res., Vol. 111 (Issue D15),* pp. 16. D15210, 2006. DOI: 10.1029/2005JD006869

[Uliasz, 1994] Uliasz, M. (1994), Lagrangian particle dispersion modeling in mesoscale applications. *Environmental Modeling, Vol. II,* pp. 71-102.

[UN, 2013] UN, (2013). United Nations Statistics Division. Retrieved from: http://unstats.un.org/unsd/default.htm

[Vay et al., 2003] Vay, S. A., J. H. Woo, B. E. Anderson, K. L. Thornhill, D. R. Blake, D. J. Westberg, C. M. Kiley, … and S. R. Nolf, (2003, October). Influence of regional-scale anthropogenic emissions on CO₂ distributions over the western North Pacific. *J. Geophys. Res. Atmospheres, Vol. 108 (Issue D20),* pp. 8801. DOI: 10.1029/2002JD003094

[Wang et al., 2014] Wang, J. S., S. R. Kawa, J. Eluszkiewicz, D. F. Baker, M. Mountain, J. Henderson, T. Nehrkorn, and T. S. Zaccheo. (2014). A Regional CO₂ Observing System Simulation Experiment for the ASCENDS Satellite Mission.

[Wang et al., 2018] Wang, J. S., S. R. Kawa, G. J. Collatz, M. Sasakawa, L.V. Gatti, T. Machida, Y. Liu, and M.E. Manyin, (2018). A global synthesis inversion analysis of recent variability in CO₂ fluxes using GOSAT and in situ observations. *Atmos. Chem. Phys., Vol. 18, Issue 15,* pp. 11097-11124, doi:10.5194/acp-18-11097-2018

[Wennberg et al., 2012] Wennberg, P. O., W. Mui, D. Wunch, E. A. Kort, D. R. Blake, E. L. Atlas, G. W. Santoni, … and M. L. Fischer. (2012). On the Sources of Methane to the Los Angeles Atmosphere. *Environmental Science & Technology, Vol. 46* (Issue 17), pp. 9282-9289. DOI: 10.1021/es301138y

[Werle et al., 1993] Werle, P., R. Mucke, and F. Slemr, (1993). The limits of signal averaging in atmospheric trace-gas monitoring by tunable diode-laser absorption spectroscopy (TDLAS). *Applied Physics B Photophysics and Laser Chemistry, Volume 57 (Issue 2)*, pp. 131-139. DOI: 10.1007/BF00425997

[Werle et al., 2004] Werle P. W., P. Mazzinghi, F. D'Amato, M. De Rosa, K. Maurer, F. Slemr. (2004). Signal processing and calibration procedures for in situ diode-laser absorption spectroscopy. *Spectrochimica Acta Part A: Molecular and Biomolecular Spectroscopy, Volume 60* (Issue 8), pp. 1685-1705. DOI: 10.1016/j.saa.2003.10.013

[Werle, 2011] Werle, Peter, (2011). Accuracy and precision of laser spectrometers for trace gas sensing in the presence of optical fringes and atmospheric turbulence. *Applied Physics B: Lasers and Optics Volume 102, Issue 2,* pp. 313-329, (February, 2011).   DOI 10.1007/s00340-010-4165-9

[Wilson et al., 2007] Wilson E.L., E. M. Georgieva, and W. S. Heaps. (2007). Development of a Fabry-Perot interferometer for ultra-precise measurements of column CO₂. *Meas. Sci. Technology, Vol. 18* (Issue 5), pp. 1495-1502, 2007

[Winker et al., 2010] Winker, D. M., J. Pelon, J. A. Coakley Jr., S. A. Ackerman, R. J. Charlson, P. R. Colarco, P. Flamant, Q. Fu, R. M. Hoff, C. Kittaka, T. L. Kubar, H. Le Treut, M. P. Mccormick, G. Mégie, L. Poole, K. Powell, C. Trepte, M. A. Vaughan, and B. A. Wielicki, (2010). The CALIPSO Mission: A Global 3D View of Aerosols and Clouds. *American Meteorological Society*, September 2010, https://doi.org/10.1175/2010BAMS3009.1

[Winker et al. 2013] Winker, D. M., J. L. Tackett, B. J. Getzewich, Z. Liu, M. A. Vaughan, and R. R. Rogers. (2013). The global 3-D distribution of tropospheric aerosols as characterized by CALIOP, *Atmos. Chem. Phys., Vol. 13,* pp. 3345-3361. Retrieved from: www.atmos-chem-phys.net/13/3345/2013/ DOI:10.5194/acp-13-3345-2013

[Worden et al., 2017] Worden, J. R., G. Doran, S. Kulawik, A. Eldering, D. Crisp, C. Frankenberg, C. O'Dell, K. Bowman, (2017). Evaluation and attribution of OCO-2 XCO₂ uncertainties. *Atmospheric Measurement Techniques, Vol. 10, Issue 7,* pp. 2759–2771. https://doi.org/10.5194/amt-10-2759-2017

[Wunch et al., 2011] Wunch, D., P. O. Wennberg, G. C. Toon, B. J. Connor, B. Fisher, G. B. Osterman, C. Frankenberg, L. Mandrake, C. O'Dell, P. Ahonen, S. C. Biraud, R. Castano, N. Cressie, D. Crisp, N. M. Deutscher, A. Eldering, M. L. Fisher, D. W. T. Griffith, M. Gunson, P. Heikkinen, G. Keppel-Aleks, E. Kyrö, R. Lindenmaier, R. Macatangay, J. Mendonca, J. Messerschmidt, C. E. Miller, I. Morino, J. Notholt, F. A. Oyafuso, M. Rettinger, J. Robinson, C. M. Roehl, R. J. Salawitch, V. Sherlock, K. Strong, R. Sussmann, T. Tanaka, D. R. Thompson, O. Uchino, T. Warneke, and S.C. Wofsy, (2011). A method for evaluating bias in global measurements of CO₂ total columns from space. *Atmospheric Chemistry and Physics , Vol. 11, Issue 23,* pp. 12317-12337, https://doi.org/10.5194/acp-11-12317-2011

[Wunch et al., 2013] Wunch, D., P. O. Wennberg, J. Messerschmidt, N. C. Parazoo, G. C. Toon, N. M. Deutscher, G. Keppel-Aleks, … and J. Notholt. (2013). The covariation of Northern Hemisphere summertime CO₂ with surface temperature in boreal regions. *Atmospheric Chemistry and Physics, Vol. 13*, pp. 9447–9459. DOI: 10.5194/acp-13-9447-2013

[Wunch et al., 2017] Wunch, D., P. O. Wennberg, G. Osterman, B. Fisher, B. Naylor, C.M. Roehl, C. O'Dell, L. Mandrake, C. Viatte, M. Kiel, D. W. T. Griffith, N. M. Deutscher, V. A. Velazco, J. Notholt, T. Warneke, C. Petri, M. De Maziere, M. K. Sha, R. Sussmann, M. Rettinger, D. Pollard, J. Robinson, I. Morino, O. Uchino, F. Hase, T. Blumenstock, D.G. Feist, S. G. Arnold, K. Strong, J. Mendonca, R. Kivi, P. Heikkinen, L. Iraci, J. Podolske, P.

W. Hillyard,, S. Kawakami, M. K. Dubey, H. A. Parker, E. Sepulveda, O. E. García, Y. Te, P. Jeseck, M. R. Gunson,, D. Crisp, and A. Eldering, (2017). Comparisons of the Orbiting Carbon Observatory-2 (OCO-2) X$_{CO2}$ measurements with TCCON. *Atmos. Meas. Tech., Vol. 10, Issue 6,* pp. 2209–2238, https://www.atmos-meas-tech.net/10/2209/2017/

[Wysocki et al., 2006] Wysocki, P., T. Wood, A. Grant, D. Holcomb, K. Chang, M. Santo, L. Braun, and G. Johnson. (2006, March 5). High Reliability 49 dB Gain, 13 W PM Fiber Amplifier at 1550 nm with 30 dB PER and Record Efficiency. Optical Society of America / Optical Fiber Communication Conference, Anaheim. ISBN: 1-55752-802-0

[Yang et al., 2006] Yang, F., H-L Pan, S.K. Kruger, S. Moorthi, and S.J.Lord, (2006). Evaluation of the NCEP Global Forecast System at the ARM SGP Site. *Monthly Weather Review, Vol. 134, Issue 12,* pp.3668-90. Retrieved from: http://journals.ametsoc.org/doi/abs/10.1175/MWR3264.1

[Yang et al., 2018] Yang, D. X., Y. Liu, Z. N. Cai, X. Chen, L. Yao, and D. R. Lu, (2018). First Global Carbon Dioxide Maps Produced from TanSat Measurements. *Adv. Atmos. Sci., Volume 35, Issue 6*, pp. 621–623, doi:10.1007/s00376-018-7312-6

[Yoshida et al., 2013] Yoshida, Y., N. Kikuchi, I. Morino, O. Uchino, S. Oshchepkov, A. Bril, T. Saeki, N. Schutgens, G. C. Toon, D. Wunch, C. M. Roehl, P. O. Wennberg, D. W. T. Griffith, N. M. Deutscher, T. Warneke, J. Notholt, J. Robinson, V. Sherlock, B. Connor, M. Rettinger, R. Sussmann, P. Ahonen, P. Heikkinen, E. Kyrö, J. Mendonca, K. Strong, F. Hase, S. Dohe, and T. Yokota, (2013), Improvement of the retrieval algorithm for GOSAT SWIR XCO$_2$ and XCH$_4$ and their validation using TCCON data. *Atmos. Meas. Tech., Vol. 6, Issue 6,* pp. 1533–1547, doi:10.5194/amt-6-1533-2013

[Yu et al., 2003] Yu J., A. Braud, and M. Petros, (2003). 600-mJ, double-pulse 2-µm laser. *Optics Letters, Vol. 28 (Issue 7)*, pp. 540-542. http://dx.doi.org/10.1364/OL.28.000540

[Yu et al., 2012] Yu J., M. Petros, K. Reithmaier, Y. Bai, B. C. Trieu, T. F. Refaat, M. J. Kavaya, and U. N. Singh, (2012). A 2-micron pulsed integrated path differential absorption lidar development for atmospheric CO$_2$ concentration measurements. *26th International Laser Radar Conference,* June 25-29, 2012, Porto Heli, Greece.

[Yu et al., 2015] Yu, A. W., J. B. Abshire, M. A. Stephen, J. R. Chen, S. Wu, B. Gonzalez, L. Han, K. Numata, G. R. Allan, W. Hasselbrack, J. W. Nicholson, M. Yan, P. Wisk, A. DeSantolo, B. Mangan, G. Puc, D. Engin, B. Mathason, and M. Storm, (2015). Fiber-Based Laser Transmitter at 1.57 µm for Remote Sensing of Atmospheric Carbon Dioxide from Satellites. *Advanced Solid State Lasers*, *OSA Technical Digest (online)* (Optical Society of America, 2015), paper ATh1A.1. https://doi.org/10.1364/ASSL.2015.ATh1A.1

[Yu et al., 2017] J. Yu, M. Petros, U. Singh. T. Refaat, K. Reithmaier, R. Remus, and W. Johnson, (2017). An Airborne 2-µm Double-Pulsed Direct-Detection Lidar Instrument for Atmospheric CO$_2$ Column Measurements. *Journal of Atmospheric and Oceanic Technology, 34*, pp. 385-400 (2017). https://doi.org/10.1175/JTECH-D-16-0112.1

[Zaccheo et al., 2014] Zaccheo, T. Scott, Timothy Pernini, Hilary E. Snell, and Edward V. Browell, (2014). Impact of atmospheric state uncertainties on retrieved XCO$_2$ columns from laser differential absorption spectroscopy measurements. *Journal of Applied Remote Sensing (SPIE) Vol. 8,* No. 1.

[Zhang et al., 1999] Zhang, T., R. G. Barry, K. Knowles, J. A. Heginbottom, and J. Brown, (1999). Statistics and characteristics of permafrost and ground-ice distribution in the Northern Hemisphere. *Polar Geography Vol. 23* (Issue 2), pp. 147–169.

[Zhao and Tans, 2006] Zhao, C. L. and P.P. Tans. (2006). Estimating uncertainty of the WMO mole fraction scale for carbon dioxide in air. *J. Geophys. Res. Vol. 111* (Issue D8), D08S09. DOI: 10.1029/2005JD006003

[Zimov et al., 1999] Zimov, S. A., S. P. Davidov, G. M. Zimova, A. I. Davidova, F. S Chapin III, M. C. Chapin & J. F. Reynolds. (1999). Contribution of Disturbance to Increasing Seasonal Amplitude of Atmospheric CO₂, *Science, Vol. 284,* pp. 1973-1976.

B. Acronyms

µm	micrometer
3D	3-Dimensional
3D	Three Dimensional
3-D	3-Dimensional
4DVAR	4-Dimensional Variational
ABL	Atmospheric Boundary Layer
ABoVE	Arctic-Boreal Vulnerability Experiment
ACGS	Atmospheric CO₂ Grating Spectrometer
ACOS	Atmospheric CO₂ Observations from Space
ACES	ASCENDS CarbonHawk Experiment Simulator
ACS	Attitude Control Subsystem
ACT-America	Atmospheric Carbon and Transport-America
AD&CS	Attitude Determination and Control System
AER	Atmospheric and Environmental Research
AFB	Air Force Base
AGCM	Atmospheric General Circulation Model
AGU	American Geophysical Union
AIRS	Atmospheric Infrared Sounder
ALS	Adaptive Launch Solutions
AMSR-E	Advanced Microwave Scanning Radiometer for EOS
AOM	Acousto-Optic Modulator
APD	Avalanche Photo Diode
APIC	Auxiliary Payload Integration Contractor
AR	Anti-Reflection
ASCENDS	Active Sensing of CO₂ Emissions over Nights, Days, and Seasons
A-SCOPE	Advanced Space Carbon and Climate Observation of Planet Earth
AVOCET	Atmospheric Vertical Observations of Carbon Dioxide in the Earth's Troposphere
BBL	Broad Band Lidar
BC	British Columbia
BCP	Ball Aerospace Commercial Platform
BRDF	Bidirectional Reflectance Distribution Function

CA	California
CALIPSO	Cloud-Aerosol Lidar and Infrared Pathfinder Satellite Observations
Caltech	California Institute of Technology
CAMS	Copernicus Atmosphere Monitoring Service
CAPABLE	Chemistry and Physics Atmospheric Boundary Layer Experiment
CASA	Carnegie-Ames-Stanford-Approach
CBE	Current Best Estimate
CCGG	Carbon Cycle Greenhouse Gas
CCSM	Community Climate System Model
CDF	Cumulative Distribution Function
CDIAC	Carbon Dioxide Information Analysis Center
CFSR	Climate Forecast System Reanalysis
CH_4	Methane, Natural Gas
CIRA	Cooperative Institute for Research in the Atmosphere
CNES	Centre National d'Etudes Spatiales (French Space Agency)
CO	Carbon Monoxide
CO	Colorado
CO_2	Carbon Dioxide
CONUS	Contiguous United States, Continental United States
CSU	Colorado State University
CT	Carbon Tracker
CW	Continuous Wave
DAOD	Differential Absorption Optical Depth
DC	Direct Current
DC	District of Columbia
DEM	Digital Elevation Model
DFB	Distributed Feedback
DFB-LD	Distributed Feedback Laser Diode
DIAL	Differential Absorption Lidar
DOD	Differential Optical Depth
DOI	Digital Object Identifier
DRS	DRS Technologies Sensors and Targeting Systems, Inc., in Dallas, TX.
DSS	Dual Spacecraft System

DSX	originally Deployable Structures Experiment
DTC	Developmental Testbed Center
e-APD	electron initiated Avalanche Photo Diode
ECMWF	European Centre for Medium-Range Weather Forecasts
EDFA	Erbium Doped Fiber Amplifier
EE8	Earth Explorer 8
EELV	Evolved Expendable Launch Vehicle
EF	Enhancement Factor
EMC	Electromagnetic Compatibility
EMI	Electromagnetic Interference
EnKF	Ensemble Kalman Filter
ENSO	El Niño Southern Oscillation
ENVISAT	Environmental Satellite
EPA	Environmental Protection Agency
Er	Erbium
ESA	European Space Agency
ESAS	Earth Science and Applications from Space
ESD	Earth Science Division
ESMPO	Earth Systematic Mission Program Office
ESPA	EELV Secondary Payload Adapter
ESRL	Earth System Research Laboratory
ESRL GMD	Earth System Research Laboratory Global Monitoring Division
ESTO	Earth Science Technology Office
EU	European Union
EVI	Earth Venture Instrument
FF	Fossil Fuel
FFCO₂	Fossil Fuel CO₂
FFT	Fast Fourier Transform
FM/CW	Frequency-Modulated/Continuous Wave
FOV	Field of View
FP	Fabry-Perot
FPGA	Field-Programmable Gate Array
FTS	Fourier Transform Spectrometer

FWHM	Full Width at Half Maximum
FY	Fiscal Year
FY-3D	FengYun-3D
GAS	Greenhouse gases Absorption Spectrometer
GAW	Global Atmospheric Watch
GCM	General Circulation Model
gC m^{-2}	grams Carbon per square meter
gC m^{-2} d^{-1}	grams Carbon per square meter per day
GeoCarb	Geostationary Carbon Observatory
GEOS-5	Goddard Earth Observing System Model, Version 5
GEVS	General Environmental Verification Specification
GFED	Global Fire Emissions Database
GFS	Global Forecast System
GIM	Geostatistical Inverse Modeling
GHG	Greenhouse Gas
GHz	Gigahertz (1 Billion Hertz)
GLAS	Geoscience Laser Altimeter System
GMAO	Global Modeling and Assimilation Office
GMI	Gaofen-5 Greenhouse-gases Monitoring Instrument
GOSAT	Greenhouse gases Observing SATellite
GPP	Gross Primary Production, Gross Primary Productivity
GPS	Global Positioning System
GSFC	Goddard Space Flight Center
Gt	Gigatons
Gt CO₂ y^{-1}	Gigatons of Carbon Dioxide per year
GTOPO30	30-arc second resolution Digital Elevation Model developed by USGS
HgCdTe	Mercury Cadmium Telluride
HITRAN	High Resolution Transmission
H₂O	Dihydrogen Monoxide, Water
HDO	Hydrogen Deuterium Oxide
Hz	Hertz, One cycle per second
IASI	Infrared Atmospheric Sounding Interferometer
IAV	InterAnnual Variability

ICESat	Ice, Cloud and land Elevation Satellite
IDCA	Integrated Detector Cooler Assembly
IF	Intermediate Frequency
IIP	Instrument Incubator Program
IM	Intensity Modulation
IM-CW	Intensity-Modulated Continuous-Wave
IN	Indiana
INFlux	Indiana Flux Study
INTEX	Intercontinental Chemical Transport Experiment
INTEX-NA	Intercontinental Chemical Transport Experiment-North America
IPCC	Intergovernmental Panel on Climate Change
IPDA	Integrated Path Differential Absorption
IR	Infrared
ISD	Integrated Surface Database
ISS	International Space Station
IWGGMS	International Workshop on Greenhouse Gas Measurements from Space
Exelis	ITT Exelis, Inc.
JAXA	Japan Aerospace Exploration Agency
JPL	Jet Propulsion Laboratory
K	Kelvin (unit of temperature)
kHz	Kilohertz (1thousand Hertz)
KTP	Potassium Titanyl Phosphate
LAI	Leaf Area Index
LaRC	Langley Research Center
LAS	Laser Absorption Spectrometer
LBLRTM	Line-By-Line Radiative Transfer Model
LCROSS	Lunar Crater Observation and Sensing Satellite
LEO	Low Earth Orbit
LGS	Lucent Government Solutions
LIDAR	Light Detection and Ranging
LMA	Large Mode Area
LO	Local Oscillator
LPJ	Lund–Potsdam–Jena Dynamic Global Vegetation Model

LPDM	Lagrangian Particle Dispersion Model
LT	Local Time
LUT	Lookup Table
MCR	Mission Confirmation Review
MCT	Mercury Cadmium Telluride
MERRA	Modern Era Retrospective-analysis for Research and Applications
MFLL	Multifunctional Fiber Laser Lidar
MHz	Megahertz (1 million Hertz)
MODIS	Moderate Resolution Imaging Spectroradiometer
MOPA	Master Oscillator Power Amplifier
NA	North America
NAM	North American Mesoscale Model
NASA	National Aeronautics and Space Administration
NASEM	National Academies of Sciences, Engineering, and Medicine
NCAR	National Center for Atmospheric Research
NCDC	National Climatic Data Center
NDP	Numeric Data Package
NEE	Net Ecosystem Carbon Exchange, Net Ecosystem Exchange
NEP	Noise-Equivalent Power
NGA	Northrop Grumman Aerospace
NIR	Near-Infrared
NJ	New Jersey
NO₂	Nitrogen Dioxide
NOAA	National Oceanic and Atmospheric Administration
NM	New Mexico
NRC	National Research Council
NV	Nevada
NWP	Numerical Weather Prediction
O₂	Oxygen
OCO	Orbiting Carbon Observatory
OCO-2	Orbiting Carbon Observatory-2
OCO-3	Orbiting Carbon Observatory-3
OD	Optical Depth

ODIAC	Open-source Data Inventory of Anthropogenic CO_2 emission
OFCM	Office of the Federal Coordinator for Meteorology
OPA	Optical Parametric Amplifier
ORNL	Oak Ridge National Laboratory
OSSE	Observing System Simulation Experiment
OU	University of Oklahoma
P	Pressure
PBL	Planetary Boundary Layer
PCI	Peripheral Component Interconnect
PCTM	Parameterized Chemistry and Transport Model
PDR	Preliminary Design Review
PEM	Photo-Electro-Magnetic
PIN	PIN diode (PIN corresponds to the diode construction)
PMT	photomultiplier
PN	Pseudorandom Noise
PN	Pseudorandom Number
POLDER	Polarization and Directionality of Earth Reflectances
PPLN	Periodically Poled Lithium Niobate crystal
ppm	Parts Per Million
ppmv	Parts Per Million by Volume
PSU	Penn State University
PWG	planar waveguide amplifier
PXI	PCI Extensions for Instrumentation
q	humidity
QE	Quantum Efficiency
RAOB	RAdiosonde OBservation
RMS	Root Mean Square
RMSE	Root Mean Square Error
RRV	Railroad Valley, Nevada
RT	Radiative Transfer
SAIF	Science and Aircraft Integration Facility
SCIAMACHY	SCanning Imaging Absorption spectroMeter for Atmospheric CartograpHY
SDT	Science Definition Team

SH	Southern Hemisphere
SiB3	Simple Biosphere model, version 3
SiB-CASA	Simple Biosphere/Carnegie-Ames-Stanford Approach
SIF	Solar Induced chlorophyll Fluorescence
SLED	SuperLuminExcent Diode
SNR	Signal to Noise Ratio
SOCCR	State of the Carbon Cycle Report
SPCM	Single Photon Counting Module
SRTM	Shuttle Radar Topography Mission
SSE	Scattering Surface Elevation
SSL	formerly SS/L, Space Systems/Loral
STILT	Stochastic Time-Inverted Lagrangian Transport
SWIR	Short-Wavelength InfraRed
SZA	Solar Zenith Angle
T	Temperature
TANSO	Thermal And Near infrared Sensor for carbon Observation
TANSO FTS	TANSO Fourier Transform Spectrometer
TBD	To Be Determined
TBR	To Be Reviewed?
TCCON	Total Carbon Column Observing Network
TgC y⁻¹	Teragrams of Carbon per year
TM5	Transport Model, Version 5
Tm/Ho	Thulium/Holmium
TOF	Time Of Flight
TransCom	Atmospheric Tracer Transport Model Intercomparison Project
TVAC	Thermal Vacuum
ULA	United Launch Alliance
UR	Unambiguous Range
US	United States
U.S.	United States
USGS	United States Geological Survey
UT	Universal Time
UTC	Universal Time Coordinated

VLMA	Very Large Mode Area
WBI	West Branch Iowa
WDCGG	World Data Centre for Greenhouse Gases
WMO	World Meteorological Organization
WRF	Weather Research and Forecasting
WV	Water Vapor
XCO$_2$	Column-averaged CO$_2$ dry air mole fraction
XHDO	Column water vapor concentration
YLF	Yttrium Lithium Fluoride

C. Detailed Comparison of Modeling Approaches

Table C-1 Detailed Comparison of Modeling Approaches

Modeling Approaches					
	4DVAR-TM5	**4DVAR-PCTM**	**EnKF-GEOS-Chem**	**Bayesian**	**GIM**
Team	OU/Melbourne	CSU-CIRA	CSU-CIRA	GSFC/AER	Stanford-Carnegie
Inversion Method	Four-dimensional variational data assimilation	Four-dimensional variational data assimilation	Ensemble Kalman filter	Batch Bayesian synthesis inversion	Batch geostatistical synthesis inversion
Transport Model	TM5 (Global Eulerian, 6°x4°, winds regridded from 1°x1.25° ECWMF)	PCTM (Global Eulerian, 6°x4.5°, winds regridded from 1°x1.25° MERRA)	GEOS-Chem (Global Eulerian, 2°x2.5°, winds regridded from 1°x1.25° MERRA)	WRF-STILT (Regional Lagrangian particle dispersion model, 40 km WRF meteorology)	WRF-STILT (Regional Lagrangian particle dispersion model, 40 km WRF meteorology)
Domain and Flux Spatial Resolution	Global 6°x4°, with North America nest at 1°x1°	Global 6°x4.5°	Global 2°x2.5° regularization via spatial covariance smoothing	North America 1°x1° (with spatial correlation)	North America 1°x1° (with spatial correlation and constrained by geostatistical model)
Flux Temporal Resolution	Monthly	Weekly	Two weeks	Weekly (with temporal correlation)	3-hourly (with temporal correlation)
Truth Emissions:					
Ocean	Takahashi et al. (2009)	NCAR Ocean Model (Doney et al., 2006; Najjar et al., 2007)	Prior + decreased seasonal cycle	--	--
Anthropogenic	CDIAC/Oak Ridge National Laboratory(ORNL) Numeric Data Package (NDP) 058 v2011	None	Same as Prior	--	VULCAN/ODIAC
Biosphere	CASA-GFED2	LPJ (Sitch et al., 2003)	Prior + enhanced sinks (Amazon, Europe, east Asia)	--	CASA-GFED2
Prior Emissions:					
Ocean	Perturbed Truth	Takahashi, et al. (1999)	Woods Hole Institute (Doney)	--	--

183

Modeling Approaches					
	4DVAR-TM5	**4DVAR-PCTM**	**EnKF-GEOS-Chem**	**Bayesian**	**GIM**
Anthropogenic	Perturbed Truth	None	ODIAC (Oda and Maksyutov, 2011)	--	--
Biosphere	Perturbed Truth	CASA land model (Randerson et al, 1997)	SiB3 (Baker et al., 2008)	--	--
Prior Uncertainties:					
Variances	Prior - Truth	Prior - Truth	Estimated by EnKF	Variability of CASA-GFED v3 NEE, scaled up to CSU/NOAA overall magnitudes	Monthly varying (See Shiga et al., 2014.)
Spatial Correlation	0km	0km	800km (land), 1600km (ocean)	Monthly varying (300-650km, Gourdji et al. (2012))	Monthly varying (See Shiga et al., 2014.)
Temporal Correlation	none	None	none	Monthly varying (2-17 days, Gourdji et al. (2012))	Monthly varying (See Shiga et al., 2014.)

EnKF Inversion Detail

NEE is optimized by estimating scaling factors to a priori GPP and respiration. As opposed to 4DVAR techniques that provide a simultaneous flux estimate across time, the EnKF proceeds sequentially, thus the prior flux (first guess) evolves through time. The initial guess for mean flux is the unperturbed flux case (annual net zero NEE SiB3 fluxes described above) while the 'truth' consists of the initial guess plus the tested perturbations. The initial uncertainty consists of an independent 15% standard deviation on both GPP and total respiration, Gaussian distributed. Due to the independent errors, this allows for the uncertainty on the difference (NEE) to be even larger than 15%. The correlation structure *within* GPP (and respiration) is then formed from an isotropic exponential covariance model which effectively constrains the solution to be smooth in geographic space (Table C-1 in Appendix C). This "initial guess" then evolves through time by weighting incremental adjustments to the state estimate over time with the original prior flux guess at time zero, as well as a small multiplicative inflation factor (5%). With this setup, there is an implicit assumption made regarding where we think flux corrections should occur, i.e. in locations of strong a priori flux but otherwise there are no a priori assumptions made on where the correction will be made. The strength of the EnKF is providing explicit uncertainty estimates, as shown in Figure 3-14, however we note that these are heavily dependent upon the nature of the propagation of the covariance between assimilation cycles, which often requires extensive testing and tuning.

Box C-1 Calculation of Model-Data Mismatch Errors

The Bayesian and GIM OSSEs carried out by teams at GSFC and Carnegie-Stanford use only observation locations that fall within the domain used in the WRF meteorological runs (excluding those within 400 km of the boundaries to provide adequate WRF coverage to simulate back trajectory calculations inside the domain). Soundings with total column cloud-plus-aerosol OD >0.7 are rejected. The errors for each 5 km (0.74 s) individual CALIPSO observation point are aggregated over 10-s intervals to increase signal-to-noise for the pseudo-data, using the formula

$$\sigma(10s) = \sqrt{\frac{\sum_{i=1}^{N} \sigma(5km)_i^2}{N^2}} \tag{C-1}$$

where N is the number of valid 5 km observations across the 10-s span. The uncertainties in the series of 10-s pseudo-data are assumed to be uncorrelated.

The 4D-VAR-TM5 and EnKF OSSEs led by the teams at OU and CSU first identify 'n' continuous (along track) soundings that fall within a single grid cell of their model. Soundings with total column OD >0.3 are rejected. Equation 3-1 is used to calculate the monthly scale factors for each observation. Finally, a variance weighted mean across all the observations in the grid cell is calculated.

In the 4D-VAR-PCTM OSSEs a single measurement is applied per orbit for each model grid box that the satellite views. This measurement characterizes the information content of all the individual measurements taken along-track inside the box. Furthermore, the same measurement uncertainty value is assumed for all satellite crossings in a single month per grid box, whatever the optical depth conditions happen to be during each overpass: the applied uncertainty in increased statistically to account for climatological optical depth conditions at that grid box during that month. If a grid box has an optical depth of zero half the time and infinity the other half, the uncertainty applied will be √2 times the clear-sky value. Using the monthly scale factors from Equation 3-1, the measurement uncertainties applied for any grid box crossing in the assimilation are given by

$$\sigma = f\sigma_{RRV} \sqrt{P_o / P} \tag{C-2}$$

where P is the time that the satellite FOV falls within the grid box in [sec], and $P_o = 10$ sec is the base time that the uncertainties are referenced to.

D. ASCENDS Surface Reflectance Considerations

This section documents the rationale and numerical values for spectral lidar backscatter that were used in the random error calculations for the ASCENDS OSSE modeling through 2014. For further discussion and updated reflectance results from experimental measurements see Sections 5.3.3, 5.3.4, and 5.5.1.

1. Land Surfaces

The IPDA approach depends on the bidirectional reflectance from land or ocean surface to provide the backscatter signals that are used to measure the differential absorption due to the atmospheric absorber (e.g., CO_2). In the reflectance nomenclature, the lidar data are a measure of the surface bidirectional reflectance factor with the view angle direction being the same as the incident angle (Nicodemus, et al., 1977), i.e., backscatter. If the surface material can be considered Lambertian, then bidirectional reflectance distribution function (BRDF) is constant for all reflected angles. Most of the Earth's land surfaces, however, have BRDF properties that deviate from Lambertian; consequently consideration of the hot spot, or opposition effect, is important. Even if a surface is Lambertian to a good approximation, the backscatter enhancement due to the hot spot effect can be significant (Hapke, 1986; Hapke et al., 1996; Breon et al., 2002). Amediek et al. (2009) observed that incorporation of a hotspot enhancement was necessary to make their 1.57-µm airborne lidar reflectance measurements consistent with predictions based on MODIS measurements.

Hot spot enhancements from various land surface types have been observed and reported using airborne spectrometers (Camacho-de Coca et al., 2004) and Earth orbiting Polarization and Directionality of Earth Reflectances (POLDER) instrument data (Breon et al., 2002). In addition measurements by Kaasalainen et al. (2006) in the visible and GLAS observations at 1064 nm show strong evidence of an opposition peak in snow reflectance data. The same physical mechanisms for an opposition enhancement should be present at 1.57 and 2.05 µm (Nayar and Oren, 1995.) Disney et al. (2009) have attempted to quantify the lidar reflectivity enhancement due to the hot spot effect, using vegetation structural models and Monte Carlo ray tracing as well as MODIS and POLDER datasets. One consistent inference from these investigations is that the magnitude of the enhancement varies over a wide range even within a particular land cover type.

The ASCENDS XCO_2 measurement precision is related to the strength of the surface backscattering when illuminated by a nadir-pointed lidar system. The surface backscatter (β) is larger than would be calculated from a diffuse reflectivity/albedo (α) in the zenith direction (α/π for a Lambertian surface), and this enhancement factor (EF) is applied to the diffuse reflectivity to represent the lidar surface backscatter factor, $\beta = EF\ \alpha/\pi$. The publication by Disney et al. (2009) attempts to quantify the value of EF for a solar zenith angle near zero for a number of land cover types. In their paper EF was found to range from 1.10 to 1.33 with an average of 1.23 for six land types (not including snow/ice).

Based on this work, the ASCENDS OSSE's use the MODIS 1.62-µm and 2.13-µm diffuse reflectances/albedos (α) with an average EF value of 1.23 for non-snow surfaces as determined from NASA Goddard's Global Modeling and Assimilation Office (GMAO) weather analysis. For the case of missing MODIS 1.62-µm reflectance data over land, we use a surface albedo of 0.2 with EF = 1.23 to fill in the data gaps.

2. Snow/Ice Surfaces

Here we have used EF = 1 for snow/ice surfaces in the current ASCENDS backscatter calculations. Continued lidar measurements of snow/ice backscatter at 1.57 and 2.06 μm are needed to improve snow/ice surface reflectance characterization and further improve modeling of ASCENDS measurements over these surfaces.

The Dumont et al., 2010, paper shows that the MODIS 1.62-μm reflectances (α) at large solar zenith angles (SZA) are significantly larger than the reflectances at low SZA's (e.g., at SZA = 60°, α = 0.1, while at SZA = 0°, α = 0.05). Based on this dataset we use a constant snow/ice albedo of 0.05 at 1.62 μm. In addition, as shown by Hudson et al. (2006), Dumont et al. (2010), and many other authors, the snow/ice albedo at 1.57 μm is about 70% of the albedo at 1.62 μm. Therefore, in lieu of using the MODIS reflectances for snow and ice, which are generally at high SZA's, we use a constant albedo for snow and ice of 0.035 at 1.57 μm.

For ice and land surfaces with a snow cover fraction >0.95, as defined by the GMAO weather analysis, the albedo is set to 0.035. Over land, where MODIS reflectances are unrealistic (that is α <0.035 or α >1.0), or where MODIS reflectance data are missing, backscatter data is filled with α from 0.2 to 0.035 and EF from 1.23 to 1.0 with both parameters scaled based on the snow cover fraction from 0 to 0.95. The same procedure is applied for backscatter at 2.06 μm using fill values of α = 0.1 for land and 0.01 for snow/ice.

The numbers in the tables below were used for all calculations in the ASCENDS white paper initial release. Subsequent measurements of lidar backscatter from aircraft over snow at 1.57 and 2.06 μm (Menzies et al., 2014) as well as review of data from Aoki et al., (2000), however, indicate that our default estimates for these values (0.0111 and 0.0032 sr^{-1}, respectively) are too low. Backscatter values of 0.016 sr^{-1} for 1.57 μm wavelength and 0.0064 sr^{-1} for 2.06 μm are more representative of snow in general, and these numbers are recommended for subsequent estimation of ASCENDS random errors (see Section 5.3.3, 5.3.4, and 5.5.1).

3. Water Surfaces

The strength of laser backscatter from a water surface from a nadir-directed laser beam depends on wind speed. Hu et al. (2008) derived the following functional relationship between the CALIPSO lidar backscatter (β) measurements at 1.064 μm and the Advanced Microwave Scanning Radiometer for EOS (AMSR-E) surface wind speed (V) measurements:

$$\beta = 0.0193/4\pi/mss$$

where   mss = 0.0146*sqrt(V) for wind speeds below 7 m/s or

mss = 0.003 + 0.00512*V for wind speeds of 7 to 13.5 m/s.

For wind speeds above ~13.5 m/s, there can be a mixture of white caps and foam on the sea surface, and at these wind speeds we recommend using a constant surface backscatter equal to the

backscatter at 13.5 m/s. This approach is consistent with the results in the Lancaster et al. (2005) paper which only had one data point at ~16 m/s, and its value was nearly the same as that at 13.5 m/s.

In addition, it is believed that these equations can be used down to very low wind speeds due to the relatively large size of the laser footprint (of order 100 m) and the ubiquitous nature of low frequency gravity waves on most large water surfaces (e.g., oceans, Great Lakes). For these conditions, it is estimated by Hu (private communication) that the backscatter would peak at a wind speed value of about 1 m/s.

For estimating the ocean backscatter, the OSSE's use the global GMAO 10-m wind speed analysis with the above relationships given by Hu.

4. Reference Surface and Atmosphere for Scaling of ASCENDS Measurements

For the scaling of the ASCENDS XCO_2 measurement precision, we have chosen to normalize the global land and water backscatter reflectances to the Railroad Valley (RRV), NV, backscatter reflectance and the global aerosol/cloud transmissions to an assumed aerosol/cloud-free condition over RRV.

The average value of the diffuse reflectance for RRV was found to be 0.45 at 1.57 µm and 0.41 at 2.05 µm (Kuze et al., 2011). Following the above treatment for land surface reflectances, the reference backscatter values for RRV are $\beta = 1.23*0.45/\pi = 0.176$ sr^{-1} and $\beta = 1.23*0.41/\pi = 0.160$ sr^{-1}, respectively.

Please see Box 3.1 for discussion of scaling the random errors in the ASCENDS XCO_2 measurement simulations. A series of OSSE's were run with different generic ASCENDS XCO_2 measurement precisions, which are presumed to be valid over RRV under clear (no aerosol/cloud) conditions. These generic XCO_2 measurement precisions are modified based on how the surface backscatter and aerosol/cloud transmissions deviate from the reference conditions over RRV.

The following table summarizes the relationships discussed above that are used to define the surface backscatter used in the ASCENDS OSSE's.

Summaries of Surface Backscatter Relationships

Table D-1 For 1.57-μm CO_2 Column Measurements

Surface Type	MODIS 1.62-μm Reflect. (α)	GMAO Snow/Ice Fract. (F)	GMAO Wind Spd (V, m/s)	Surface Backscatter (β, sr^{-1})
Land	0.035≤α≤1.0	0≤F≤0.95	N/A	β=(1.23-0.23*F)(α/π)
	α<0.035, α>1.0, or α missing	0≤F≤0.95	N/A	β=(1.23-0.23*F)(0.2-0.165*F)/π
	All cases	F>0.95	N/A	β=0.035/π=0.0111
Water	N/A	no ice	V≤1	Set V=1, β=0.105
	N/A	no ice	1<V<7	β=0.00154/(0.0146*$\sqrt{V}$)
	N/A	no ice	7≤V≤13.5	β=0.00154/(0.003+0.00512*V)
	N/A	no ice	V>13.5	Set V=13.5, β=0.0213
	N/A	ice	N/A	β=0.035/π=0.0111
Reference: Railroad Valley	N/A	N/A	N/A	β=1.23*0.45/π=0.176 at 1.57 μm

Table D-2 For 2.06-μm CO_2 Column Measurements

Surface Type	MODIS 2.1-μm Reflect. (α)	GMAO Snow/Ice Fract. (F)	GMAO Wind Spd (V, m/s)	Surface Backscatter (β, sr^{-1})
Land	0.01≤α≤1.0	0≤F≤0.95	N/A	β=(1.23-0.23*F)(α/π)
	α<0.01, α>1.0, or α missing	0≤F≤0.95	N/A	β=(1.23-0.23*F)(0.1-0.09*F)/π
	all cases	F>0.95	N/A	β=0.01/π=0.00318
Water	N/A	no ice	N/A	Same as for 1.57 μm
	N/A	ice	N/A	β=0.01/π=0.00318
Reference: Railroad Valley	N/A	N/A	N/A	β=1.23*0.41/π=0.161 at 2.0 μm

Table D-3 For 1.26-μm O$_2$ Column Measurements

Surface Type	MODIS 1.24-μm Reflect. (α)	GMAO Snow/Ice Fract. (F)	GMAO Wind Spd (V, m/s)	Surface Backscatter (β, sr^{-1})
Land	0.035≤α≤1.0	0≤F≤0.95	N/A	β=(1.23-0.23*F)(α/π)
	α<0.035, α>1.0, or α missing	0≤F≤0.95	N/A	β=(1.23-0.23*F)(0.31)/π
	0.035≤α≤1.0	F>0.95	N/A	β=0.31/π=0.0987
Water	N/A	no ice	N/A	Same as for 1.57 μm
	N/A	ice	N/A	β=0.36/π=0.115
Reference: Railroad Valley	N/A	N/A	N/A	β=1.23*0.43/π=0.168 at 1.26 μm

Table D-4 For 0.765-μm O$_2$ Column Measurements

Surface Type	MODIS 0.86-μm Reflect. (α)	GMAO Snow/Ice Fract. (F)	GMAO Wind Spd (V, m/s)	Surface Backscatter (β, sr^{-1})
Land	0.035≤α≤1.0	0≤F≤0.95	N/A	β=(1.23-0.23*F)(0.95+0.13*F)(α/π)
	α<0.035, α>1.0, or α missing	0≤F≤0.95	N/A	β=(1.23-0.23*F)(0.33)/π
	0.035≤α≤1.0	F>0.95	N/A	β=(1.23-0.23*F)(1.08)/(α/π)
Water	N/A	no ice	N/A	Same as for 1.57 μm
	0.035≤α≤1.0	ice	N/A	β=1.08(α/π)
	missing	ice	N/A	β=0.85/π=0.271
Reference: Railroad Valley	N/A	N/A	N/A	β=1.23*0.43/π=0.168 at 0.76 μm

E. Summary of Calculations for Dynamic Range of Received CO_2 Lidar Signal

To provide global coverage, the lidar must make and record measurements to a wide variety of surface types and through atmospheres with some thin cloud and/or aerosol attenuation. These will present a wide range of signal strengths to the lidar receiver. Calculations are shown below for candidate CO_2 lidar that operate in the 1570-nm and 2050 nm CO_2 bands.

Table E-1 Return Signal Dynamic Range for 1570-nm CO_2 lidar

Case:		Surface beta(pi) (ster^-1)	Effective Lambertian Albedo	Atm Optical Depth	Beta(pi)* atm trans^2	Received Signal Relative to RRV clear	Received signal as Percent of RRV Clear	Measurement Error Mult*
Clear	RRV	0.176	0.553	0.0	0.176	1.00	100	1.00
Clear	Snow**	0.016	0.050	0.0	1.60E-02	9.09E-02	9.09	3.32
Clear	Calm ocean	0.528		0.0	0.53	3.00E+00	300.00	0.58
Thin clouds &	RRV	0.176	0.553	1.0	2.38E-02	1.35E-01	13.5	8.61
Polar clouds &	Snow**	0.016	0.050	0.2	1.07E-02	6.09E-02	6.09	4.05
Thin clouds &	Rough ocean	0.025		1.0	3.38E-03	1.92E-02	1.92	7.22
Thin clouds &	Calm ocean	0.528		1.0	7.15E-02	4.06E-01	40.6	1.57
** Snow albedo from Aoki (2000)					Total Signal Dynamic Range (Ratio Strongest to Weakest)			156
Rough Ocean ~12 m/sec wind speeds					* based on an ideal signal shot-noise limited lidar receiver			

Table E-2 Return Signal Dynamic Range for 2051-nm CO_2 Lidar

Case:		Surface beta(pi) (ster^-1)	Effective Lambertian Albedo	Atm Optical Depth	Beta(pi)* atm trans^2	Received Signal Relative to RRV clear	Received signal as Percent of RRV Clear	Measurement Error Mult*
Reference case	RRV	1.61E-01	0.506	0.0	0.161	1.00	100	1.00
Clear atm &	Snow**	6.40E-03	0.020	0.0	6.40E-03	3.98E-02	3.98	5.02
Clear atm &	Calm ocean	5.28E-01		0.0	0.528	3.28E+00	328	0.55
Reference case	RRV	1.61E-01	0.506	1.0	2.18E-02	1.35E-01	13.5	2.72
Polar clouds &	Snow**	6.40E-03	0.020	0.2	4.29E-03	2.66E-02	2.66	6.13
Thin clouds &	Rough ocean	2.50E-02		1.0	3.38E-03	2.10E-02	2.10	6.90
Thin clouds &	Calm ocean	5.28E-01		1.0	7.15E-02	4.44E-01	44.4	1.50
** Snow albedo from Aoki (2000)					Total Signal Dynamic Range (Ratio Strongest to Weakest)			156
Rough Ocean ~12 m/sec wind speeds					* based on an ideal signal shot-noise limited lidar receiver			

F. Progress in Developing IPDA Lidar Approaches to Measure Oxygen

The most recent ASCENDS Mission concept does not utililize a lidar channel to measure Oxygen. However, if future work determines that a lidar measurement of Oxygen is required for the mission, then a summary of the Oxygen-lidar-related measurement requirements is given below.

Table F-1 Summary of Oxygen Measurement Requirements, if Chosen for ASCENDS

Summary of Oxygen Measurement Requirements, if Chosen for ASCENDS
1. Measure & report the lidar measurements stated below with a spatial resolution equivalent to a sampling rate of at least 50 Hz. (This implies a compatible laser footprint diameter). This spatial resolution is related to (a) the ability to measure scattering surface elevation (SSE) with sufficient accuracy over sloping terrain (R-7), and (b) the ability to obtain data in scattered cloud conditions (R-4, R-8).   These three measurements are: (1) O_2 DAOD,   (2) Range to the surface at an "offline" wavelength within the O_2 absorption band, to allow determination of column length and SSE of O_2 column density or surface pressure measurement in the O_2 wavelength region, and   (3) Range spreading at the "offline" O_2 wavelength.
2. The O_2 and CO_2 lidar measurements must be co-aligned spatially
3. The CO_2 & O_2 measurements must have sufficient resolution and precision to enable computing CO_2 dry air mixing ratio over a virtual bright flat reference surface (with lidar reflectance equivalent to that of Railroad Valley NV) in a clear atmosphere to $\leq\sim10$ ppm at a 50-Hz rate, or ≤0.3 ppm using 10-second averaging.
4. The lidar measurements must be processed using adaptable algorithms ("measurement models") that allow the algorithm parameters and computations to be updated post-launch, for the purpose of improving the processed measurement data accuracy and coverage by incorporating improved knowledge of instrument behavior from on-orbit calibrations, etc.

F.1   Return Signal Dynamic Range for Oxygen Lidar

To provide global coverage, the Oxygen lidar must make and record measurements to a wide variety of surface types and through atmospheres with some thin cloud and/or aerosol attenuation. These will present a wide range of signal strengths to the lidar receiver. Calculations are shown for candidate O_2 lidar that operate in the 760-nm O_2 A-band and 1270-nm singlet-delta band.

Table F-2 Return Signal Dynamic Range for 765-nm-based O$_2$ Lidar

Case:		Surface beta(pi) (ster^-1)	Effective Lambertian Albedo	Atm Optical Depth	Beta(pi)* atm trans^2	Received Signal Relative to RRV clear	Received signal as Percent of RRV Clear	Measurement Error Mult*
Reference case	RRV	0.168	0.528	0.0	0.168	1.00	100	1.00
Clear	Snow**	0.271	0.851	0.0	2.71E-01	1.61E+00	161	0.79
Clear	Calm ocean	0.528		0.0	0.53	3.14E+00	314	0.56
Thin clouds	RRV	0.168	0.528	1.0	2.27E-02	1.35E-01	13.5	2.72
Polar clouds	Snow**	0.271	0.851	0.2	1.81E-01	1.08E+00	108	0.96
Thin clouds	Rough ocean	0.025		1.0	3.38E-03	2.01E-02	2.01	7.05
Thin clouds	Calm ocean	0.528		1.0	7.15E-02	4.25E-01	42.5	1.53
** Snow albedo from Aoki (2000)				Total Signal Dynamic Range (Ratio Strongest to Weakest)			156	
Rough Ocean ~12 m/sec wind speeds				* based on an ideal signal shot-noise limited lidar receiver				

Table F-3   Return Signal Dynamic Range for 1262-nm-based O$_2$ Lidar

Case:		Surface beta(pi) (ster^-1)	Effective Lambertian Albedo	Atm Optical Depth	Beta(pi)* atm trans^2	Received Signal Relative to RRV clear	Received signal as Percent of RRV Clear	Measurement Error Mult*
Clear	RRV	0.168	0.528	0.0	0.168	1.00	100	1.00
Clear	Snow**	0.175	0.550	0.0	1.75E-01	1.04E+00	104	0.98
Clear	Calm ocean	0.528		0.0	0.528	3.14E+00	314	0.56
Thin clouds	RRV	0.168	0.528	1.0	2.27E-02	1.35E-01	13.5	2.72
Polar clouds	Snow**	0.175	0.550	0.2	1.17E-01	6.99E-01	69.8	1.20
Thin clouds	Rough ocean	0.025		1.0	3.38E-03	2.01E-02	2.01	7.05
Thin clouds	Calm ocean	0.528		1.0	7.15E-02	4.25E-01	42.5	1.53
** Snow albedo from Aoki (2000)				Total Signal Dynamic Range (Ratio Strongest to Weakest)			156	
Rough Ocean ~12 m/sec wind speeds				* based on an ideal signal shot-noise limited lidar receiver				

F.2   Progress in developing a Pulsed IPDA Oxygen Lidar (NASA Goddard)

F.2.1   Introduction

In order to achieve the required precision and accuracy for XCO_2 measurements, knowledge of the surface pressure, temperature, and water vapor are also needed (IPCC 2007; NRC 2007; Jucks et al., 2015). Since Oxygen (O_2) is a stable and uniformly mixed molecule in the atmosphere at 20.95%, it can be used to infer the surface pressure. Initial analysis by the ASCENDS working group (Jucks et al., 2015) and Crowell (Crowell et al., 2015) shows that in order to keep the XCO_2 error below 1 ppm, an error of ~0.2% (or ~2 hPa) will be needed for O_2 over a 10 sec averaging period. The precision and accuracy requirement are very stringent and a lidar capable of making such measurements has to be able to address both random and systematic error sources.

Surface pressure information can be obtained from meteorological sensors and numerical weather prediction models. The European Space Agency A-SCOPE Mission Assessment report (ESA, 2008) had determined that for most of the globe, meteorological models could provide the necessary surface pressure information and there was no need for an Oxygen lidar. However, questions remain regarding the spatial resolution of the meteorological models and the lack of information in parts of the globe where sensors are sparse or not available.

F.2.2   Oxygen Line Selection

Satellite-borne measurements of O_2 with a laser using the A-band were proposed by Singer (1968), Barton and Scott (1986), and Mitchell and O'Brien (1987), and were demonstrated with airborne lidar systems by Korb and Weng (1983), Schwemmer et al. (1987), and more recently by Dobler et al. (2011a,b) and Riris et al. (2013). Suitable O_2 absorption line(s) must meet several requirements: The line(s) should not have interferences from other atmospheric constituents; it must not form a solid continuum with adjacent lines; it should have low temperature sensitivity; suitable lasers, detectors and other component technologies must be available in the selected spectral region. Two spectral regions at ~761 nm and ~1270 nm are best suited for O_2 remote sensing measurements from space. The lines in these regions do not have interferences from other atmospheric constituents and have (mostly) the right linestrengths.

For the pulsed O_2 lidar, we selected the 761 nm spectral region primarily because suitable lasers and photon counting detectors are available. The minimum temperature sensitivity occurs near 760 nm and near 765 nm. The lines near 760 nm are not suitable for remote sensing form space since they are too strong and almost form a continuum. Fortunately, the lines near 765 nm are well suited for remote sensing from space. We selected an O_2 doublet at ~764.7 nm for our lidar (Figure F-1). These lines have clear separation from adjacent lines, have no significant interferences from other atmospheric constituents and their temperature sensitivity is small.

F.2.3   Measurement Approach and Airborne Instrument Description

Our approach uses Integrated Differential Path Absorption (IPDA), which has been used by several groups to measure CO_2, CH_4, and O_2 from airborne platforms (Dobler et al., 2011 a,b; Abshire et al., 2014; Ehret et al., 2008; Riris et al., 2017; Spiers et al., 2011a; Fix et al., 2011; Menzies et al., 2014; Fix et al., 2015; Amediek et al., 2017; Singh et al., 2015b; Refaat et al., 2015a). Our technique uses a sequence of laser pulses at increasing wavelengths, which sample the selected pair of absorption lines in the Oxygen A-band at 764.7 nm. The laser pulses are generated by an Erbium Doped Fiber Amplifier (EDFA) and a frequency doubler and are detected by single photon counting modules (SPCMs). Errors due to scattering from aerosols and clouds are eliminated since our lidar

directly measures the range from the aircraft to the surface (Amediek et al., 2013). Using the instrument in a sounding (surface reflection) mode enables integrated O_2 measurements with relatively modest laser power. The multi-wavelength approach attempts to minimize systematic errors, such as etalon fringes and baseline structure that may be difficult to account for in a two-wavelength lidar (Chen et al., 2012, 2014). Since the multi-wavelength IPDA fits the entire lineshape it can account for the spectral shift of the absorption line with changing atmospheric pressure (Ramanathan et al., 2013) and can retrieve mixing ratios above the boundary layer (Ramanathan et al., 2015) and backscatter profiles (Mao et al., 2018).

Without considering effects like scattering or stimulated emission from ambient O_2 (Sharp et al., 2014) the differential optical depth (DOD) for a two-wavelength lidar (on and off the absorption line) for an atmospheric column R is defined as the ratio of the transmittance through the column at the on and off wavelengths.
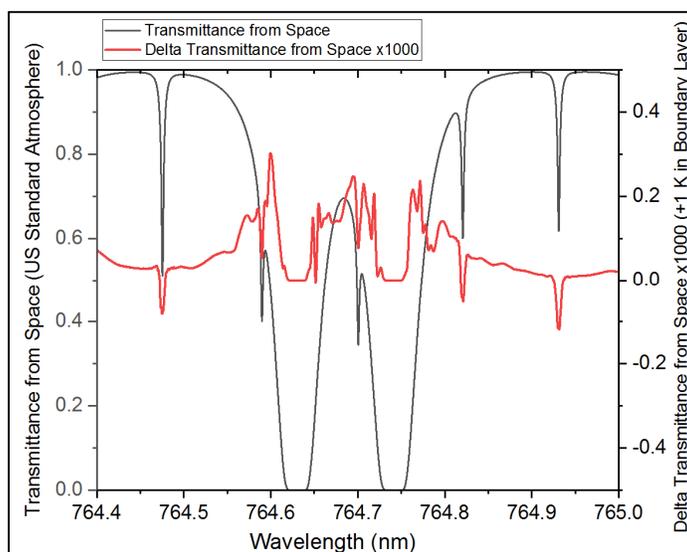
Figure F-1 Two-way transmittance of O_2 doublet at 764.7 nm (black trace) and the change in transmittance x1000 (red trace) for 1 K temperature change in the atmospheric boundary layer (lowest 2 km). The two lines have clear separation from adjacent lines, have no significant interferences from other atmospheric constituents and their temperature sensitivity is smaller than other lines. The weaker, narrower lines are O2 isotope lines. The HITRAN 2008 (Rothman et al., 2009) was used for the transmittance calculations.

A simple way to illustrate the measurement requirement is to plot the OD for slightly different elevations. Increasing the elevation reduces the air mass (i.e. pressure) in the atmospheric column. For a US standard atmosphere, an increase of ~17 m in elevation will result in a change of ~2 hPa which is the measurement requirement. Figure F-2 shows the OD from a 400 km orbit for zero and 17 m elevation and the corresponding OD difference, Δ(OD). The ODs for the two cases are virtually identical (the plots overlap). The OD difference Δ(OD), is plotted on an expanded scale on the right hand axis for clarity. The other obvious observation from Figure F-2 is that there is no real "off" wavelength. The wings of the line (along with several O_2 isotope lines on either side) extend far enough in wavelength (or frequency) to interfere with adjacent lines and the OD is different on left and right side. The choice of "on" and "off" wavelengths is arbitrary and for our case, they are shown in solid squares in Figure F-2. The exact wavelength positions can be adjusted programmatically and do not need to be evenly spaced. It is clear from Figure F-2 the IPDA lidar

must have the accuracy and precision to measure very small changes in OD and account for both random and systematic errors.
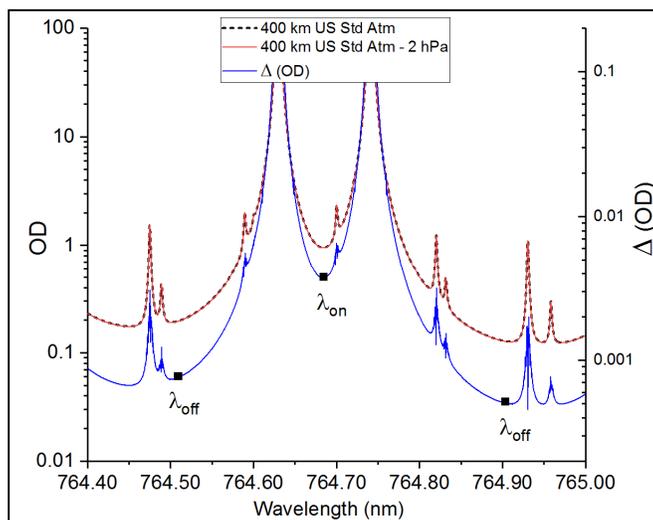
Figure F-2 Optical depth (OD) using a US standard atmosphere from a 400 km orbit with two different observer elevations (0 m and 17 m).   An elevation change of 17 m will result in a change in pressure of ~2 hPa which is the ASCENDS measurement requirement for O_2. The two plots (black and red trace) are virtually identical and overlap (left axis). The difference in OD, Δ(OD), is shown on the right hand axis in blue. The choice of "on" and "off" wavelengths for differential optical depth (DOD) calculations is arbitrary and is shown in solid black squares.

Our instrument (Figure F-3) was part of a combined CO_2-O_2 lidar. The transmit CO_2 and O_2 beams are combined by a dichroic beam combiner with a small angular separation (500 µrad) and the receiver telescope has two fiber-coupled fields of view (FOV) corresponding to each transmit beam. The O_2 lidar used a continuous wave (CW) distributed feedback (DFB) diode laser operating at 1529.4 nm. Its wavelength was rapidly scanned over the O_2 absorptions by applying a ramp waveform to the drive current. A wavelength calibration procedure using a heterodyne technique and an acetylene cell was used to calibrate our wavelength scan. The output of the CW diode laser was externally modulated with a fiber-coupled acousto-optic modulator (AOM) to yield relatively short (~200 ns FWHM (Full Width at Half Maximum)) laser pulses with approximately 25 dB extinction ratio. A trigger, from a GPS receiver 1 pulse per second (pps) signal, initiated a wavelength scan with 20 laser pulses separated by 100 µs that were used to sample the oxygen absorption lines. The 100 µs time separation between pulses (equivalent to a range of ~15 km) ensured that all wavelength pulses in the scan were sufficiently separated in time so that there was no ambiguity on each pulse wavelength when it was detected by the receiver. The optical pulses from the AOM were amplified by a custom an Erbium Doped Fiber Amplifier (EDFA). The EDFA output is directly fiber-coupled into a periodically poled Lithium Niobate crystal (PPLN) assembly which frequency doubles the 1529.4 nm laser light to 764.7 nm. The free-space output from the doubling crystal is directed to the transmit optics assembly which includes two turning mirrors, a beam combiner, a beam expander to reduce the beam divergence to ~110 µrad and an integrating sphere with a detector to measure the outgoing laser energy.
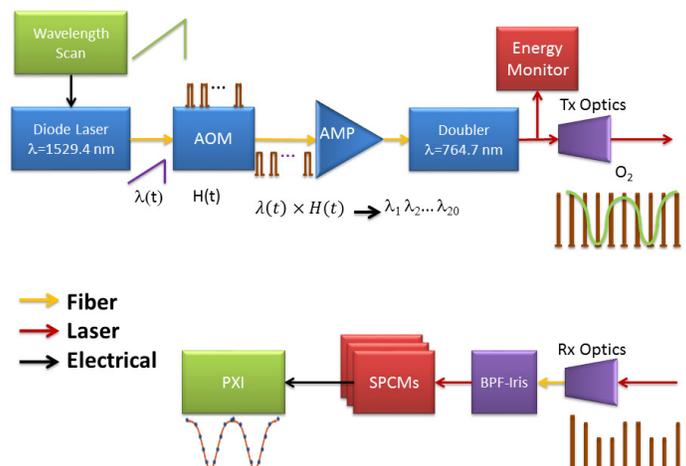
Figure F-3   Simplified block diagram of the 2014 Oxygen IPDA lidar. In 2014, we replaced the single SPCM with eight SPCMs and the multichannel scaler with a PXI based data acquisition system using an FPGA digital counter.

The output signal from the energy monitor is digitized by the data acquisition system. The outgoing laser energy after the transmit optics was ~1.0-1.5 μJ and it exhibited large fluctuations due to the large mode area (LMA) fiber of the EDFA. The transmitted laser pulses travel through the aircraft nadir window to the ground. The nadir port windows are anti-reflection (AR) coated for 765 nm and have a wedge to minimize unwanted etalon fringes and back reflections into the receiver. The spot diameter from a 10 km altitude is 1.1 m and the separation between successive pulses (wavelengths) is 2-2.5 cm, using a nominal aircraft speed of 200-250 m/s. This separation minimizes the changes in reflectivity between successive wavelengths.

The reflected ground echoes are collected by a commercial 20 cm diameter receiver telescope and are coupled into an AR coated 400-μm core multi-mode fiber. The receiver field of view (FOV) was 200 μrad. The fiber output from the receiver is collimated and directed through a narrow (0.5 nm in 2013 and 0.8 nm in 2014 FWHM) bandpass filter, an adjustable iris to adjust the amount of light onto the detector, and then focused onto a single photon-counting module. The fiber collimator, filter, iris, and focusing lens reside in a single opto-mechanical assembly to minimize alignment sensitivity and optimize the transmission of the bandpass filter. In 2014, we split the output of the multi-mode receiver fiber into eight separate SPCMs using a 1x8 fiber optic splitter to maximize the dynamic range of the receiver. Although there is a significant insertion loss in the splitter (~15-20%), increasing the dynamic range and operating the SPCMs in their linear range is highly desirable. The computer averages, digitizes, and stores the return histograms every 125 ms. The averaging period is adjustable but is limited by the data transfer rate. The bin width for the histogram was 32 ns and the duty cycle for the data acquisition was >96%. By digitizing returns from the entire atmospheric column, we can separate contributions from clouds and the ground, and determine the range to the ground using the time of flight (TOF) of the first laser pulse (25). The parameters of the airborne system in 2014 are summarized in Table F-4.

Table F-4 Parameters of the Airborne Oxygen IPDA Lidar in 2014

Parameter	2014 Value
Center Wavelength λ (nm)	764.685
Wavelength Scan (pm)	~380
Wavelength separation (pm)	~21 pm
Pulse repetition rate (kHz)	10
Pulsewidth (ns)	~200
Wavelength Scan Rate (Hz)	500
Energy per pulse[*] (µJ)	1.5-2.0
Bin Width (ns)	10
Divergence (µrad)	~110
Instrument Field of View-IFOV (µrad)	200
Receiver bandwidth FWHM (nm)	0.8
Averaging Time[**] (s)	0.125
Detector Quantum efficiency (%)	~50

*This is the energy measured out of the EDFA. The actual energy out of the transmit optics (after the transmit optics) is closer to ~1-1.5 µJ/pulse.

**This is the data acquisition averaging time. The data presented below, is further averaged in post processing with a 10 sec averaging time.

F.2.4 Results from the 2013-2014 Airborne Campaigns

In 2013 and 2014, we participated in a multi-instrument airborne campaign sponsored by the NASA ASCENDS program to measure CO_2 fluxes in the United States. The O_2 lidar was part of a Goddard instrument suite, which included a CO_2 IPDA lidar and an in-situ cavity ring down spectrometer (Picarro G1301-m). The instruments were installed on NASA's DC-8 airborne laboratory based at Armstrong Flight Research Center Science and Aircraft Integration Facility (SAIF) in Palmdale, CA. Five science and one engineering flight in the continental US (CONUS) were carried out in 2013 and one engineering flight and four science flights in 2014. The O_2 lidar collected data for all 2013 flights but only one 2014 flight. At the start of our 2014 flight campaign a laser current driver in our fiber amplifier failed. By the time we identified the problem, received and installed a replacement driver the ASCENDS airborne campaign was nearly complete and we collected data only during the last flight. In addition, data from the first leg of the 2014 flight (to Iowa) was compromised by telemetry issues with the adjustable iris. We managed to correct the problem during flight but we only collected data for the return segment of the flight (from Iowa to Palmdale). This unfortunate turn of events limited our ability to assess the improvements we implemented in 2014.

The flight paths and spiral locations for the campaign were selected to optimize the science objectives for CO_2. They typically included multiple segments at increasing altitudes from 3 to 13.5 km over varying topography, land cover, and atmospheric conditions. In addition, for most flights, a spiral descent from ~13.5 km to near the surface (30-70 m) was included in the flight plan in order to sample vertical profiles of meteorological parameters (pressure, temperature, humidity, etc.)

using the aircraft's on-board sensors and the CO$_2$ mixing ratio profile using the in-situ sensor. Table F-5 summarizes the 2013 and 2014 flights when the O$_2$ lidar collected data.

Our retrieval algorithm first isolates the ground return and determines the range to the surface by correlating the first return pulse with the outgoing energy monitor pulse and measuring the time delay of the correlation peak (25). Fixed time delays due to fibers and electronics are calibrated prior to flight during ground testing. The lidar range is also compared with the GPS altitude and the DC-8 radar altimeter. This ensures that only ground returns are used in the O$_2$ retrievals and cloud returns are flagged accordingly. Then the ground return pulses at each wavelength are integrated and a dead time correction is applied. The returns are normalized by the integrated transmitted pulse energy, the filter response, iris size, and other instrument calibrations. The data is further averaged in 10 s intervals and the algorithm then compares the experimentally derived transmittance with the theoretically calculated transmittance values and adjusts the fit parameters to minimize the root mean square error (RMSE). The theoretical predictions use the lidar range and DC-8 radar altimeter information to obtain the range to the ground, a Voigt lineshape, and the lineshape parameters from the HITRAN 2008 database (Rothman et al., 2009), the vertical profile of the atmosphere, and line-by-line radiative transfer calculations (Clough and Iacono, 1995). The impact of Dicke narrowing, line mixing, and ambient airglow were not included in the calculations (Long et al., 2010; Long and Hodges, 2012, Tran et al., 2006). The meteorological data for the vertical profile of the atmosphere for the flights are obtained from the Goddard Global Modeling and Assimilation Office (GMAO) Modern Era Retrospective Analysis for Research and Applications (Rienecker et al., 2011). The theoretical and experimental DOD values are then determined by the difference in OD at 764.684 nm (the on wavelength) and the average value of the OD at the off wavelengths (764.509 and 764.903 nm).

Table F-5 Flight Summary 2013-2014

| Date	Approximate Location
February 22 2013	Blythe, AZ-Southern Sierra Nevada
February 26 2013	Railroad Valley, NV
February 28 2013	Central and Owens Valley, CA
March 1 2013	Northern CA
March 3 2013	Colorado-Utah
March 7 2013	Wisconsin-Iowa
September 3 2014	Iowa

Figure F-4 (a) and Figure F-4 (b) show the time series and the corresponding scatterplot for the lidar DOD and model DOD prediction for our first flight on 22nd of February 2013, near Blythe, AZ and the southern Sierra Nevada. The lidar DOD agreed well with the model DOD prediction and the linear fit of the scatterplot had a slope of 0.95 and an offset of 0.02. The R2 value was 0.96. Figure F-5 (a) and Figure F-5 (b) show the time series and scatterplot for the model DOD prediction and the lidar DOD for our flight on 26th of February 2013, in Railroad Valley, NV. Again, the lidar DOD agreed well with the model DOD prediction and the linear fit of the scatterplot had a

slope of 1.08 and an offset of -0.03. The R2 value was 0.94. Figure F-6 and Figure F-7 show the results from the February 28 2013 flight in Central Valley, CA and the March 7 2013 flight to Wisconsin and Iowa. The other two flights in Northern California and Colorado-Utah produced similar results. Figure F-8 shows the results from the September 3, 2014 from Iowa to Palmdale and back. A 10 sec averaging period was used in all plots.

The agreement between the DOD prediction and the lidar DOD depends on the IPDA lidar performance but also on the accuracy of the theoretical prediction at that location. If our model atmosphere is not an accurate representation of what is being measured by the lidar then the agreement will not be very good. This may be particularly problematic in areas where the topography varies rapidly or where our weather models do not accurately capture the local state of the atmosphere. For all of our flights the model DOD prediction and the lidar DOD agreed fairly well. The average slope of the scatterplots of all the analyzed flights was 1.018 and the average offset was -0.012. These results indicate that our measurement accuracy is within a few percent (<2%) of the predicted DOD value with a modest amount of laser energy. The precision of our measurement can be estimated from the difference between the model DOD prediction and the lidar DOD. The Central Valley flight is probably suited for the precision estimation since it was mostly over flat terrain, except for the portion of the flight northwest of Palmdale where it crossed the southernmost end of the Sierra Nevada. The standard deviation of the difference between the model DOD prediction and the lidar DOD for that flight was 2.5% with a 10 sec averaging time.
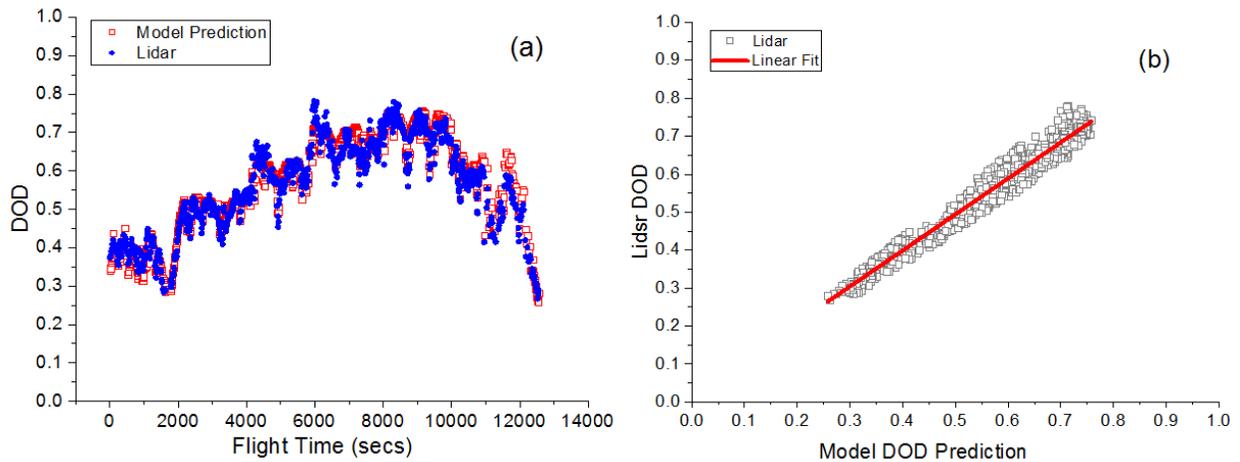

Figure F-4 (a) Time series of the model DOD prediction and the lidar DOD for our first flight on 22nd of February 2013, near Blythe AZ. (b) Scatterplot of the same data. A linear fit of the scatterplot had a slope of 0.95 and an offset of 0.02. The R^2 value was 0.96.
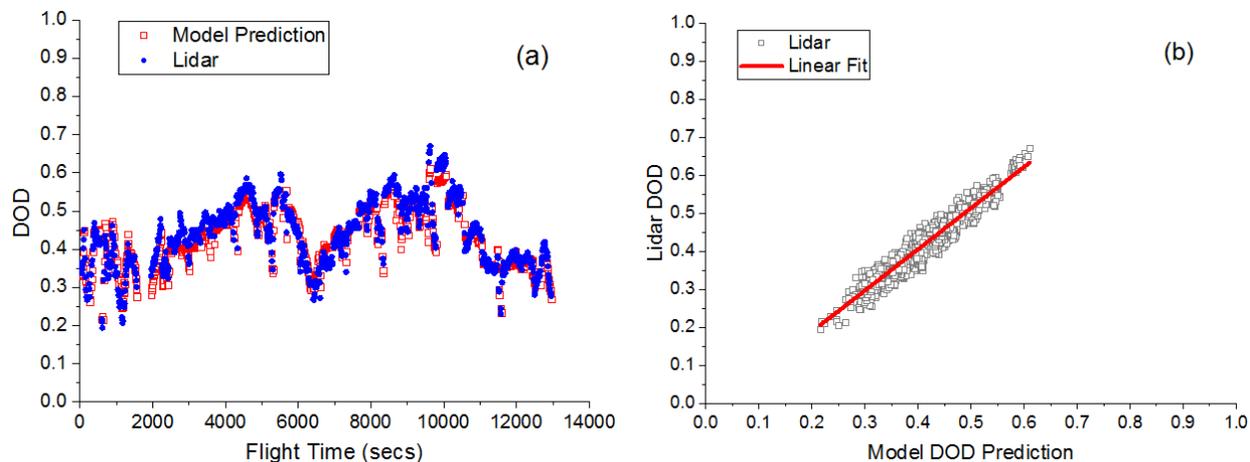
Figure F-5 (a) Time series of the model DOD prediction and the lidar DOD for our flight on 26th of February 2013, Railroad Valley, NV.   (b) Scatterplot of the same data. A linear fit of the scatterplot had a slope of 1.08 and an offset of -0.03. The R^2 value was 0.94.
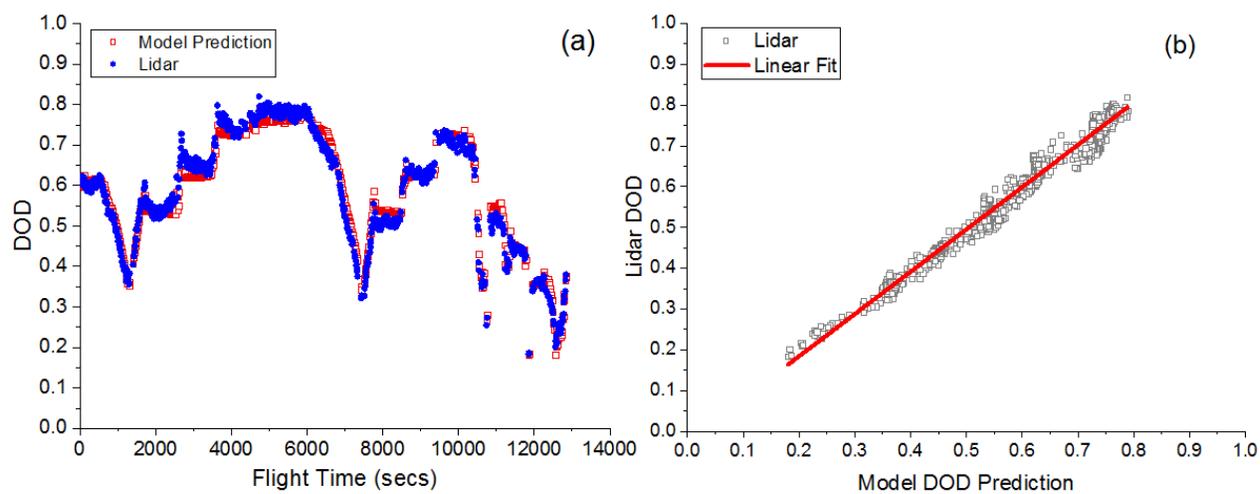
Figure F-6 (a) Time series of the model DOD prediction and the lidar DOD for our flight on 28th of February 2013, Central Valley, CA. (b) Scatterplot of the same data. A linear fit of the scatterplot had a slope of 1.04 and an offset of -0.02. The R^2 value was 0.97.
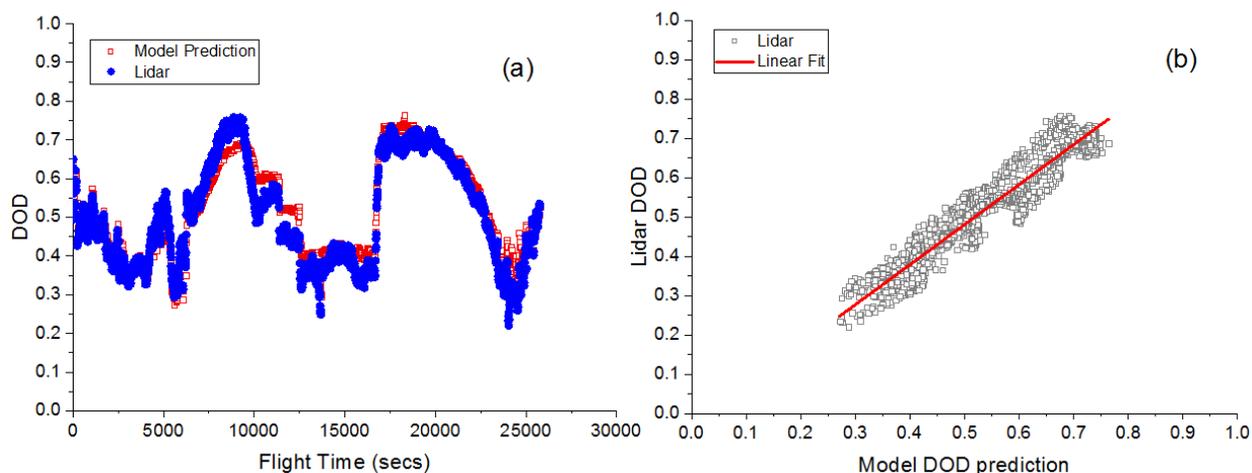
Figure F-7 (a) Time series of the model DOD prediction and the lidar DOD for our flight to Iowa-Wisconsin on March 7, 2013. (b) Scatterplot of the same data. A linear fit of the scatterplot had a slope of 1.02 and an offset of -0.03. The R^2 value was 0.93.
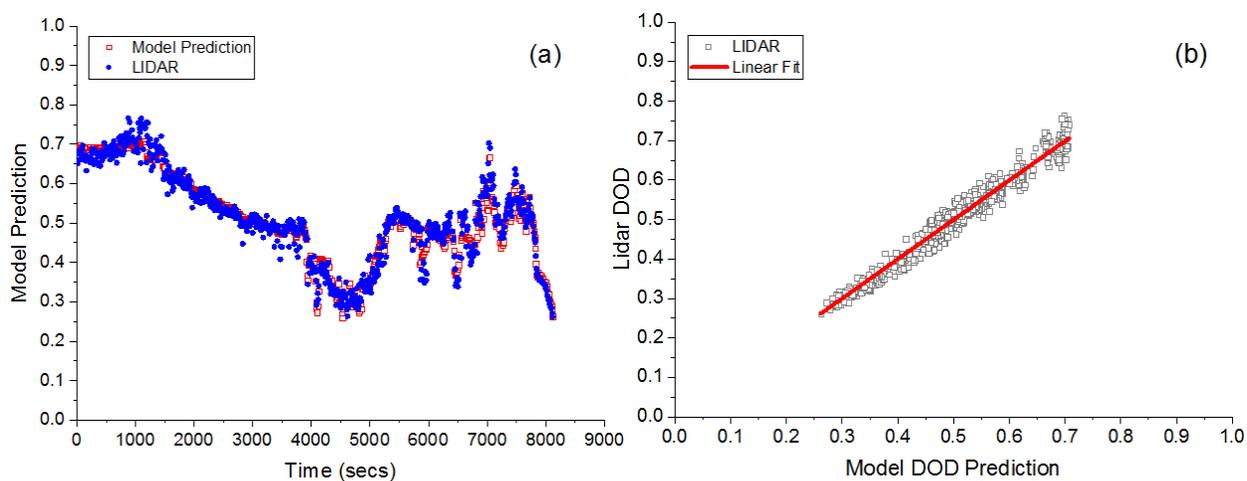
Figure F-8 (a) Time series of the model DOD prediction and the lidar DOD for our flight on 3 September 2014, from Iowa to Palmdale. (b) Scatterplot of the same data. For this flight, we analyzed data only during the return leg of the flight (from Iowa to Palmdale). A linear fit of the scatterplot had a slope of 1.00 and an offset of 0.00. The R^2 value was 0.97.

F.2.5. Discussion, Areas for Improvement and Approach for space

The high accuracy and precision needed for this measurement pose several challenges for the instrument design. An IPDA lidar like all spectroscopic instruments regardless of the approach will have systematic and random error sources that limit accuracy and precision. The total error is an aggregate of random and systematic errors. The random errors for an IPDA lidar has several contributions that have been addressed in detail by several groups, and will not be reproduced here (see for example Ehret (Ehret et al., 2008), Sun (Sun and Abshire, 2012), Kiemle (Kiemle et al., 2011), and Refaat (Refaat et al., 2015ab). Typically they include detector excess and/or dark noise, signal shot noise, thermal noise, solar background, amplifier circuit noise, speckle noise, laser noise,

202

etc. For high signal levels most of these noise terms have approximately normal distributions and the Signal to Noise ratio (SNR) can be improved by increasing the averaging time.

Our SNR is currently limited by the low laser energy. The SNR for a single wavelength of a pulsed IPDA lidar was derived by Sun and Abshire (2012). Using Eq. (29) from Sun, and the IPDA lidar values in   for our off wavelength pulse (last pulse), with a 10 sec averaging period the best we could expect is a SNR of ~68 or a precision of ~1.6%. Thus, we can never expect our DOD precision to Table F-4 exceed the theoretical SNR limit for a single wavelength.

After the flights, we received and tested the repaired power amplifier and scaled the 1529.3 nm energy up to 60 µJ with a corresponding energy increase at 764.7 nm up to 9-10 µJ, a factor of 6-7 increase. With the increased energy, we would expect to reduce the shot noise by a √6 and improve the theoretical precision from 1.6% to 0.67%. However, that is still more than factor of three above the requirement and we would need about 64 µJ to meet 0.2%. Recently demonstrated Raman fiber amplifiers have produced more than 400 µJ per pulse at 1572 nm (40). If the Raman fiber amplifier design is modified for transmission at 1529.3 nm and it is coupled with an efficient frequency doubling crystal, then 764.7 nm energy could be scaled to 64 µJ or higher. For space, we would need approximately 2 mJ to get the required precision. It is unclear at this point how that energy can be reliably achieved.

The solar background is another source of noise. It is proportional to the receiver optical efficiency, the width of the optical bandpass filter, the square of the FOV, the square of the receiver aperture and surface reflectance. We can reduce the solar background by reducing the FOV or the width of the bandpass filter. Reducing the FOV can make boresight alignment difficult. Reducing the width of the bandpass filter is possible but it comes at a cost. Our bandpass filter in 2013 was 0.5 nm wide (FWHM) which was roughly the span of our wavelength scan. The filter's narrow spectral width distorted the wings of the line shape. Although we calibrated the filter transmission prior to flight, small changes in the incidence angle and temperature may introduce an additional bias. In 2014, we changed the bandpass filter to 0.8 nm to minimize the effect of these potential errors. Although the solar background increased by a factor of 1.6 (=0.8nm/0.5nm) we believe the distortion in the wings of the baseline was less and the retrieval algorithm did not need to adjust the filter transmission curve.

The energy monitor is another source of systematic error that is seldom taken into account in most theoretical analyses. Refaat addressed several calibration issues for a 2-µm IPDA lidar and proposed a self-calibration feature to reduce measurement uncertainty (Refaat et al., 2015a). Ideally, the monitor should be a perfect representation of the outgoing pulse energy and can always be used to normalize the received energy. In 2013 one of the biggest issues we encountered was the large energy fluctuations of the EDFA due to movement of the LMA fiber. Energy changes at the EDFA fiber output are then amplified in a non-linear fashion by the doubler. The energy monitor is supposed to capture the energy changes to a precision of 0.2% or better. However, the energy fluctuations we observed were 30% or higher and normalizing to 0.2% was extremely challenging. In 2014, we enclosed the LMA fiber from the EDFA to the doubler in rigid tubing to minimize fiber movement and reduce energy fluctuations. Our stabilization approach was not as effective, as we would have hoped and the energy still varied by more than 5-10%. In the future, fiber and energy stabilization should be addressed at the amplifier design stage.

Even if the energy monitor were perfect various other instrument "drifts" due to etalon fringes, detector responsivity and linearity, temperature changes, polarization and energy changes of the

transmitter, and other instruments effects degrade the performance and limit the averaging time of the instrument. While these "drifts" are often difficult to separate and model analytically it is important to quantify the overall "stability" and optimum averaging time of the instrument. The Allan variance is often used as a metric to estimate the stability and the optimum averaging time of a laser spectrometer (Werle 1993, 2011). Laboratory calibration experiments and ground-based open path tests showed that our instrument is stable for up to ~60 secs. Averaging longer than 60 seconds increased the Allan variance and did not improve the SNR of the IPDA lidar. Similar results were obtained in flight although the flight data are harder to assess since the ground returns vary significantly because of varying reflectivity and range.

In 2013, the SPCM nonlinearity and saturation was the most significant systematic error. This was particularly problematic in flights when we flew over bright, highly reflecting clouds. The SPCM dynamic range could not accommodate the rapid change in background signal resulting in lower counts and distortion in the wings of the line shape. In 2014, we significantly reduced this problem by adding seven more SPCMs. We split the output of the multi-mode receiver fiber into eight separate SPCMs using a 1x8 fiber optic splitter and the dynamic range increased by almost two orders of magnitude. Another option for the future would be to replace the SPCMs with a low-noise, high quantum efficiency, HgCdTe avalanche photodiode (APD; Sun et al., 2017b) that has been used in our airborne CO_2 and CH_4 IPDA lidars.

There are other challenges with the retrievals that are caused by the wide spectral scan and the strength of the O_2 lines. Since the O_2 absorptions completely extinguish the laser light at their peak, the SPCMs must still be able to respond to large laser ground returns over highly reflective surfaces and laser light extinction in a single wavelength scan. In addition, our decision to increase the width of the bandpass filter to minimize the wing distortion increased the solar background. Finally, the wavelength scan must be wide enough (~0.4 nm) to trace the O_2 lines. We scan the wavelength by scanning the diode laser current. The diode laser scan is not perfectly linear and the larger the scan the more difficult it is to calibrate the wavelength. In addition, the diode laser output power changes as function of current. The wider the wavelength span the bigger the power changes. Large diode laser power changes result in large changes in the output of the fiber amplifier and even larger changes in the output of the non-linear doubler.

These competing requirements can be reconciled by using a narrower and weaker O_2 line. A weak line that does not completely absorb the laser light imposes less stringent dynamic requirements on the detector. If the line is also narrower, we can reduce the wavelength scan avoid some of the issues associated with the wide scan described above. Finally, with a narrow line we could reduce the width of the bandpass filter without distorting the lineshape and reduce the solar background noise contribution. Of course, such a line must have suitable temperature dependence and be within the EDFA emission range to be viable.

We identified a suitable, weak and narrow O_2 isotope line ($O^{16}O^{18}$) at 764.93 nm that has low temperature dependence. Figure F-9 (Left) shows the expected transmittance from 400 km for a US standard atmosphere and the transmission curves for two narrow etalon filters, 50 and 100 pm, and the resulting $O^{16}O^{18}$ transmittance lineshapes using the two etalon filters. The distortion with the 100 pm etalon filter is small, the laser is no longer extinguished at the peak, and the wavelength scan needed to trace the line is only ~20-30 pm vs. 400 pm. Using a 100 pm etalon filter vs. 0.8 nm will also reduce the solar background by a factor of eight. The weaker line should reduce the dynamic range requirements for the SPCMs and the narrower wavelength scan from should make the wavelength calibration easier and reduce the effects associated with the wide scan.
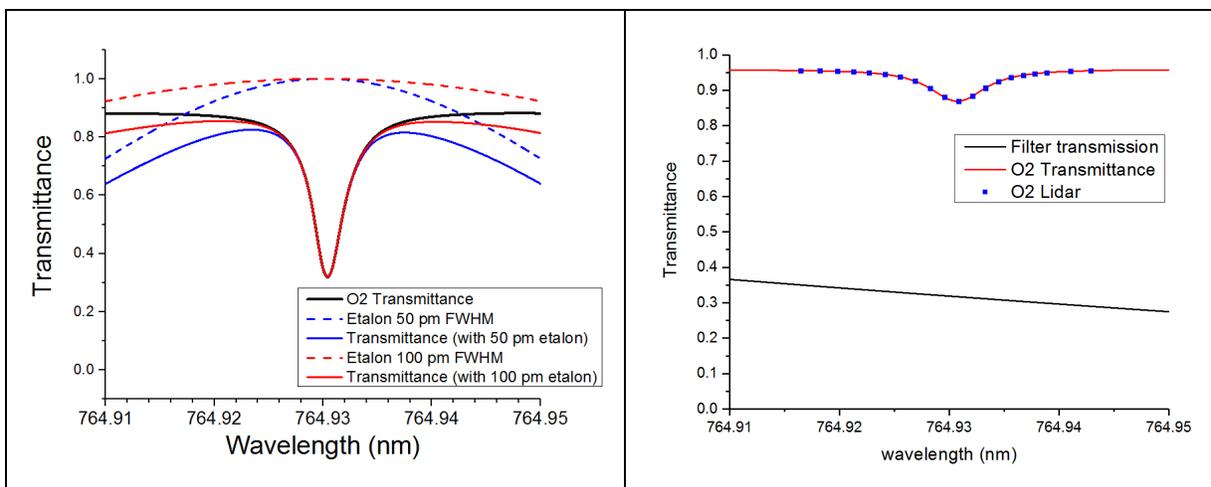
Figure F-9 *(Left)* Expected transmittance from 400 km for a US standard atmosphere (black trace) and the transmission curves for two narrow etalon filters, 50 and 100 pm (blue and red dash traces respectively), and the resulting O_2 transmittance lineshapes using the two etalon filters (blue and red solid line traces respectively). The distortion with the 100 pm etalon filter is minimal, and the minimum transmittance is ~30% and the wavelength scan needed to trace the line is ~20 pm. *(Right)* Theoretical (red) and experimental lidar (blue dots) transmittance from a 3 km open path ground test at GSFC and the associated transmission curve of our existing 0.8 nm filter. Our filter, which is centered near 764.7 nm has a 30% transmittance at 764.93 nm where the $O^{16}O^{18}$ isotope line is centered.

We were able to scan over the isotope line with our existing laser but we did not have a suitable etalon filter. Figure F-9 (Right) shows the theoretical (red) and experimental lidar transmittance (blue dots) obtained from a 3 km open path ground test at GSFC and the transmission curve of our existing 0.8 nm bandpass filter. Our filter, which is centered near 764.7 nm, has a ~30% transmittance at 764.93 nm. However, we were able to retrieve the normalized isotope line transmittance with our lidar, demonstrating the feasibility of the idea. To assess the performance of the lidar for the isotope line a suitable filter needs to be procured and integrated in the instrument. Fitting this line should be significantly easier as the fit will not be as dependent on dynamic range effects that have proven so challenging. Also, the isotopic fractionation, which can lead to variations in the relative abundances of isotopologues, must be well-understood (Keeling, 1995) if this line is to be used.

F.2.6 Summary

Our results show that the DOD measurement accuracy is within 2% of the predicted DOD values with a modest amount of laser energy (1-2 μJ) and the precision is 2.5% in a 10 sec averaging time. These results show that significant improvements are needed to achieve the 0.2% accuracy and precision required for ASCENDS. The laser power must by scaled significantly to reduce the random noise contribution but also various systematic errors must be adequately addressed and quantified to achieve the needed accuracy and precision. Currently the O_2 GSFC IPDA lidar is in hiatus until the ASCENDS ad hoc SDT clarifies the need for O_2 measurements.

F.3 Progress in developing an Airborne Oxygen Lidar with the MFLL (NASA Langley)

Section 5.3.2 discussed lidar column CO_2 measurements made using the MFLL lidar. In order to convert the measured column CO_2 from MFLL or ACES to an averaged column XCO_2 of dry air, we need an accurate estimate of the profiles of temperature (T), pressure (P), and humidity (q) along

the line of sight of the CO_2 optical depth measurement to account for the column dry air amount (or the dry air surface pressure) in the column CO_2 mixing ratio estimates. This could be achieved by using numerical weather/climate model results. Atmospheric assimilations, analyses and reanalyses can provide this kind of information as shown in Section 4.

Another approach is to directly measure the column dry-air amount. Since Oxygen (O_2) is well mixed in the atmosphere, a measure of column O_2 amount is equivalent to a observation of total dry air column. Thus, Harris and Langley started a program to develop an IM-CW lidar to measure O_2 column amount for the surface pressure estimation. More recently, MFLL has been modified to measure O_2 column amounts with an O_2 lidar subsystem.

The same architecture used in the design of IM-CW CO_2 lidar (see Section 5.3.2) can also be used to probe O_2. The CO_2 and O_2 subsystems in MFLL are both similar in form and function, but they use a 5-W Erbium-Doped Fiber Amplifier (EDFA) and a 1.6-W fiber Raman amplifier (Dobler et al., 2011a,b), respectively. The O_2 lasers operating at an online of 1262.531 nm and an offline of 1262.578 nm are used for O_2 IPDA measurements. Like the CO_2 subsystem of MFLL, O_2 wavelengths were selected to minimize water vapor and other trace gas interference effects on the IPDA measurements and to simultaneously maximize the signal-to-noise ratio of the differential absorption optical depth measurements (Ismail and Browell, 1989; Remsberg and Gordley, 1978). Figure 5-10 shows the placement of on-line and off-line laser beams transmitted with respect to the O_2 absorption lines used in the MFLL IPDA O_2 measurements. The key line parameters of the 1.26 μm O_2 absorption lines are summarized in Table F-6.
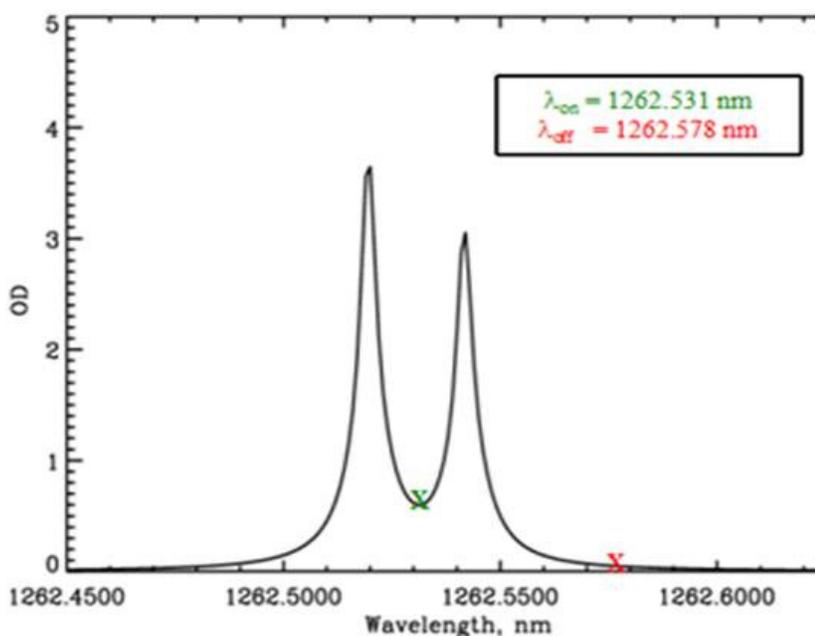
Figure F-10 Calculated spectral profile of the O_2 absorption line doublet at 1262.52195 and 1262.5416 nm (c.f.,Table F-6) and the spectral locations of the on- and off-line laser beams. The plotted values represent the vertically integrated optical depth (OD) of the O_2 absorption lines.

Table F-6 Line Parameters of the O_2 Absorption Lines

	Line center (μm)	ID	Line strength (cm/mol.)	Linewidth (cm^{-1})	Energy of lower state (E") (cm^{-1})
O_2 (1)	1.2625195	RQ5	4.99E-26	0.047	260.50
O_2 (2)	1.2625416	SR5	4.63E-26	0.052	42.224

Table F-7 Parameters for O_2 Lidar Subsystem

| Parameters for Airborne MFLL O_2 Lidar Subsystem	
Seed laser type:	DFB diode laser
Line width	<6 MHz each wavelength
Side mode suppression	Ratio >45 dB
O_2 lines: (vacuum)	1.262531 μm (On), 1.262578 μm (Off)
Modulator:	Semiconductor Optical Amplifier
Modulation type:	Intensity-modulated continuous-wave (IM-CW)
Optical amplifier:	Raman Amplifier
Output power:	1.6 Watts
Optical bandpass filter:	2.4 nm
Telescope	Cassegrain, 8-in. diameter.
Receiver optical throughput	8.5%
Detectors	PIN
Sample rate of digitizer	2 MHz
Encoding scheme:	Rolling tone; Swept-frequency; ~350 ±250 kHz;
Max unambiguous range:	30 km (or 400 samples)
Laser divergence angle:	190 urad (half angle)
Receiver FOV:	240 urad (half angle)
Receiver duty cycle:	100%
Reporting interval:	100 msec (10 Hz)

Furthermore, the same range-encoded intensity-modulation technique used by the CO_2 lidar subsystem is applied to the O_2 lidar subsystem for O_2 column measurements and range determination. The key parameters for the MFLL O_2 lidar subsystem are listed in Table 5-7. Extensive demonstrations of this O_2 capability with the MFLL system were conducted in laboratory and horizontal ground test range environments and in airborne flight campaigns.

The 2011 flight campaign provided the proof-of-concept demonstration of the O_2 lidar subsystem and utilized a standard PIN diode as the detector. The low gain of the PIN detector and low transmitted power at the O_2 wavelengths resulted in lower O_2 SNR_{DAOD} than that for CO_2 SNR_{DAOD} during the same measurement period. The PIN detector was replaced by the DRS HgCdTe APD detector cited in Table 5-4 during the March 2013 DC-8 flight campaign. A rolling tone modulation scheme was used for O_2 transmitted laser beams during the 2011 campaigns. This modulation scheme had four discrete frequencies in the 50-kHz region and allowed independent detection and discrimination of the O_2 on-line and off-line backscatter signals. During the 2013 campaign, the swept frequency IM scheme was used. Besides the CO_2 and O_2 lidars, a Pseudorandom Noise (PN) code laser altimeter was used during the flight campaigns to independently determine the reference range to compare to the swept-frequency-derived range.

Figure F-11 shows a rapid spectral scan of the O_2 doublet measured from 6-km altitude on 7 August 2011 with approximately the same spectral coverage as the O_2 doublet spectra shown in Figure F-10. It illustrates the ability to tune across the absorption feature resulting from the O_2 absorption lines with high spectral resolution (Browell et al., 2012). Column O_2 optical depths were calculated using the IPDA approach, and Figure F-12 shows the variation of O_2 SNR_{DAOD} as a function of range to the surface. The data with diamond points in Figure F-12 were collected on two flights (27 July and 3 August, 2011) that each operated from several altitudes. No background subtraction was included in the calculations, but the data were screened to remove cloudy regions. The 10-s O_2 SNR_{DAOD} values were estimated using the 10-Hz O_2 SNR_{DAOD} statistics.

Figure F-12 shows that the O_2 SNR_{DAOD} varied as the inverse of the range squared, as expected from shot noise limited performance, in the presence of daytime background. Initial analysis of the measurements from the March 2013 flight campaign shows significant improvement in O_2 SNR_{DAOD} as shown by the triangle data points in Figure F-12. These data were collected from several altitude levels in a single flight on 26 March 2013 over similar terrain as that of the 2011 data. More than an order of magnitude improvement in SNR over long ranges (6-12 km) has been found. This improvement is the result of the incorporation of the DRS HgCdTe detector in place of the PIN diode detector used in the 2011 campaign. This demonstrates the capability of airborne retrieval of O_2 column amounts in the presence of high solar background conditions. Figure F-13 shows a comparison between the measured and in-situ derived column O_2 DAOD to the surface from a range of about 3.5 km (Browell et al., 2012). These data were taken from a flight to Castle, CA on 27 July 2011. In situ measurements were used within 10 km of the MFLL DAOD measurement region. A 10-s signal averaging was done prior to DAOD calculation, and in-situ derived DAODs were calculated using a procedure similar to that for the CO_2 DAODs. The 1-σ difference between the in situ and measured DAODs was 1.26% and the average difference of the DAODs was <0.5% (Browell et al., 2012). These measurements show an encouraging result that an O_2 SNR_{DAOD} of 700 or higher can be achieved by current technology development. Further SNR improvement with DRS detector can be expected. Still, using this kind of O_2 lidar system to achieve the precision requirement of <0.25 ppm (or within ~0.06%) for space XCO_2 measurements within

10-s integration time is a challenge when additional variability for O_2 measurements introduced by O_2 laser and other lights at the operating wavelengths are considered (Sharp et al., 2014).
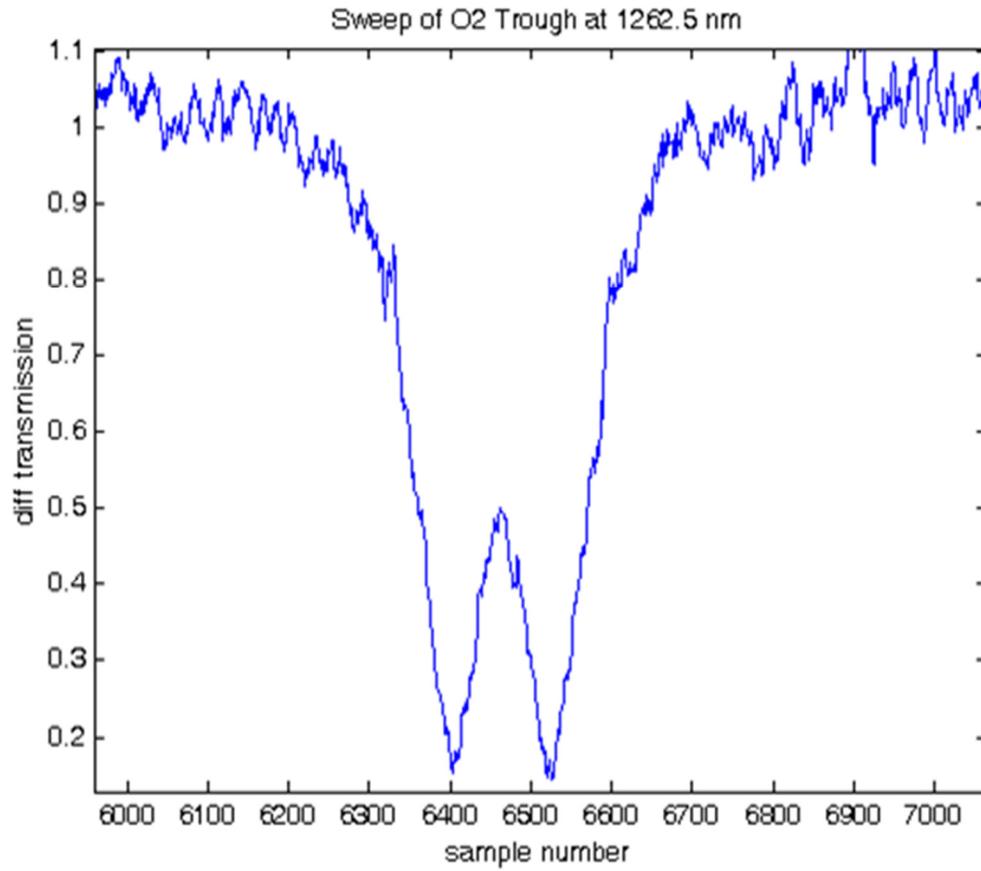
Figure F-11 A lidar spectral sweep across the O_2 doublet made from 6 km altitude on 7 August 2011.
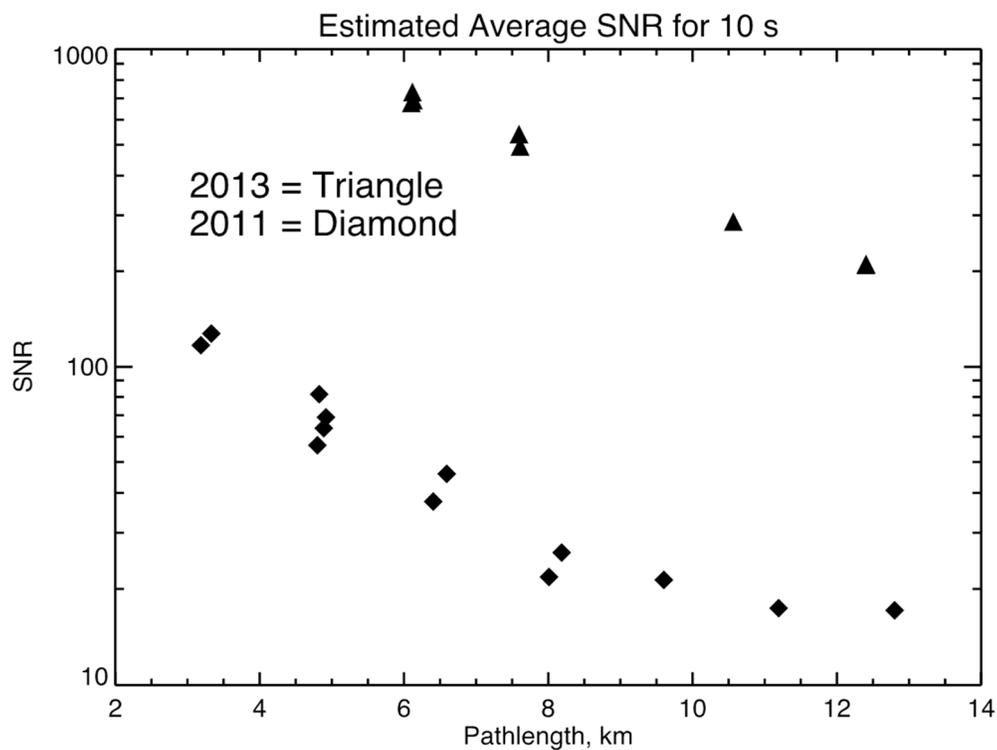
Figure F-12 Variation of SNR in the measurements of O_2 SNR_{DAOD} with range from the DC-8 on 27 July and 3 August 2011 (diamonds) compared with measurements from the 26 March 2013 flight with an improved detector (triangles).
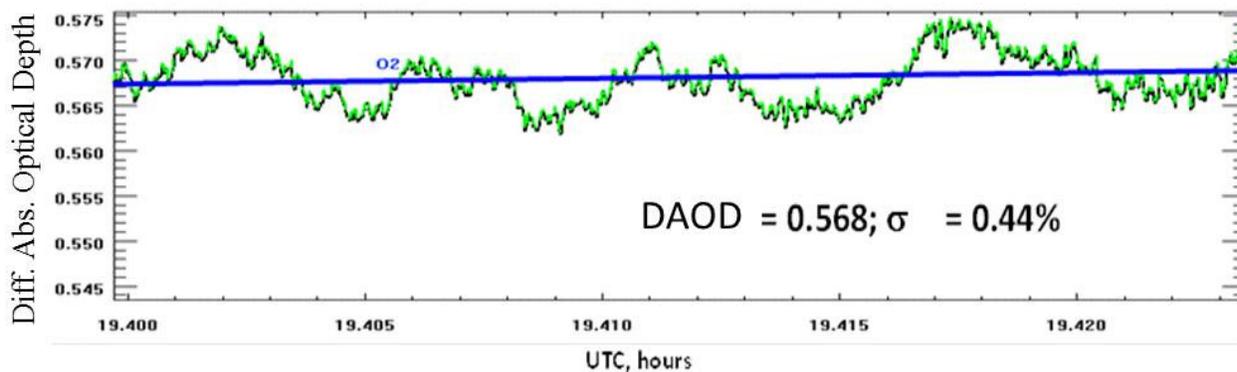
Figure F-13 Comparison of measured and in-situ derived O_2 DAOD from the DC-8 flight on 27 July 2011. Measured values (green line) and in-situ derived values (blue line) are plotted. The figure illustrates precise measurements of O_2 DAODs.